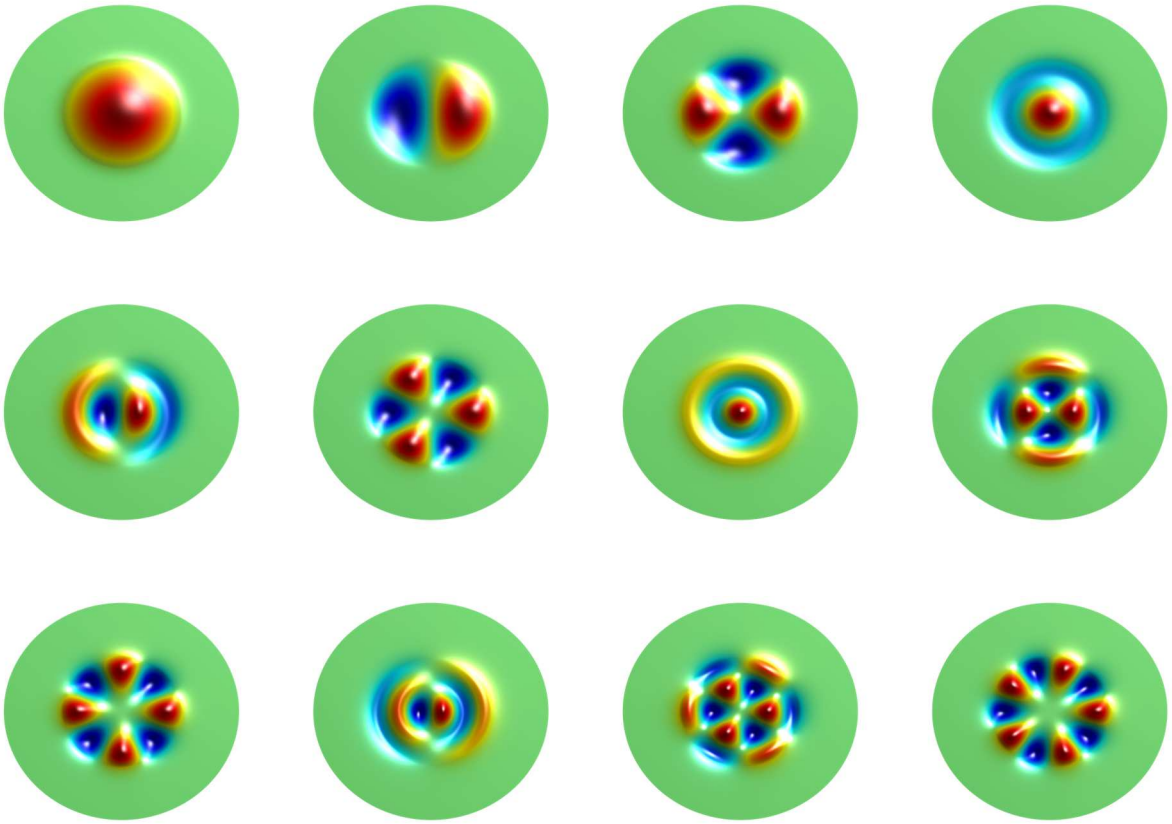

Filipe Marques Ferreira

HIGH CAPACITY OPTICAL TRANSMISSION SYSTEMS BASED ON MODE DIVISION MULTIPLEXING

Tese de Doutoramento em Engenharia Electrotécnica e de Computadores, ramo de especialização em Telecomunicações, orientada pelo Senhor Professor Doutor Henrique José Almeida da Silva e coorientada pelo Senhor Doutor Daniel Diogo Ferrão da Trindade Fonseca, e apresentada ao Departamento de Engenharia Electrotécnica e de Computadores da Faculdade de Ciências e Tecnologia da Universidade de Coimbra.

Junho de 2014

· U C ·

UNIVERSIDADE DE COIMBRA

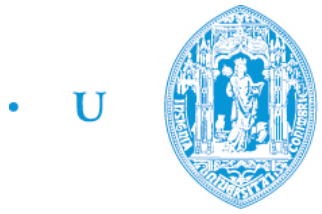

Faculty of Sciences and Technology
Department of Electrical and Computer Engineering

High Capacity Optical Transmission Systems Based on Mode Division Multiplexing

Supervisor:
Professor Doctor Henrique José Almeida da Silva

Co-Supervisor:
Doctor Daniel Diogo Ferrão da Trindade Fonseca

Thesis submitted in accordance with the requirements of the University of Coimbra for the degree of Doctor of Philosophy in Electrical and Computer Engineering

Filipe Marques Ferreira

June 2014

This work was supported by *Fundação para a Ciência e a Tecnologia* and *Coriant Portugal Unipessoal Lda* under Grant Agreement Number SFRH/BDE/51094/2010, and by *European Communities 7th Framework Programme* under Grant Agreement Number FP7-258033 (MODE-GAP).

Aos meus pais, Carlos e Esmeralda

Agradecimentos
Acknowledgments

Os presentes agradecimentos são endereçados a todas as pessoas que contribuíram com o seu apoio e colaboração para a elaboração do trabalho descrito neste documento. Agradeço ao meu orientador, Professor Doutor Henrique Silva por me introduzido no mundo das comunicações por fibra óptica, pelo constante apoio, estímulo e disponibilidade, bem como pela cuidada supervisão científica do meu trabalho. Ao Professor Doutor Paulo Monteiro por me ter dado a inestimável oportunidade de fazer o meu doutoramento num ambiente estimulante na Coriant Portugal. Ao Doutor Daniel Fonseca pela orientação, apoio incansável e meticulosa atenção aos detalhes. Ao Doutor Sander Jansen pela sua orientação no início do meu doutoramento.

The following acknowledgments are addressed to all the people that have contributed with their support and collaboration for the success of this work. Firstly, I would like to express my sincere gratitude to my supervisor, Professor Doctor Henrique Silva for introducing me to the world of optical fiber communications, by the continued support, encouragement and availability, as well as by the careful scientific review of my work. I would like to thank Professor Doctor Paulo Monteiro for giving me the invaluable opportunity to do my Ph.D in a stimulating environment at Coriant Portugal. I wish also to thank Doctor Daniel Fonseca for his supervision, tireless support, availability and painstaking scientific review of my work. In addition, I would like to thank Doctor Sander Jansen for his guidance in the beginning of my Ph.D.

No âmbito do projecto ModeGap, agradeço à Adriana Lobato, Beril Inan, Dirk van der Borne, Maxim Kuschnerov e Marc Bohn pelo empenho nas nossas discussões e resultados científicos, que resultaram num produtivo trabalho conjunto.

As a part of the ModeGap project, I would like to acknowledge Adriana Lobato, Beril Inan, Dirk van der Borne, Maxim Kuschnerov and Marc Bohn for their commitment in our scientific discussions and outcomes, resulting in a productive teamwork.

Todo este trabalho não teria sido o mesmo sem os amigos que fiz nos últimos anos. Primeiro quero agradecer à Sílvia Pato, João Santos e João Pedro pela forma como me ajudaram a integrar em Lisboa e na Coriant. Ao Rui Morais, João Ferreira, Miguel Drummond e José Girão pelas vibrantes tertúlias à volta da mesa de almoço. Por todos os momentos bem passados agradeço ao Nelson Costa, António Eira, Nataša Pavlović, Rui Meleiro, Fernando Jesus, Lara Pellegrino e Pedro Inácio. Em especial quero agradecer ao Paulo Almeida e ao Filipe Bugalho pela amizade que construímos primeiro em Coimbra.

Finalmente, o agradecimento mais importante, aos meus pais, a quem devo tudo o que sou hoje. Os meus pais foram incansáveis na forma como procuraram colocar-me sempre no melhor caminho e proporcionar-me as melhores condições. À minha irmã que tem estado sempre por perto.

Por fim, um agradecimento muito especial à Vânia Almeida pelo carinho, pela paciência, pela compreensão, e por todos os momentos bons que trouxeram felicidade a este caminho.

Obrigado!

Abstract

The present work reports the investigation on high capacity optical transmission systems based on mode division multiplexing (MDM) over few-mode fibers (FMFs). MDM over FMFs is as an attractive solution to overcome the impending capacity crunch of conventional single-mode fiber (SMF) systems, with potential cost, space, and energy savings. An N-fold capacity increase is obtained using a FMF with N independent modes, since each mode can support the same amount of information of a SMF. However, there are some impairments arising from the multimode nature of FMFs, which have to be addressed in order to reach their full capacity: differential mode delay (DMD), linear mode crosstalk (XT), mode-dependent loss (MDL), and inter-modal nonlinearities. Furthermore, a basic MDM-FMF system is composed by: mode multiplexers (MMUXs) and demultiplexers (MDMUXs), multimode amplifiers (MMAs), and multiple-input-multiple-output (MIMO) digital signal processing (DSP). The MMAs are a key component for economic and energy efficient MDM-FMF systems. In order to reduce cost and energy consumption in comparison to N parallel single-mode amplifiers, the MDM channels have to share the pumps power. One of the main difficulties experienced in the design of MMAs is the achievement of low mode dependent gain (MDG). The MMUXs/MDMUXs are responsible for an approximately unitary mapping from the input signals to the FMF modes and vice-versa, such that the transmission impairments can be reverted through MIMO-DSP.

In this thesis, the main impairments of MDM-FMF systems identified above are modeled, allowing to develop several techniques to reduce their impact. A nonlinear semi-analytical model (NSAM) for transmission over FMFs is developed. The design requirements of mode selective phase masks for MMUXs/MDMUXs are investigated regarding the mask resolution, mask phase noise and mask alignments. The design of FMFs with up to 12 non-degenerate linearly polarized (LP) modes, suitable for long-haul transmission, is addressed. Moreover, three methods to extend the transmission reach of MDM-FMFs, by limiting the accumulation of DMD and MDL/MDG along

transmission, are proposed. Finally, an extensive study of the inter-modal nonlinear effects in MDM-FMF systems is presented, identifying the dominant effects as well as possible techniques to reduce the corresponding induced penalty.

Keywords: mode division multiplexing, few-mode fibers, differential mode delay, linear mode crosstalk, mode dependent losses, inter-modal nonlinear effects.

Resumo

O presente trabalho relata a investigação de sistemas de transmissão de alta capacidade com multiplexação por divisão modal (MDM) em fibras com poucos modos (FMFs). MDM em FMFs é uma solução atractiva para ultrapassar a iminente exaustão das fibras monomodais (SMFs) convencionais com uma poupança potencial no custo, espaço e consumo energético. Um aumento da capacidade de N vezes pode ser obtido utilizando uma FMF com N modos independentes, uma vez que cada modo tem uma capacidade igual à de uma SMF. Contudo, a natureza multimodal das FMFs introduz limitações ausentes nas SMFs: atraso modal diferencial (DMD), diafonia modal linear (XT), atenuação dependente do modo (MDL), e efeitos não-lineares intermodais. Estas limitações têm que ser abordadas para cumprir todo o potencial das FMFs. Para além disso, um sistema MDM-FMF básico é composto por: multiplexadores modais (MMUXs) e demultiplexadores modais (MDMUXs), amplificadores multimodais (MMAs), e processamento digital de sinal (DSP) para sistemas de múltiplas entradas e múltiplas saídas (MIMO). Os MMAs são um componente chave no projecto de sistemas MDM-FMF economicamente competitivos e energeticamente eficientes. A potência das bombas tem que ser partilhada entre os canais MDM para atingir uma poupança no custo e consumo energético. Uma das maiores dificuldades no projecto de MMAs é a obtenção de um ganho dependente do modo (MDG) reduzido. Os MMUXs/MDMUXs são responsáveis por um mapeamento aproximadamente unitário entre os sinais de entrada e os modos guiados pelas FMF e vice-versa, para que seja possível reverter os efeitos de transmissão utilizando DSP-MIMO.

Nesta tese, as principais limitações dos sistemas MDM-FMF acima identificadas são modeladas de forma a permitir o desenvolvimento de várias técnicas para reduzir o seu impacto. Um modelo não-linear semi-analítico para a transmissão em FMFs é desenvolvido. O projecto de máscaras de fase para MMUXs/MDMUXs é realizado, especificando os requisitos na resolução, ruído de fase e alinhamento. O projecto

de FMFs adequadas para transmissão de longo alcance é realizado considerando até 12 modos não-degenerados linearmente polarizados. Além disso, são propostos três métodos para a extensão do alcance de transmissão de sistemas MDM-FMF através da redução da DMD e MDL/MDG acumuladas. Finalmente, um estudo alargado dos efeitos não-lineares intermodais é apresentado, identificando os efeitos dominantes bem como potenciais técnicas para a redução da penalidade induzida pelos mesmos.

Palavras-chave: multiplexação por divisão modal, fibras com poucos modos, atraso modal diferencial, diafonia modal linear, atenuação dependente do modo, efeitos não-lineares intermodais.

Contents

List of Abbreviations

BER	bit-error rate.
CIR	channel impulse response.
CMA	constant modulus algorithm.
CMT	coupled mode theory.
CNLSE	coupled nonlinear Schröndinger equations.
CP	cyclic prefix.
CW	continuous-wave.
DC	DMD compensated.
DC-FMF	DMD compensated FMF.
DCF	dispersion-compensating fiber.
DCI	depressed-cladding index.
DMD	differential mode delay.
DSP	digital signal processing.
DWDM	dense wavelength-division multiplexing.
dXT	distributed XT.
EDF	erbium-doped fiber.
EDFA	erbium-dopped fiber amplifier.
ER	extinction ratio.
FDE	frequency-domain equalization.
FEC	forward-error correction.
FIR	finite impulse response.
FMF	few-mode fiber.
FWM	four-wave mixing.
GCCT	graded-core and a cladding trench.
GI	graded-index.
GSS	golden section search.

HCF	hollow-core fiber.
IL	insertion loss.
ILD	inherently low DMD.
ILD-FMF	inherently low DMD FMF.
IM	intensity modulation.
IM-DD	intensity modulation with direct detection.
IM-FWM	inter-modal four-wave mixing.
IM-NL	inter-modal nonlinear.
IM-XPM	inter-modal cross-phase modulation.
ITU-T	International Telecommunication Union-Telecommunication Standardization Sector.
LCoS	liquid crystal on silicon.
LED	light emitting diode.
LHS	left-hand side.
LP	linearly polarized.
LPFG	long period fiber grating.
MBL	macro-bend losses.
MC-MMF	multicore-multimode fiber.
MCF	multi-core fiber.
MDD	maximum DMD deviation.
MDG	mode dependent gain.
MDL	mode-dependent loss.
MDM	mode-division multiplexing.
MDMUX	mode demultiplexer.
MER	mode extinction ratio.
MIMO	multiple-input-multiple-output.
ML	maximum-likelihood.
MM-CNLSE	multimode coupled nonlinear Schrödinger equations.
MM-EDFA	multimode erbium-doped fiber amplifier.
MM-MW-CNLSE	multimode multi-wavelength coupled nonlinear Schrödinger equations.
MM-RFA	multimode Raman fiber amplifier.
MMA	multimode amplifier.
MMF	multimode fiber.
MMSE	minimum mean square error.
MMUX	mode multiplexer.
MP	maximum input power.

MSI	multiple-step index.
MTD	maximum tolerable deviation.
MW	multi-wavelength.
NLSE	nonlinear Schrödinger equation.
NRZ	non-return-to-zero.
NSAM	nonlinear semi-analytical model.
OF	objective function.
OFDM	orthogonal frequency division multiplexing.
OOK	on-off keying.
OSNR	optical signal-to-noise ratio.
PDM	polarization-division multiplexing.
PM	phase mask.
PMD	polarization-mode dispersion.
PMF	polarization maintaining fiber.
QPSK	quaternary phase-shift keying.
RHS	right-hand side.
RK45	Runge-Kutta 4th-5th order.
ROSNR	required optical signal-to-noise ratio.
RX	receiver.
SA	semi-analytical.
SDM	spatial-division multiplexing.
SE	spectral efficiency.
SI	step-index.
SM	single-mode.
SMF	single-mode fiber.
SMT	single-mode transmission.
SPM	self-phase modulation.
SSFM	split-step Fourier method.
SSMF	standard single-mode fiber.
sXT	splice XT.
TDE	time-domain equalization.
TMF	two-mode fiber.
TS	training symbol.
TX	transmitter.

WDM	wavelength-division multiplexing.
xM	x non-degenerate LP modes.
XPM	cross-phase modulation.
XT	crosstalk.
ZF	zero forcing.

List of Symbols

(ρ_d, ϕ_d)	random position of the fiber core axis in cylindrical coordinates.
(ρ, ϕ)	radial distance ρ and azimuth ϕ in a cylindrical coordinate system.
(x,y)	abscissa and ordinate coordinates in Cartesian coordinate system.
α	fiber core exponential decay factor.
α_{ui}	attenuation of the polarization i of mode u.
$\beta_{l,u}$	l^{th} order angular frequency derivative of $\beta_u(\omega)$ at $\omega = \omega_0$.
$\beta_{l,ui}$	l^{th} order angular frequency derivative of $\beta_{ui}(\omega)$ at $\omega = \omega_0$.
$\beta_{l,uvi}$	l^{th} order angular frequency derivative of $\beta_{ui}(\omega)$ at $\omega = \omega_v$.
$\beta_u(\omega)$	propagation constant of mode u at ω.
$\beta_{ui}(\omega)$	propagation constant of the polarization i of mode u at ω.
$\chi^{(3)}_{xxxx}$	third-order silica susceptibility.
$\delta_{i_1,i}$	Kronecker delta, $\delta_{i_1,i} = 1$ for $i_1 = i$ and 0 otherwise.
δx	random displacement of the abscissa coordinate.
δy	random displacement of the ordinate coordinate.
$\Delta n(\rho)$	relative refractive index difference profile.
Δn_{co}	relative refractive index difference profile at $\rho = 0$.
Δn_{tr}	relative refractive index difference profile at the trench of a GCCT profile.
$\Delta\beta_{u_1i_1,u_2i_2,u_3i_3,ui}$	phase mismatch between waves u_1i_1, u_2i_2, u_3i_3 and ui, at $\omega = \omega_0$.

$\Delta\beta_{u_1,u}$	phase mismatch between modes u_1 and u at $\omega = \omega_0$.
$\Delta\varepsilon(x,y)$	waveguide imperfection.
Δn_i	relative refractive index of step i of a MSI profile.
ε_0	permittivity of free space.
$\varepsilon_p(x,y)$	ideal profile permittivity.
$\gamma_{u_1u_2u_3u}$	nonlinear coefficient between modes u_1,u_2,u_3 and u.
k_0	propagation constant in free space.
λ	wave wavelength.
μ_0	permeability of free space.
ω	angular frequency.
ω_z	spatial frequency.
ψ	DMD target for fiber profile optimization.
ψ_i	groups the independent inter-modal polarization combinations.
$\rho_{d,max}$	maximum random radial displacement of the fiber core axis.
$\left(\sigma_{u_1u}^{xFWM}\right)^2$	variance of the symbol "1" considering only the MM-MW-CNLSE $xFWM$ terms for modes u_1 and u.
$\left(\sigma_{u_1u}^{xXPM}\right)^2$	variance of the symbol "1" considering only the MM-MW-CNLSE $xXPM$ terms for modes u_1 and u.
ξ_i	groups the independent intra-modal polarization combinations.
$aDMD$	average DMD of a DC-FMF segment.
$A_{u_1u_2u_3u}^{eff}$	inter-modal effective area of mode combination (u_1,u_2,u_3,u).
$A_u(z,t)$	slowly varying field envelope of mode u.
$A_{ui}(z,t)$	slowly varying field envelope of polarization i mode u.
$\tilde{A}_u(z,\omega)$	time Fourier transform of $A_u(z,t)$.
$\tilde{A}_{ui}(z,\omega)$	time Fourier transform of $A_{ui}(z,t)$.
A_u^{NUM}	mode u numerical amplitude solution.
A_u^{SA}	mode u semi-analytical amplitude solution.
c_0	light velocity in free space.
$C_{TX\text{-}u}$	coupling coefficient between the filtered SMF LP_{01} mode incident on the FMF surface and the mode u guided by the FMF.

C_{u,u_1}	linear XT coupling coefficient between mode u and mode u_1.
C_{FWM}	nonlinear contribution due to FWM in the MM-MW-CNLSE equation.
$C_{IM\text{-}FWM}$	nonlinear contribution due to IM-FWM in the MM-MW-CNLSE.
$C_{IM\text{-}XPM}$	nonlinear contribution due to IM-XPM in the MM-MW-CNLSE.
$C_{IM\text{-}NL}$	inter-modal nonlinear contribution in the MM-CNLSE equation.
$C_{INTRA\text{-}NL}$	intra-modal nonlinear contribution in the MM-CNLSE equation.
C_{SPM}	nonlinear contribution due to SPM in the MM-MW-CNLSE equation.
C_{XPM}	nonlinear contribution due to XPM in the MM-MW-CNLSE equation.
$d_{u_1v_1,uv}$	walkoff parameter between the (u_1v_1) pump channel and the (uv) probe channel.
DMD	differential mode delay parameter.
$DMD^{LP_{\mu\nu}}$	DMD of the $\mathrm{LP}_{\mu\nu}$ mode measured relatively to the LP_{01}.
$DMD_{u_1,u}$	DMD between two modes u_1 and u at $\omega = \omega_0$, where u is the reference mode.
$DMD_{u_1vi_1,uvi}$	DMD between the polarization i_1 of mode u_1 and the polarization i of mode u at $\omega = \omega_v$, taking uvi as reference.
D	chromatic dispersion parameter.
D_u	chromatic dispersion parameter of mode u at $\omega = \omega_0$.
D_{uv}	chromatic dispersion parameter of mode u at $\omega = \omega_v$.
D_{uvi}	chromatic dispersion parameter of the polarization i mode u at $\omega = \omega_v$.
$\widetilde{\mathbf{E}}(\mathbf{r},\omega)$	total electric field in the spectral domain.
$\mathbf{E}(\mathbf{r},t)$	total electric field in the time domain.
E_i	$\widehat{i}$ polarization component of $\mathbf{E}(\mathbf{r},t)$.
$F_{LP_{01}}^{PM\text{-}SMF}$	phase mask design: LP_{01} field distribution after transmission through the phase mask (PM).

$F_{LP_{01}}^{SMF}$	phase mask design: LP_{01} field distribution at SMF front end.
$F_u(x,y)$	electrical field distribution of mode u.
F_u^{FMF}	phase mask design: phase of the electric field distribution of the target FMF mode u.
H_{u_1}	magnetic field distribution of mode u_1.
$H_{u_1v_1,u0}^{xXPM}(\omega)$	linear transfer function of the $xXPM$ induced intensity modulation in the $(u, v = 0)$ probe channel associated with the (u_1, v_1) pump channel.
$\widehat{i}$	unit linear polarization vector.
j	imaginary unit.
L	fiber length.
$lDMD$	DMD parameter of a ILD-FMF.
L_n	length of the negative DMD FMF in a DC-FMF segment.
L_p	length of the positive DMD FMF in a DC-FMF segment.
L_s	fiber segment length.
$maxDMD$	maximum DMD among the guided modes and over the defined wavelength range ($maxDMD$).
MBL	macro-bend losses parameter.
MDD	maximum DMD deviation relatively to the targeted DMD over the C-band.
MP_{ba}^{xFWM}	maximum input power per channel for a Q-factor of 7 considering only the MM-MW-CNLSE $xFWM$ terms for modes b and a.
MP_{ba}^{xXPM}	maximum input power per channel for a Q-factor of 7 considering only the MM-MW-CNLSE $xXPM$ terms for modes b and a.
MSE_u	mean squared error between the semi-analytical results and the numerical results calculated for mode u.

MTD	maximum tolerable deviation of the fabricated fiber parameters for $DMD \leq 12\,\text{ps/km}$.
n_2	Kerr coefficient.
$n(\rho)$	refractive index profile.
N_{st}	number of steps of a MSI profile.
n_{cl}	refractive index of the cladding.
n_{co}	refractive index of the core axis.
$nDMD$	DMD parameter the negative DMD FMF in a DC-FMF segment.
$\overline{n}^u$	effective index of mode u.
$\overline{n}_g^u$	effective group index of mode u.
N_u	normalization factor for the field distribution of mode u.
OF	objective function for fiber profile optimization.
$pDMD$	DMD parameter the positive DMD FMF in a DC-FMF segment.
$\widetilde{\mathbf{P}}_{\mathbf{NL}}(\mathbf{r},\omega)$	time Fourier transform of the nonlinear polarization $\mathbf{P}_{\mathbf{NL}}(\mathbf{r},t)$.
$\mathbf{P}_{\mathbf{NL}}(\mathbf{r},t)$	nonlinear polarization due to the third-order nonlinear silica susceptibility.
P_{NL_i}	$\widehat{i}$ polarization component of $\mathbf{P}_{\mathbf{NL}}(\mathbf{r},t)$.
$PSD_{pump}(\omega)$	power spectral density of an intensity modulated pump.
P_u	optical power of mode u at $\omega = \omega_0$.
P_{uv}	optical power of the channel at $\omega = \omega_v$ in mode u.
$P^{xFWM}_{uv_1,u_1v_2,u_1v_3,u0}$	power of the $xFWM$ product generated at $(u, v = 0)$ considering three CW signals in (uv_1, u_1v_2, u_1v_3).
Q	Q-factor.
$Q^{xFWM}_{u_1u}$	Q-factor of a channel in $(u, v = 0)$ considering three CW signals in (uv_1, u_1v_2, u_1v_3).
$Q^{xXPM}_{u_1u}$	Q-factor of a probe channel in $(u, v = 0)$ considering a pump in (u_1, v_1).

$\mathbf{r}$	position vector in Cartesian coordinates (x, y, z).
R_c	fiber curvature radius.
S	chromatic dispersion slope parameter.
S_u	chromatic dispersion slope parameter of mode u at $\omega = \omega_0$.
S_{uv}	chromatic dispersion slope parameter of mode u at $\omega = \omega_v$.
S_{uvi}	chromatic dispersion slope parameter of the polarization i mode u at $\omega = \omega_v$.
sXT	splice XT.
t	time unit.
V	normalized frequency.
$v_{g,u}$	group velocity of mode u.
w_1	fiber core radius.
w_2	radial distance between the end of the core and the beginning of the trench in a GCCT profile.
w_3	trench width in a GCCT profile.
w_{st}	step width of a MSI profile.
$xFWM$	equal to FWM for $u_1 = u$ or equal to IM-FWM for $u_1 \neq u$.
$xXPM$	equal to XPM for $u_1 = u$ or equal to IM-XPM for $u_1 \neq u$.
xM	x non-degenerate LP modes.
$XT_{u_1,u}$	XT from mode u to mode u_1.
$XT_{TX\text{-}u}$	phase mask design: linear XT generated at the transmitter during the conversion of the SMF LP_{01} into the FMF mode u.
z	height coordinate in Cartesian coordinate system or distance of propagation.
z_n	discrete points considered in a specific fiber length.

List of Tables

List of Figures

Chapter 1

Introduction

1.1 Motivation and Scope of the Thesis

Fiber optic communication systems are today present in all telecommunication networks: access, metropolitan area, regional, long-haul, ultra long-haul and submarine. The success of optical networks is truly spectacular, remembering that in the mid-1970s almost all communication systems relied on the transmission of information over electrical cables or unguided propagation of electromagnetic radiation. The success of optical networks has its roots in one critical invention: low-loss silica based optical fibers, namely single-mode fibers (SMFs). Modern SMFs present a loss of 0.17-0.35 dB/km over ∼40 THz centered at ∼200 THz, such as the so-called low water peak fibers like AllWave™ and SMF-28e™. The broad low-loss frequency band of SMFs allows transmitting large quantities of information over long distances. Other telecommunications systems present frequency bands several orders of magnitude shorter: a few hundreds of MHz in satellite telecommunications, a few tens of MHz in digital subscriber lines, and a few tens of MHz in wireless systems.

The optical networks capacity has increased more than 10000 times since the second generation of commercial systems deployed in the 1980s with bit rates of ∼1 Gb/s. In the mid-1990s, the introduction of wavelength-division multiplexing (WDM) and large bandwidth erbium-dopped fiber amplifiers (EDFAs) allowed an extremely rapid growth of the available capacity. At that time, the capacity growth was firstly achieved by increasing the number of channels and then increasing the bit rate per channel. Bit rates for WDM systems started at 2.5 Gb/s in the 1990s, increased to 10 Gb/s in 1996, and to 40 Gb/s in 2003. Up to 2003, almost all the optical transmission systems were using the intensity modulation with direct detection (IM-DD) scheme, by encod-

ing the binary digits with different power levels. However, later on, the development of 40 Gb/s IM-DD systems has shown that the next capacity increase could not be attained by further increasing the bit rate per channel, since signal bandwidth could no longer be accommodated in a 50 GHz channel spacing grid (the most common grid spacing). Consequently, further capacity increase was obtained by increasing spectral efficiency (SE), using two properties of optical waves unexplored until then: phase and polarization. Today high-capacity systems use quadrature phase-shift keying (QPSK) modulation and polarization-division multiplexing (PDM). QPSK modulation consists on the encoding of two bits per time slot on four possible phase values, and PDM consists in sending simultaneously two independent signals (QPSK modulated, for example) into two orthogonal polarizations. However, modulation formats enhancing the spectral efficiency get increasingly susceptible to signal distortions induced by nonlinear effects on the optical fiber [1].

One main limitation of silica based fibers is its inherent nonlinearity, known as the Kerr effect [2]. The Kerr effect is responsible for introducing nonlinear signal distortion that increases with signal power, being the distortion increase faster than signal power increase. Consequently, there is a maximum quantity of information that can be transmitted over the low-loss frequency band in optical fibers. The capacity limit can be calculated using the Shannon-Hartley theorem modified to include fiber nonlinearities [1, 3]. The nonlinear capacity limit in SMFs depends on their physical properties, namely: attenuation, chromatic dispersion and nonlinear coefficients [3]. The nonlinear capacity limit for a 500 km long standard single-mode fiber (SSMF) is between 70 Tb/s and 175 Tb/s, using only the C-band and using the C+L band, respectively [1]. The ever growing demand for higher data rate will eventually drive the systems to approach the SSMFs nonlinear capacity limit.

The current annual growth rates of internet traffic and capacity of commercial optical fiber systems are approximately 50 % and 20 %, respectively [3]. Furthermore, the capacity of under development systems is a factor of 2 below the SSMFs nonlinear capacity limit. Consequently, in the next decade a massive deployment of parallel fibers/systems or regenerators is inevitable [4]. Besides, if the traffic and capacity growth rates remain constant, the required number of fibers and systems will double every 3 years. An alternative to parallel fibers might be the development of advanced SMFs with reduced loss and nonlinear coefficients. However, it has been shown in [5] that even if significant improvements of SMFs are achieved, the expectable capacity increase is lower than a factor of 2. For instance, decreasing attenuation from 0.2 dB/km to 0.05 dB/km, conjectured to be achieved using hollow-core fibers (HCFs)

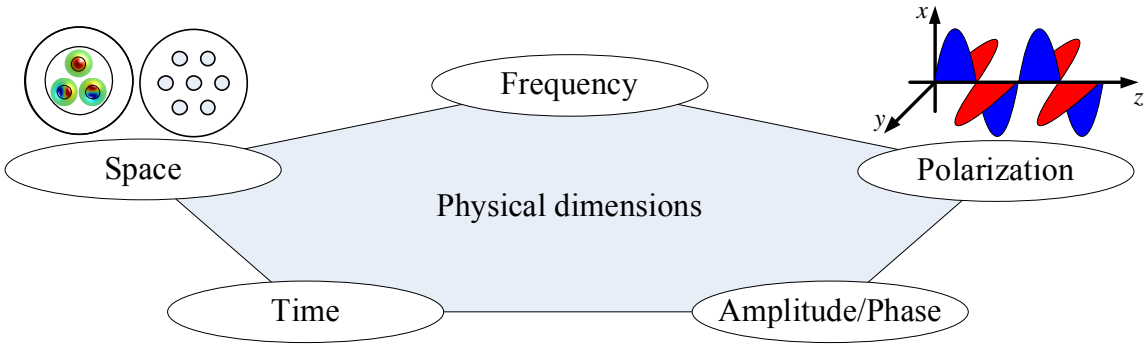

Figure 1.1: Optical fibers capacity known physical dimensions. Multimode and multi-core fibers support multiple spatial modes.

at a wavelength of 2 µm [6], increases capacity only from 8 bits/s/Hz to 9 bits/s/Hz, for 1000 km. Similarly, a reduction of the fiber nonlinear coefficient by a factor of 1000, that is conjectured to be achieved using HCFs [6], would only increase capacity by approximately 30 % (increasing the signal power by 1000 times). The tunning of the fiber chromatic dispersion produces even smaller capacity improvement than the reduction of loss and nonlinear coefficients [5]. As a result, the remaining alternative that appears to be the most effective way to increase the capacity per fiber is to use fibers supporting multiple spatial modes, since the other known physical dimensions of optical fibers capacity, shown in Fig. 1.1, have already been used: amplitude/phase, time, frequency and polarization. Systems based on multimode fibers (MMFs) or multi-core fibers (MCFs) have the potential to reduce the cost per bit. MCFs are fibers with a different number of cores placed on a hexagonal grid (typically). Fibers that contain a single large core that can support multiple spatial modes are called MMFs. If the number of spatial modes supported is between 2 and 10-20, one generally refers to these as few-mode fibers (FMFs). A fiber with several cores, each core guiding multiple modes is also possible, called multicore-multimode fibers (MC-MMFs). Fig. 1.2 shows the cross-sections of these fiber types. The additional capacity of MCFs and FMFs is exploited using as independent channels each core and each mode, respectively, a technique known as spatial-division multiplexing (SDM). In the particular case of FMFs, SDM is referred as mode-division multiplexing (MDM). FMFs present higher potential to reduce the cost per bit, because they carry more data per unit area and provide higher power efficiency in terms of optical amplification and nonlinearity tolerance, with respect to MCFs [7]. Therefore, the work in this thesis is focused on MDM-FMF systems.

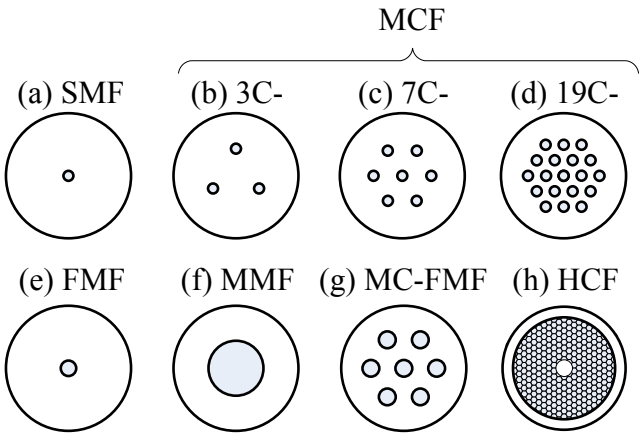

Figure 1.2: Cross-section of a: (a) SMF, (b) 3C-MCF, (c) 7C-MCF, (d) 19C-MCF, (e) FMF, (f) MMF, (g) MC-FMF and (h) HCF.

1.1.1 Few-Mode Fibers

The key characteristic of FMFs is their theoretically higher capacity, since each mode can support the same amount of information of a SMF. However, there are also some impairments arising from the multimode nature of the fiber, which reduce their capacity: the differential mode delay (DMD), linear mode crosstalk (XT), mode-dependent loss (MDL), and inter-modal nonlinearities (IM-NLs). DMD arises from the different propagation velocities of the guided modes. As a consequence, fractions of the same light pulse travelling in different modes reach the receiver at different instants, leading to pulse broadening. Linear XT occurs due to the fiber imperfections [8], fiber splices, mode multiplexers (MMUXs) and mode demultiplexers (MDMUXs). The combined effect of DMD and linear XT [9] is to spread the channel impulse response (CIR) over time, thereby increasing the equalization complexity [10]. The MDL origin includes all inline components such as amplifiers, MMUXs/MDMUXs or even the own fiber, as the result of modes different attenuation coefficients. Unlike DMD and XT, MDL poses a fundamental performance limitation on the equalization. In the extreme case, MDL is equivalent to a reduction in the number of propagating modes, leading to a proportional decrease in data rate or channel capacity.

The first research works on FMFs were conducted as early as 1980 [11]. At that time, two-mode fibers (TMFs) were used as large-core alternatives to SMFs in order to ease the splicing tolerance requirements and to obtain lower bending losses [11]. Later, in the 1990s, TMFs were also considered as dispersion-compensating fibers (DCFs) [12]. The fiber was designed in such a way that the higher-order mode

guided presented a large negative chromatic dispersion, allowing effective chromatic dispersion compensation.

Recently, several works were reported about FMFs used in high-capacity MDM systems [13–17]. These FMFs present significantly lower DMD, lower XT and lower MDL, compared to MMFs. The most significant research demonstrations have so far concentrated on the simplest FMF, supporting only 2 non-degenerate linearly polarized (LP) modes: LP_{01} and LP_{11} (composed by two degenerate modes: LP_{11a} and L_{11b}). The first FMFs presented were built using simple refractive index profiles: step-index (SI) and graded-index (GI). For the reported SI-FMFs, the DMD values were on the order of ns/km, limiting the distance reach to a few tens of kilometers [13, 18, 19]. The development of GI-FMFs contributed to achieve DMD values lower than 50 ps/km [20, 21]. Later, more flexible profiles composed by a graded-core and a cladding trench (GCCT) were proposed, enabling the design of FMFs with 2 non-degenerate LP modes presenting DMD values lower than 10 ps/km [22], denoted inherently low DMD FMFs (ILD-FMFs). Furthermore, it has been shown that, combining FMFs with opposite sign, DMD mitigation could be achieved, called DMD compensated FMFs (DC-FMFs). In such way, a net DMD as low as 5 ps/km has been demonstrated [23]. However, the development of fibers with higher number of modes and DMD values lower than 10 ps/km remains a necessity. It has been shown in [24] that, considering similar levels of complexity for nonlinearity mitigation in a SSMF, only FMF systems with 4 or more LP modes (counting degenerate modes) offer an actual capacity increase. In this thesis, the design of FMFs with 12 non-degenerate LP modes (21 LP modes, counting degenerate modes) with a DMD lower than 10 ps/km over the C-band is addressed.

1.1.2 Mode-Division Multiplexing

MDM relies on spatial multiplexing of light signals using the fiber modes orthogonality, and hence is orthogonal to WDM. Thus, the capacity enhancing factors for MDM and for WDM are multiplied. At the receiving end of the link, the MDM signals have to be demultiplexed using again the modes orthogonality. In FMF links, some coupling between the modes can arise even before transmission, in the MMUX. Successful MDM demultiplexing without high-order multiple-input-multiple-output (MIMO) equalization requires that only a limited amount of mode coupling occurs, which is typically the case for short distances. Considering a FMF with the lowest distributed XT value reported, -40 dB/km [25], and the XT tolerance value for

PDM-QPSK signals, -16 dB, for 1 dB of required optical signal-to-noise ratio (OSNR) penalty at bit-error rate (BER) equal to 10^{-3} [26], the distance reach is shorter than 240 km. Therefore, a long-haul MDM system requires the use of high-order MIMO to compensate for DMD and XT effects.

The MDM concept was first proposed on conventional MMFs in the early 1980s [27–29]. These proposals used spatial filtering techniques (different radial and/or angular offsets) to launch and detect two modes at the ends of a 10 m conventional GI-MMF. Since 2000, MDM has been proposed for capacity extension of datacom MMF based systems [30]. In this case, MIMO digital signal processing (DSP) is used to recover transmission channels previously established selectively launching light into a given mode group [31, 32]. Even so, the transmission distance is limited to less than ∼10 km due to MMF impairments [31], such as: high loss, high DMD, high MDL and strong XT that arises due to close propagation constants between mode groups.

Recent works have reported experimental high-capacity MDM systems over FMFs. In 2011, three experiments were reported at the same conference (*Optical Fiber Communication Conference*) using FMFs with 3 LP modes (LP_{01}, LP_{11a} and LP_{11b}): two experiments reported the transmission of 100 Gb/s signals in 2 LP modes over 4.5 km [13] and 40 km [15], and the other one reported the transmission of 56 Gb/s signals in each of the 3 LP modes over 10 km [14]. Afterwards, the introduction of multimode amplifiers (MMAs) allowed to increase the number of WDM channels, either using multimode erbium doped-fiber amplifiers (MM-EDFAs) or using multimode Raman fiber amplifiers (MM-RFAs). In [33] the transmission of 88 WDM channels over 50 km using a MM-EDFA was demonstrated. At the same time, the development of FMFs with more complex profiles and low DMD values allowed to extend the distance reach. In [23], using a DC-FMF with net DMD as low as 5 ps/km, a recirculating loop and a MMA composed by 3 single-mode (SM)-EDFAs, the present transmission distance record was set at 1200 km.

Innovations presented over the last years have demonstrated the feasibility to increase capacity by more than ten times using MDM over FMFs. Despite the achieved progress, current implementations have not yet met the requirements of commercialization necessitating technological leaps in terms of both functionality and performance, namely: i) FMFs supporting an higher number of modes (10 to 20 modes) presenting at the same time low values of DMD adequate for long-haul transmission; ii) advanced transmission schemes that can ensure low DMD accumulation; iii) MIMO-DSP techniques to maximize the transmitted capacity keeping the complexity

at realizable levels. The work developed along this thesis addressed the aforementioned challenges.

1.2 Objectives and Organization of the Thesis

The main objectives of the present thesis have been the research and development of MDM-FMF systems. The main impairments of MDM-FMF systems are identified and modeled, enabling the development of several techniques to reduce their impact, namely: DMD, modal XT, MDL/mode dependent gain (MDG) and IM-NLs. A nonlinear semi-analytical model (NSAM) for transmission over FMFs is developed. The design of MMUXs/MDMUXs based on mode selective phase masks is investigated regarding the mask resolution, mask phase noise and mask alignments. The design of FMFs with low DMD suitable for long-haul transmission is addressed, considering up to 12 non-degenerate LP modes. Moreover, three methods to extend the transmission reach of MDM-FMFs by limiting the accumulation of DMD and MDL/MDG along transmission are proposed. Finally, an extensive study of the inter-modal nonlinear effects in MDM-WDM-FMF systems is presented, where the dominant effects as well as possible techniques to reduce their induced penalty are identified.

This thesis is structured in 7 chapters and 3 appendices that support the main document. In chapter 2, a brief summary on the theory of modal propagation in FMFs is presented, in order to gain a clear insight on the major properties of FMFs. In this chapter, the main concepts and notions used throughout the thesis are introduced. Moreover, an extensive review of the literature about FMFs is presented with emphasis on fiber properties such as DMD and modal XT. The basic system concept common to the majority of the MDM-FMF systems proposed in the literature is explained, and different implementations of system components are reviewed, namely: MMUXs/MDMUXs, MMAs and MIMO-DSP.

In chapter 3, a method for the semi-analytical solution of the coupled linear differential equations that describe the linear XT in FMFs due to waveguide imperfections is proposed. A set of multimode coupled nonlinear Schrödinger equations (MM-CNLSE) for nonlinear simulation of FMF transmission including the linear XT is derived, considering a pulse envelope per mode per polarization. The MM-CNLSE obtained can be solved modifying the split-step Fourier method (SSFM) to include the respective linear effects and to allow the simulation of FMFs with M modes. Moreover, MMUXs/MDMUXs based on phase masks (PMs) are optimized in order

to enable the study of MDM transmission in the following chapters. Afterwards, the general simulation setup of a MDM-FMF system used along this thesis is presented. Finally, simulation results for the transmission over a SI-TMF are obtained, allowing a qualitative validation of experimental results provided in the literature.

In chapter 4, the design of FMFs with up to 12 non-degenerate LP modes using a GCCT or a multiple-step index (MSI) profile is proposed. The profiles parameters are optimized in order to achieve the lowest DMD and macro-bend losses (MBL) lower than the International Telecommunication Union-Telecommunication Standardization Sector (ITU-T) recommendation. Firstly it is shown that, for 2 non-degenerate LP modes, by optimizing the core grading exponent and the dimensioning of the trench of a GCCT profile, a given DMD target (between -200 ps/km and 200 ps/km) can be attained with a deviation lower than 1.8 ps/km over the C-band. A simple design rule considering just those two parameters is derived, allowing the design of ILD-FMFs and DC-FMFs. Afterwards, the design of FMFs with up to 12 non-degenerate LP modes is studied considering a GCCT profile and a MSI profile. The optimization results show that the MSI profiles present lower DMD compared to the minimum obtained for a GCCT profile. Moreover, it is shown that the optimum DMD and the MBL increase with the number of modes for both profiles. Finally, the impact of the fabrication margins on the optimum DMD is analyzed. The probability of having a manufactured FMF with 12 non-degenerate LP modes and a DMD lower than 12 ps/km is 4 times higher for a GCCT profile than for a MSI profile.

In chapter 5, three techniques for the improvement of the distance reach of MDM-FMF transmission systems are proposed. The first technique proposed is the introduction of discrete modal XT through fiber splices, in order to reduce the CIR spread. The effectiveness of the method is assessed through simulation considering 3×136 Gbit/s MDM-PDM-QPSK ultra-long haul transmission systems employing ILD-FMFs or DC-FMFs. The maximum distance reach is optimized by varying the optimum number of splices per span and the splice XT level. Furthermore, alternative methods for distance reach improvement mitigating the MMAs MDG are presented, using strong coupling modes and maximum-likelihood (ML) detection.

In chapter 6, the impact of IM-NLs on MDM-FMF systems carrying WDM channels is investigated. A set of multimode multi-wavelength coupled nonlinear Schrödinger equations (MM-MW-CNLSE) including linear XT is derived, considering one pulse envelope per wavelength in each polarization and mode. The derived MM-MW-CNLSE allows studying each IM-NL process separately, namely: inter-modal

cross-phase modulation (IM-XPM) and inter-modal four-wave mixing (IM-FWM). The CNLSE are validated against experimental results provided in the literature for a GI-FMF. Afterwards, the impact of XPM/IM-XPM and FWM/IM-FWM in MDM-WDM systems is assessed. The IM-FWM for pairs of degenerate modes proves to be particularly harmful, determining the system performance. The performance of non-degenerate modes is found to be determined by IM-XPM with a magnitude similar to XPM. This allows concluding that the impact of IM-NLs has to be taken into account in the design of MDM-FMF systems.

In chapter 7, the main conclusions of this thesis are gathered and future work is delineated.

1.3 Main Contributions

The main contributions of the work developed within this thesis are:

1. Proposal of a method for the semi-analytical solution of the coupled linear differential equations that describe the linear XT arising in FMFs imperfections [34].

2. Development of a NSAM for simulation of FMF transmission, including the modal crosstalk arising from waveguide imperfections and from the Kerr nonlinear effect [35], based on a set of MM-CNLSE considering a pulse envelope per mode and polarization.

3. Design optimization of PMs for MMUXs and MDMUXs, focusing on optimization of mask resolution and offset tolerance to minimize linear XT [36].

4. Simulation validation of the weaker nonlinearity offered by single mode transmission over FMFs, observed experimentally [35].

5. Proposal of a refractive index profile for FMFs guiding 2 non-degenerate LP modes with a DMD lower than 0.01 ps/km over the C-band [37, 38], based on a GCCT profile.

6. Derivation of a simple design rule for FMFs with 2 non-degenerate LP modes which guarantees a maximum DMD deviation of 1.8 ps/km for a DMD target in the range -200 ps/km to 200 ps/km [37]. This simple rule allows the design of ILD-FMFs and DC-FMFs.

7. Comparison of the minimum net DMD achievable for ILD-FMFs and DC-FMFs, considering a GCCT profile [39].

8. Design of FMFs guiding up to 12 non-degenerate LP modes with DMD lower than 12 ps/km over the C-band, suitable for long-haul transmission, considering a GCCT and a MSI profile [40].

9. Comparison of the minimum DMD achievable considering a GCCT profile and considering a MSI profile [40]. The MSI is found to provide slightly lower DMD. The optimum DMD obtained for 12 non-degenerate LP modes is lower than 3 ps/km for the GCCT and 2.5 ps/km for the MSI profile.

10. Assessment of the fabrication tolerances required for the fabrication of FMFs with DMD lower than 12 ps/km from 2 to 12 non-degenerate LP modes considering a GCCT and a MSI profile [37, 40]. The probability of having a manufactured FMF guiding 12 LP modes with DMD lower than 12 ps/km is approximately 4 times higher for a GCCT than for a MSI profile.

11. Proposal of the introduction of discrete modal XT through fiber splices for the improvement of the distance reach of MDM transmission systems over FMFs [41]. A maximum reach increase factor of 1.9 is obtained for the optimum number of splices per span and optimum splice XT level [41].

12. Derivation of a set of MM-MW-CNLSE including linear XT, considering a pulse envelope per wavelength in each polarization and mode, allowing the study of each IM-NL process (IM-XPM and IM-FWM) separately, in MDM-WDM systems [42].

13. Investigation of the impact of IM-NLs on MDM-WDM systems over FMFs, allowing concluding that the NL degradation in a MDM system is higher than for a conventional WDM system, considering a similar nonlinear coefficient for the fundamental mode [42].

References

[1] R. Essiambre, G. Kramer, P. Winzer, G. Foschini, and B. Goebel, "Capacity Limits of Optical Fiber Networks," *IEEE/OSA Journal of Lightwave Technology*, vol. 28, no. 4, pp. 662–701, February 2010.

[2] G. Agrawal, *Nonlinear Fiber Optics*, 3rd ed. Academic Press, 2001.

[3] R. Essiambre and R. Tkach, "Capacity Trends and Limits of Optical Communication Networks," *Proceedings of the IEEE*, vol. 100, no. 5, pp. 1035–1055, May 2012.

[4] P. Winzer, "Energy-Efficient Optical Transport Capacity Scaling Through Spatial Multiplexing," *IEEE Photonics Technology Letters*, vol. 23, no. 13, pp. 851–853, July 2011.

[5] R. Essiambre and A. Mecozzi, "Capacity limits in single-mode fiber and scaling for spatial multiplexing," in *Proc. Optical Fiber Communication Conference and Exposition*, March 2012, p. OW3D.1.

[6] P. Roberts, F. Couny, H. Sabert, B. Mangan, D. Williams, L. Farr, M. Mason, A. Tomlinson, T. Birks, J. Knight, and P. Russell, "Ultimate low loss of hollow-core photonic crystal fibres," *Optics Express*, vol. 13, no. 1, pp. 236–244, January 2005.

[7] P. Krummrich, "Optical amplification and optical filter based signal processing for cost and energy efficient spatial multiplexing," *Optics Express*, vol. 19, no. 17, pp. 16 636–16 652, August 2011.

[8] D. Marcuse, *Theory of Dielectric Optical Waveguides*. Academic Press, Inc., 1974, chapters 3 and 5.

[9] R. Ryf, R. Essiambre, J. Hoyningen-Huene, and P. Winzer, "Analysis of mode-dependent gain in Raman amplified few-mode fiber," in *Proc. Optical Fiber Communication Conference and Exposition*, March 2012, p. OW1D.2.

[10] B. Inan, B. Spinnler, F. Ferreira, A. Lobato, S. Adhikari, V. Sleiffer, D. van den Borne, N. Hanik, and S. Jansen, "Equalizer complexity of mode division multiplexed coherent receivers," in *Proc. Optical Fiber Communication Conference and Exposition*, March 2012, p. OW3D.4.

[11] L. Cohen, W. Mammel, C. Lin, and W. French, "Propagation Characteristics of Double-Mode Fibers," *Bell System Technical Journal*, vol. 59, no. 6, pp. 1061–1072, July 1980.

[12] C. Poole, J. Wiesenfeld, D. DiGiovanni, and A. Vengsarkar, "Optical fiber-based dispersion compensation using higher order modes near cutoff," *IEEE/OSA Journal of Lightwave Technology*, vol. 12, no. 10, pp. 1746–1758, October 1994.

[13] A. Li, A. Al Amin, X. Chen, and W. Shieh, "Reception of Mode and Polarization Multiplexed 107-Gb/s CO-OFDM Signal over a Two-Mode Fiber," in *Proc. Optical Fiber Communication Conference and Exposition*, March 2011, p. PDPB8.

[14] R. Ryf, S. Randel, A. Gnauck, C. Bolle, R. Essiambre, P. Winzer, D. Peckham, A. McCurdy, and R. Lingle, "Space-division multiplexing over 10 km of three-mode fiber using coherent 6×6 MIMO processing," in *Proc. Optical Fiber Communication Conference and Exposition*, March 2011, p. PDPB10.

[15] M. Salsi, C. Koebele, D. Sperti, P. Tran, P. Brindel, H. Mardoyan, S. Bigo, A. Boutin, F. Verluise, P. Sillard, M. Bigot-Astruc, L. Provost, F. Cerou, and G. Charlet, "Transmission at 2×100 Gb/s, over Two Modes of 40 km-long Prototype Few-Mode Fiber, using LCOS based Mode Multiplexer and Demultiplexer," in *Proc. Optical Fiber Communication Conference and Exposition*, March 2011, p. PDPB9.

[16] C. Doerr, N. Fontaine, M. Hirano, T. Sasaki, L. Buhl, and P. Winzer, "Silicon photonic integrated circuit for coupling to a ring-core multimode fiber for space-division multiplexing," in *Proc. European Conference and Exhibition on Optical Communication*, September 2011, p. Th.13.A.3.

[17] D. Sperti, M. Salsi, C. Koebele, P. Tran, H. Mardoyan, S. Bigo, A. Boutin, P. Sillard, and G. Charlet, "Experimental Investigation of Modal Crosstalk using LCOS-based Spatial Light Modulator for Mode Conversion," in *Proc. European Conference and Exhibition on Optical Communication*, September 2011, p. Th.12.B.2.

[18] C. Koebele, M. Salsi, L. Milord, R. Ryf, C. Bolle, P. Sillard, S. Bigo, and G. Charlet, "40 km transmission of five mode division multiplexed data streams at 100 Gb/s with low MIMO-DSP complexity," in *Proc. European Conference and Exhibition on Optical Communication*, September 2011, pp. 1–3.

[19] P. Sillard, M. Bigot-Astruc, D. Boivin, H. Maerten, and L. Provost, "Few-Mode Fiber for Uncoupled Mode-Division Multiplexing Transmissions," in *Proc. European Conference and Exhibition on Optical Communication*, September 2011, pp. 1–3.

[20] M. Li, B. Hoover, S. Li, S. Bickham, S. Ten, E. Ip, Y. Huang, E. Mateo, Y. Shao, and T. Wang, "Low delay and large effective area few-mode fibers for mode-division multiplexing," in *Proc. OptoElectronics and Communications Conference*, 2012, pp. 495–496.

[21] N. Bai, E. Ip, Y. Huang, E. Mateo, F. Yaman, M. Li, S. Bickham, S. Ten, J. L. nares, C. Montero, V. Moreno, X. Prieto, V. Tse, K. Chung, A. Lau, H. Tam, C. Lu, Y. Luo, G. Peng, G. Li, and T. Wang, "Mode-division multiplexed transmission with inline few-mode fiber amplifier," *Optics Express*, vol. 20, no. 3, pp. 2668–2680, January 2012.

[22] L. Grüner-Nielsen, Y. Sun, J. Nicholson, D. Jakobsen, R. Lingle, and B. Palsdottir, "Few mode transmission fiber with low DGD, low mode coupling and low loss," in *Proc. Optical Fiber Communication Conference and Exposition*, March 2012, pp. 1–3.

[23] S. Randel, R. Ryf, A. Gnauck, M. Mestre, C. Schmidt, R. Essiambre, P. Winzer, R. Delbue, P. Pupalaikis, and A. Sureka, "Mode-multiplexed 6×20-GBd QPSK transmission over 1200-km DGD-compensated few-mode fiber," in *Proc. Optical Fiber Communication Conference and Exposition*, March 2012, p. PDP5C.5.

[24] A. Ellis and N. Doran, "Are few-mode fibres a practical solution to the capacity crunch?" in *Proc. International Conference on Transparent Optical Networks*, June 2013, pp. 1–4.

[25] L. Grüner-Nielsen, Y. Sun, J. W. Nicholson, D. Jakobsen, K. Jespersen, R. Lingle, and B. Palsdottir, "Few Mode Transmission Fiber With Low DGD, Low Mode Coupling, and Low Loss," *IEEE/OSA Journal of Lightwave Technology*, vol. 30, no. 23, pp. 3693–3698, December 2012.

[26] P. Winzer, A. Gnauck, A. Konczykowska, F. Jorge, and J.-Y. Dupuy, "Penalties from In-Band Crosstalk for Advanced Optical Modulation Formats," in *Proc. European Conference and Exhibition on Optical Communication*, September 2011, p. Tu.5.B.7.

[27] P. Facq, P. Fournet, and J. Arnaud, "Observation of tubular modes in multimode graded-index optical fibres," *Electronics Letters*, vol. 16, no. 17, pp. 648–650, August 1980.

[28] U. Levy, H. Kobrinsky, and A. Friesem, "Angular multiplexing for multichannel communication in a single fiber," *IEEE Journal of Quantum Electronics*, vol. 17, no. 11, pp. 2215–2224, November 1981.

[29] S. Berdagué and P. Facq, "Mode division multiplexing in optical fibers," *Applied Optics*, vol. 21, no. 11, pp. 1950–1955, June 1982.

[30] H. Stuart, "Dispersive multiplexing in multimode fiber," in *Proc. Optical Fiber Communication Conference and Exposition*, vol. 3, March 2000, pp. 305–307.

[31] J. Carpenter, B. Thomsen, and T. Wilkinson, "Degenerate Mode-Group Division Multiplexing," *IEEE/OSA Journal of Lightwave Technology*, vol. 30, no. 24, pp. 3946–3952, December 2012.

[32] K. Shi, G. Gordon, M. Paskov, J. Carpenter, T. Wilkinson, and B. Thomsen, "Degenerate mode-group division multiplexing using MIMO digital signal processing," in *Proc. Photonics Society Summer Topical Meeting Series*, July 2013, pp. 141–142.

[33] E. Ip, N. Bai, Y. Huang, E. Mateo, F. Yaman, M. Li, S. Bickham, S. Ten, J. Linares, C. Montero, V. Moreno, X. Prieto, V. Tse, K. Chung, A. Lau, H. Tam, C. Lu, Y. Luo, G. Peng, and G. Li, "88×3×112-Gb/s WDM transmission over 50 km of three-mode fiber with inline few-mode fiber amplifier," in *Proc. European Conference and Exhibition on Optical Communication*, September 2011, pp. 1–3.

[34] F. Ferreira, P. Monteiro, and H. Silva, "Semi-analytical model for linear modal coupling in few-mode fiber transmission," in *Proc. International Conference on Transparent Optical Networks*, July 2012, p. Th.A1.5.

[35] F. Ferreira, S. Jansen, P. Monteiro, and H. Silva, "Nonlinear Semi-Analytical Model for Simulation of Few-Mode Fiber Transmission," *IEEE Photonics Technology Letters*, vol. 24, no. 4, pp. 240–242, February 2012.

[36] F. Ferreira, D. van den Borne, H. Silva, and P. Monteiro, "Crosstalk optimization of phase masks for mode multiplexing in few mode fibers," in *Proc. Optical Fiber Communication Conference and Exposition*, March 2012, p. JW2A.37.

[37] F. Ferreira, D. Fonseca, and H. Silva, "Design of Few-Mode Fibers with Arbitrary and Flattened Differential Mode Delay," *IEEE Photonics Technology Letters*, vol. 25, no. 5, pp. 438–441, March 2013.

[38] ——, "Design of Few-Mode Fibers with Low Differential Modal Delay," in *Proc. Conference on Telecommunications*, May 2013, p. OC2.1.

[39] ——, "On the dependence of differential mode delay in few-mode fibers on the number of modes," in *Proc. International Conference on Transparent Optical Networks*, June 2013, p. Tu.C2.3.

[40] ——, "Design of Few-Mode Fibers with M-modes and Low Differential Mode Delay," *IEEE/OSA Journal of Lightwave Technology*, vol. 32, no. 3, pp. 353–360, February 2014.

[41] F. Ferreira, D. Fonseca, A. Lobato, B. Inan, and H. Silva, "Reach Improvement of Mode Division Multiplexed Systems Using Fiber Splices," *IEEE Photonics Technology Letters*, vol. 25, no. 12, pp. 1091–1094, June 2013.

[42] F. Ferreira, D. Fonseca, and H. Silva, "Impact of Inter-Modal Nonlinearities on Mode- and Wavelength-Division-Multiplexing Systems," *submitted to IEEE/OSA Journal of Lightwave Technology*, 2014.

Chapter 2

Modern MDM-FMF Systems

2.1 Introduction

Along this chapter, an extensive review of the MDM-FMF systems and components proposed in the last years is presented. The main impairments of each component are identified as well as the respective mitigation techniques proposed in the literature. The MDM-FMF systems capacity and distance reach can be significantly limited by FMFs impairments (DMD, MDL and linear XT), by MMUXs/MDMUXs impairments (linear mode XT, insertion losses (ILs) and MDL) and by MMAs MDG. In order to minimize FMFs impairments, flexible refractive index profiles have been proposed such as GCCT [1–5] and MSI [4, 6, 7]. In the MMUXs case, different implementations based on PMs and adiabatic tapers, among others, were presented. The MMUXs based on PMs [8] present low linear XT, high ILs and low MDL. On the other hand, MMUXs based on adiabatic tapers [9] present high linear XT, low ILs and low MDL. Regarding MMAs, two different implementations were presented, namely: MM-EDFAs and MM-RFAs. In order to reduce MMAs MDG, two techniques were presented, one based on the optimization of the modal distribution of the pumps power and another one based on the optimization of the erbium-doped fiber (EDF) doping profile. Finally, different MIMO equalization algorithms are reviewed with emphasis on the complexity required and the maximum distance reach allowed.

The chapter is structured as follows. Section 2.2 starts by presenting a brief summary on the theory of modal propagation in FMFs, in order to gain a clear insight on the major properties of FMFs. Moreover, an extensive review of the literature about FMFs is presented, with emphasis on characteristics such as DMD and modal XT. In section 2.3, the basic system concept common to the majority of the MDM-

FMF systems is explained, and the different implementations of system components are reviewed.

2.2 Few-Mode Fibers

2.2.1 Fiber Modes

An optical fiber is a cylindrical dielectric waveguide, constituted by a higher refractive index core surrounded by a low index cladding. This structure enables the guidance of optical modes in the core. Optical fibers are usually made of silica (SiO_2) glass, and the refractive index profile is controlled by the concentration and distribution of dopants, like germania (GeO_2) or alumina (Al_2O_3). The optical fibers characteristics are defined by the refractive index profile ($n(\rho)$ - where ρ is the radial coordinate). There are two main groups: SI fibers with an abrupt refractive index change between the core and the cladding, and GI fibers with a gradual refractive index change from the axis to the cladding. Fig. 2.1 shows the refractive index profile as a function of ρ for: (a) a SI fiber and (b) a GI fiber. In Fig. 2.1, the key parameters of both profiles are indicated: w_1 is the core radius, n_{co} is the refractive index at the core axis, n_{cl} is the refractive index at the cladding, and α is the core shape parameter.

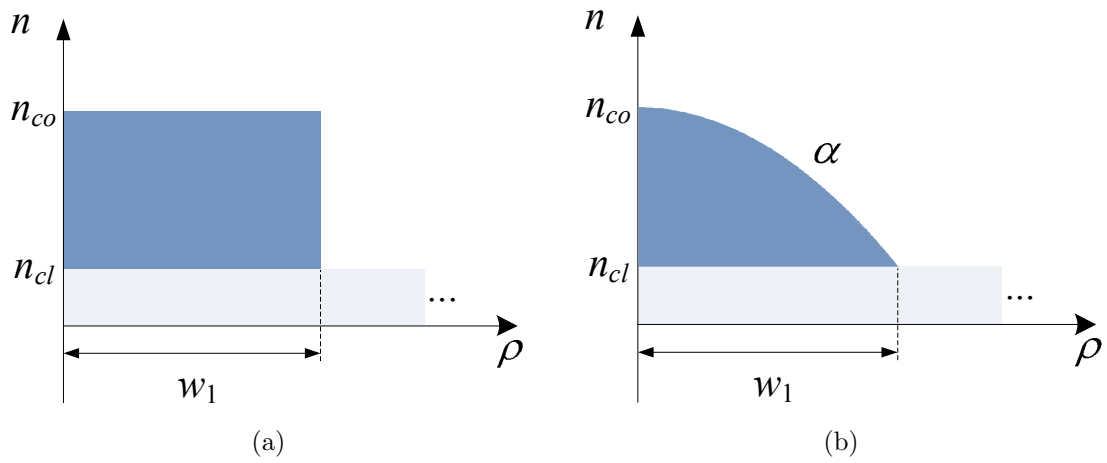

Figure 2.1: Simple refractive index profiles: (a) SI and (b) GI.

The refractive index profiles in Fig. 2.1 are analytically described by:

$$n(\rho) = \begin{cases} n(0)\left[1 - \Delta n_{co}(\rho/w_1)^{\alpha}\right], & |\rho| < w_1 \\ n_{cl}, & |\rho| \geq w_1 \end{cases} \tag{2.1}$$

where α is equal to ∞ for SI fibers (and $\alpha = 2$ for a parabolic index fiber), and Δn_{co} is the relative refractive index difference (Δn) at $\rho = 0$, with $\Delta n(\rho)$ given by:

$$\Delta n(\rho) = \frac{n^2(\rho) - n_{cl}^2}{2n^2(\rho)} \tag{2.2}$$

The characteristics of the modes supported by a fiber with a profile $n(\rho)$ are solutions of the wave equation with appropriate boundary conditions [10]. Those characteristics for a given mode u are: the spatial electric field distribution, $\mathbf{F}_u(x, y)$, and the effective index, $\overline{n}^u$. Moreover, the propagation constant of a given mode u (β_u) is given by $\beta_u = \overline{n}^u k_0$, where k_0 is the propagation constant of a plane wave in free space ($k_0 = \omega_0/c_0$). It can be shown that, for a fiber defined by Eq. 2.1, $\overline{n}^u$ of a given mode must satisfy the inequality:

$$n_{cl} < \overline{n}^u < n_{co} \tag{2.3}$$

The energy of a mode with $\overline{n}^u$ greater than n_{cl} is well contained in the core, since the transverse field is radially evanescent in the cladding region. The energy confinement is as high as $\overline{n}^u$ is closer to n_{co}, resulting in smaller bending losses [11]. On the other hand, a mode is said to be cut-off when $\overline{n}^u \leq n_{cl}$, since the transverse field in the cladding is oscillatory, rather than evanescent, and energy is carried away from the fiber core. Often, the normalized effective index $b_u = (\overline{n}^u - n_{cl})/(n_{co} - n_{cl})$ is used, since it characterizes the mode guiding strength.

The mode field distribution $\mathbf{F}_u(x, y)$ in an optical fiber is a mixture of: transverse electric (TE) modes with no electric field along the longitudinal axis; transverse magnetic (TM) modes with no magnetic field along the longitudinal axis; and hybrid modes for which neither the electric nor the magnetic field are zero along the longitudinal axis, denoted by HE or EH, depending on whether longitudinal magnetic or electric field dominates. A simplification of the solutions has been presented by Gloge [12] for fibers with $\Delta n_{co} \ll 1$, the so-called weak guiding approximation. Accordingly, the longitudinal components of the fields can be considered negligible, and the nearly degenerate true modes can be linearly combined and approximated by two

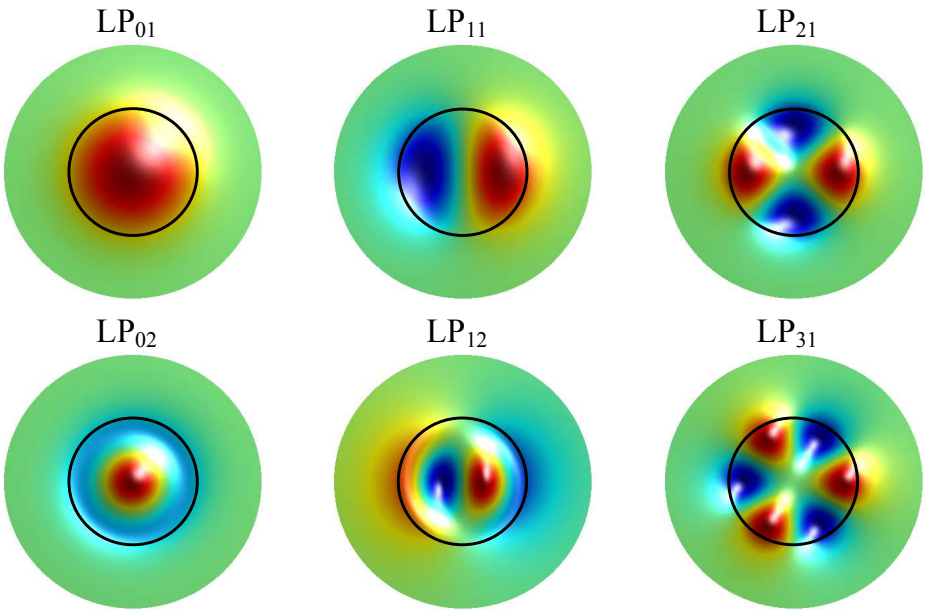

Figure 2.2: Few modes field distribution. Black circle: core-cladding boundary.

linearly polarized components, called linearly polarized (LP) modes. Furthermore, two indexes are used to describe the electric field distribution, l and m, LP_{lm}. Considering a cylindrical coordinate system with origin at the fiber core axis, there are $2l$ intensity field maxima along the azimuthal coordinate and m intensity field maxima along the radial coordinate. Fig. 2.2 shows the electric field distribution of LP_{01}, LP_{11}, LP_{21}, LP_{02}, LP_{12}, and LP_{31}. Except for LP_{0m} modes, which are just HE_{1m} modes, all other LP modes are linear combinations of different true fiber modes. Their relationships and degeneracy order are summarized in Table 2.1. The degeneracy of LP_{0m} modes is 2, given the two orthogonal polarizations. The degeneracy of LP_{lm} modes with $l \geq 1$ is 4, since besides the two orthogonal polarizations, two orthogonal field distributions can be obtained through a $\pi/(2l)$ rad rotation. For example, rotating the LP_{11} distribution in Fig. 2.2 by $\pi/2$ rad, an orthogonal distribution is obtained, and those two distributions are usually referenced as $\mathrm{LP}_{11\mathrm{a}}$ and $\mathrm{LP}_{11\mathrm{b}}$. Furthermore, the field distributions of all modes, degenerate and non-degenerate, have an important and useful orthogonality property which, for two modes u and u_1, is expressed as:

$$\iint \mathbf{F}_u(x,y) \cdot \mathbf{F}^*_{u_1}(x,y)\, dxdy = \frac{2\omega\mu_0}{\beta_u}\delta_{u,u_1} \tag{2.4}$$

where μ_0 is the permeability of free space, * stands for complex conjugate and δ_{u,u_1}

Table 2.1: LP_{lm} fiber modes.

LP modes	Degeneracy excluding polarization	Degeneracy including polarization	True modes	Degeneracy including polarization
LP_{0m}	1	2	HE_{1m}	2
LP_{1m}	2	4	TE_{0m}	1
			TM_{0m}	1
			HE_{2m}	2
$LP_{lm}(l \geq 2)$	2	4	$HE_{l+1,m}$	2
			$EH_{l-1,m}$	2

is the Kronecker delta, $\delta_{u,u_1} = 1$ for $u = u_1$ and 0 otherwise. Equation (2.4) is valid assuming a normalized power flow of 1 W in the z direction, resulting:

$$\frac{1}{2}\iint [\mathbf{F}_u(x,y) \times \mathbf{H}^*_{u_1}(x,y)] \cdot \widehat{z}\, dxdy = \delta_{u,u_1} \tag{2.5}$$

where $\mathbf{H}^*_{u_1}$ is the complex conjugate of the magnetic field distribution of the mode u_1. The orthogonality property enables the use of MDM as explained in section 2.3.

An important parameter related to the number of guided modes by a given refractive index profile is the normalized frequency (V) defined by:

$$V = k_0 w_1 \sqrt{n_{co}^2 - n_{cl}^2} \tag{2.6}$$

It has been shown that the total number of guided modes M for SI fibers and GI fibers, with $V > 20$, is given by, respectively:

$$M \approx V^2/2 \tag{2.7}$$

$$M \approx \frac{\alpha}{\alpha + 2} V^2/2 \tag{2.8}$$

Therefore, when designing a fiber with a given number of modes, one must first choose the normalized frequency V value. Fig. 2.3 shows b_u as a function of V for a parabolic-index profile ($\alpha = 2$ in (2.1)). It is visible that, when V increases, given a mode u, b_u

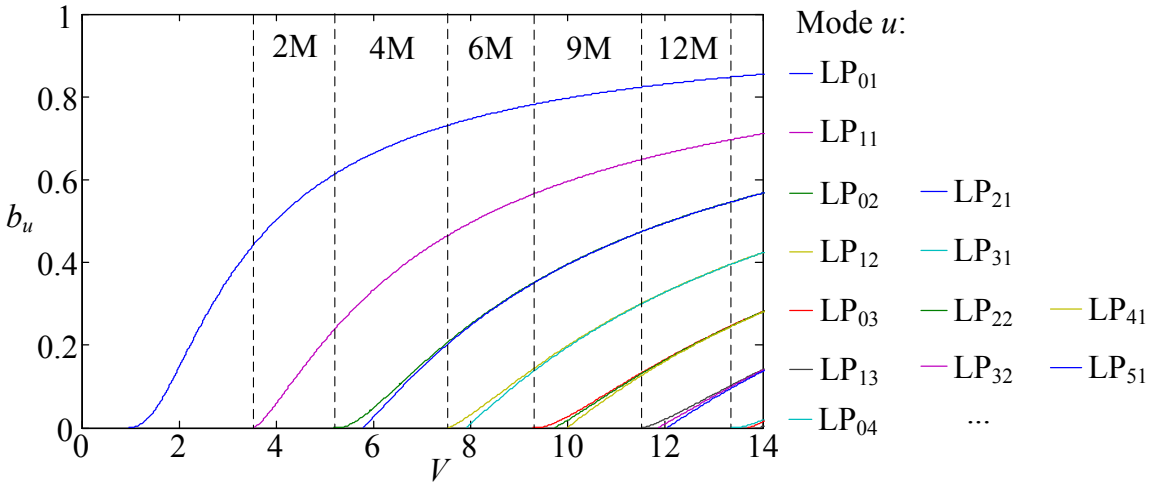

Figure 2.3: b_u as a function of V for a few propagation modes in a parabolic index fiber.

increases monotonically. In Fig. 2.3, the range of V values for which x non-degenerate modes (xM) are guided is identified by: 2M, 4M, 6M, 9M and 12M. For example, the V range for 2M is delimited by the cut-off V for LP_{11} and the cut-off V for LP_{02}. Moreover, the numbers of guided modes, counting the degenerate modes (but still ignoring polarization), for the 2M, 4M, 6M, 9M and 12M ranges are 3, 6, 10, 15, and 21 modes, respectively, according to Table 2.1. Note that the notation xM is used throughout this thesis to express the number of non-degenerate guided modes.

2.2.2 FMFs Impairments

Dispersion

One of the main causes of the transmission bandwidth limitation in optical fibers is dispersion, which can be roughly described as a phenomenon in which the propagation constant (β_u) and group velocity ($v_{g,u}$) of a wave depend of the frequency ω and of the waveguide mode u. Consequently, the spectral components of a pulse transmitted over one or more modes can experience different propagation delays, leading to the pulse broadening.

There are three types of dispersion: material dispersion, waveguide dispersion and modal dispersion. The material dispersion resides on the change of the refractive index of the waveguide material with frequency. The dispersion properties of doped silica are usually modeled using the Sellmeier equation and the Sellmeier coefficients [10, 13].

Similarly, the waveguide dispersion is also dependent on the frequency, but in this case the dependent variable is the mode $\overline{n}^u$. The combination of these two types of dispersion is called chromatic dispersion (D) or intra-modal dispersion, since both are frequency dependent. Finally, the modal dispersion resides on the variation of the $\overline{n}^u$ from mode to mode, and is therefore called inter-modal dispersion or DMD. This type of dispersion occurs only when multiple modes are excited in a MMF.

The frequency dependence of $\beta_u(\omega)$ is often represented using the Taylor series expansion around the carrier frequency ω_0, given by:

$$\beta_u(\omega) = \beta_{0,u} + (\omega - \omega_0)\beta_{1,u} + \frac{1}{2}(\omega - \omega_0)^2\beta_{2,u} + \frac{1}{6}(\omega - \omega_0)^3\beta_{3,u} + \dots \tag{2.9}$$

with:

$$\beta_{m,u} = \left(\frac{d^m\beta_u}{d\omega^m}\right)_{\omega=\omega_0} (m = 1, 2, ...) \tag{2.10}$$

where $\beta_{1,u}$ is the inverse of the group velocity of mode u (group delay per unit length), $\beta_{1,u} = 1/v_{g,u}$. The Taylor series in (2.9) is usually truncated, retaining the terms up to third order. D and DMD can be defined using the Taylor series terms. D_u is defined as the wavelength derivative of the inverse of $v_{g,u}$, given by:

$$D_u = \frac{d}{d\lambda}\left(\frac{1}{v_{g,u}}\right) = -\frac{2\pi c_0}{\lambda^2}\beta_{2,u} \tag{2.11}$$

In the spectral regions where D_u value is negligible, the higher-order dispersion effects have to be considered. The dispersion slope, S_u, is given by:

$$S_u = \frac{dD_u}{d\lambda} = \left(\frac{2\pi c_0}{\lambda^2}\right)^2\beta_{3,u} + \left(\frac{4\pi c_0}{\lambda^3}\right)\beta_{2,u} \tag{2.12}$$

The DMD resides on the variation of the group delay per unit length between modes. The DMD between two modes u_1 and u is defined by:

$$DMD_{u_1,u} = \frac{1}{v_{g,u_1}} - \frac{1}{v_{g,u}} \tag{2.13}$$

where u is the reference mode. Fig. 2.4 shows $DMD_{u_1,u}$ as a function of V for a parabolic-index fiber ($\alpha = 2$ in Eq. 2.1), with $u = \mathrm{LP}_{01}$. The V ranges for which xM

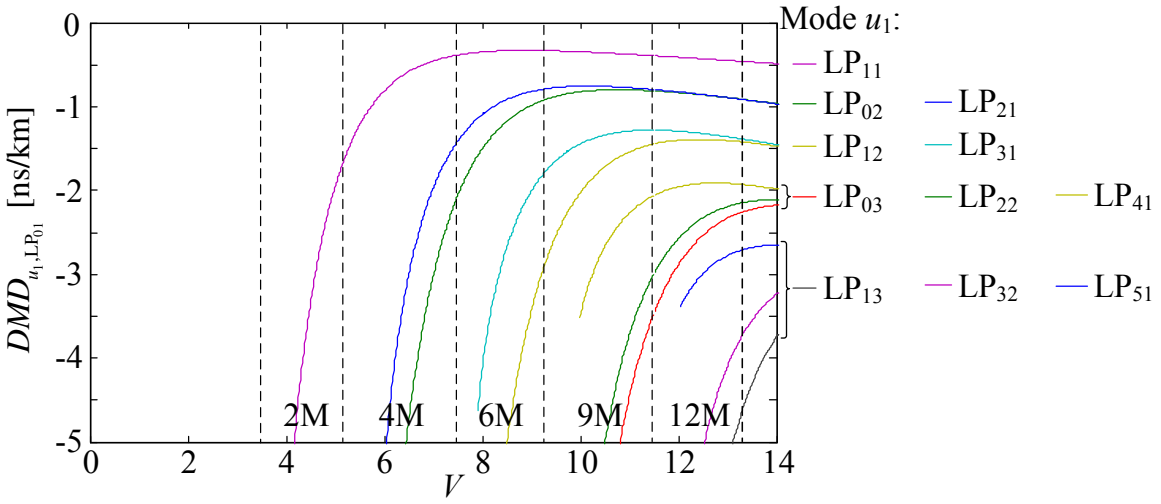

Figure 2.4: $DMD_{u_1,u}$ as a function of V for a parabolic-index fiber, with $u = \mathrm{LP}_{01}$.

are guided has been identified as in Fig. 2.3. Fig. 2.4 shows that the $DMD_{u_1,\mathrm{LP}_{01}}$ magnitude for a given mode u_1 close to its cut-off is very-high. Increasing V, the $DMD_{u_1,\mathrm{LP}_{01}}$ magnitude decreases, but above a given V it starts increasing slowly. Moreover, Fig. 2.4 shows that, for a given V range, $DMD_{u_1,\mathrm{LP}_{01}}$ decreases with the order of u_1. In this range, no crossover between $DMD_{u_1,\mathrm{LP}_{01}}$ curves for any pair of modes is verified. Thus, it can be concluded that, for $\alpha = 2$, it is not possible to have negligible DMD between the guided modes. In order to reduce the DMD, more flexible profiles have to be considered, as discussed in chapter 4.

Linear XT

The guided modes of an ideal fiber satisfy an orthogonality condition (2.4), and thus energy does not couple among the modes [14]. However, in the real world, imperfections in the fiber and splices can brake the modes' orthogonality, resulting in the coupling of energy among the modes. The fiber imperfections can be caused by perturbations introduced during the fabrication process or by mechanical stresses imposed on the fiber in the field, such as bends. The fiber splices imperfections can be caused by displaced cores and/or refractive index profile deformation during the fusion process. Fig. 2.5(a) and Fig. 2.5(b) show a schematic representation of fiber and splice deformations, respectively. Additionally, linear XT can be introduced by MMUXs/MDMUXs. The coupling strength between a pair of modes (u_1, u) depends on the propagation constant difference ($\beta_{u_1} - \beta_u$) and on the overlap integral of the

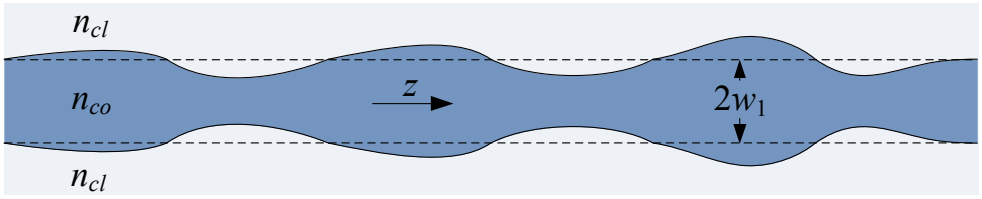

(a)

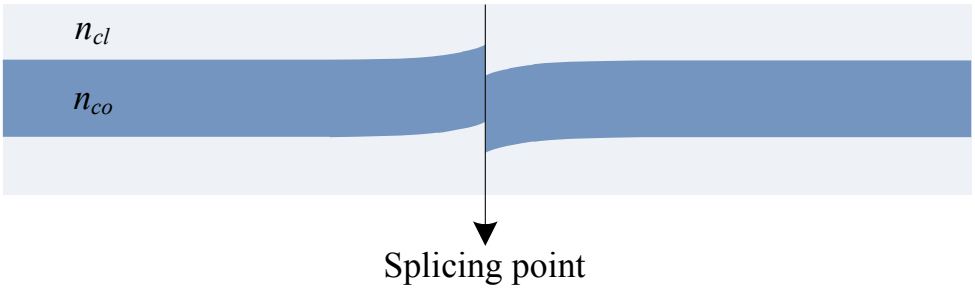

(b)

Figure 2.5: Example of deformations in: (a) fiber core-cladding boundary and (b) splices.

modes field distribution over the fiber permittivity perturbation $\Delta\varepsilon(x, y)$, this is:

$$\iint \Delta\varepsilon\,(x, y)\,\mathbf{F}_{u_1}\cdot\mathbf{F}_u\;dxdy \tag{2.14}$$

Between pairs of degenerate modes (for example, LP_{11a} and LP_{11b}), the mode coupling is usually strong, and thus a substantial amount of power is transferred between the modes within a few hundreds of meters. In the case of non-degenerate pairs of modes (for example, LP_{01} to LP_{11}) the coupling can be much weaker, and they may travel tens of kilometers before significant coupling is observed.

The XT introduced by waveguide imperfections and fiber bends can be described as distributed XT (dXT) along the FMF. The splice XT (sXT) and the XT introduced by MMUX/MDMUX can be considered as discrete XT introduced at a specific point of the link. Along this thesis, XT (discrete XT or accumulated dXT) is calculated as:

$$XT = \sum_{u_1 \neq u} P_{u_1} \Big/ P_u \tag{2.15}$$

where P_u and P_{u_1} are, respectively, the powers of the launched mode u and of the

remaining modes u_1, after the fiber segment (or splice, MMUX/MDMUX) under test, when only mode u was launched.

The first linear modal coupling models appeared early in the study of MMFs [14]. There are mainly two types of models: field coupling models, which account for complex-valued modal electric fields [14], or power coupling models, a simplified description that accounts only for real-valued modal powers [15, 16]. Both types of models are able to describe the exchange of energy between modes and the XT strength dependencies on the modes field distribution and propagation constant. However, only field coupling models account for the evolution of complex-valued modal amplitudes, enabling understanding how mode coupling affects modes characteristics, such as DMD and MDL. Therefore, in this thesis, a field coupling model is considered, following the work presented in [14]. More details of the model developed can be found in Section 3.2.1.

Mode-Dependent Losses

FMFs may introduce loss that is dependent on the mode, MDL. Such losses are strongly influenced by the bending losses of the modes [17], which can be minimized by maximizing the $\overline{n}^u$ of the higher-order mode. This can be achieved during the designing process of a FMF with M modes, choosing the $\overline{n}^u$ of the next higher-order mode $(M+1)$ to be approximately n_{cl}. Though technically still bound, that mode is said to be effectively cut-off due the high loss. Besides fiber imperfections, MDL can also be introduced by fiber splices, MMUX/MDMUX and MMAs. Fig. 2.6 shows an idealized representation of the mode gain of a 2M-MMA, as a function of λ. Actually, according to the experimental reports of MDM-FMF systems presented in the literature [18, 19], the main source of MDL is the MDG in MMAs, and the MDL introduced by fiber imperfections can be considered negligible. Different MMA implementations to reduce MDG are presented in section 2.3.2. Furthermore, in section 5.3, two methods to reduce the impact of MMAs MDL, thus improving the reach of MDM-FMF systems, are proposed.

The average loss (or gain), α_{avg}, and MDL (or MDG) of a given segment/device are computed as described in [20]. Given the channel transfer function of the segment/device under test, a $2M \times 2M$ matrix H (M modes with 2 polarizations), MDL is the ratio between the maximum and the minimum of the square root of the

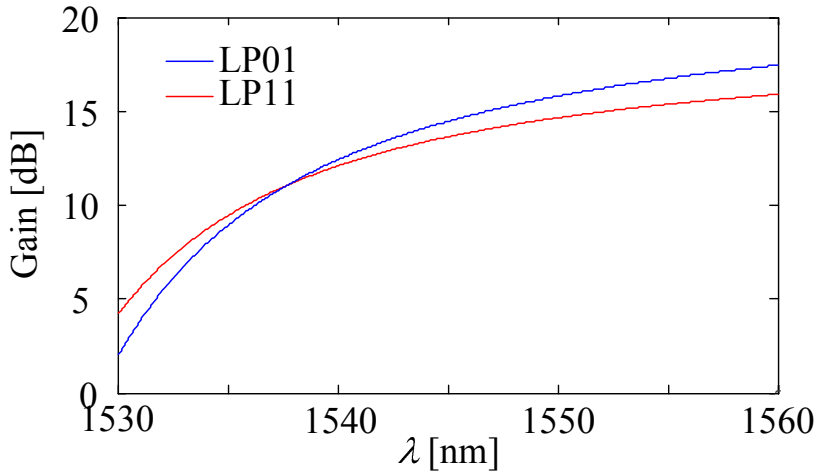

Figure 2.6: Idealized sketch of the mode gain of a 2M-MMA as a function of λ.

eigenvalues ${\lambda_i}^2$ of HH^* or the singular values λ_i of H:

$$MDL = \frac{\max\limits_i \{\lambda_i\}}{\min\limits_i \{\lambda_i\}} \tag{2.16}$$

where i denotes the spatial and polarization mode number, and * the transpose conjugate. The average loss is:

$$\alpha_{avg} = \frac{1}{2M} \sum_{i=1}^{2M} \lambda_i \tag{2.17}$$

Nonlinear Effects

In FMFs, the guidance of multiple modes introduces IM-NL effects, namely: IM-FWM and IM-XPM, besides the nonlinear effects already present in SMFs: self-phase modulation (SPM), cross-phase modulation (XPM) and four-wave mixing (FWM). Fig. 2.7(a) shows a schematic representation of the spurious signals generated by IM-FWM, and Fig. 2.7(b) shows a schematic representation of the spectral broadening induced by IM-XPM.

Recent experimental investigations on NL effects in FMFs have shown that IM-NLs are non-negligible. In [21], IM-XPM has been observed through a pump-probe scheme with a pump intensity modulated at 10 Gb/s, using a GI-FMF. The IM-XPM magnitude was found to be comparable to intra-modal XPM. In [22], non-degenerate

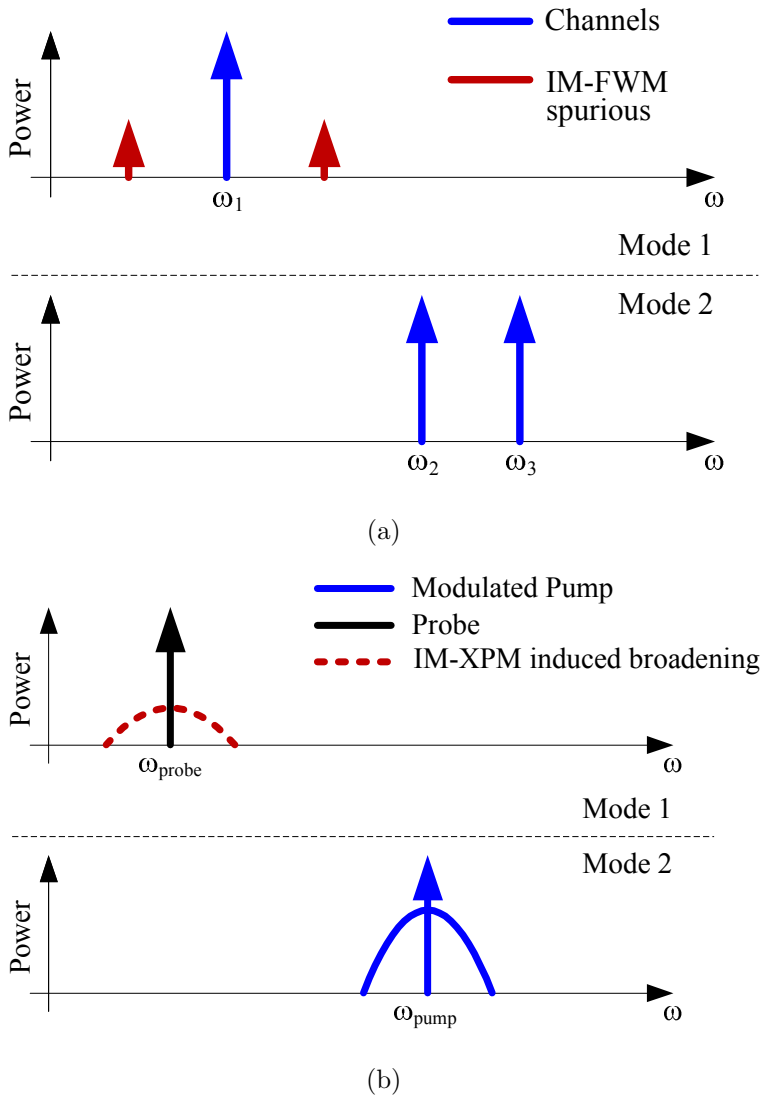

Figure 2.7: Schematic representation of the: (a) spurious signals generated by IM-FWM and (b) spectral broadening induced by IM-XPM.

IM-FWM has been experimentally observed, demonstrating that IM-FWM can be fully matched over very large frequency separations, with large chromatic dispersion in each mode. Therefore, a theoretical description of nonlinear propagation in MMFs is required to study IM-NLs.

The theoretical description of nonlinear propagation in SMFs is commonly based on the nonlinear Schrödinger equation (NLSE), modeling the evolution of the pulse envelope [10]. For MMFs, a set of coupled nonlinear Schröndinger equations (CNLSE) considering a limited range of IM-NLs has been presented in [23]. In [24], a generic set of CNLSE for MMFs including polarization, high-order dispersion, Kerr and Raman nonlinearities, has been presented. However, none of these models considered the

introduction of the linear XT described above. In this thesis, two sets of CNLSE including the linear XT are derived: one considering a pulse envelope per mode and polarization, referenced as MM-CNLSE and presented in section 3.2.2; and another for the WDM scenario considering a pulse envelope per wavelength in each polarization and mode, referenced as MM-MW-CNLSE and presented in chapter 6. Afterwards, MM-CNLSE similar to [25] have been presented in [26, 27]. Furthermore, in [28] a generalization of Manakov equations for MMFs was presented. However, to correctly model the IM-NL process between degenerate modes, linear XT has to be considered, as concluded in [28].

2.2.3 Modern FMFs

The requirements on FMFs for modern MDM-FMF systems are:

- Support of M different modes with low-loss propagation (similar to SSMF loss), with M between 2 and 10-20;
- Low MDL, for example lower than 0.02 dB/km, assuming that no fundamental impairment limiting the MIMO performance is introduced;
- Low net DMD between all the low-loss modes over the wavelength range of interest, such that MIMO DSP is feasible with present technology for long and ultra-long distances;
- Optimized linear XT strength, either weak XT or strong XT may be desirable;
- Low nonlinear coefficients, in order to enable the use of higher-order modulation formats over long distances.

Two different schemes concerning low net DMD have been proposed, namely: ILD-FMFs and DC-FMFs (FMFs with positive DMD and FMFs with negative DMD, concatenated). ILD-FMFs and DC-FMFs have different requirements regarding linear XT: in the ILD-FMFs case, strong XT is preferable in order to reduce the CIR spread with distance. However, in the DC-FMFs case, higher XT may lead to inefficient DMD compensation. Furthermore, a low net DMD over a broad wavelength range is required for the transmission of WDM signals. In [29], it has been shown that a net DMD as low as 12 ps/km is required for 2000 km of FMF transmission, limiting

additional overheads (due to DMD) to 10 %. Note that the 12 ps/km value will be used as a DMD threshold along this thesis.

A review of the FMFs design evolution is presented in Table 2.2. The analysis focused on: the refractive index profile, the net DMD maximum value, the wavelength range, the linear XT value, and the fiber length (L). The first studies on modern MDM-FMF systems focused on the conceptual demonstration using 2M-FMFs (LP_{01} and LP_{11}) with mainly two simple refractive index profiles: SI and GI. Note that, in Table 2.2, some of the studies described the profile simply as depressed-cladding index (DCI) [10], which is unclear about the core profile, that can be either SI or GI. Table 2.2 shows that the first ILD-FMFs using these simple profiles presented high DMD values, ranging from 50 ps/km to 3000 ps/km, thus limiting the distance reach. Afterwards, a more flexible refractive index profile, the GCCT profile, was introduced allowing to obtain lower DMD values. As shown in Table 2.2, by using a GCCT was possible to draw 2M-ILD-FMFs with a maximum DMD of 6 ps/km over the C-band, below the 12 ps/km threshold. Regarding DC-FMFs, low net DMD values ranging from 3 to 6 ps/km were obtained, using the GCCT or simpler profiles as GI or MSI. In section 4.2, the design of 2M-FMFs with negligible DMD (lower than 0.01 ps/km) over the C-band is presented, considering the GCCT profile. Moreover, a simple rule for the design of 2M-FMFs with a constant DMD over the C-band between -200 ps/km and 200 ps/km is presented, allowing the design of DC-FMFs.

After the first MDM demonstrations using 2M-FMFs, the research effort is now focused on the demonstration of the scalability potential of MDM-FMF systems, since the equalization complexity required by MDM-FMF systems partially erodes the benefit of deploying FMFs. It has been shown in [40] that, considering similar levels of complexity for nonlinearity mitigation in a SSMF, only FMF systems with 4 or more independent modes offer an actual capacity increase. Accordingly to Table 2.2 in [39], a 4M-DC-FMF with 59 km and a differential group delay of 350 ps over the C-band (the equivalent DMD is 5.9 ps/km), allowing long-haul transmission, was presented. However, such tightly DMD compensated span required 4 FMFs with different DMDs. Therefore, increasing xM an even higher number of FMFs with different DMDs will be required, imposing difficulties in the field deployment compared to ILD-FMFs. At the present date, no 4M-ILD-FMF with a DMD below the 12 ps/km has been presented. In section 4.3, the design of xM-ILD-FMFs with DMD $<$ 12 ps/km over the C-band is presented, with x between 2 and 12, considering GCCT and MSI profiles.

Table 2.2: Summary of progress in FMFs design.

Year	Ref.	FMF Type	Profile	L [km]	max. DMD [ps/km]	λ [band]	XT [dB/km]
2011	[30]	2M-ILD	SI	4.5	3000	-	-36.53
2011	[31]	2M-ILD	DCI	10	60	C-band	-30.00
2011	[7]	4M-ILD	MSI	-	20	0.4 nm	-
2012	[5]	2M-ILD	GCCT	30	81	C-band	-39.77
2012	[5]	2M-ILD	GCCT	10	6	C-band	-39.77
2012	[32]	2M-ILD	GI	50	80	C-band	-
2012	[33]	2M-ILD	DCI	96	50	C-band	-30.82
2012	[34]	2M-ILD	GI	22	150	C-band	-
2012	[34]	2M-DC	GI	100	6	C-band	-
2012	[35]	2M-DC	GCCT	13.5	3	C+L band	-
2012	[19]	2M-DC	GI	30	3.33	C-band	-34.77
2012	[6]	2M-DC	MSI	20.4	5.55	C-band	-
2013	[36]	2M-ILD	GI	5	36	C-band	-
2013	[37]	2M-DC	GI	50	25	C-band	-
2013	[38]	4M-ILD	GCCT	7	135	C+L band	-30.21
2013	[38]	4M-DC	GCCT	10.5	50	C+L band	-30.21
2013	[39]	4M-DC	GI	59	5.9	C-band	-

2.3 Mode-Division Multiplexing

The basic system concept for a MDM system is shown in Fig. 2.8, and is composed by: FMFs, MMUXs/MDMUXs, MMAs, and MIMO-DSP that compensates the DMD and XT accumulated along transmission. The concept is based on N independent optical transmitters at one end of the system and N coherent receivers at the other end, where N is equal to the total number of distinguishable optical modes. Each transmitter launches a data signal into a different mode. Each mode selective receiver detects a mixture of the N signals, and in a subsequent electrical signal processor the XT and DMD are reversed in order to produce the N separated signals. For this, the signal processor needs to invert the transmission matrix which describes the signal transfer from the N transmitters to the N receivers. The coefficients of this transmission matrix may be determined by initializing the system through the transmission of some training symbols (TSs) known by the receiving site.

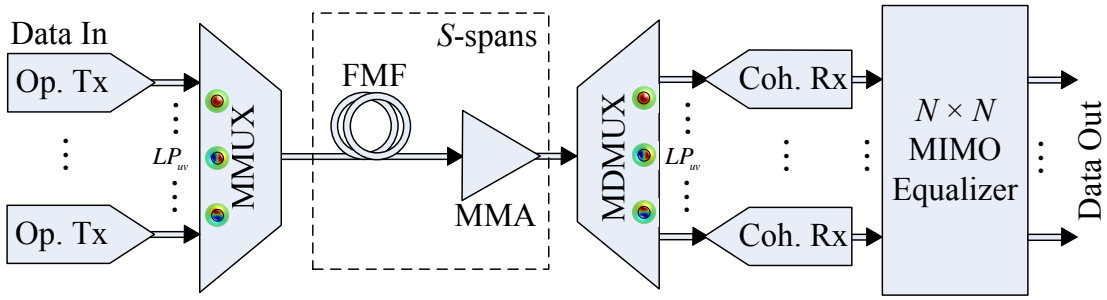

Figure 2.8: Basic system concept for a long-haul MDM system.

2.3.1 Mode Multiplexers and Demultiplexers

The fiber modes are orthogonal to each other, therefore in theory it is possible to design a lossless MMUX/MDMUX, similarly to PDM in SMFs. There are two main types of MMUX/MDMUX designs for M modes [17], namely:

- Broadcast and select mode shapers: these MMUXs start with M copies of a fundamental mode (LP_{01}) source, or M fundamental mode sources, and shape each copy into each one of the M modes supported by the FMF using spatial filters. Before fiber launching, these shaped copies have to be passively combined. As MDMUX, the light coming out of the FMF is split into M copies, and each copy is transmitted through a spatial filter. Examples of this MMUX

type are designs based on: PM [18, 41] (see Fig. 2.9(a)), liquid crystal on silicon (LCoS) [42, 43], and long period fiber gratings (LPFGs) [44, 45]. This type of MMUX/MDMUX presents high mode extinction ratio (MER) and low MDL. However, its IL is high, theoretically $1/M$ (due to the passive combining). Moreover, difficulties in the scaling of M have been experienced. For example, PM are unable to guarantee high MER for $M > 3$ without the use of additional amplitude shaping.

- Mode transformers: M fundamental mode inputs are transformed into M optical field patterns and launched into the FMF, without prior passive combining. As MDMUX, the light coming from a FMF is mode-selectively split into M SMFs. The mode transformation can be made in a single-step or distributed:

  - Single-step mode transformers: the mode conversion happens abruptly in the FMF facet. One example of this type of MMUX is the spot coupler [9, 46] (see Fig. 2.9(b)). The abrupt mode conversion is generally not perfectly matched to the FMF modes, and thus may induce MDL. However, a spot coupler with negligible MDL for $M = 3$ has been presented in [46].
  - Distributed mode transformers: mode conversion happens over a certain length. MMUXs of this type have the potential of being lossless for arbitrary values of M. An example of this type of MMUX is the photonic lantern based on adiabatic tapers [47] (see Fig. 2.9(c)).

The main types of MMUX/MDMUX are shown in Fig. 2.9: (a) PM [8], (b) spot coupler [46] and (c) photonic lantern [9].

In the beginning of the development of modern MDM-FMF systems, one of the requirements established was low XT in order to avoid high-order MIMO (order higher than 2) processing in short reach experiments. Therefore, broadcast and select mode shapers were the first type of MMUX/MDMUX used. In chapter 3, the design optimization of PM for low MER is performed. However, in the latest long-haul MDM-FMF systems demonstrations, the linear XT accumulated required the use of MIMO processing for signal recovery. Therefore, in long-haul MDM-FMF systems, a MMUX need not map each input signal to a distinct FMF mode, but need only to provide an approximately unitary mapping from the input signals to those modes. Analogous considerations apply to MDMUX. In conclusion, the absence of a requirement for MMUX/MDMUX with high MER, together with the mode scalability issues of

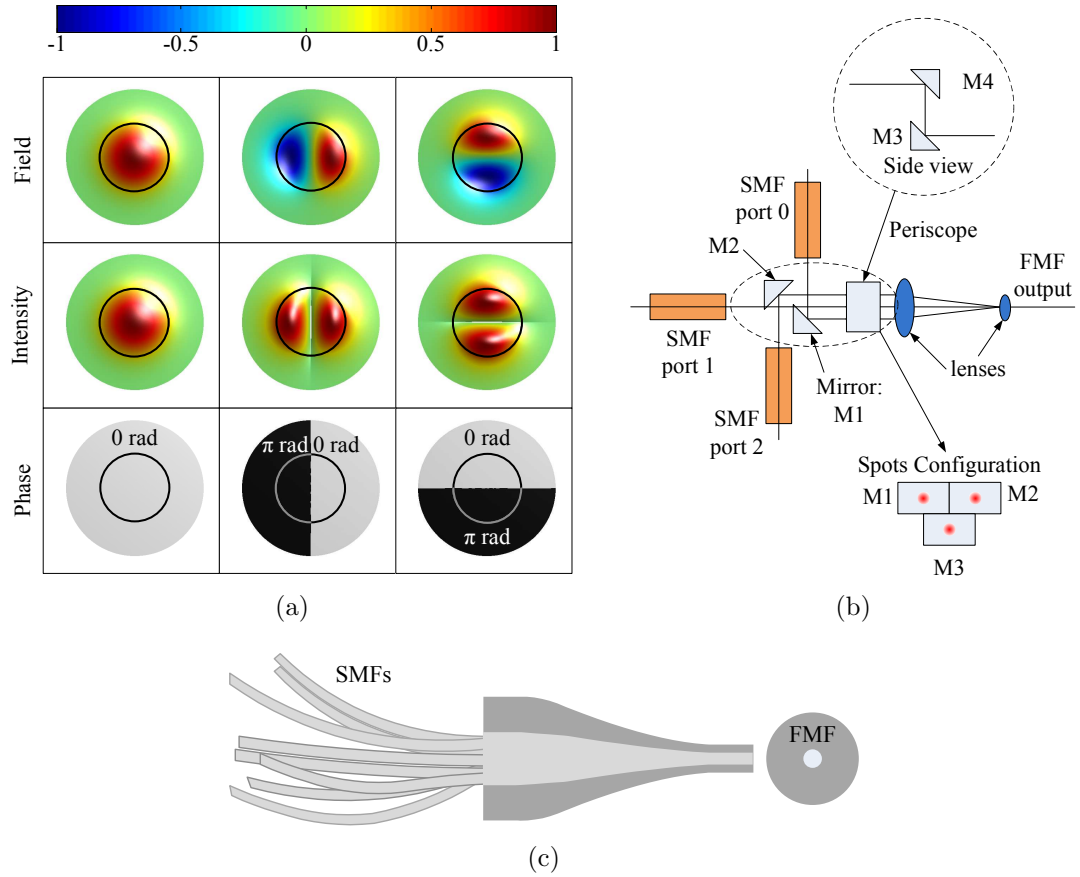

Figure 2.9: Main MMUX/MDMUX types: (a) PMs [8], (b) spot coupler [46] and (c) photonic lantern [9].

broadcast and select mode shapers, make the mode transformers the preferred solution for long-haul applications. The long-haul transmission simulations in chapter 5 considered the use of spot couplers.

2.3.2 Multimode Amplifiers

The MMAs are a key component for economic and energy efficient MDM systems. In order to reduce cost and energy consumption in comparison to M parallel SM amplifiers, the MDM channels have to share the pumps power. WDM systems are a very successful case where the pump power and amplifier hardware are shared among all channels. In MDM-FMF systems, the pump power can be coupled into different fiber modes just like the transmitted signal. Optical amplification in FMFs has been shown based on the Raman effect in passive FMFs (MM-RFA) as well as on EDFs (MM-EDFA). Fig. 2.10 shows the general setup of a MMA considering forward and/or

backward pump propagation. Note that, in the MM-RFA case, the amplification takes place in the actual transmission FMF. One of the main difficulties experienced in the design of MMAs is to achieve low MDG. Different strategies to minimize MDG have been followed on MM-EDFAs and MM-RFAs.

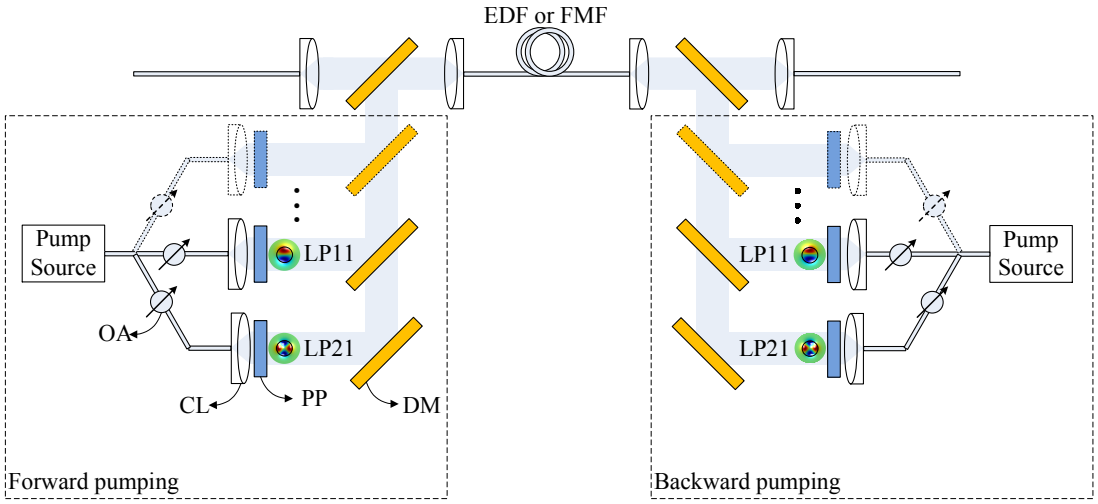

Figure 2.10: General MMA setup. Abbreviations: optical attenuator (OA), phase plate (PP), collimator lens (CL) and dichroic mirror (DM).

MM-EDFAs

For the first 2M-EDFAs studies, the MDG minimization was achieved through the optimization of the pump power distribution across the fiber modes. In [32], using a SI-EDF supporting 2M modes at the signal wavelength (around 1550 nm) and 4M modes at the pump wavelength (around 980 nm), a MDG lower than 1 dB has been achieved pumping into the LP_{21} mode in a backward configuration. However, the modal gain variation with wavelength has shown to be high, more than 8 dB. In [37], using an EDF with a ring-shaped Er-doping profile, a gain of 15 dB has been achieved with a MDG lower than 0.6 dB and a gain spectrum reasonably flat over the C-band, again pumping into the LP_{21} mode in a backward configuration. Furthermore, it has been found that, increasing the number of modes, the MDG control becomes increasingly difficult, such that for more than 4M modes, optimization of the EDF doping profile and pump control are both required [48].

MM-RFAs

The experimental implementations of MM-RFAs using a backward pumping configuration and optimized pump power distribution across the fiber modes have shown lower MDG, comparatively to the optimized MM-EDFAs. The lower MDG in MM-RFAs is a consequence of distributed linear XT introduced by the transmission FMF, which spreads the pump power among all guided modes, thereby equalizing the modal gain. In [18], a theoretical study of Raman amplification on 2M-FMFs predicts a residual MDG of 0.13 dB for each 10 dB of Raman gain, with optimization of the pump power distribution in a backward pumping configuration. In [49], an experimental 2M-RFA has shown a MDG lower than 0.5 dB for a maximum gain of 8 dB, pumping into the LP_{11} mode in a backward configuration.

M parallel SM-EDFAs

In the beginning of the development of modern MDM-FMF systems, a simpler MMA has been used in some studies [19], composed by M parallel SM-EDFAs between a MMUX and a MDMUX, as shown in Fig. 2.11. However, this MMA is impractical for real networks due to its energy inefficiency. Even so, it is an useful tool for the development of the remaining components and sub-systems of MDM-FMF systems. Therefore, since the study of MMAs is out of the scope of this thesis, the MMA configuration presented in Fig. 2.11 is used in the transmission simulations.

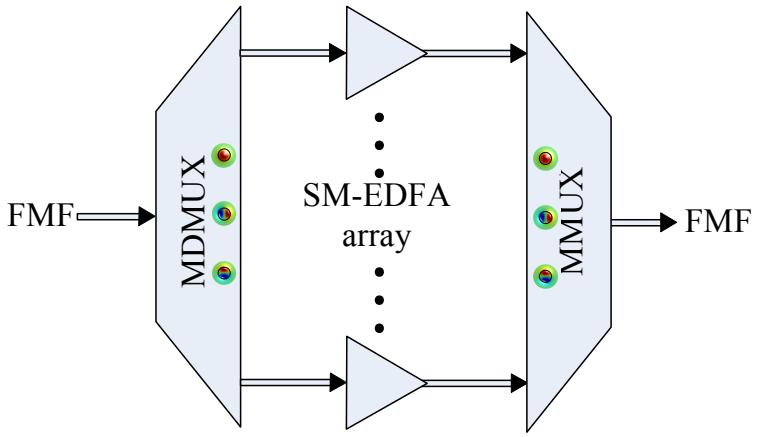

Figure 2.11: MMA composed by M parallel SM-EDFAs.

2.3.3 MIMO DSP

The use of DSP is required to reconstruct the transmitted data from the received signal. The main blocks of a DSP used in a digital coherent receiver are schematically represented in Fig. 2.12 [50]. The first three blocks are responsible for signal conditioning, so that the N channels are synchronized with an integer number of samples per symbol. The normalization and orthogonalization block compensates for the imperfections in the 90° hybrid and the responsivity variation of the photodiodes. Afterwards, digital filtering is used to compensate for intra-modal transmission impairments (chromatic dispersion, polarization rotations and PMD) and inter-modal transmission impairments (DMD and modal XT). Before the data is finally recovered and FEC is applied, phase and frequency mismatches between the incoming signals and the local oscillators are compensated for using algorithms such as those detailed in [51].

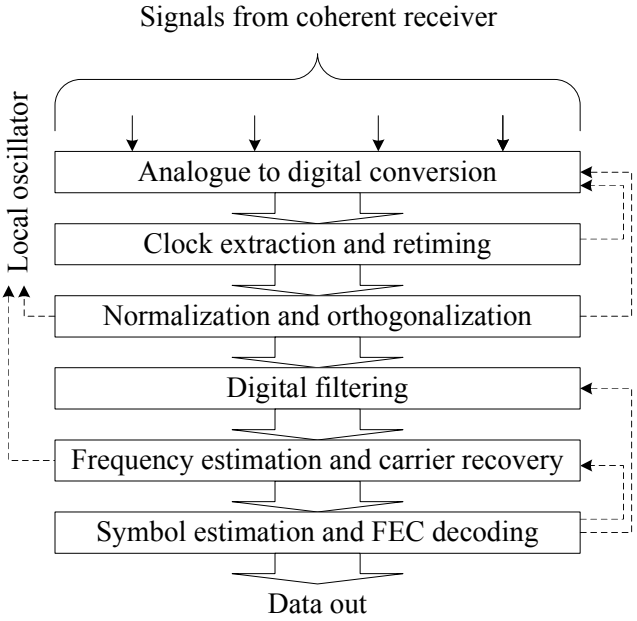

Figure 2.12: DSP blocks in a digital coherent receiver.

Commonly, digital filtering is performed using finite impulse response (FIR) filters, since the CIR is finite, implemented as tapped delay lines given their non-recursive structure. Moreover, the FIR filters can be designed in the time domain or in the frequency domain [52], referenced as time-domain equalization (TDE) scheme or frequency-domain equalization (FDE) scheme, respectively. The digital filtering block is usually composed by two cascaded sub-blocks. The first digital filtering block compensates for chromatic dispersion, which is independent of polarization rotation

and linear XT. For this block, FDE is preferable over TDE for accumulated dispersion higher than 2000 ps/nm in 100 Gbit/s systems [52]. The second digital filtering block compensates for polarization rotation, PMD, linear XT, and DMD, since the four impairments are interdependent. In the second block, FDE is also the preferable option since it has been shown that, for long-haul MDM transmission, TDE is unfeasible with present technology even for low DMD values, on the order of ∼10 ps/km [29]. In order to mitigate the polarization rotation, PMD, linear XT, and DMD, the $2M \times 2M$ fiber matrix H has to be estimated (for a FMF guiding M modes, each with two polarizations), inverted and applied to the received signal through a matrix multiplication operation. In contrast to the chromatic dispersion, which may be considered constant, H may evolve in time due to effects such as rapid variations in the polarization state or linear XT, and thus the compensation scheme must be adaptive. The problem of the estimation of H is addressed using the formalism of MIMO systems, as in PDM-SSMFs systems, where each H matrix element is an adaptive FIR filter. The optimum number of taps of FIR filters depends on the CIR length, determined by the combined effect of DMD and linear XT. The methods for H estimation can be divided in two types: algorithms based on TS, or blind algorithms based on the characteristics of the signal [53]. In [29], it has been shown that TS-based equalization provides several orders of lower complexity, compared to blind equalization, for long-haul transmission systems. However, the reach is limited by the maximum TS overhead allowed, since the TS length has to be at least the CIR length. Limiting these additional overheads to 10 %, a fiber with a DMD as low as 12 ps/km is required for 2000 km of FMF transmission at 100 Gb/s [29]. Considering the use of TS, H is estimated in the time domain by correlating the received and transmitted training symbols, and is subsequently inverted. There are three main equalization and detection schemes:

- The zero forcing (ZF) equalization undoes the channel distortions by evaluating the pseudo-inverse of H and multiplying it by the equalizer input signal vector [54];
- The minimum mean square error (MMSE) equalization has an additional term which prevents noise amplification as in the ZF case [52–54];
- The ML detection searches for the set of transmitted symbols which, when multiplied by H, have the smallest Euclidean distance to the received signal [54, 55].

At the output of the digital filter, frequency and phase tracking lock the phase of the

symbol constellation before hard-decision or soft-decision decoding can take place.

The study of equalization techniques for MDM-FMF systems is out of the scope of this thesis. Therefore, the equalizer structure described in [54, 56] is used along this thesis, which corresponds to a TS based FDE-MIMO.

2.3.4 Progress in Systems Demonstrations

Recent FMFs and MMAs development has enabled rapid progress in the capacity and reach of MDM systems demonstrations, as shown in Table 2.3. The development pace was set by the two main conferences on optical communications, the Optical Fiber Communication Conference and Exposition (OFC) and the European Conference and Exhibition on Optical Communication (ECOC). The first MDM-FMF systems carrying high data rate channels ($\sim$100 Gb/s) over tens of km were presented at OFC 2011. Three MDM-FMF experiments using a simple 2M-FMF were reported, the top three entries in Table 2.3. In the first two experiments [30, 42], two data streams were transmitted, one over the LP_{01} mode and another over the LP_{11a} mode (or LP_{11b} mode), recovered using 2×2 and 4×4 MIMO equalization, respectively. Note that, due to the strong XT between LP_{11a} and LP_{11b}, 4×4 MIMO equalization was necessary to recover the data transmitted in the LP_{11} mode, even for the short distances reported (4.5 km [30] and 40 km [42]). The third experiment [31] was the first demonstration of the full use of all spatial dimensions in a 2M-FMF transmitting over each orthogonal polarization of each one of the 3 LP guided modes, and recovering the transmitted signals using 6×6 MIMO processing. Later in ECOC 2011, the first MDM-WDM experiment [57] and the first MM-RFA implementation [49] were reported. The first MDM-WDM transmission was also reported [57], where 88 wavelengths carrying 112 Gb/s PDM-QPSK signals were transmitted over 50 km of 2M-FMF using an inline MM-EDFA. In [49], the first experimental demonstration of MM-RFA was tested in a record 137 km MDM single-span transmission, where 6×20 Gbaud-QPSK signals were successfully recovered using 6×6 MIMO DSP. In OFC 2012, [19] set the present transmission distance record at 1200 km, using a re-circulating loop and a MMA composed by 3 SM-EDFAs (see Fig. 2.11). In OFC 2013, the first all-FMF re-circulating loop (this is, no MMUX/MDMUX is used inside the loop) was reported in [37], using a 50 km 2M-FMF span and an inline MM-EDFA: 146 wavelengths were transmitted over 500 km (wavelength-dependent gain limited), and 16 wavelengths were transmitted over 1000 km. Also in OFC 2013, a record spectral efficiency of 32 bit/s/Hz per core for MDM-FMF transmission using 12 spatial and

Table 2.3: Summary of progress in MDM-FMF systems demonstrations.

Year	Ref.	$\lambda \times 2M \times R$	N	DMD	MO	MMUX	MMA	$S \times L$
2011	[30]	$1 \times 4 \times 25$	2	3000	2/4	LPFG	none	1×4.5
2011	[42]	$1 \times 4 \times 25$	2	4350	2/4	LCoS	none	1×40
2011	[31]	$1 \times 6 \times 14$	2	60	6	PM	none	1×10
2011	[59]	$1 \times 6 \times 28$	2	60	6	PM	none	1×33
2011	[60]	$1 \times 10 \times 28$	2	8500	2/4	PM	none	1×40
2011	[57]	$88 \times 6 \times 28$	2	80	6	PM	MM-EDFA	1×50
2011	[49]	$1 \times 6 \times 20$	2	27	6	PM	MM-RFA	1×137
2012	[19]	$1 \times 6 \times 20$	2	1.67	6	PM	M-SM-EDFA	40×30
2012	[61]	$5 \times 6 \times 20$	2	0	6	Spot	MM-RFA	1×209
2012	[62]	$1 \times 6 \times 28$	2	1.4	6	PM	MM-EDFA	1×80
2012	[63]	$96 \times 6 \times 32$	4	6	6	PM	MM-EDFA	1×119
2013	[37]	$146 \times 6 \times 19$	2	5	6	PM	MM-EDFA	10×50
2013	[39]	$32 \times 12 \times 20$	4	5.9	12	PL	M-SM-EDFA	3×59
2013	[64]	$20 \times 6 \times 32$	5	0.5	6	PM	MM-EDFA	1×60
2013	[65]	$5 \times 6 \times 32$	3	0.5	6	Spot	MM-EDFA	8×60
2014	[66]	$5 \times 6 \times 32$	2	0.5	6	PM	MM-EDFA	17×60

Table abbreviations and symbols:

R - baud rate in Gbaud/s	N - number of bits per symbol
$2M$ - number of polarizations and modes	λ - number of WDM channels
DMD - in ps/km	MO - MIMO order
S - number of spans	L - span length in km
PL - photonic lantern	Spot - Spot coupler

polarization modes (4M-FMF) was established in [39], and a transmission length of 177 km was achieved for 32 WDM channels. For the first time, a spectral efficiency per fiber core was achieved exceeding significantly the theoretical limit of ~ 20 bit/s/Hz predicted by the nonlinear Shannon capacity limit for a 200 km long SSMF [58]. Further scaling of MDM-FMF systems on the number of modes is envisioned for the following years.

2.4 Conclusions

In this chapter, an extensive review about FMFs and MDM-FMF systems reported in the literature has been performed. Moreover, a brief summary on the theory of modal propagation in FMFs has been presented, introducing notions and concepts to be used in the following chapters.

In section 2.2, the two main refractive index profiles presenting lower DMD (GCCT and MSI) have been identified, as well as the two main schemes used to obtain low DMD fiber spans (ILD-FMFs and DC-FMFs). It has been concluded that only FMFs with 4 or more independent modes offer an actual capacity increase. Moreover, the increase of xM is easier to achieve using ILD-FMFs, given the deployment difficulties associated with DC-FMFs. However, up to date, no 4M-ILD-FMF (or with an higher number of modes), suitable for long haul transmission, has been reported. In chapter 4, optimized ILD-FMFs with up to 12M, suitable for long haul transmission, are designed and evaluated.

In section 2.3, a review of MDM-FMF systems implementations was presented. The main components were also discussed, namely: MMUXs/MDMUXs, MMAs, and MIMO-DSP. The MMAs presented in the literature can be divided in three groups: MM-EDFAs, MM-RFAs, and the MMA composed by M parallel SM-EDFAs, as shown in Fig. 2.11 [19]. From these three groups, the last one is chosen for MDM-FMF systems simulation, along the next chapters, since it was used to establish the present experimental transmission distance record in laboratory. Although this MMA is impractical for long-haul transmission in a real network, it represents the best performance scenario among all MMAs discussed. Furthermore, the MMUXs based on PM proved to be critical in the development of the MDM-FMF systems, as can be observed in Table 2.3 due to their higher MER. The design optimization of PM is presented in section 3.3. However, the MMUXs based on photonic lanterns are likely to be the choice for future MDM-FMF systems due to their lower IL and easier scalability on the number of modes. Finally, the different MIMO-DSP domain implementations, TDE or FDE, were presented as well as the different fiber matrix estimation techniques, blind or TS based. The FDE-MIMO TS based equalizer presented in [54, 67] is used in the following chapters for MDM-FMF systems simulation, since it presents the lowest complexity.

References

[1] F. Ferreira, D. Fonseca, and H. Silva, "Design of Few-Mode Fibers with Arbitrary and Flattened Differential Mode Delay," *IEEE Photonics Technology Letters*, vol. 25, no. 5, pp. 438–441, March 2013.

[2] ——, "On the dependence of differential mode delay in few-mode fibers on the number of modes," in *Proc. International Conference on Transparent Optical Networks*, June 2013, p. Tu.C2.3.

[3] ——, "Design of Few-Mode Fibers with Low Differential Modal Delay," in *Proc. Conference on Telecommunications*, May 2013, p. OC2.1.

[4] ——, "Design of Few-Mode Fibers with M-modes and Low Differential Mode Delay," *IEEE/OSA Journal of Lightwave Technology*, vol. 32, no. 3, pp. 353–360, February 2014.

[5] L. Grüner-Nielsen, Y. Sun, J. W. Nicholson, D. Jakobsen, K. Jespersen, R. Lingle, and B. Palsdottir, "Few Mode Transmission Fiber With Low DGD, Low Mode Coupling, and Low Loss," *IEEE/OSA Journal of Lightwave Technology*, vol. 30, no. 23, pp. 3693–3698, December 2012.

[6] T. Sakamoto, T. Mori, T. Yamamoto, and S. Tomita, "Differential Mode Delay Managed Transmission Line for Wide-band WDM-MIMO System," in *Proc. Optical Fiber Communication Conference and Exposition*, March 2012, p. OM2D.1.

[7] N. Riesen and J. Love, "Dispersion equalisation in few-mode fibres," *Optical and Quantum Electronics*, vol. 42, no. 9-10, pp. 577–585, June 2011.

[8] F. Ferreira, D. van den Borne, H. Silva, and P. Monteiro, "Crosstalk optimization of phase masks for mode multiplexing in few mode fibers," in *Proc. Optical Fiber Communication Conference and Exposition*, March 2012, p. JW2A.37.

[9] R. Ryf, M. Mestre, A. Gnauck, S. Randel, C. Schmidt, R. Essiambre, P. Winzer, R. Delbue, P. Pupalaikis, and A. Sureka, "Low-loss mode coupler for mode-multiplexed transmission in few-mode fiber," in *Proc. Optical Fiber Communication Conference and Exposition*, March 2012, p. PDP5B.5.

[10] G. Agrawal, *Nonlinear Fiber Optics*, 3rd ed. Academic Press, 2001.

[11] J. Sakai and T. Kimura, "Bending loss of propagation modes in arbitrary-index profile optical fibers." *Applied Optics*, vol. 17, no. 10, pp. 1499–506, May 1978.

[12] D. Gloge, "Weakly Guiding Fibers," *Applied Optics*, vol. 10, no. 10, pp. 2252–2258, October 1971.

[13] W. Hermann and D. Wiechert, "Refractive index of doped and undoped PCVD bulk silica," *Materials Research Bulletin*, vol. 24, no. 9, pp. 1083–1097, September 1989.

[14] D. Marcuse, *Theory of Dielectric Optical Waveguides*. Academic Press, Inc., 1974, chapters 3 and 5.

[15] R. Olshansky, "Mode coupling effects in graded-index optical fibers," *Applied Optics*, vol. 14, no. 4, pp. 935–945, April 1975.

[16] D. Gloge, "Optical Power Flow in Multimode Fibers," *Bell System Technical Journal*, vol. 51, no. 8, pp. 1767–1783, October 1972.

[17] I. Kaminow, T. Li, and A. Willner, *Optical Fiber Telecommunications*, 6th ed. Elsevier, 2013, vol. A, chapter 8.

[18] R. Ryf, R. Essiambre, J. Hoyningen-Huene, and P. Winzer, "Analysis of mode-dependent gain in Raman amplified few-mode fiber," in *Proc. Optical Fiber Communication Conference and Exposition*, March 2012, p. OW1D.2.

[19] S. Randel, R. Ryf, A. Gnauck, M. Mestre, C. Schmidt, R. Essiambre, P. Winzer, R. Delbue, P. Pupalaikis, and A. Sureka, "Mode-multiplexed 6×20-GBd QPSK transmission over 1200-km DGD-compensated few-mode fiber," in *Proc. Optical Fiber Communication Conference and Exposition*, March 2012, p. PDP5C.5.

[20] P. Winzer and G. Foschini, "MIMO capacities and outage probabilities in spatially multiplexed optical transport systems." *Optics Express*, vol. 19, no. 17, pp. 16 680–16 696, August 2011.

[21] R. Essiambre, M. Mestre, R. Ryf, A. Gnauck, R. Tkach, A. Chraplyvy, Y. Sun, X. Jiang, and R. Lingle, "Experimental Observation of Inter-Modal Cross-Phase Modulation in Few-Mode Fibers," *IEEE Photonics Technology Letters*, vol. 25, no. 6, pp. 535–538, March 2013.

[22] ——, "Experimental Investigation of Inter-Modal Four-Wave Mixing in Few-Mode Fibers," *IEEE Photonics Technology Letters*, vol. 25, no. 6, pp. 539–542, March 2013.

[23] T. Chaipiboonwong, P. Horak, J. Mills, and W. Brocklesby, "Numerical study of nonlinear interactions in a multimode waveguide," *Optics Express*, vol. 15, no. 14, pp. 9040–9047, July 2007.

[24] F. Poletti and P. Horak, "Description of ultrashort pulse propagation in multimode optical fibers," *Journal of the Optical Society of America B*, vol. 25, no. 10, pp. 1645–1654, October 2008.

[25] F. Ferreira, S. Jansen, P. Monteiro, and H. Silva, "Nonlinear Semi-Analytical Model for Simulation of Few-Mode Fiber Transmission," *IEEE Photonics Technology Letters*, vol. 24, no. 4, pp. 240–242, February 2012.

[26] A. Mecozzi, C. Antonelli, and M. Shtaif, "Optical Nonlinearity in Multi-Mode Fibers with Random Mode Coupling," in *Proc. European Conference and Exhibition on Optical Communication*, September 2012, p. P1.11.

[27] A. Li, X. Chen, and W. Shieh, "Nonlinear tolerance of few-mode fiber based transmission systems with random mode coupling," in *Proc. Optical Fiber Communication Conference and Exposition*, March 2013, p. JTh2A.12.

[28] S. Mumtaz, R. Essiambre, and G. Agrawal, "Nonlinear Propagation in Multimode and Multicore Fibers: Generalization of the Manakov Equations," *IEEE/OSA Journal of Lightwave Technology*, vol. 31, no. 3, pp. 398–406, February 2013.

[29] B. Inan, B. Spinnler, F. Ferreira, A. Lobato, S. Adhikari, V. Sleiffer, D. van den Borne, N. Hanik, and S. Jansen, "Equalizer complexity of mode division multiplexed coherent receivers," in *Proc. Optical Fiber Communication Conference and Exposition*, March 2012, p. OW3D.4.

[30] A. Li, A. Al Amin, X. Chen, and W. Shieh, "Reception of Mode and Polarization Multiplexed 107-Gb/s CO-OFDM Signal over a Two-Mode Fiber," in *Proc. Optical Fiber Communication Conference and Exposition*, March 2011, p. PDPB8.

[31] R. Ryf, S. Randel, A. Gnauck, C. Bolle, R. Essiambre, P. Winzer, D. Peckham, A. McCurdy, and R. Lingle, "Space-division multiplexing over 10 km of three-mode fiber using coherent 6×6 MIMO processing," in *Proc. Optical Fiber Communication Conference and Exposition*, March 2011, p. PDPB10.

[32] N. Bai, E. Ip, Y. Huang, E. Mateo, F. Yaman, M. Li, S. Bickham, S. Ten, J. L. nares, C. Montero, V. Moreno, X. Prieto, V. Tse, K. Chung, A. Lau, H. Tam, C. Lu, Y. Luo, G. Peng, G. Li, and T. Wang, "Mode-division multiplexed transmission with inline few-mode fiber amplifier," *Optics Express*, vol. 20, no. 3, pp. 2668–2680, January 2012.

[33] R. Ryf, S. Randel, A. Gnauck, C. Bolle, A. Sierra, S. Mumtaz, M. Esmaeelpour, E. Burrows, R. Essiambre, P. Winzer, D. Peckham, A. McCurdy, and R. Lingle, "Mode-Division Multiplexing Over 96 km of Few-Mode Fiber Using Coherent 6×6 MIMO Processing," *IEEE/OSA Journal of Lightwave Technology*, vol. 30, no. 4, pp. 521–531, February 2012.

[34] M. Li, B. Hoover, S. Li, S. Bickham, S. Ten, E. Ip, Y. Huang, E. Mateo, Y. Shao, and T. Wang, "Low delay and large effective area few-mode fibers for mode-division multiplexing," in *Proc. OptoElectronics and Communications Conference*, 2012, pp. 495–496.

[35] R. Maruyama, N. Kuwaki, S. Matsuo, K. Sato, and M. Ohashi, "DMD Free Transmission Line Composed of TMFs with Large Effective Area for MIMO Processing," in *Proc. European Conference and Exhibition on Optical Communication*, September 2012, p. Tu.1.F.2.

[36] K. Sato, R. Maruyama, N. Kuwaki, S. Matsuo, and M. Ohashi, "Optimized graded index two-mode optical fiber with low DMD, large Aeff and low bending loss," *Optics Express*, vol. 21, no. 14, pp. 1489–1492, July 2013.

[37] E. Ip, M. Li, K. Bennett, Y. Huang, A. Tanaka, A. Korolev, K. Koreshkov, W. Wood, E. Mateo, J. Hu, and Y. Yano, "146×6×19-Gbaud wavelength- and mode-division multiplexed transmission over 10×50-km spans of few-mode fiber with a gain-equalized few-mode EDFA," in *Proc. Optical Fiber Communication Conference and Exposition*, March 2013, pp. 1–3.

[38] T. Mori, T. Sakamoto, M. Wada, T. Yamamoto, and F. Yamamoto, "Low DMD Four LP Mode Transmission Fiber for Wide-band WDM-MIMO System," in *Proc. Optical Fiber Communication Conference and Exposition*, March 2013, p. OTh3K.1.

[39] R. Ryf, S. Randel, N. Fontaine, M. Montoliu, E. Burrows, S. Chandrasekhar, A. Gnauck, C. Xie, R. Essiambre, P. Winzer, R. Delbue, P. Pupalaikis, A. Sureka, Y. Sun, L. Grüner-Nielsen, R. Jensen, and R. Lingle, "32-bit/s/Hz Spectral Efficiency WDM Transmission over 177-km Few-Mode Fiber," in *Proc. Optical Fiber Communication Conference and Exposition*, March 2013, p. PDP5A.1.

[40] A. Ellis and N. Doran, "Are few-mode fibres a practical solution to the capacity crunch?" in *Proc. International Conference on Transparent Optical Networks*, June 2013, pp. 1–4.

[41] W. Thornburg, B. Corrado, and X. Zhu, "Selective launching of higher-order modes into an optical fiber with an optical phase shifter," *Optics Letters*, vol. 19, no. 7, pp. 454–456, April 1994.

[42] M. Salsi, C. Koebele, D. Sperti, P. Tran, P. Brindel, H. Mardoyan, S. Bigo, A. Boutin, F. Verluise, P. Sillard, M. Bigot-Astruc, L. Provost, F. Cerou, and G. Charlet, "Transmission at 2×100 Gb/s, over Two Modes of 40 km-long Prototype Few-Mode Fiber, using LCOS based Mode Multiplexer and Demultiplexer," in *Proc. Optical Fiber Communication Conference and Exposition*, March 2011, p. PDPB9.

[43] J. Carpenter, B. Thomsen, and T. Wilkinson, "Degenerate Mode-Group Division Multiplexing," *IEEE/OSA Journal of Lightwave Technology*, vol. 30, no. 24, pp. 3946–3952, December 2012.

[44] C. Poole, J. Wiesenfeld, D. DiGiovanni, and A. Vengsarkar, "Optical fiber-based dispersion compensation using higher order modes near cutoff," *IEEE/OSA Journal of Lightwave Technology*, vol. 12, no. 10, pp. 1746–1758, October 1994.

[45] I. Giles, A. Obeysekara, R. Chen, D. Giles, F. Poletti, and D. Richardson, "Fiber LPG Mode Converters and Mode Selection Technique for Multimode SDM," *IEEE Photonics Technology Letters*, vol. 24, no. 21, pp. 1922–1925, November 2012.

[46] R. Ryf, N. Fontaine, and R. Essiambre, "Spot-Based Mode Couplers for Mode-Multiplexed Transmission in Few-Mode Fiber," *IEEE Photonics Technology Letters*, vol. 24, no. 21, pp. 1973–1976, November 2012.

[47] N. Fontaine, R. Ryf, S. Leon-Saval, and J. Bland-Hawthorn, "Evaluation of Photonic Lanterns for Lossless Mode-Multiplexing," in *Proc. European Conference and Exhibition on Optical Communication*, September 2012, p. Th.2.D.6.

[48] E. Ip, "Advances in transmisssion over a few modes fiber: state of the art and research results," in *Proc. European Conference and Exhibition on Optical Communication*, September 2012, p. Tu.1.C.5.

[49] R. Ryf, A. Sierra, R. Essiambre, S. Randel, A. Gnauck, C. Bolle, M. Esmaeelpour, P. Winzer, R. Delbue, P. Pupalaikise, A. Sureka, D. Peckham, A. McCurdy, and R. Lingle, "Mode-equalized distributed Raman amplification in 137-km few-mode fiber," in *Proc. European Conference and Exhibition on Optical Communication*, September 2011, p. Th.13.K.5.

[50] S. Savory, "Digital filters for coherent optical receivers," *Optics Express*, vol. 16, no. 2, pp. 804–817, January 2008.

[51] S. Savory, G. Gavioli, R. Killey, and P. Bayvel, "Electronic compensation of chromatic dispersion using a digital coherent receiver," *Optics Express*, vol. 15, no. 5, pp. 2120–2126, March 2007.

[52] M. Kuschnerov, F. Hauske, K. Piyawanno, B. Spinnler, M. Alfiad, A. Napoli, and B. Lankl, "DSP for Coherent Single-Carrier Receivers," *IEEE/OSA Journal of Lightwave Technology*, vol. 27, no. 16, pp. 3614–3622, August 2009.

[53] M. Kuschnerov, M. Chouayakh, K. Piyawanno, B. Spinnler, E. de Man, P. Kainzmaier, M. Alfiad, A. Napoli, and B. Lankl, "Data-Aided Versus Blind Single-Carrier Coherent Receivers," *IEEE Photonics Journal*, vol. 2, no. 3, pp. 387–403, June 2010.

[54] A. Lobato, F. Ferreira, B. Inan, S. Adhikari, M. Kuschnerov, A. Napoli, B. Spinnler, and B. Lankl, "Maximum-Likelihood Detection in Few-Mode Fiber Transmission With Mode-Dependent Loss," *IEEE Photonics Technology Letters*, vol. 25, no. 12, pp. 1095–1098, June 2013.

[55] M. Kuschnerov, M. Chouayakh, K. Piyawanno, B. Spinnler, M. Alfiad, A. Napoli, and B. Lankl, "On the Performance of Coherent Systems in the Presence of Polarization-Dependent Loss for Linear and Maximum Likelihood Receivers," *IEEE Photonics Technology Letters*, vol. 22, no. 12, pp. 920–922, June 2010.

[56] A. Lobato, F. Ferreira, M. Kuschnerov, D. van den Borne, S. Jansen, A. Napoli, B. Spinnler, and B. Lankl, "Impact of mode coupling on the mode-dependent loss tolerance in few-mode fiber transmission," *Optics Express*, vol. 20, no. 28, pp. 29 776–29 783, December 2012.

[57] E. Ip, N. Bai, Y. Huang, E. Mateo, F. Yaman, M. Li, S. Bickham, S. Ten, J. Linares, C. Montero, V. Moreno, X. Prieto, V. Tse, K. Chung, A. Lau, H. Tam, C. Lu, Y. Luo, G. Peng, and G. Li, "88×3×112-Gb/s WDM transmission over 50

km of three-mode fiber with inline few-mode fiber amplifier," in *Proc. European Conference and Exhibition on Optical Communication*, September 2011, pp. 1–3.

[58] R. Essiambre, G. Kramer, P. Winzer, G. Foschini, and B. Goebel, "Capacity Limits of Optical Fiber Networks," *IEEE/OSA Journal of Lightwave Technology*, vol. 28, no. 4, pp. 662–701, February 2010.

[59] S. Randel, R. Ryf, A. Sierra, P. Winzer, A. Gnauck, C. Bolle, R. Essiambre, D. Peckham, A. McCurdy, and R. Lingle, "6×56-Gb/s mode-division multiplexed transmission over 33-km few-mode fiber enabled by 6×6 MIMO equalization," *Optics Express*, vol. 19, no. 17, pp. 16 697–16 707, August 2011.

[60] C. Koebele, M. Salsi, L. Milord, R. Ryf, C. Bolle, P. Sillard, S. Bigo, and G. Charlet, "40 km transmission of five mode division multiplexed data streams at 100 Gb/s with low MIMO-DSP complexity," in *Proc. European Conference and Exhibition on Optical Communication*, September 2011, pp. 1–3.

[61] R. Ryf, S. Randel, M. Mestre, C. Schmidt, A. Gnauck, R. Essiambre, P. Winzer, R. Delbue, P. Pupalaikis, A. Sureka, Y. Sun, X. Jiang, A. McCurdy, D. Peckham, and R. Lingle, "209-km single-span mode- and wavelength-multiplexed transmission over hybrid few-mode fiber," in *Proc. European Conference and Exhibition on Optical Communication*, September 2012, pp. 1–3.

[62] V. Sleiffer, Y. Jung, B. Inan, H. Chen, R. van Uden, M. Kuschnerov, D. van den Borne, S. Jansen, V. Veljanovski, T. Koonen, D. Richardson, S. Alam, F. Poletti, J. Sahu, A. Dhar, B. Corbett, R. Winfield, A. Ellis, and H. Waardt, "Mode-division-multiplexed 3×112-Gb/s DP-QPSK transmission over 80 km few-mode fiber with inline MM-EDFA and Blind DSP," in *Proc. European Conference and Exhibition on Optical Communication*, September 2012, p. Tu.1.C.2.

[63] V. Sleiffer, Y. Jung, V. Veljanovski, R. van Uden, M. Kuschnerov, Q. Kang, L. Grüner-Nielsen, Y. Sun, D. Richardson, S. Alam, F. Poletti, J. Sahu, A. Dhar, H. Chen, B. Inan, T. Koonen, B. Corbett, R. Winfield, A. Ellis, and H. Waardt, "73.7 Tb/s (96×3×256-Gb/s) mode-division-multiplexed DP-16QAM transmission with inline MM-EDFA," *Optics Express*, vol. 20, no. 26, pp. 428–438, December 2012.

[64] V. Sleiffer, P. Leoni, Y. Jung, J. Surof, M. Kuschnerov, V. Veljanovski, D. Richardson, S. Alam, L. Grüner-Nielsen, Y. Sun, B. Corbett, R. Winfield, S. Calabrò, B. Sommerkorn-Krombholz, H. Kirchbauer, and H. Waardt, "20×960-Gb/s MDM-DP-32QAM transmission over 60 km FMF with inline MM-EDFA," in *Proc. European Conference and Exhibition on Optical Communication*, September 2013, p. We.2.D.2.

[65] V. Sleiffer, H. Chen, Y. Jung, M.Kuschnerov, D. Richardson, S. Alam, Y. Sun, L. Grüner-Nielsen, N. Pavarelli, B. Snyder, P. O'Brien, A. Ellis, A. Koonen, and H. Waardt, "480 km transmission of MDM 576-Gb/s 8-QAM using a few-mode

re-circulating loop," in *Proc. IEEE Photonics Conference*, September 2013, pp. 1–2.

[66] V. Sleiffer, Y. Jung, M. Kuschnerov, S. Alam, D. Richardson, L. Grüner-Nielsen, Y. Sun, and H. Waardt, "Optical chopper-based re-circulating loop for few-mode fiber transmission," *Optics Letters*, vol. 39, no. 5, pp. 1181–1184, March 2014.

[67] A. Lobato, F. Ferreira, B. Inan, M. Kuschnerov, D. van den Borne, S. Jansen, B. Spinnler, and B. Lankl, "The Impact of Differential Mode Delay on Mode-Division Multiplexed Coherent Optical OFDM Transmission," in *Proc. Optical Fiber Communication Conference and Exposition*, March 2012, p. OTu2C.2.

Chapter 3

Models for MDM-FMF Systems

3.1 Introduction

FMFs have been investigated in the last years due to their larger information transport capacity, when compared with SMFs [1]. An N-fold capacity increase, with N equal to the number of independent modes of the FMF, is obtained using MDM. However, such increase is only attained at the cost of higher complexity of the equalizer, as it needs to compensate for the combined effect of DMD and linear XT, which originates a CIR spread over a long time interval [2]. Despite the lower nonlinear coefficients of FMFs, the nonlinear impairments have to be considered since the MDM-FMF systems will operate close to the nonlinear threshold as present SMF systems. The remaining main impairments in MDM-FMF systems are introduced by MMUXs/MDMUXs, fiber splices, and MMAs. The MMUXs/MDMUXs and splices introduce linear XT as well as MDL. The MMAs are the main source of MDL (or MDG) posing a fundamental performance limitation on the equalization performance.

In this chapter, the models required for the study and design of long-haul MDM-FMF systems are derived. Section 3.2.1 presents the set of coupled linear differential equations describing the linear XT in FMFs and proposes a semi-analytical (SA) solution. Section 3.2.2 derives a set of MM-CNLSE for nonlinear propagation in MMFs including linear XT. Section 3.3 presents the optimization design of MMUXs/MDMUXs based on PMs for low linear XT. Section 3.4 presents the general simulation setup for long-haul MDM-FMF systems that integrates the simulation models developed along the chapter. Finally, transmission simulation results over a TMF are presented in section 3.4.1. The main conclusions are gathered in section 3.5.

The work presented along this chapter is based on the work reported in [3–5].

3.2 Few-Mode Fibers Model

Along this section, a NSAM for propagation over FMFs taking into account the linear XT and the Kerr nonlinear effects is presented.

3.2.1 FMF Linear Crosstalk

In order to correctly understand and simulate the performance of MDM-FMF systems, the linear XT that arises from the waveguide imperfections distributed along the fiber length [6] (dXT), needs to be correctly modeled. This section describes the linear XT through a set of the coupled linear differential equations and proposes a SA solution. The SA solutions are compared to the numerical solutions obtained through the Runge-Kutta 4th-5th order (RK45) method. In this section, the linear XT between orthogonal polarizations is not considered at first since, for SMFs, it has already been shown that such XT can be modeled by a random rotation following an uniform distribution between 0 and 2π [7]. After modeling the linear XT between the LP modes for a given polarization, the linear XT between the orthogonal polarizations of a given LP mode can be introduced using the SMFs model.

Waveguide Imperfections Model

The waveguide imperfections [6] were modeled by random fluctuations of the core axis position, given by: $\varepsilon\left(x,y\right)=\varepsilon_p\left(x+\delta x,y+\delta y\right)$, where ε is the perturbed permittivity, $\varepsilon_p(x,y)$ is the ideal profile permittivity, δx and δy are the random displacement of the abscissa and ordinate coordinates in each fiber section, respectively. The proposed model divides the fiber in multiple sections, each one with a constant random displacement of the core axis position, as shown in Fig. 3.1. Therefore, each section has constant coupling coefficients. In order to analytically describe the XT arising from the waveguide imperfections, the coupled mode theory (CMT) presented in [6] is used, particularly the following coupled-mode equations:

$$\partial_z\tilde{A}_u(z,\omega)=-\mathrm{j}\left[\beta_u(\omega)-\beta_{0,u}\right]\tilde{A}_u(z,\omega)-\mathrm{j}\sum_{u_1\neq u}C_{u,u_1}\tilde{A}_{u_1}(z,\omega)\exp(\mathrm{j}\Delta\beta_{u,u_1}z) \quad (3.1)$$

where j is the imaginary unit, t is the time variable, z is the fiber longitudinal coordinate, $\tilde{A}_u(z,\omega)$ is the Fourier transform of the mode u slowly varying field envelope $A_u(z,t)$ ($\tilde{A}_u(z,\omega)=\int_{-\infty}^{+\infty}A_u(z,t)\exp(-\mathrm{j}\omega t)dt$), $\beta_u(\omega)$ is the mode u frequency depen-

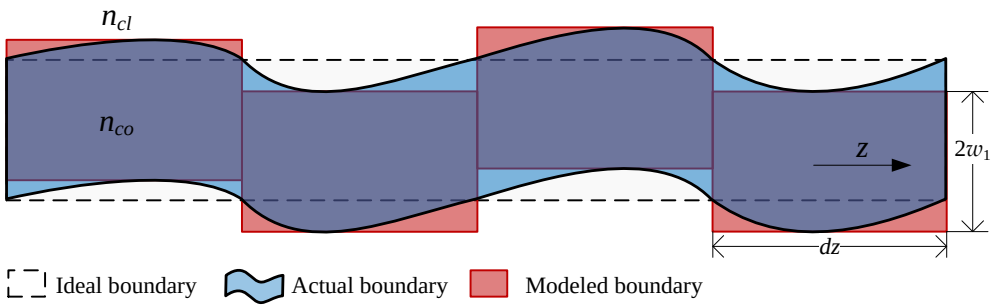

Figure 3.1: Sketch of a fiber with distorted core-cladding boundary.

dent propagation constant, $\beta_{l,u}$ is the l^{th} order coefficient of a Taylor series expansion of $\beta_u(\omega)$ centered at the carrier frequency ω_0, $\Delta\beta_{u,u_1} = (\beta_{0,u} - \beta_{0,u_1})$, and C_{u,u_1} are the coupling coefficients. C_{u,u_1} is given by [6]:

$$C_{u,u_1} = \frac{\omega_0}{4} \iint \Delta\varepsilon(x,y) F_u^* \cdot F_{u_1} \, dxdy \tag{3.2}$$

where $\Delta\varepsilon(x,y) = \varepsilon(x,y) - \varepsilon_p(x,y)$. The first and second term in the right-hand side (RHS) of (3.1) are responsible for the dispersion effects and for the linear XT, respectively. Note that, for z varying along a single fiber section, C_{u,u_1} is constant.

Considering, the simple case of a TMF, where only the coupling between the LP_{01} mode ($u = 1$) and the LP_{11} mode ($u_1 = 2$) is present, equations (3.1) can be written in a simpler form that can be solved analytically for continuous-wave (CW) signals in each fiber section [6]:

$$A_1(z) = \exp\left(\mathrm{j}\frac{\Delta\beta}{2}z\right)\left[\left(\cos sz - \mathrm{j}\frac{\Delta\beta}{2}\frac{\sin sz}{s}\right)A_1(0) - \mathrm{j}\kappa\frac{\sin sz}{s}A_2(0)\right] \tag{3.3}$$

$$A_2(z) = \exp\left(-\mathrm{j}\frac{\Delta\beta}{2}z\right)\left[-\mathrm{j}\kappa^*\frac{\sin sz}{s}A_1(0) + \left(\cos sz + \mathrm{j}\frac{\Delta\beta}{2}\frac{\sin sz}{s}\right)A_2(0)\right] \tag{3.4}$$

where $\Delta\beta = \Delta\beta_{12}$, $s^2 = \kappa\kappa^* + (\Delta\beta/2)^2$, and $\kappa = C_{12} = {C_{21}}^*$. From (3.3) and (3.4), it can be concluded that the coupling strength depends on the relation between $|\kappa|^2$ and $\Delta\beta^2$. Fig. 3.2(a) and Fig. 3.2(b) show the mode powers $|A_1|^2$ and $|A_2|^2$ as functions of the interaction distance z, for $\Delta\beta = 0$ and for $\Delta\beta = 4|\kappa|$, respectively, with $\kappa = \pi/2$. Fig. 3.2(a) shows that, for $\Delta\beta = 0$, the power is transfered back and forward between the two modes, with a complete transfer occurring for $|\kappa|z$ odd multiple of $\pi/2$. On the other hand, Fig. 3.2(b) shows that coupling is incomplete for $\Delta\beta \neq 0$. Moreover, for $\Delta\beta = 2|\kappa|$ the maximum coupling is 1/2.

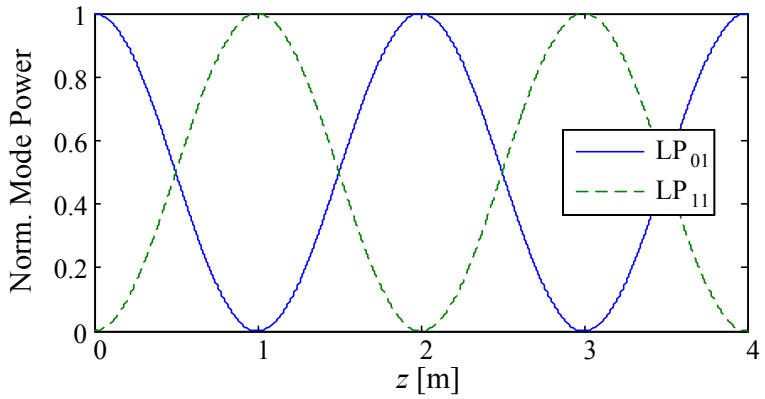

(a)

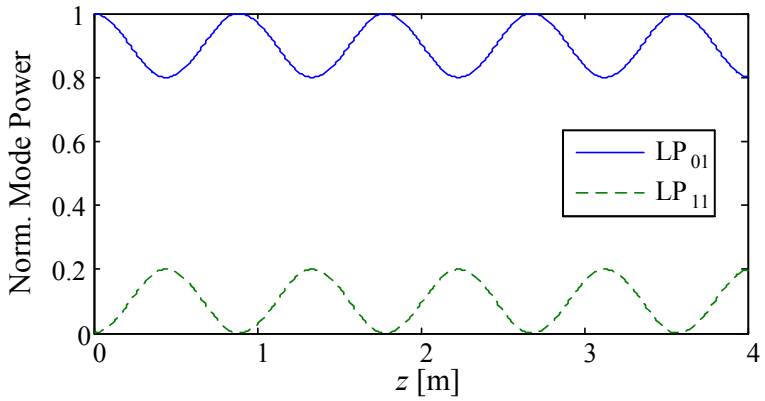

(b)

Figure 3.2: Plots the mode powers $|A_1|^2$ and $|A_2|^2$ as functions of the interaction distance z, for (a) $\Delta\beta = 0$ and for (b) $\Delta\beta = 4|\kappa|$, with $\kappa = \pi/2$.

In the following, the proposed model is applied to a fiber with more than one section. The random position of the core axis, (ρ_d, ϕ_d) in cylindrical coordinates, is assumed to follow an uniform distribution. In order to find a typical value for the maximum random displacement ($\rho_{d,max}$), the proposed model is applied to a polarization maintaining fiber (PMF) with published experimental measurements (note that at the time of this work no experimental results for FMFs were available). The characteristics of the FlatCladd PMF fiber shown in Table I of [8] are considered. According to [8], the experimental measurements of the linear XT between the polarizations along the fiber length z are fitted by:

$$XT = \tanh(hz) \tag{3.5}$$

where h is the mode coupling parameter. The mode coupling parameter can be made higher or lower during the fiber fabrication process controlling the fiber birefringence

(B). The birefringence is defined by the difference $B = (\overline{n}^{\mathrm{LP}_{01x}} - \overline{n}^{\mathrm{LP}_{01y}})$, where $\overline{n}^{\mathrm{LP}_{01x}}$ and $\overline{n}^{\mathrm{LP}_{01y}}$ are the effective indexes for the orthogonal polarizations of the LP_{01}. The parameters h and B of the PMF fiber presented in [8] are $5.9 \cdot 10^{-6}$ and $2.5 \cdot 10^{-4}$, respectively. $\Delta\beta$ is given by Bk_0, where k_0 is the propagation constant in free space. Finally, the experimental fitted function (3.5) can be compared to simulation results obtained with the proposed model (discretized core displacements). In order to find the $\rho_{d,max}$ value leading to the best match, a set of simulations has been executed sweeping the $\rho_{d,max}$ value with a step of $10^{-4} \cdot w_1$ considering a given section size. Considering that only one of the polarization modes is excited at the fiber input, the best match is obtained for $\rho_{d,max} = 10^{-2} \cdot w_1$ and a 50 meter section size. Fig. 3.3(a) and Fig. 3.3(b) show the mode power and the XT as a function of the fiber length, respectively. A very good agreement of the evolution of the power in each polarization modes and of the XT along the fiber length is seen. Furthermore, a similar match has been obtained for other section sizes and corresponding optimum $\rho_{d,max}$ values.

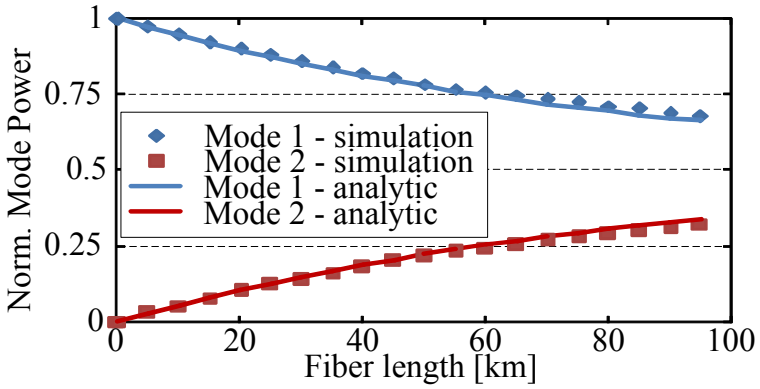

(a)

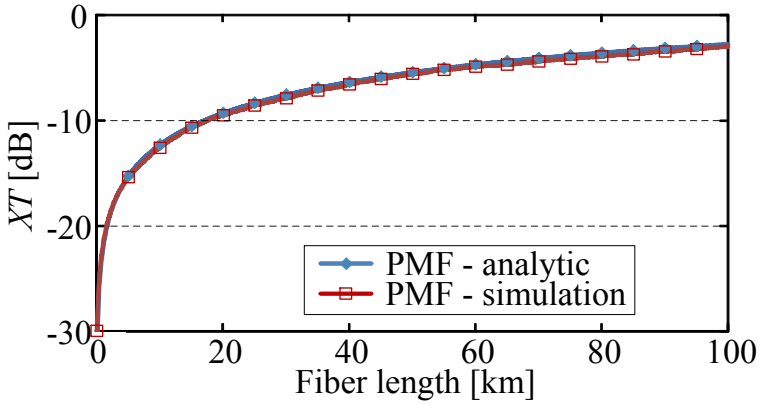

(b)

Figure 3.3: (a) Normalized power in each of polarization modes as a function of the fiber length. (b) XT as a function of the fiber length.

Semi-Analytical Solutions

The analytical solution of (3.1) was easily obtained by hand for two modes. However, for a higher number of modes, this method become endless. Moreover, numerical methods, such as the RK45 method [9], are not adequate to solve (3.1) since they would require computation times that are unfordable in most applications. Note that equations (3.1) have to be solve for each fiber section with different fiber displacements. Therefore, a SA solution is desirable.

In the following, a SA solution of (3.1) for CW signals is presented. With the purpose of avoiding the complex exponentials in (3.1), which would generate a very high number of terms when successively differentiated in order to z, the Fourier transform can be applied to (3.1), obtaining:

$$\mathrm{j}\omega_z \widetilde{A}_u(\omega_z) = -\mathrm{j}\sum_{u_1 \neq u} C_{u,u_1}\widetilde{A}_{u_1}(\omega_z - \Delta\beta_{u,u_1}) \tag{3.6}$$

where ω_z is the spatial frequency. The system of equations (3.6) can be solved by substitution, eliminating $\widetilde{A}_{u_1}$ with $u_1 \neq u$, obtaining the following system of equations:

$$\widetilde{A}_u(\omega_z) \times \left[a_{u,N}(\mathrm{j}\omega_z)^N + ... + a_{u,0}(\mathrm{j}\omega_z)^0\right] = 0 \tag{3.7}$$

where N is equal to $2(M-1)$ with M equal to the number of independent modes, and $a_{u,i}$ with $i = 1, ..., N$ are constant coefficients function of $\Delta\beta_{u,u_1}$ and C_{u,u_1}. Now, by applying the inverse Fourier transform to (3.7), a system of differential equations with constant coefficients is obtained which can be solved using the method of the characteristic polynomial, obtaining as solution:

$$A_u(z) = c_{u,1}\exp(s_{u,1}z) + ... + c_{u,N}\exp(s_{u,N}z) \tag{3.8}$$

where $s_{u,i}$ are the characteristic polynomial roots and $c_{u,i}$ are constants that can be determined from the initial conditions at $z = 0$, obtained by differentiating (3.1) and (3.8), and equating the results. After some algebra, it can be found that $c_{u,i}$ are the solutions of the following system of linear equations:

$$\begin{bmatrix} s_{u,1} & \cdots & s_{u,N} \\ \vdots & \ddots & \vdots \\ s_{u,1}^N & \cdots & s_{u,N}^N \end{bmatrix} \begin{bmatrix} c_{u,1} \\ \vdots \\ c_{u,N} \end{bmatrix} = \begin{bmatrix} \left(d_z^0 A_u\right)_{z=0} \\ \vdots \\ \left(d_z^{N-1} A_u\right)_{z=0} \end{bmatrix} \tag{3.9}$$

where $(d_z^i A_u)_{z=0}$ is the i-th derivative of (3.1). In this way, the system of coupled differential equations in (3.1) has been simplified to a system of linear equations (3.9). The solution of the system of linear equations (3.9) allows computing the linear XT along the fiber length. However, the system may be bad conditioned when considering non-degenerate and degenerate modes simultaneously, since the value of $\Delta\beta_{u,u_1}$ between pairs of non-degenerate modes and the value of $\Delta\beta_{u,u_1}$ between pairs of degenerate modes may differ by several orders of magnitude. Since the linear XT between the degenerate modes is much stronger than the linear XT with any of the other modes, the linear XT calculation/modeling can be divided in two stages in order to avoid a bad conditioned system. In the first stage, only the linear XT between non-degenerate modes are considered and, in the second stage, only the linear XT between the degenerate modes is considered.

The analytical equations for $a_{u,i}$ and $(d_z^i A_u)_{z=0}$ as functions of $\Delta\beta_{u,u_1}$ and C_{u,u_1} can be obtained using a software tool with symbolic math computation capability. In this thesis, the Symbolic Math Toolbox of Matlab R2011b has been used. The appendix A shows $a_{u,i}$ and $(d_z^i A_u)_{z=0}$ as a function of $\Delta\beta_{u,u_1}$ and C_{u,u_1} for $M = 3$. Replacing the $\Delta\beta_{u,u_1}$ and C_{u,u_1} numeric values in the $a_{u,i}$ analytical equations, the $s_{u,i}$ values can be calculated using algorithms for the calculation of polynomials roots. Moreover, $(d_z^i A_u)_{z=0}$ values are obtained replacing the $\Delta\beta_{u,u_1}$ and C_{u,u_1} numeric values in the analytical formulas presented in appendix A. Finally, the system of linear equations (3.9) can be numerically solved.

Semi-Analytical Solutions Validation

In this section, the SA solutions are validated using the RK45 method [9] considering a SI-FMF with six non-degenerate LP modes: LP_{01}, LP_{11}, LP_{21}, LP_{02}, LP_{31} and LP_{12}. The fiber profile parameters are: $\Delta n_{co} = 2.5 \cdot 10^{-3}$ and $w_1 = 14\,\mu m$. Table 3.1 shows the $\Delta\beta$ value for each pair of modes at 1550 nm (for the sake of clarity, the modes were numbered from one to six). Fig. 3.4 depicts the amplitude of C_{u,u_1} as a function of the fiber displacement vector for a radial displacement from 0 to $0.02 \cdot w_1$. From this figure, the pairs of modes with higher coupling strength can be identified, and it can be verified that the coupling between symmetric modes (LP_{01}, for example) and anti-symmetric modes (LP_{11}, for example) requires a non-symmetrical perturbation. The surfaces shown in Fig. 3.4 allow the rapid calculation of the coupling coefficients C_{u,u_1} using interpolation for a random displacement.

Table 3.1: Propagation constants differences at 1550 nm.

$\frac{\Delta\beta_{u,u1}}{k_0}(\cdot 10^{-3})$	1-LP_{01}	2-LP_{11}	3-LP_{21}	4-LP_{02}	5-LP_{32}	6-LP_{12}
1-LP_{01}	0	0.68	1.55	1.83	2.58	3.01
2-LP_{11}	-0.68	0	0.87	1.15	1.90	2.33
3-LP_{21}	-1.55	-0.87	0	0.28	1.03	1.46
4-LP_{02}	-1.83	-1.15	-0.28	0	0.75	1.19
5-LP_{31}	-2.58	-1.90	-1.03	-0.75	0	0.43
6-LP_{12}	-3.01	-2.33	-1.46	-1.19	-0.43	0

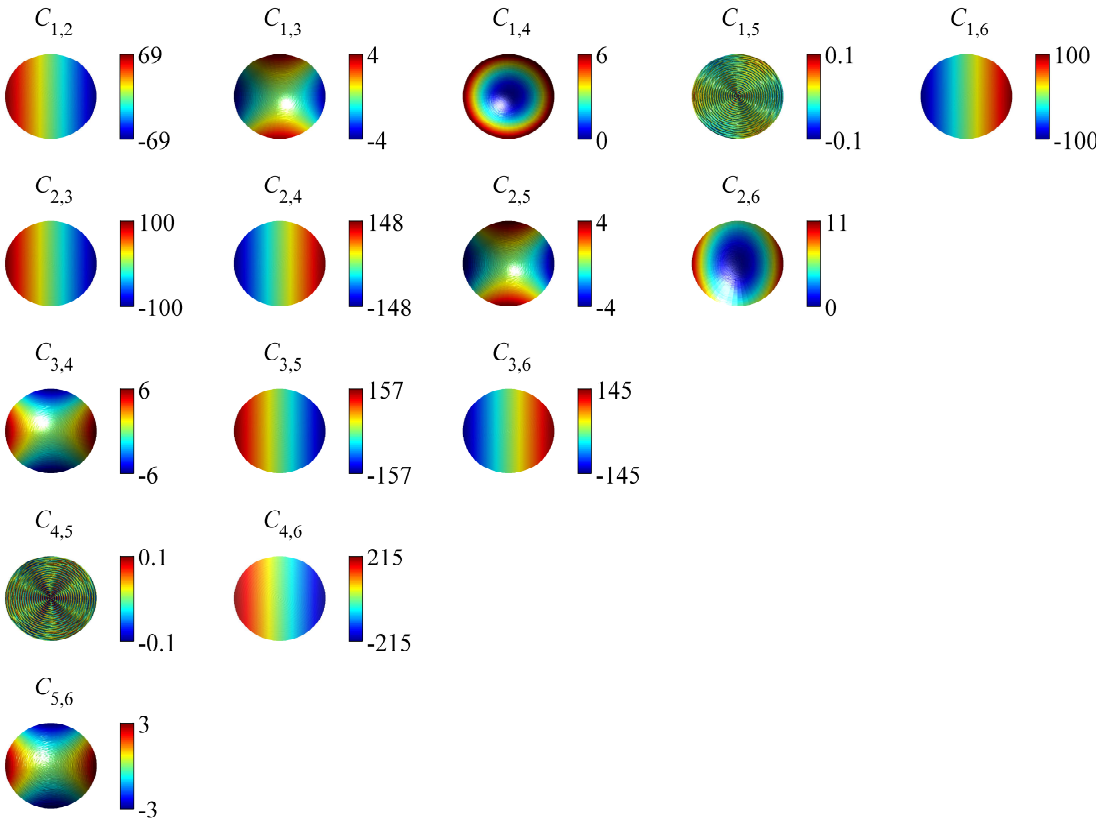

Figure 3.4: C_{u,u_1} (z-axis, orthogonal to the page) as a function of the fiber displacement vector (xy-plane, page plane).

In the following the SA solutions are compared to the numerical solutions using the RK45 method. The variable-step width of the RK45 method is specified considering a relative error tolerance of 10^{-6} and an absolute error tolerance of 10^{-9}. Fig. 3.5 shows the overlap of the modal powers given by the SA solutions and the modal powers given by the numerical method as a function of z, considering a fiber core displacement of $\rho_d = 0.02 \cdot w_1$ and $\phi_d = 45°$, for: (a) $A(0) = \sqrt{1/6} \cdot [1\ 1\ 1\ 1\ 1\ 1]$ and (b) $A(0) = \sqrt{1/21 \cdot [1\ 2\ 3\ 4\ 5\ 6]}$, where $A(0) = [A_1(0) \dots A_6(0)]$. A very good agreement between the SA and numerical solutions is obtained for both input conditions. For both input conditions, an approximate periodic exchange of power can be seen with a mode power variation up to 28 %.

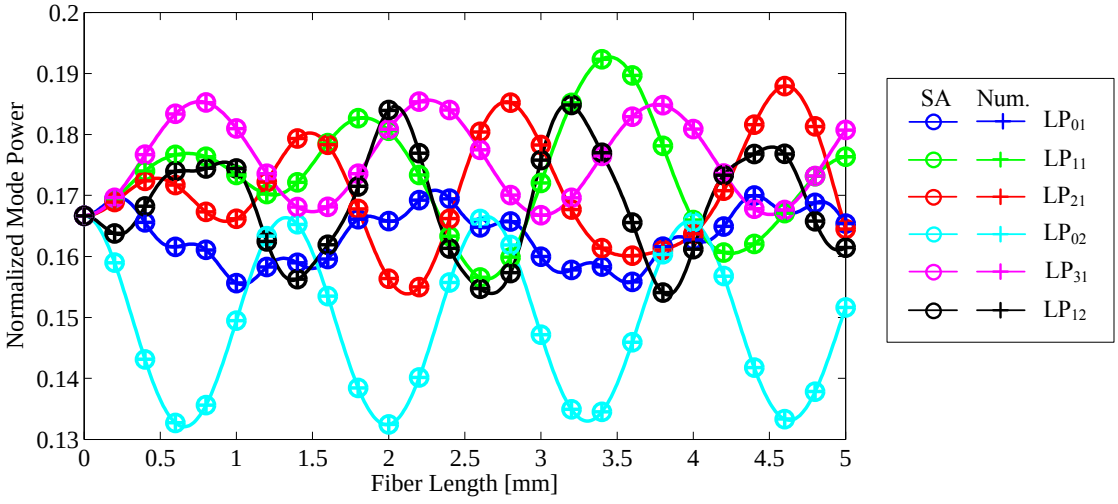

(a)

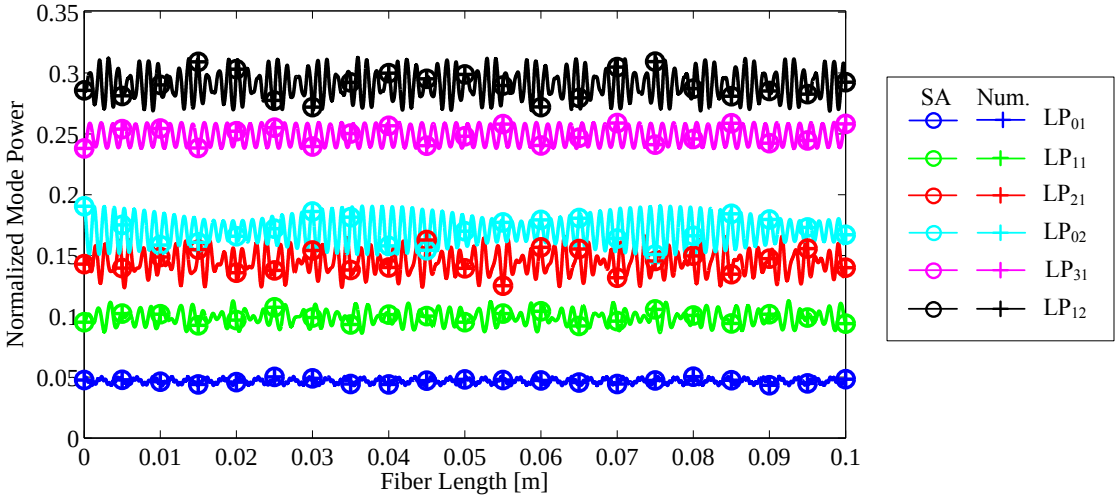

(b)

Figure 3.5: Normalized mode power as a function of the fiber length, for: (a) $A(0) = \sqrt{1/6} \cdot [1\ 1\ 1\ 1\ 1\ 1]$, and (b) $A(0) = \sqrt{1/21} \cdot [1\ 2\ 3\ 4\ 5\ 6]$.

In order to have a better measure of the error magnitude, the mean squared error between the SA results and the numerical results is calculated for each mode, MSE_u, given by:

$$MSE_u = \frac{1}{N}\sum_{n=1}^{N}\left|A_u^{SA}(z_n) - A_u^{NUM}(z_n)\right|^2 \tag{3.10}$$

where A_u^{SA} is the SA mode amplitude solution, A_u^{NUM} is the numerical mode amplitude solution, and z_n are the discrete points considered in a specific fiber length. MSE_u has been calculated considering 10^5 discrete points equally spaced along a fiber with 1 m. Fig. 3.6 shows the MSE_u as a function of ρ_d between 0 and $0.02 \cdot w_1$. Fig. 3.6 shows that MSE_u increases with ρ_d, still, the highest MSE_u for $0.02 \cdot w_1$ (two times the maximum displacement found in section 3.2.1) is lower than $2.5 \cdot 10^{-9}$. Therefore, it can be concluded that the SA method proposed provides an accurate estimative of the linear XT taking place along a FMF. More importantly, using the SA method proposed the computation time required to calculate the linear XT along a fiber with a few meters is reduced by three orders of magnitude compared to the RK45 method which required tens of seconds executing on a standard personal computer operating at 2.8 GHz. In conclusion, the SA solutions obtained enable a time efficient and accurate computation of the linear XT occurring along the fiber length. They are therefore a valuable alternative to the numerical solution, which would not be practical due to computation time constraints.

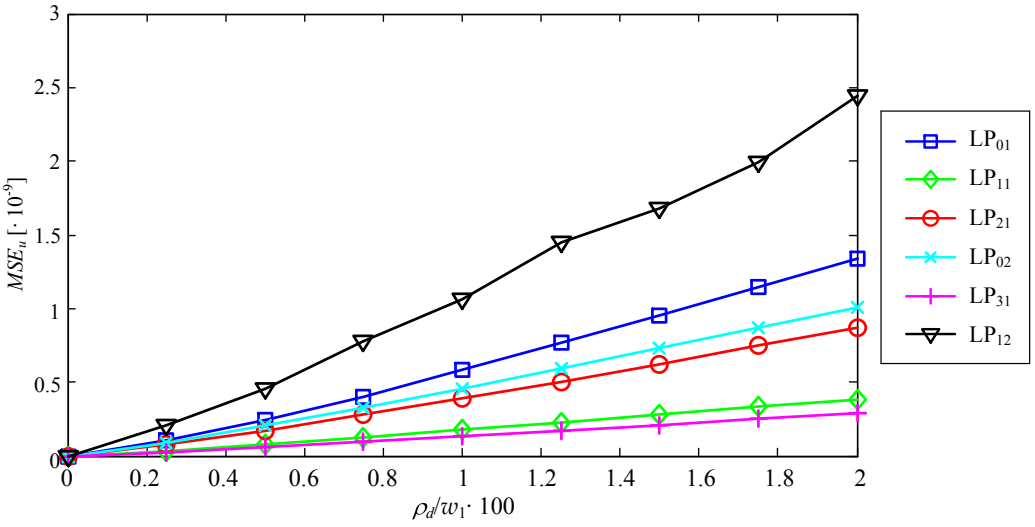

Figure 3.6: MSE_u along the azimuthal coordinate as a function of ρ_d.

3.2.2 FMF Nonlinear Propagation

The total electric field in the frequency domain expanded into M modes and two polarizations is given by:

$$\begin{aligned}\widetilde{\mathbf{E}}(\mathbf{r},\omega) &= \frac{1}{2}\widetilde{E}_x(\mathbf{r},\omega)\,\hat{x} + \frac{1}{2}\widetilde{E}_y(\mathbf{r},\omega)\,\hat{y} + c.c. \\ &= \sum_{ui}\left[\frac{1}{2}\frac{F_u(x,y)}{\sqrt{N_u}}\widetilde{A}_{ui}(z,\omega-\omega_0)\exp\left(-\mathrm{j}\beta_{0,ui}z\right)\hat{i} + c.c.\right]\end{aligned} \tag{3.11}$$

where $\mathbf{r}$ is the position vector in Cartesian coordinates (x,y,z), ω is the angular frequency variable, $\widehat{i}$ is the unit linear polarization vector, j is the imaginary unit, u is the mode index, i is the polarization index ($i=1$ stands for x-polarization and $i=2$ stands for y-polarization), $\sum_{ui} = \sum_{u=1}^{M}\sum_{i=1}^{2}$, $F_u(x,y)$ is the transversal field distribution of mode u, $\tilde{A}_{ui}(z,\omega)$ is the Fourier transform of the slowly varying wave envelope $A_{ui}(z,t)$ ($\tilde{A}_{ui}(z,\omega) = \int_{-\infty}^{+\infty} A_{ui}(z,t)\exp(-\mathrm{j}\omega t)dt$, where t is the time variable), $N_u = \iint_{-\infty}^{+\infty}|F_u(x,y)|^2 dxdy$ such that $|A_{ui}(z,t)|^2$ is the instantaneous optical power, $\beta_{l,ui}$ is the l^{th} order angular frequency derivative of $\beta_{ui}(\omega)$ at ω_0, and *c.c.* stands for complex conjugate. Note that in (3.11), $F_u(x,y)$ is assumed to vary negligibly with polarization and ω within the C-band as well as with small waveguide imperfections and the nonlinear induced polarization [7]. $F_u(x,y)$ and $\beta_{ui}(\omega)$ are solutions of the eigenvalue equation [7]:

$$\nabla^2 F_u(x,y) + \left[\omega^2\mu_0\varepsilon_p(x,y) - \beta_{ui}^2(\omega)\right]F_u(x,y) = 0 \tag{3.12}$$

where μ_0 is the permeability of free space, $\varepsilon_p(x,y)$ is the transverse permittivity profile of the optical fiber. $\beta_{ui}(\omega)$ can be expanded in a Taylor series around ω_0 as:

$$\beta_{ui}(\omega) = \beta_{0,ui} + \beta_{1,ui}\Delta\omega + \frac{\beta_{2,ui}}{2}(\Delta\omega)^2 + \frac{\beta_{3,ui}}{6}(\Delta\omega)^3 + ... \tag{3.13}$$

where $\Delta\omega = \omega - \omega_0$. The Taylor series in (3.13) is usually truncated, retaining the terms up to third order.

The propagation of the total electric field in a FMF is governed by the wave equation [7]:

$$\nabla^2\widetilde{\mathbf{E}}(\mathbf{r},\omega) = -\omega^2\mu_0\varepsilon_p(x,y)\,\widetilde{\mathbf{E}}(\mathbf{r},\omega) - \omega^2\mu_0\widetilde{\mathbf{P}}_{\mathbf{NL}}(\mathbf{r},\omega) \tag{3.14}$$

where $\widetilde{\mathbf{P}}_{\mathbf{NL}}(\mathbf{r},\omega)$ is the Fourier transform of the nonlinear polarization $\mathbf{P}_{\mathbf{NL}}(\mathbf{r},t)$ due

to the third-order nonlinear silica susceptibility. In order to include in (3.14) the linear XT due to small waveguide imperfections along the fiber, $\varepsilon_p(x,y)$ is replaced by $\varepsilon\left(x,y\right) = \varepsilon_p\left(x,y\right) + \Delta\varepsilon\left(x,y\right)$ [6], where $\Delta\varepsilon(x,y)$ varies randomly in each fiber section. In a birefringent fiber, the orthogonal polarization components of $\mathbf{P_{NL}}\left(\mathbf{r},t\right)$, $P_{NL_x}(\mathbf{r},t)$ and $P_{NL_y}(\mathbf{r},t)$, can be written as a function of $\mathbf{E}\left(\mathbf{r},t\right)$ orthogonal polarization components, $E_x(\mathbf{r},t)$ and $E_y(\mathbf{r},t)$, as [7]:

$$P_{NL_i} = \frac{3}{8}\varepsilon_0\chi^{(3)}_{xxxx}\left[\left(|E_i|^2 + \frac{2}{3}|E_j|^2\right)E_i + \frac{1}{3}\left(E_i^* E_j\right)E_j\right] \tag{3.15}$$

where $(i,j) = (x,y)$ or $(i,j) = (y,x)$, P_{NL_i} and E_i dependence on $(\mathbf{r},t)$ have been omitted, ε_0 is the permittivity of free space, and $\chi^{(3)}_{xxxx}$ is the third-order silica susceptibility [7]. The wave equation (3.14) can be solved replacing (3.11)-(3.13) and applying the inverse Fourier transform. Considering the slowly varying envelope approximation (in space and in time) [7], the following MM-CNLSE is obtained:

$$\begin{aligned}
&\sum_{ui}\left(\partial_z A_{ui} + \mathfrak{D}A_{ui}\right)\beta_{0,ui}\tfrac{F_u}{\sqrt{N_u}}\exp\left[\mathrm{j}\left(\omega_0 t - \beta_{0,ui}z\right)\right] = \\
&-\mathrm{j}\tfrac{3}{8}\varepsilon_0\mu_0\chi^{(3)}_{xxxx}\cdot\sum_{u_1i_1,u_2i_2,u_3i_3}\left[\begin{array}{l}\xi_i\omega_0^2\dfrac{F_{u_1}F_{u_2}F^*_{u_3}}{\sqrt{N_{u_1}N_{u_2}N_{u_3}}}A_{u_1i_1}A_{u_2i_2}A^*_{u_3i_3}\\ \exp\left[\mathrm{j}\omega_0 t - \mathrm{j}\left(\beta_{0,u_1i_1} + \beta_{0,u_2i_2} - \beta_{0,u_3i_3}\right)z\right]\end{array}\right] \\
&-\mathrm{j}\tfrac{1}{2}\mu_0\Delta\varepsilon\sum_{u_1i_1}\omega_0^2 A_{u_1i_1}\tfrac{F_{u_1}}{\sqrt{N_{u_1}}}\exp\left[\mathrm{j}\left(\omega_0 t - \beta_{0,u_1i_1}z\right)\right]
\end{aligned} \tag{3.16}$$

with:

$$\mathfrak{D} = \beta_{1,ui}\partial_t - \mathrm{j}\frac{\beta_{2,ui}}{2}\partial_t^2 - \frac{\beta_{3,ui}}{6}\partial_t^3$$

where the dependence of A_{ui} on (z,t), F_u on (x,y) and $\Delta\varepsilon$ on (x,y) have been omitted. In (3.16), ξ_i groups the independent polarization combinations and is given by:

$$\xi_i = \delta_{i_1i}\delta_{i_2i}\delta_{i_3i} + \frac{2}{3}\delta_{i_1i}\delta_{i_2j}\delta_{i_3j} + \frac{1}{3}\delta_{i_1j}\delta_{i_2j}\delta_{i_3i} \tag{3.17}$$

where $\delta_{i_1,i}$ is the Kronecker delta function such that $\delta_{i_1i} = 1$ when $i_1 = i$ and zero otherwise. The left-hand side (LHS) of (3.16) is responsible by the dispersion effects. The first term on the RHS of (3.16) is responsible by all the NL effects taking place between the $2 \times M$ waves. The second term on RHS of (3.16) is responsible by the

linear XT. From equation (3.16), a set of coupled equations per mode and polarization can be derived, multiplying both sides by F_u^* and integrating over the x-y transverse plane:

$$\begin{aligned}\partial_z A_{ui} + \mathfrak{D} A_{ui} + \frac{\alpha_{ui}}{2} A_{ui} = & \\ \sum_{u_1 i_1, u_2 i_2, u_3 i_3} & \left[-\mathrm{j}\xi_i \gamma_{u_1,u_2,u_3,u} A_{u_1 i_1} A_{u_2 i_2} A^*_{u_3 i_3} \exp\left(-\mathrm{j}\Delta\beta_{u_1 i_1, u_2 i_2, u_3 i_3, ui} z\right)\right] \\ - \mathrm{j} \sum_{u_1 i_1} & C_{u,u_1} A_{u_1 i_1} \exp\left(\mathrm{j}\Delta\beta_{ui,u_1 i_1} z\right)\end{aligned} \tag{3.18}$$

with:

$$\Delta\beta_{u_1 i_1, u_2 i_2, u_3 i_3, ui} = \beta_{0,u_1 i_1} + \beta_{0,u_2 i_2} - \beta_{0,u_3 i_3} - \beta_{0,ui} \tag{3.19}$$

$$\gamma_{u_1,u_2,u_3,u} = \frac{n_2 \omega_0}{c_0 A^{eff}_{u_1,u_2,u_3,u}} \tag{3.20}$$

$$A^{eff}_{u_1,u_2,u_3,u} = \frac{\sqrt{N_{u_1} N_{u_2} N_{u_3} N_u}}{\iint F_{u_1} F_{u_2} F^*_{u_3} F^*_u dxdy} \tag{3.21}$$

$$n_2 \approx \frac{3}{8} \frac{\sqrt{\varepsilon_0 \mu_0}\, \chi^{(3)}_{xxxx}}{\beta_{0,ui}} \omega_0 \tag{3.22}$$

$$C_{u,u_1} = \frac{\omega_0}{4} \iint \Delta\varepsilon(x,y) F^*_u \cdot F_{u_1}\, dxdy \tag{3.23}$$

where α_{ui} is the attenuation of ui included in a perturbation manner [7], (3.19) is the phase mismatch between waves $u_1 i_1$, $u_2 i_2$, $u_3 i_3$ and ui, (3.20) is the nonlinear coefficient between modes u_1,u_2,u_3 and u, (3.21) is the IM effective area (A^{eff}) of modes combination (u_1,u_2,u_3, u), (3.22) is the Kerr coefficient, approximately equal to $2.6 \cdot 10^{-26}\,\mathrm{m}^2/\mathrm{W}$ [7], and (3.23) is the linear XT coupling coefficient between mode u and mode u_1 (same as (3.2)). (3.23) has been obtained replacing N_u and N_{u_1} using (2.4).

The MM-CNLSE in (3.18) can be further simplified considering $A^{eff}_{u_1,u_2,u_3,u}$ properties. $A^{eff}_{u_1,u_2,u_3,u}$ is non-zero only when one or two different modes are involved, given the modes orthogonality. In case only one mode u is involved ($u_1 = u_2 = u_3 = u$), the NL effects present are: SPM, XPM and FWM (as in case of transmission over SMF). In case two distinct modes a and b are involved, the NL effects present are IM-XPM and IM-FWM, and the possible mode matching conditions for IM-NL terms falling in $u = a$ are:

$$u_1 = a, u_2 = b, u_3 = b, u = a \tag{3.24}$$

$$u_1 = b, u_2 = a, u_3 = b, u = a \tag{3.25}$$

$$u_1 = b, u_2 = b, u_3 = a, u = a \tag{3.26}$$

In [10], it has been experimentally demonstrated that, for mode matching condition (3.26), none efficient IM-NL process occur since for (3.26) the phase matching depends on effective index difference between modes a and b, and is therefore sensitive to fluctuations of the effective indexes with distance. Therefore, the nonlinear terms satisfying mode matching condition (3.26) are excluded from MM-CNLSE (3.18). Finally, using $A^{eff}_{u_1,u_2,u_3,u}$ properties in (3.18), the MM-CNLSE are given by:

$$\begin{aligned} \partial_z A_{ui} + \mathfrak{D} A_{ui} + \frac{\alpha_{ui}}{2} A_{ui} = & -\mathrm{j}\left(C_{INTRA\text{-}NL} + C_{IM\text{-}NL}\right) \\ & -\mathrm{j}\sum_{u_1 i_1} A_{u_1 i_1} C_{u,u_1} \exp\left(\mathrm{j}\Delta\beta_{ui,u_1 i_1} z\right) \end{aligned} \tag{3.27}$$

with:

$$\begin{aligned} C_{INTRA\text{-}NL} = & \ \gamma_{u,u,u,u}|A_{ui}|^2 A_{ui} + \frac{2}{3}\gamma_{u,u,u,u}|A_{uj}|^2 A_{ui} \\ & + \sum_{i_1,i_2\neq i_3} \xi_i \gamma_{u,u,u,u} A_{ui_1} A_{ui_2} A^*_{ui_3} \exp\left(-\mathrm{j}\Delta\beta_{ui_1,ui_2,ui_3,ui} z\right) \end{aligned} \tag{3.28}$$

$$\begin{aligned} C_{IM\text{-}NL} = & \ 2\sum_{u_1\neq u} \gamma_{u,u_1,u_1,u}\left[|A_{u_1 i}|^2 + \frac{1}{3}|A_{u_1 j}|^2\right] A_{u_1 i} \\ & + \sum_{u_1\neq u, i_1, i_2\neq i_3} \psi_i \gamma_{u,u_1,u_1,u} A_{u_1 i_1} A_{u_1 i_2} A^*_{u_1 i_3} \exp\left(-\mathrm{j}\Delta\beta_{u_1 i_1,u_1 i_2,u_1 i_3,ui} z\right) \end{aligned} \tag{3.29}$$

$$\psi_i = 2\delta_{i_1 i}\delta_{i_2 i}\delta_{i_3 i} + \frac{2}{3}\delta_{i_1 i}\delta_{i_2 j}\delta_{i_3 j} + \frac{2}{3}\delta_{i_1 j}\delta_{i_2 i}\delta_{i_3 j} + \frac{2}{3}\delta_{i_1 j}\delta_{i_2 j}\delta_{i_3 i} \tag{3.30}$$

In the RHS of (3.27), the terms responsible by intra-modal nonlinearities (3.28) and inter-modal nonlinearities (3.29) are identified. Noting that, in (3.18), $A_{u_1 i_1} A_{u_2 i_2} A^*_{u_3 i_3}$ is equal to $A_{u_2 i_2} A_{u_1 i_1} A^*_{u_3 i_3}$ and $\Delta\beta_{u_1 i_1,u_2 i_2,u_3 i_3,ui}$ is equal to $\Delta\beta_{u_2 i_2,u_1 i_1,u_3 i_3,ui}$, (3.29) and (3.30) have been written in such a way that only mode combinations (u, u_1, u_1, u) appear. Moreover, along this thesis, only mode combinations (u, u_1, u_1, u) are discussed without lack of generality.

The MM-CNLSE obtained (3.27) considers three main sources of degradation: DMD, linear XT, and nonlinear effects. Equation (3.27) can be solved considering the linear XT acting independently of the other effects. In this way, the SSMF can be modified to consider not only the dispersion and the nonlinear effects but also the linear XT. The linear XT is given by the SA solution method provided in section 3.2.1.

3.3 MMUX/MDMUX Model

In order to selectively launch and detect modes in MFM-FMF systems, MMUXs and MDMUXs are required. As explained in section 2.3.1, there are two main types of MMUXs/MDMUXs: broadcast and select mode shapers and mode transformers. Broadcast and select mode shapers were used in the first experiments on modern MDM-FMF systems in order to avoid the need of higher-order MIMO equalization due to their lower linear XT. Broadcast and select mode shapers can be implemented using PMs, SLMs and LPFGs. PMs are usually preferred over SLMs and LPFGs given their lower linear XT and lower wavelength dependence [11]. In this context, the optimization design of PMs to minimize linear XT is desirable.

In this section, the design of mode selective PMs for MMUXs and MDMUXs is investigated for the 2M case (LP_{01}, LP_{11a} and LP_{11b}) considering the linear XT tolerance of coherently detected PDM-QPSK signals. The PMs requirements regarding mask resolution, mask phase noise and mask alignments are provided. Such requirements allow establishing the simulation characteristics of MMUXs/MDMUXs based on PMs.

3.3.1 Phase Masks

PMs are able to convert efficiently the LP_{01} into the LP_{11a} and into the LP_{11b} (and vice-versa) due to the field distribution similarity between them. Comparing the LP_{01} and LP_{11} field distributions presented in Fig. 2.2, one can concluded that a simple PM with a π phase difference between the mask halves might be sufficient to convert the LP_{01} into the $LP_{11a/b}$ since their intensity distribution is similar. Using such simple PM, a conversion between the LP_{01} and the $LP_{11a/b}$ has been experimentally demonstrated with a XT lower than -20 dB in [12, 13]. The PMs are usually made of a fused silica plate with a given thickness where a phase structure is etched using a photo-lithography process.

Mode Selective Launching/Detection Setup

The selective launch of a given LP mode in a FMF requires a scheme similar to the one depicted in Fig. 3.7. This scheme employs two collimator lenses and a PM. The SMF front end is located on the input focal plane of the first lens (L_1) and the FMF front end on the output focal plane of the second lens (L_2). The PM is placed in the common focal plane. The collimator lenses are chosen such that the SMF LP_{01} mode field radius is magnified to match the FMF LP_{01} mode field radius. Note that, the receiver setup and the transmitter setup are approximately reciprocal.

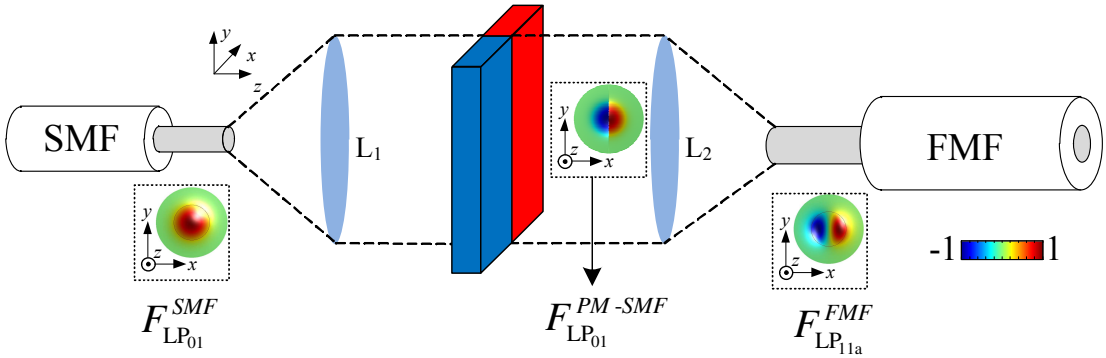

Figure 3.7: Sketch of the mode selective launching setup in the transmitter side.

The transmitter PMs are given by the phase of the electric field distribution of the target FMF mode u (F_u^{FMF}). The phase should be π for $F_u^{\mathrm{FMF}} < 0$, and zero for $F_u^{\mathrm{FMF}} \geq 0$. Therefore, a phase jump of π occurs along x-axis or y-axis depending if the target mode is the LP_{11a} or the LP_{11b} mode. Fig. 3.7 shows the different field distributions along a conversion between the SMF LP_{01} and the FMF LP_{11a} at the transmitter: the LP_{01} field distribution at SMF front end, $F_{LP_{01}}^{SMF}$, the field distribution after transmission through the PM, $F_{LP_{01}}^{PM\text{-}SMF}$, and the field distribution of the FMF LP_{11a}, $F_{\mathrm{LP}_{11a}}^{FMF}$. On the other hand, the receiver PMs are given by the symmetric of the phase of the electric field distribution of the target FMF output. Note that, there is no need for a PM to convert between the LP_{01} SMF mode and the LP_{01} FMF mode or the other way around.

In the following, since the transmitter setup and the receiver setup are approximately reciprocal, only the limitations of the transmitter setup are studied. The coupling coefficient between the filtered SMF LP_{01} mode incident on the FMF surface and the mode u guided by the FMF, denoted as $C_{TX\text{-}u}$, is given by an overlap integral of the respective field distributions over the FMF surface [6]:

$$C_{TX\text{-}u} = \frac{\iint F_u^{FMF}(x,y) F_{\mathrm{LP}_{01}}^{PM\text{-}SMF}(x,y)\ dxdy}{\sqrt{\iint \left|F_u^{FMF}(x,y)\right|^2\ dxdy}\sqrt{\iint \left|F_{\mathrm{LP}_{01}}^{PM\text{-}SMF}(x,y)\right|^2\ dxdy}} \tag{3.31}$$

where $u = \mathrm{LP}_{11a}$ or $u = \mathrm{LP}_{11b}$. Given the coupling coefficients, the linear XT is defined as the ratio between the coupling coefficients to the undesired modes and the coupling coefficient to the target mode u. In this way, the linear XT generated at the transmitter during the conversion of the SMF LP_{01} into the FMF mode u is given by:

$$XT_{TX\text{-}u} = \frac{\sum\limits_{u_1 \neq u} C_{TX\text{-}u_1}^2}{C_{TX\text{-}u}^2} \tag{3.32}$$

Phase Masks Design and Optimization

Real world PMs have a limited spatial resolution since they are built as a square grid with a limited number of pixels ($N \times N$). The mask resolution limits the linear XT introduced because there is a fabrication inaccuracy about the positioning of the pixels that can go typically from 0 to half a pixel. Additionally, linear XT is introduced by the random deviation of each pixel phase from the desired value, designated as mask noise, as well as by the misalignment between the PM and the other components in the MMUX/MDMUX setup. At the transmitter, the alignment between the center of SMF LP_{01} mode, the phase transition line of the mask, and the phase transition line of the target mode (LP_{11a} or LP_{11b}) is critical. Similar comments are applicable to the receiver alignment. Therefore, in the following the PM requirements are investigated only for the transmitter case. Moreover, only the conversion between the SMF LP_{01} and the FMF LP_{11a} is considered.

In order to find the mask requirements and tolerances, the linear XT threshold for 112 Gb/s coherently detected PDM-QPSK signals is considered. The linear XT threshold is calculated using the DSP algorithms described in [14] with twofold oversampling and FDE equalization to compensate for the bulk of accumulated chromatic dispersion. Fig. 3.8 shows the required optical signal-to-noise ratio (ROSNR) for a BER of 10^{-3} as a function of the linear XT introduced by the hybrid coupler of the coherent receiver. Assuming a maximum ROSNR penalty of 0.5 dB, the linear XT threshold is -17 dB according to Fig. 3.8 (the same threshold has been found in [15]).

The mask resolution requirement is investigated first considering an offset of half

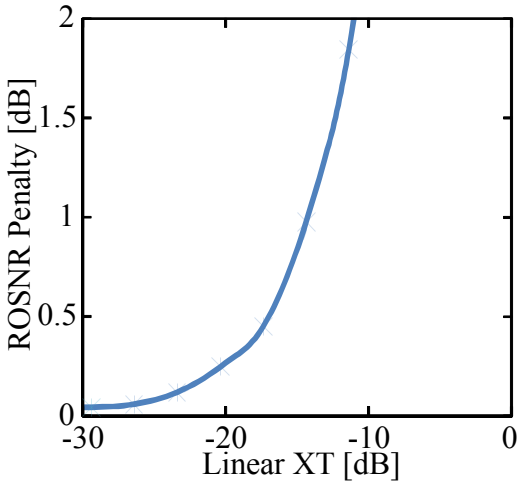

Figure 3.8: ROSNR for a BER of 10^{-3} as a function of the XT introduced by the hybrid coupler of a coherent receiver.

a pixel introduced during fabrication of the phase mask. When the positioning of the PM is not optimized with an active feedback mechanism (or manual tuning in a lab setup), this half a pixel offset leads to the coupling of a larger fraction of the transmitted power to the FMF LP_{01} instead of to the target mode LP_{11a}, degrading the conversion. Fig. 3.9(a) shows $XT_{TX\text{-}LP_{11a}}$ as a function of the mask resolution ($N \times N$) from $N = 16$ to 1024. From Fig. 3.9(a) can be seen that for $N \geq 128$ the linear XT is below the the -17 dB threshold. However, for an offset slightly higher than 0.5 pixels, $N = 128$ might not be enough. Fig. 3.9(b) shows $XT_{TX\text{-}LP_{11a}}$ as a function of the pixel offset, for several PM resolutions. The figure shows that for $N = 256$ an offset as high as 0.8 pixel can be tolerated. Moreover, for a 0.5 pixel offset the linear XT is approximately -19 dB. Regarding the mask noise, assuming that the random deviation of the pixel phase is described by a Normal distribution, the maximum standard deviation tolerable can be calculated. Fig. 3.10(a) shows $XT_{TX\text{-}LP_{11a}}$ as a function of the standard deviation for $N = 256$. From the results, it can be concluded that the mask noise is not a limiting parameter, since for a standard deviation as high as 0.5 rad, $XT_{TXLP_{11a}}$ is lower than -17 dB and $C_{TX\text{-}LP_{11a}}$ is close to its maximum value. Note that, for a standard deviation higher than 0.5 rad, $XT_{TX\text{-}LP_{11a}}$ remains lower than -17 dB but $C_{TX\text{-}LP_{11a}}$ starts to decrease. Finally, the mask misalignment is investigated considering that only the PM is displaced. Fig. 3.10(b) shows $XT_{TX\text{-}LP_{11a}}$ as a function of the misalignment between phase transition line of the PM and the phase transition line of the FMF LP_{11a} for $N = 256$ (the misalignment considered is perpendicular to the phase transition lines). The results show that the alignment tolerance is approximately 0.8 pixel for a linear XT threshold of -17 dB. Therefore,

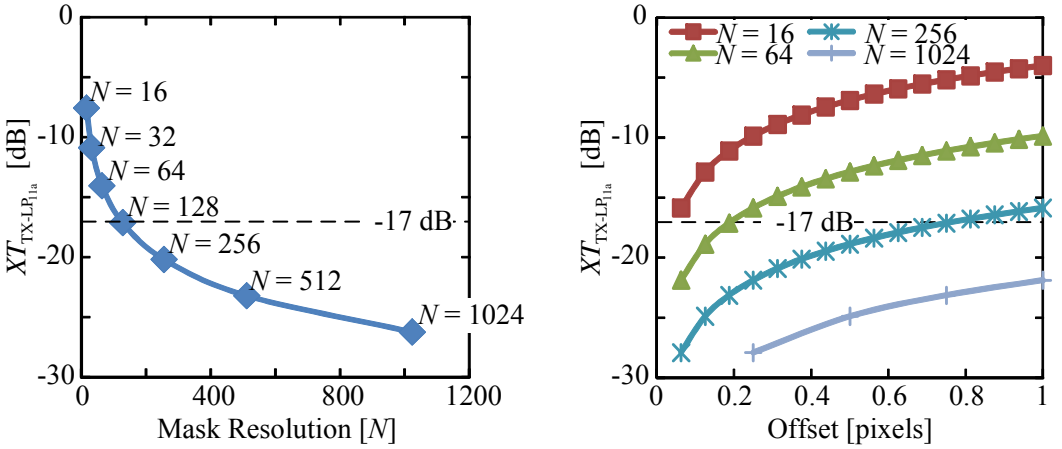

(a) (b)

Figure 3.9: (a) $XT_{TX\text{-}\mathrm{LP}_{11a}}$ as a function of the PM pixel resolution. (b) $XT_{TX\text{-}\mathrm{LP}_{11a}}$ as a function of the pixel grid offset.

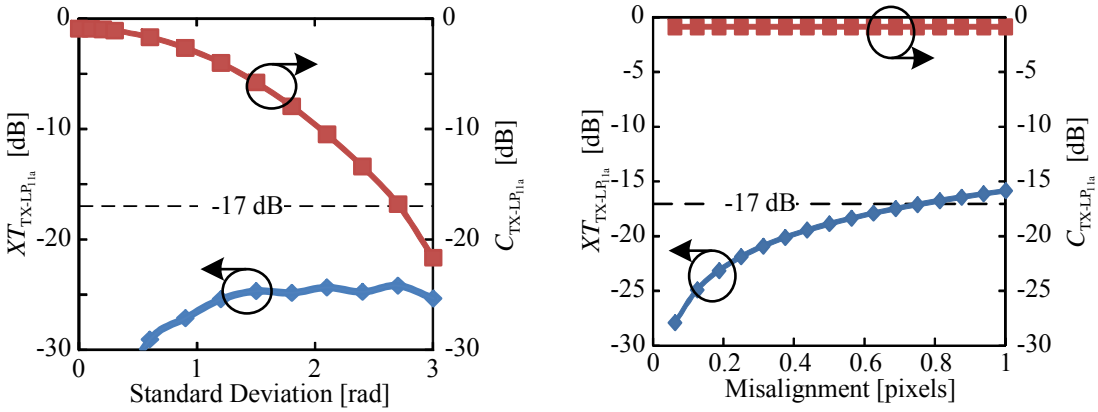

(a) (b)

Figure 3.10: $XT_{TX\text{-}\mathrm{LP}_{11a}}$ and $C_{TX\text{-}\mathrm{LP}_{11a}}$ as a function of the: (a) standard deviation and (b) PM misalignment, for $N = 256$.

this is also a critical parameter as the pixel position inaccuracy.

In conclusion, a mask resolution of 256 × 256 is sufficient for selective launch in TMFs, assuming PDM-QPSK and a mask alignment tolerance below 0.8 pixel. Furthermore, for a typical misalignment of 0.5 pixel, the linear XT is approximately -19 dB. Therefore, the linear XT introduced by a MMUX/MDMUX based on PMs is approximately equal or lower than the dXT accumulated over a fiber length of 80 km (-20 dB to -10 dB).

3.4 General Transmission Simulation Setup

In this section, the models developed along this chapter are integrated in the general simulation setup for MDM-WDM-FMF systems used along this thesis, shown in Fig. 3.11. At the transmitter, at each wavelength, $2 \times M$ signals are modulated with data streams and mapped into two polarizations (using a polarization multiplexer) and M orthogonal spatial guided modes by the FMF (using a MMUX). N signals at different wavelengths are combined by a WDM multiplexer (WDM-MUX), as in a conventional SMF system. As signals propagate through S spans of fiber with length L, total span loss is compensated by a MMA. At the receiving end, different wavelengths are separated by a WDM demultiplexer (WDM-DMUX). The signal at each wavelength is separated into M spatial modes and two polarizations using a MDMUX and a polarization demultiplexer, respectively. The signal in each mode is mixed with a local oscillator (LO), downconverting it to baseband. After sampling, DSP-MIMO compensates for the transmission impairments (such as: chromatic dispersion, DMD and linear XT), separating the $2 \times M$ multiplexed data signals.

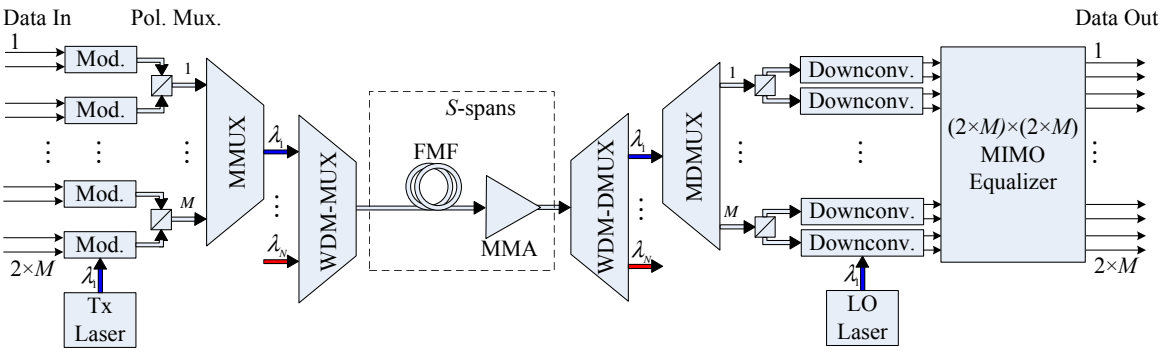

Figure 3.11: Long-haul MDM-WDM-FMF system setup.

Along this thesis, the MMUXs/MDMUXs considered are based on the PMs presented in section 3.3 or ideal spot couplers. The MMA structure used is composed by M parallel SM-EDFAs as presented Fig. 2.11 such that MDG can be easily modeled varying the gain of each SM-EDFA. The simulations consider PDM-QPSK transmitters and coherent detection receivers. At the transmitter, each tributary is modulated with QSPK and a net symbol rate of 25 Gbaud, resulting in a total net bit rate of $M \times 100$ Gbit/s. The gross bit rate is obtained considering overheads of 24 % and 10 % to account for forward-error correction (FEC) and TS, respectively. Two different MIMO-DSP algorithms are considered along this thesis: one with 2×2 MIMO

processing (thus, without linear XT compensation) and one with $(2 \times M) \times (2 \times M)$ MIMO processing. In both cases the channel estimation is based on the MMSE criterion. The transmission simulations with 2×2 MIMO processing consider the blind coherent digital receiver presented in [14]. The bulk of accumulated chromatic dispersion is compensated using FDE equalization. The polarization rotation and PMD are equalized in a butterfly 13 taps FIR filter estimated using the constant modulus algorithm (CMA). The transmission simulations with $(2 \times M) \times (2 \times M)$ MIMO processing consider the data-aided coherent digital receiver presented in [16]. Constant amplitude zero autocorrelation (CAZAC) sequences are used as training sequences, due to their impulse-like autocorrelation properties [17]. To preserve orthogonality between the $(2 \times M)$ training sequences, each one of them is cyclically shifted [18]. For this reason, the training sequences length have to be at least $(2 \times M)$ times the maximum CIR length. The synchronization at the receiver is performed with the Schmidl and Cox method proposed in [19].

3.4.1 TMF Transmission Simulation

In this section, simulation results for single-mode transmission (SMT) and MDM transmission over a TMF are presented considering 2×2 MIMO processing and ideal MMUXs/MDMUXs based on PMs. The results presented below provide a qualitative validation of the weak coupling strength and of the small nonlinear effects in SI-FMFs.

The fiber considered has a SI profile defined by: $\Delta n_{co} = 2.5 \cdot 10^{-3}$ and $w_1 = 9$ µm. The fiber guides two non-degenerate modes, LP_{01} and LP_{11}, with an effective index difference of $\Delta n_{eff} \approx 1.32 \cdot 10^{-3}$ and $DMD \approx 4\,\mathrm{ps/m}$. For this fiber, the average linear XT at the end of 75 km for $\rho_{d,max} = 0.01 \cdot w_1$ and a 50 m step size is approximately -20 dB, obtained using (3.3) and (3.4). Table 3.2 gathers some of the TMF properties at 1550 nm, together with those of the SMF used as reference for performance comparison. The BER after transmission is measured using Monte Carlo simulation, considering SM-EDFAs with a spontaneous emission factor of 2 and a gain adjusted to compensate for the total span losses. The minimum power required (P_{REQ}) and the nonlinear threshold power ($P_{NL\text{-}TR}$ - maximum power allowed) for a $BER = 3.8 \cdot 10^{-3}$ (FEC limit) are compared between the following configurations: SMT over the TMF, SMT over the SMF and MDM over the TMF.

The simulation results for SMT over the TMF and over the SMF are analyzed first. In the SMT over the TMF simulations, after each span, the power coupled

Table 3.2: Fiber properties at 1550 nm.

Property	Unit	TMF LP_{01}	TMF LP_{11}	SMF LP_{01}
Dispersion	ps/(nm·m)	22.64	20.86	15.35
Dispersion slope	ps/(nm^2·m)	0.063	0.053	0.057
A_{eff}	μm^2	206.7	322.9	91.4
γ - intra-modal	W^{-1}/km	0.510	0.326	1.153
γ - inter-modal	W^{-1}/km	0.314	0.314	-
PMD	ps/$\sqrt{km}$	0.069	0.687	0.069
Attenuation	dB/km	0.22	0.22	0.22

to the undesired mode is filtered. Fig. 3.12 shows $\log_{10}(BER)$ after 6000 km as a function of the average launch power per mode. In the linear region, Fig. 3.12 shows that the P_{REQ} for SMT over the TMF is 1 dB higher than for SMT over the SMF, using either the TMF LP_{01} or the TMF LP_{11}. Further results without linear XT have shown that this low penalty is due to the linear XT present in the TMF, thereby, agreeing with the weak coupling strength in SI-FMFs, as experimentally observed in [20]. In the nonlinear region, taking as reference the $P_{NL\text{-}TR}$ for SMT over the SMF, the $P_{NL\text{-}TR}$ for SMT over the TMF LP_{01} and for SMT over the TMF LP_{11} are approximately 4.5 dB and 6.5 dB higher, respectively. These $P_{NL\text{-}TR}$ improvements are related with the higher effective area of the TMF modes, compared to the SMF, as shown in Table 3.2. These results demonstrate that by transmitting over only one of the two modes on TMF, a longer transmission distance can be realized compared to transmission on SMF without increase of receiver complexity (except for the necessary mode converters). These enhancements are in line with the experimental results presented in [20] for transmission over the LP_{01} of a similar TMF.

Fig. 3.13 shows $\log_{10}(BER)$ after 300 km as a function of the average launch power per mode, for MDM transmission over the TMF. From Fig. 3.13 can be seen the maximum transmission reach is severely reduced compared to the SMT case. The transmission reach decrease is due to the linear XT introduced that is not compensated by the 2×2 MIMO processing considered. Note that, the linear XT at the end of 300 km is -15.23 dB, close to the maximum tolerable XT level for 0.5 dB of ROSNR penalty as found in section 3.3. Ultra-long haul transmission for MDM operation can be achieved considering higher-order MIMO processing as shown in chapter 5.

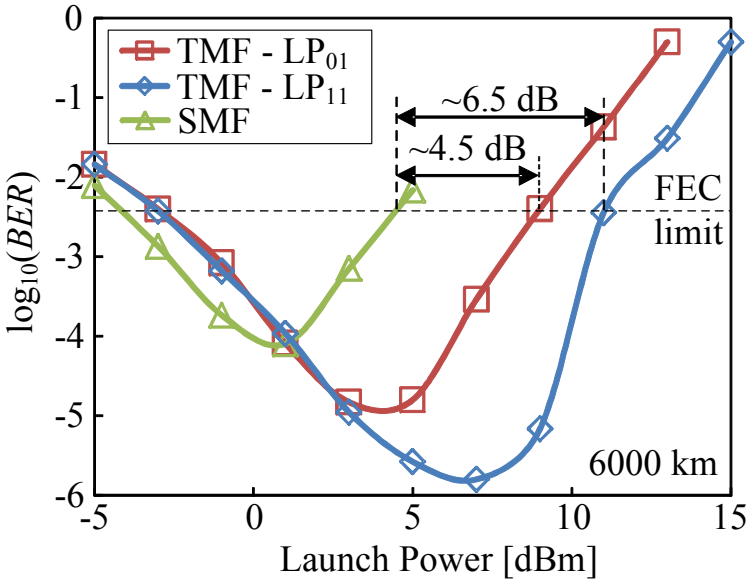

Figure 3.12: $\log_{10}$(BER) for SMT over the TMF and over the SMF as a function of the mode launch power, after 6000 km

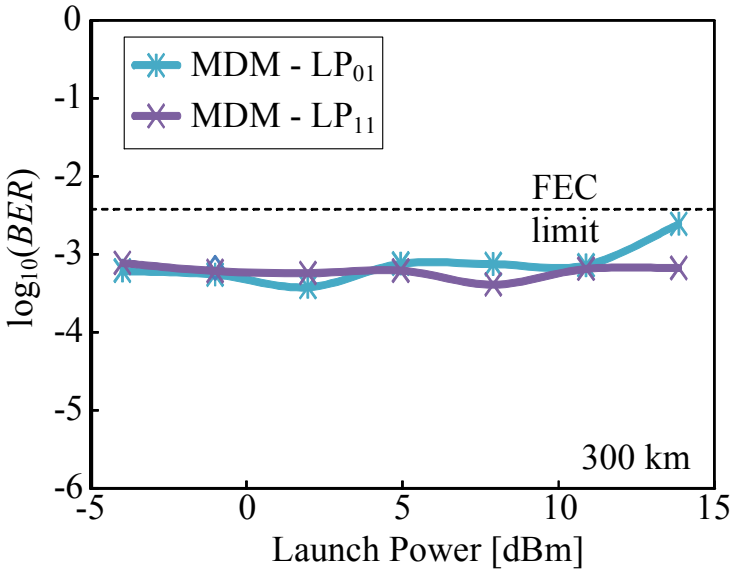

Figure 3.13: $\log_{10}(BER)$ for MDM transmission over the TMF as a function of the mode launch power, after 300 km.

3.5 Conclusions

In this chapter, the general models required for the study and design of long-haul MDM-FMF systems along this thesis have been derived taking into account the main impairments of FMFs, MMUXs/MDMUXs and MMAs.

In section 3.2, a NSAM for propagation over FMFs has been developed which can be solved using a modified SSFM method for multimode propagation. The NSAM is composed by the SA solution method for the coupled linear differential equations describing the linear XT proposed in section 3.2.1 and by the set of MM-CNLSE derived in section 3.2.2. The MM-CNLSE obtained considers the main sources of signal degradation: chromatic dispersion, DMD, linear XT, and nonlinear effects. Considering that the linear XT acts independently of the other effects, the SSFM method can be modified for multimode propagation and the linear XT is introduced using the SA solutions derived.

Section 3.3 presented the optimization design of MMUXs/MDMUXs based on PMs assessing the mask resolution, phase noise and alignment requirements considering the linear XT threshold for coherently detected PDM-QPSK signals. A mask resolution of 256×256 is required for selective launching/detecting $\mathrm{LP}_{11\mathrm{a/b}}$ considering a mask alignment tolerance below 0.8 pixel. Moreover, it has been shown that the linear XT introduced by a MMUX/MDMUX based on PMs is approximately equal or lower than the dXT accumulated over a fiber length of 80 km.

In section 3.4, the general simulation setup for long-haul MDM-WDM-FMF systems used along this thesis has been presented, integrating the simulation models developed along the chapter. In section 3.4.1, a set of SMT and MDM transmission simulations over a SI-TMF has been presented. The SMT simulations provided a qualitative validation of the weak coupling strength and of the low nonlinear effects in SI-FMFs. Moreover, the MDM simulations showed that, for long-haul transmission, higher-order MIMO processing is required to recover the transmitted signals.

References

[1] R. Essiambre and R. Tkach, "Capacity Trends and Limits of Optical Communication Networks," *Proceedings of the IEEE*, vol. 100, no. 5, pp. 1035–1055, May 2012.

[2] B. Inan, B. Spinnler, F. Ferreira, A. Lobato, S. Adhikari, V. Sleiffer, D. van den Borne, N. Hanik, and S. Jansen, "Equalizer complexity of mode division multiplexed coherent receivers," in *Proc. Optical Fiber Communication Conference and Exposition*, March 2012, p. OW3D.4.

[3] F. Ferreira, P. Monteiro, and H. Silva, "Semi-analytical model for linear modal coupling in few-mode fiber transmission," in *Proc. International Conference on Transparent Optical Networks*, July 2012, p. Th.A1.5.

[4] F. Ferreira, S. Jansen, P. Monteiro, and H. Silva, "Nonlinear Semi-Analytical Model for Simulation of Few-Mode Fiber Transmission," *IEEE Photonics Technology Letters*, vol. 24, no. 4, pp. 240–242, February 2012.

[5] F. Ferreira, D. van den Borne, H. Silva, and P. Monteiro, "Crosstalk optimization of phase masks for mode multiplexing in few mode fibers," in *Proc. Optical Fiber Communication Conference and Exposition*, March 2012, p. JW2A.37.

[6] D. Marcuse, *Theory of Dielectric Optical Waveguides*. Academic Press, Inc., 1974, chapters 3 and 5.

[7] G. Agrawal, *Nonlinear Fiber Optics*, 3rd ed. Academic Press, 2001.

[8] J. Noda, K. Okamoto, and Y. Sasaki, "Polarization-maintaining fibers and their applications," *IEEE/OSA Journal of Lightwave Technology*, vol. 4, no. 8, pp. 1071–1089, August 1986.

[9] J. Mathews and K. Fink, *Numerical methods using MATLAB*, 3rd ed. Prentice Hall, 1999, chapter 9.

[10] R. Essiambre, M. Mestre, R. Ryf, A. Gnauck, R. Tkach, A. Chraplyvy, Y. Sun, X. Jiang, and R. Lingle, "Experimental Observation of Inter-Modal Cross-Phase Modulation in Few-Mode Fibers," *IEEE Photonics Technology Letters*, vol. 25, no. 6, pp. 535–538, March 2013.

[11] D. Sperti, M. Salsi, C. Koebele, P. Tran, H. Mardoyan, S. Bigo, A. Boutin, P. Sillard, and G. Charlet, "Experimental Investigation of Modal Crosstalk using LCOS-based Spatial Light Modulator for Mode Conversion," in *Proc. European Conference and Exhibition on Optical Communication*, September 2011, p. Th.12.B.2.

[12] R. Ryf, S. Randel, A. Gnauck, C. Bolle, R. Essiambre, P. Winzer, D. Peckham, A. McCurdy, and R. Lingle, "Space-division multiplexing over 10 km of three-mode fiber using coherent 6×6 MIMO processing," in *Proc. Optical Fiber Communication Conference and Exposition*, March 2011, p. PDPB10.

[13] M. Salsi, C. Koebele, D. Sperti, P. Tran, P. Brindel, H. Mardoyan, S. Bigo, A. Boutin, F. Verluise, P. Sillard, M. Bigot-Astruc, L. Provost, F. Cerou, and G. Charlet, "Transmission at 2×100 Gb/s, over Two Modes of 40 km-long Prototype Few-Mode Fiber, using LCOS based Mode Multiplexer and Demultiplexer,"

in *Proc. Optical Fiber Communication Conference and Exposition*, March 2011, p. PDPB9.

[14] M. Kuschnerov, F. Hauske, K. Piyawanno, B. Spinnler, M. Alfiad, A. Napoli, and B. Lankl, "DSP for Coherent Single-Carrier Receivers," *IEEE/OSA Journal of Lightwave Technology*, vol. 27, no. 16, pp. 3614–3622, August 2009.

[15] P. Winzer, A. Gnauck, A. Konczykowska, F. Jorge, and J.-Y. Dupuy, "Penalties from In-Band Crosstalk for Advanced Optical Modulation Formats," in *Proc. European Conference and Exhibition on Optical Communication*, September 2011, p. Tu.5.B.7.

[16] A. Lobato, F. Ferreira, M. Kuschnerov, D. van den Borne, S. Jansen, A. Napoli, B. Spinnler, and B. Lankl, "Impact of mode coupling on the mode-dependent loss tolerance in few-mode fiber transmission," *Optics Express*, vol. 20, no. 28, pp. 29 776–29 783, December 2012.

[17] D. Chu, "Polyphase codes with good periodic correlation properties," *IEEE Transactions on Information Theory*, vol. 18, no. 4, pp. 531–532, July 1972.

[18] T. Schenk, *RF Imperfections in High-Rate Wireless Systems*. Springer, 2008.

[19] T. Schmidl and D. Cox, "Robust frequency and timing synchronization for OFDM," *IEEE Transactions on Communications*, vol. 45, no. 12, pp. 1613–1621, December 1997.

[20] F. Yaman, N. Bai, B. Zhu, T. Wang, and G. Li, "Long distance transmission in few-mode fibers." *Optics Express*, vol. 18, no. 12, pp. 13 250–13 257, June 2010.

Chapter 4

Design of Few-Mode Fibers

4.1 Introduction

The ever growing demand for higher data rate is rapidly exhausting the capacity available for SMFs. During the last years, only a marginal increase in the maximum bit rate distance product using SMFs was observed [1], since the nonlinear Shannon limit is being reached [2]. Moreover, it has been demonstrated that even if significant reduction of the fiber attenuation or of the fiber nonlinear coefficient of SSMFs are achieved, the capacity increase per fiber is limited [3]. MDM over FMFs is emerging as an attractive solution for the required capacity increase with potential cost, space, and energy savings [3, 4]. However, FMFs require the usage of MIMO equalization to compensate for the combined effect of DMD and linear modal XT, which originates a CIR spread over time [5]. Therefore, the additional processing complexity partially erodes the benefit of deploying FMFs. It has been shown in [6] that, considering similar levels of complexity for nonlinearity mitigation in a SSMF, only FMF systems with 4 or more independent LP modes offer an actual capacity increase. One of the approaches proposed to reduce the equalizer complexity is the minimization of XT along the transmission system so that each mode can be detected individually without MIMO processing. However, experimental interfaces/couplers with such property present high loss [7] (see section 2.3). Therefore, in this chapter another approach is followed, the reduction of DMD, and investigation of techniques to design FMFs with low DMD over the C-band guiding x non-degenerate LP modes (xM) from 2M to 12M.

In the literature, reviewed in section 2.2.3, two different schemes have been proposed to limit the accumulation of DMD in FMFs: the usage of ILD-FMFs [8–11],

and the usage of DC-FMFs (FMFs with positive DMD followed by FMFs with negative DMD) [12–17]. The main target in this chapter is a DMD lower than 12 ps/km over the C-band, since this is the DMD required for 2000 km of MDM transmission at 100 Gb/s using an overhead of up to 10 % [5]. Note that the DMD should be lower than 12 ps/km over the C-band, in order to allow the transmission of WDM signals. In Table 2.2, the ILD-FMFs and DC-FMFs with the lowest DMD have been designed using a GCCT profile. Therefore, in this chapter the design of ILD-FMFs and DC-FMFs with a DMD lower than 12 ps/km over the C-band is presented considering a GCCT profile. Moreover, a MSI profile is also considered in order to evaluate alternative profiles.

The chapter is structured as follows. In section 4.2 focus on the design of 2M-FMFs suitable for the conceptual demonstration of the first MDM-FMF systems. In section 4.3 focus on the design of FMFs with up to 12M assessing the scalability potential of MDM-FMF systems. The main conclusions are gathered in section 4.4.

The work presented along this chapter is based on the work reported in [18–20].

4.2 Design of 2M-FMFs With Arbitrary DMD

In this section, the design of 2M-FMFs with an arbitrary DMD over the C-band is presented considering a GCCT profile. The impact on the DMD (average and slope) of the core grading exponent and of the dimensioning of the trench is described in section 4.2.1, as well as the parameters search domains and the optimizing function. Section 4.2.2 presents the optimization results for three target DMD values: 0 ps/km suitable for ILD-FMFs, 100 ps/km and -100 ps/km suitable for DC-FMFs. The results show that it is possible to reduce the DMD difference to the target DMD to less than 0.01 ps/km, and that the dimensioning of the trench is almost independent of the target DMD. Therefore, a simple design rule has been derived, which guarantees a maximum DMD deviation over the C-band lower than 1.8 ps/km for a DMD target between -200 ps/km to 200 ps/km. Additionally, tolerance of the designed 2M-FMFs to manufacturing margins was evaluated and found to be insufficient.

4.2.1 Fiber Profile Description, Analysis and Optimization

The GCCT profile is presented in Fig. 4.1 and analytically described by:

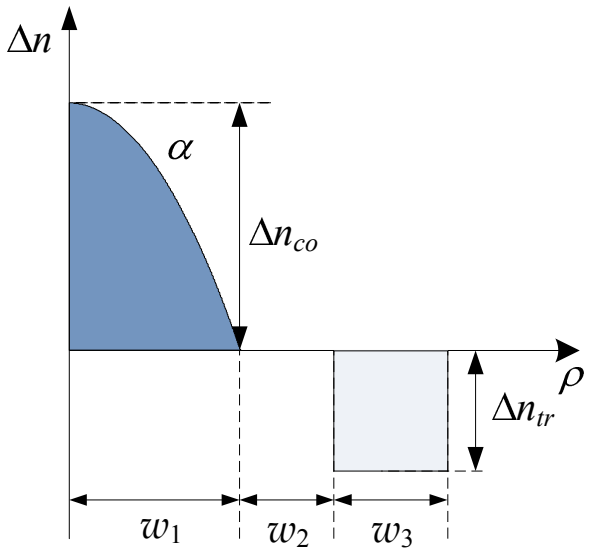

Figure 4.1: GCCT profile.

$$n(\rho) = \begin{cases} n(0)\left[1 - \Delta n_{co}(\rho/w_1)^{\alpha}\right], & |\rho| < w_1 \\ n_{cl}, & w_1 \le |\rho| < w_1 + w_2 \\ n_{cl}/(1 - \Delta n_{tr}), & w_1 + w_2 \le |\rho| < w_1 + w_2 + w_3 \\ n_{cl}, & |\rho| \ge w_1 + w_2 + w_3 \end{cases} \tag{4.1}$$

where $n(\rho)$ is the refractive index as function of the radial distance (ρ) and n_{cl} is the cladding refractive index (approximately 1.444 at 1550 nm). w_1 is the core radius, w_2 is the radial distance between the end of the core and the beginning of the trench, and w_3 is the trench width. Δn_{co} is the relative refractive index difference (Δn) at $\rho = 0$ and Δn_{tr} is Δn at the trench, with $\Delta n(\rho)$ given by: $\Delta n(\rho) = [n(\rho) - n_{cl}]/n(\rho)$. During the optimization for each different combination of these parameters, the guided modes supported by the fiber and their characteristics, as well as the effective group index ($\overline{n}_g$) were calculated by solving the Maxwell equations numerically [21] using the Runge-Kutta method. The dispersion properties of the doped silica have been modeled by using the Sellmeier coefficients provided in [22].

There are two parameters in (4.1) that can be defined without optimization: w_1 and Δn_{co}. w_1 should be as large as possible in order to reduce the nonlinear coefficients for all modes. Therefore, the highest core radius reported to date for a FMF, $w_1 = 9\,\mu$m, was considered [23]. In order to determine Δn_{co}, the highest value of the normalized frequency V (2.6) that guarantees the support of only two LP modes for $\alpha = 2$ and $\Delta n_{tr} = 0$ is used, $V = 5.1$. Consequently, Δn_{co} was found to be $4.5 \cdot 10^{-3}$, for the lowest λ of the C-band.

In order to understand the impact of the core grading exponent and of the trench dimensioning on the DMD, one has to consider that the DMD is proportional to the difference between the values of $\overline{n}_g$ for the supported modes LP_{01} ($\overline{n}_g^{LP_{01}}$) and LP_{11} ($\overline{n}_g^{LP_{11}}$):

$$DMD\left(\lambda\right) = \frac{1}{c_0}\left[\overline{n}_g^{LP_{11}}\left(\lambda\right) - \overline{n}_g^{LP_{01}}\left(\lambda\right)\right] \tag{4.2}$$

where c_0 is the light velocity in free space. The $\overline{n}_g$ of a mode depends on the fraction of the mode power that propagates in each region of the fiber cross section. Thus, a tightly confined mode has a $\overline{n}_g$ that is dominated by the group index of the core (as the LP_{01}). On the other hand, a weakly confined mode will propagate with a smaller $\overline{n}_g$, closer to the group index of the cladding (as the LP_{11}, since the confinement decreases with the mode order).

Based on the explanation presented in the last paragraph, the impact of α on $\overline{n}_g$ is explained first in order to understand its impact on the DMD. Fig. 4.2(a) presents $\overline{n}_g$ for the LP_{01} and LP_{11} modes as a function of the wavelength and α, in the absence of trench. In Fig. 4.2(a) it can be seen that the difference between the $\overline{n}_g^{LP_{11}}$ and $\overline{n}_g^{LP_{01}}$ curves, which is proportional to the DMD, decreases with increasing α, and that the decrease seems to vary only slightly in the C-band, since the $\overline{n}_g^{LP_{01}}$ and $\overline{n}_g^{LP_{11}}$ curves for different values of α are almost parallel. To understand this effect, the inset in Fig. 4.2(a) presents the normalized amplitude of the field for the LP_{01} and LP_{11} modes as a function of ρ/w_1 and α. It shows that with increasing α the power confinement of the LP_{01} mode in the core decreases slightly, compared to the increase of the power confinement of the LP_{11} mode. This, combined with the increase of the group index in the core itself, is sufficient for the increase of $\overline{n}_g$ for both modes. This increase is higher for $\overline{n}_g^{LP_{11}}$, due to the slight decrease of the power confinement for the LP_{01} mode, and thus the DMD decreases. In order to assess the impact of the trench on $\overline{n}_g$, and thus on the DMD, Fig. 4.2(b) presents $\overline{n}_g$ as a function of the wavelength and Δn_{tr}. As can be seen in Fig. 4.2(b), the trench affects mainly the LP_{11} mode and allows controlling the DMD slope. This can be understood by looking into the field distribution. The inset in Fig. 4.2(b) presents the normalized amplitude of the field for the LP_{01} and LP_{11} modes as a function of ρ/w_1 and Δn_{tr}. It shows that the power confinement of the LP_{11} mode in the core increases with decreasing Δn_{tr} (creating a deeper trench), and that the field distribution of the LP_{01} mode is only slightly affected, so the DMD decreases. Furthermore, the increase with wavelength of the mode field radius for the LP_{11} mode is counteracted by the power confinement

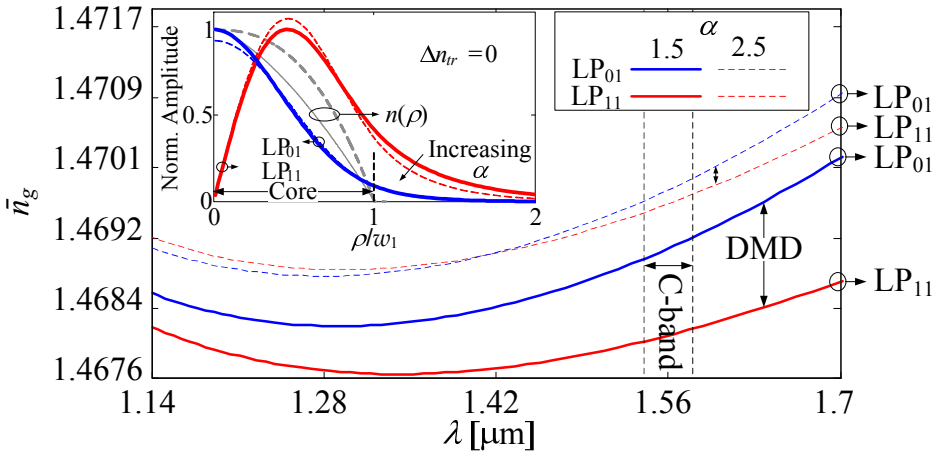

(a)

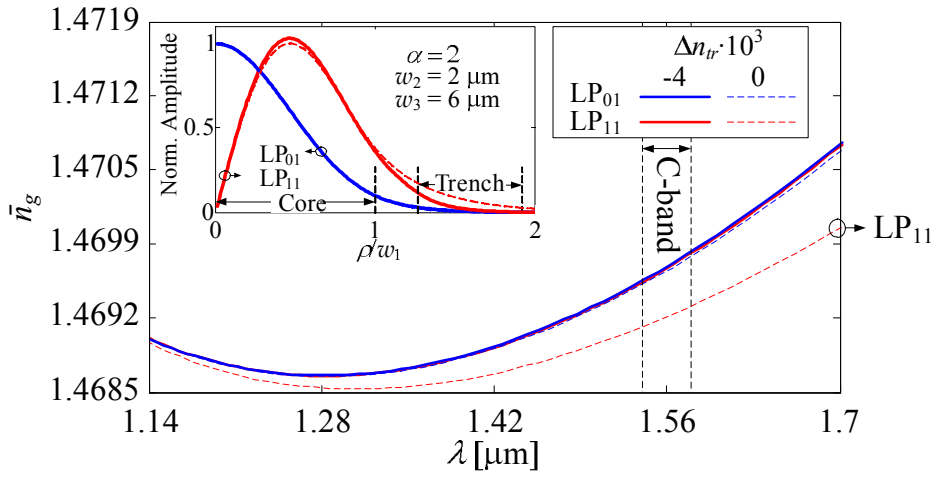

(b)

Figure 4.2: $\overline{n}_g$ of the LP_{01} and of the LP_{11} as a function of λ: (a) varying α; (b) varying Δn_{tr}. Inset (a) and (b): Normalized amplitude of the field for the LP_{01} and LP_{11} modes as a function of ρ/w_1, considering $\lambda = 1550\,\text{nm}$.

effect of the trench. Thus, the trench has the effect of flattening the DMD over a certain wavelength band, with an adequate trench dimensioning.

In order to search for the optimum α and dimensioning of the trench (Δn_{tr}, w_2, w_3), an optimization function was introduced with the objective of minimizing the magnitude of the DMD error relative to the DMD target (ψ) over a defined λ range:

$$OF\left(\alpha, \Delta n_{tr}, w_2, w_3\right) = \frac{\int_{\lambda^-}^{\lambda^+} \left|DMD\left(\lambda, \alpha, \Delta n_{tr}, w_2, w_3\right) - \psi\right| d\lambda}{\lambda^+ - \lambda^-} \tag{4.3}$$

The minimization of the integral of the modulus of the DMD deviation from ψ forces its reduction over the whole wavelength range. This objective function is subject to the following constraints:

$$\left(\alpha^- = 1.5\right) \leq \alpha \leq \left(\alpha^+ = 2.5\right) \tag{4.4}$$

$$\left({\Delta n_{tr}}^- = -0.0045\right) \leq \Delta n_{tr} \leq \left({\Delta n_{tr}}^+ = 0\right) \tag{4.5}$$

$$\left({w_2}^- = 0\right) \leq w_2 \leq \left({w_2}^+ = w_1/2\right) \tag{4.6}$$

$$\left({w_3}^- = 0\right) \leq w_3 \leq \left({w_3}^+ = w_1\right) \tag{4.7}$$

$$\left(\lambda^- = 1530\,\mathrm{nm}\right) \leq \lambda \leq \left(\lambda^+ = 1565\,\mathrm{nm}\right) \tag{4.8}$$

The search domain for α, defined by (4.4), was selected since it is well known that $\alpha \approx 2$ minimizes the DMD for conventional MMFs [24]. (4.5) constrains Δn_{tr} to values higher than -0.0045, since a deeper trench would be difficult and expensive to fabricate [25]. In (4.6), w_2 is limited to $w_1/2$ as a trench farther away from the core has reduced or none effect on the core modes. (4.7) constrains w_3 to values smaller than w_1, since a wider trench would make the fabrication more expensive. The wavelength domain (4.8) is bounded to the C-band.

Finally, in order to find the full optimum $(\alpha, \Delta n_{tr}, w_2, w_3)$ set, an exhaustive search (ES) is performed over OF. The ES optimizes the α, Δn_{tr}, w_2 and w_3 with tolerances of 0.001, $5 \cdot 10^{-4}$, 0.125 µm and 0.250 µm, respectively. Further reducing these tolerances by a factor of 2 changed OF negligibly.

4.2.2 Results and Discussion

Fiber Profile Optimization

In this sub-section three different ψ values are considered: 0 ps/km, 100 ps/km and -100 ps/km. In order to find the (w_2, w_3) pairs that allow the reduction of the DMD slope to negligible levels, Fig. 4.3 shows the contour map of the minimum OF [ps/km] as a function of w_2 and w_3 for $\psi = 0$ ps/km. For each pair (w_2, w_3), the optimum pair $(\alpha, \Delta n_{tr})$ that minimizes OF is used. A subset of the domain of w_2 and w_3, defined by (4.6) and (4.7), is shown in order to improve the visualization of the OF variation around the optimum values. The shaded area covers values where OF is obtained for optimum $\Delta n_{tr} < -4.5 \cdot 10^{-3}$ and, therefore, out of the domain defined in section 4.2.1. Fig. 4.3 shows OF below 0.1 ps/km for a clearly delimited area, with w_2 ranging from ~1.7 µm to ~2 µm and w_3 from ~4.5 µm to ~9 µm. Additionally to OF, the maximum DMD deviation (MDD) relatively to the targeted DMD over the C-band, $MDD(\alpha, \Delta n_{tr}, w_2, w_3) = \max_\lambda |DMD(\lambda, \alpha, \Delta n_{tr}, w_2, w_3) - \psi|$, was calculated, since OF is an indirect measure of the DMD. Note that MDD has been chosen over DMD slope, as used in [12], because the accuracy of MDD does not depend on the linearity of the DMD. In the case of the OF minimum presented in Fig. 4.3 for $\psi = 0$ ps/km, the MDD is 0.01 ps/km, revealing an almost flattened DMD dependence on the λ.

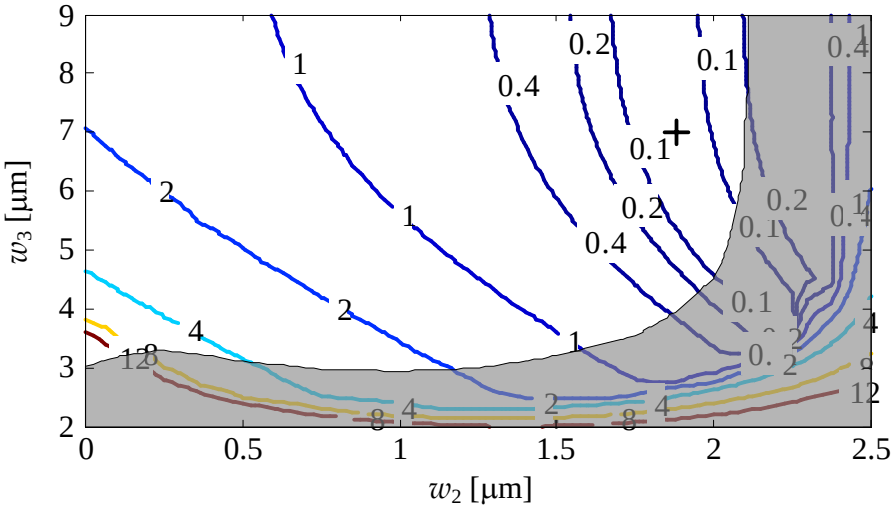

Figure 4.3: Contour map of OF [ps/km] as a function of w_2 and w_3, for $\psi = 0$ ps/km. "+" marks the OF minimum, which is 0.004 ps/km.

Table 4.1 shows the OF minimum, the MDD and the corresponding optimum profile parameters for the three ψ values. The minimum OF is below 0.004 ps/km and the MDD is below 0.01 ps/km, for any of the ψ values. The propagation characteristics of the designed fibers were also evaluated: the curvature radius (R_c) for a macrobending loss (MBL) of 0.5 dB, calculated according to [26], the chromatic dispersion (D), the chromatic dispersion slope (S) and the nonlinear coefficient (γ). The R_c values determined for the LP_{11} mode (the mode with higher MBL) are around 4.5 mm, and thus below the value of 7.5 mm specified by [27] for all cases. The D values are around 22 ps/km/nm, only slightly higher than the dispersion of ∼17 ps/(nm·km) characteristic of standard SSMFs. The S values are around 0.06 ps/(nm^2·km), lower than ∼0.08 ps/(nm^2·km) typical of SSMF. The γ value is around 1.04 for the LP_{01} and 0.75 for the LP_{11}, for all cases, significantly lower than the SSMF typical value of 1.3, as expected.

Table 4.1: Optimized fiber characteristics and parameters.

	ψ [ps/km]		
	-100	0	100
OF [ps/km]	0.0005	0.0040	0.0019
MDD [ps/km]	0.0017	0.0101	0.0050
α	2.158	2.093	2.032
$\Delta n_{tr} \cdot 10^3$	-3.897	-3.953	-4.010
w_2 [µm]	1.875	1.875	1.875
w_3 [µm]	8.750	7.000	6.250

Simple Design Rule

In order to derive a simple design rule some of the profile parameters have to be fix. From Table 4.1 and Fig. 4.3 one can conclude that the optimum (w_2, w_3) pair for the three ψ values is inside the area delimited by $OF < 0.1$ ps/km. Moreover, for the three ψ values, additional results have shown that such area are overlap and that the Δn_{tr} contour map as a function of w_2 and w_3 is approximately the same. Therefore, the optimum dimensioning of the trench can be detached from the optimization of α, with a small DMD penalty. Given this, a simple design rule for the quasi-optimum

α value as a function of ψ can be derived. The motivation for the derivation of such design rule with a fixed set $(\Delta n_{tr}, w_2, w_3)$ is the simplification of the optimization procedure in the fabrication process, since only the concentrations of dopants in the core change between different DMD targets.

The first step in the derivation of the design rule was the dimensioning of the trench. The (w_2, w_3) pair was determined minimizing OF simultaneously for the three targets, obtaining: $w_2 = 1.875\,\mu m$ and $w_3 = 7\,\mu m$. For this (w_2, w_3) pair, the variation of the optimum Δn_{tr} value for each of the targeted ψ values is lower than 1.5 %, and the OF deviation from the optimum results shown in Table 4.1 is lower than 0.05 ps/km. Therefore, the Δn_{tr} chosen for the design rule was the optimum Δn_{tr} for $\psi = 0$ ps/km: $\Delta n_{tr} = 3.953 \cdot 10^{-3}$. Fig. 4.4 shows the optimum α and the respective MDD as a function of ψ. It can be seen from Fig. 4.4 that the variation of the optimum α with ψ is approximately linear, and that the MDD is always lower than 1.8 ps/km. By fitting a second order polynomial to the optimum α values, the equation shown in the inset of Fig. 4.4 was obtained. Using this equation, Fig. 4.4 shows the quasi-optimum α line and the corresponding MDD line. From these lines it can be concluded that the fitting equation shown in the inset of Fig. 4.4 is sufficient for the design of a FMF with any DMD value from -200 ps/km to 200 ps/km, and a MDD lower than 1.8 ps/km over the C-band. Regarding the propagation characteristics R_c, D, S and γ, of the fibers designed following the given rule, their values are very similar to the values obtained with the optimum parameters given by a full optimization. Therefore, similar comments are applicable.

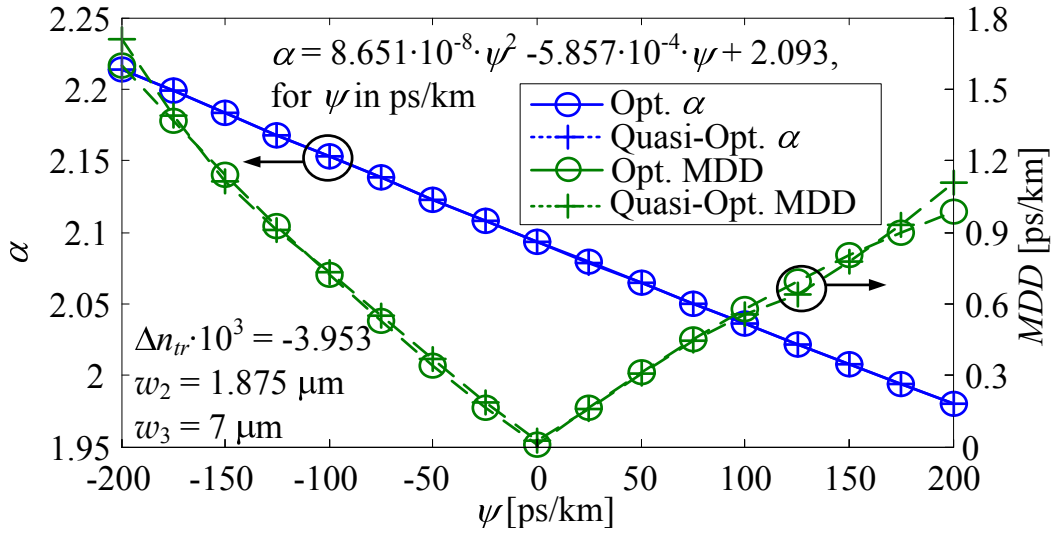

Figure 4.4: Optimum α and MDD as a function of ψ.

Manufacturing Margins

The optimized parameters presented in Table 4.1 and the parameters obtained from the simple design rule were obtained ignoring the finite precision margins of the manufacturing control processes. Those margins may lead to some deviation of the manufactured fiber parameters from the optimum values. The typical fabrication tolerance for Δn_{co} or Δn_{tr} is ± 0.0001 [28], for w_1 is $\pm 0.25\,\mu$m, and for α is ± 0.01 [24]. These deviations result in a corresponding deviation of the DMD relative to the targeted value. In order to evaluate the tolerance to these deviations, the MDD value considered acceptable over the C-band is 12 ps/km, since this is the DMD required for 2000 km of multimode transmission at 100 Gb/s using PDM-QPSK [5], for an overhead of up to 10 %. Table 4.2 shows the parameters maximum tolerable deviation (MTD), such that MDD remains lower than the 12 ps/km requirement, for the optimum parameters of Table 4.1 and for the parameters given by the simple design rule presented in section 4.2.2. The tolerance of each parameter was determined considering the remaining parameters fixed at their optimum values. The MTD values for w_1, w_2 and w_3 were obtained considering simultaneous and proportional deformation of w_1, w_2 and w_3 (independent deformations are also possible and can lead to less tolerance).

Table 4.2 shows that the tolerance of any of the parameters is close or slightly below the manufacture margins, for all cases, except Δn_{co} for $\psi = -100$ ps/km. As no significant MTD difference is visible between the optimized values of section 4.2.2 and the values obtained using the simple design rule, one concludes about the usefulness of the proposed simplification. Further results have shown that, for the case of a simultaneous drift of two or more parameters, the MTD is reduced by one half

Table 4.2: Maximum tolerable deviation of the optimum parameters [%].

	Manufacturing Margin	Full Optimization ψ [ps/km]			Simple Design Rule ψ [ps/km]		
		-100	0	100	-100	0	100
Δn_{co}	$\sim\pm 2.5$	± 3.735	± 2.676	± 2.19	± 3.885	± 2.816	± 2.229
w_1, w_2, w_3	$\sim\pm 2.5$	± 2.358	± 2.328	± 2.289	± 2.427	± 2.316	± 2.208
α	$\sim\pm 0.5$	± 0.577	± 0.577	± 0.577	± 0.560	± 0.577	± 0.563
Δn_{tr}	$\sim\pm 2.5$	± 2.002	± 2.002	± 2.002	± 2.002	± 2.002	± 2.002

or more. These results demonstrate that a non-negligible number of pre-forms will produce FMFs with a MDD higher than 12 ps/km, resulting in an increase of the fabrication costs. Therefore, an improvement of the fabrication control process will be necessary. This problem can be partially circumvented by concatenating FMFs exhibiting positive and negative DMD deviations.

4.3 Design of xM-FMFs with Low DMD

In this section, the optimization of a GCCT profile and of a MSI profile is performed for 2M to 12M, with the objective of obtaining a DMD lower than the 12 ps/km over the C-band requirement. Although the GCCT profile designs in Table 2.2 have presented lower DMD over a wider wavelength range, the MSI profile is also considered in order to evaluate alternative profiles. The optimization of the GCCT profile proposed in this section extends the work presented in section 4.2. In appendix B, it is shown that following the optimization procedure in section 4.2 the optimized DMD grows significantly with xM. Therefore, in this section it is proposed to optimize Δn_{co}, which was fixed in section 4.2. However, as Δn_{co} has a direct impact on the MBL [26], such impact is taken into account on the optimization function. Finally, the impact of fabrication margins on the DMD of the optimum profiles is analyzed, since high sensitivity of FMFs to such margins has already been identified in section 4.2 and [9].

This section is organized as follows. Section 4.3.1 describes the profiles considered and provides an analysis of the impact of their parameters on DMD and MBL. Section 4.3.2 presents the optimization function algorithms. Section 4.3.3 presents the optimization results, whereas Section 4.3.4 presents the tolerance to the fabrication margins of the optimum designs.

4.3.1 Fiber Profile Description and Analysis

The GCCT description provided in section 4.2.1 is used again. The MSI profile is shown in Fig. 4.5, where each step i has an arbitrary Δn value (Δn_i) and step width w_{st}. The number of steps is N_{st}. The MSI profile allows evaluating arbitrary profiles by simultaneously increasing N_{st} and decreasing w_{st}. For both profiles, the guided modes ($\mathrm{LP}_{\mu\nu}$) and their characteristics are calculated solving the Maxwell equations numerically using the method described in [29]. The $\mathrm{LP}_{\mu\nu}$ mode characteristics calculated are the effective index $\overline{n}^{\mathrm{LP}_{\mu\nu}}$, the effective group index $\overline{n}_g^{\mathrm{LP}_{\mu\nu}}$, the DMD and

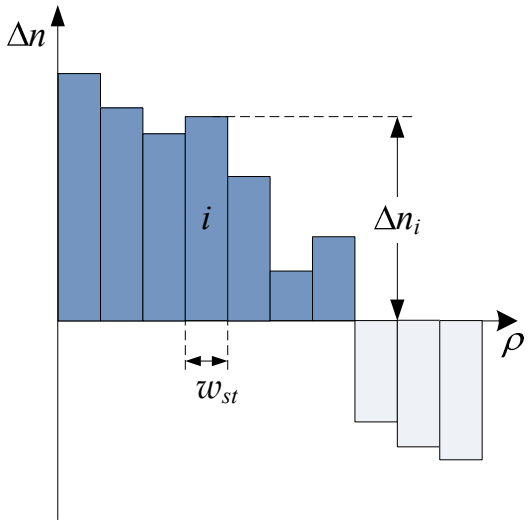

Figure 4.5: MSI profile with constant w_{st}.

the MBL. The DMD of the $LP_{\mu\nu}$ mode is measured relatively to the LP_{01} mode and is given by:

$$DMD^{LP_{\mu\nu}}(\lambda) = \frac{1}{c_0}\left[\overline{n}_g^{LP_{\mu\nu}}(\lambda) - \overline{n}_g^{LP_{01}}(\lambda)\right] \tag{4.9}$$

where λ is the wavelength and c_0 is the light velocity in free space. The MBL are calculated according to [26]. The dispersion properties of the doped silica have been modeled using the Sellmeier coefficients provided in [22].

The design of a graded core fiber with a given xM starts by choosing the normalized frequency value V. For each xM fiber, the highest possible V value that guarantees the guidance of the first x-modes while cutting off the next higher-order modes is chosen, as in [30], considering a GCCT profile with $\alpha = 2.3$ and $\Delta n_{tr} = 0$. As a result, for 2M, 4M, 6M, 9M and 12M, the V values are chosen to be 5.10, 7.25, 9.00, 11.15 and 12.95, respectively. As a consequence, the x-modes have the highest possible $\overline{n}_g^{LP_{\mu\nu}}$ values and are thus more strongly guided. The w_1 for each xM fiber is obtained using (2.6) and considering the lowest λ of the C-band (1530 nm). Along this section, references to a Δn_{co} change imply a w_1 change such that V remains constant.

The impact of α and Δn_{tr} on the DMD of a GCCT profile were explained in section 4.2.1 for a 2M-FMF: α allows controlling the DMD average and Δn_{tr} allows controlling the DMD slope. In the following, the impact of Δn_{co} on the DMD of a GCCT profile is explained, considering a 2M-FMF with $\alpha = 2$ and $\Delta n_{tr} = 0$. Fig. 4.6 shows the DMD as a function of λ, for different Δn_{co} values (very low Δn_{co}

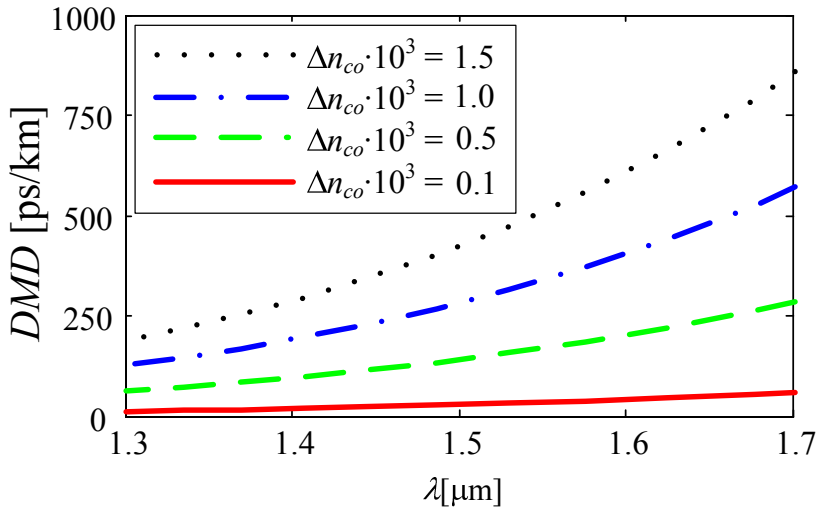

Figure 4.6: DMD [ps/km] as a function of λ, for different Δn_{co} values.

values are considered in order to increase its impact). From Fig. 4.6 one can conclude that the DMD decreases with Δn_{co}, over a wide wavelength range. Further reducing Δn_{co}, negligible levels of DMD are obtained since, for an infinitesimal Δn_{co} value, the difference $\left|\overline{n}^{\mathrm{LP}_{11}} - \overline{n}^{\mathrm{LP}_{01}}\right|$ would be also infinitesimal ($\overline{n}^{\mathrm{LP}_{\mu\nu}}$ is bounded by n_{co} and n_{cl}) as well as $\left|\overline{n}_g^{\mathrm{LP}_{11}} - \overline{n}_g^{\mathrm{LP}_{01}}\right|$ (proportional to DMD) since $\overline{n}_g^{\mathrm{LP}_{\mu\nu}} = \overline{n}^{\mathrm{LP}_{\mu\nu}} + \lambda\left(d\overline{n}^{\mathrm{LP}_{\mu\nu}}/d\lambda\right)$. Therefore, reduction of Δn_{co} has the potential to further reduce the DMD values obtained in appendix B. The drawback of the utilization of a low Δn_{co} is related to MBL. According to [26], the power loss at bends increases with decreasing Δn_{co} for a certain curvature radius and, as a consequence, low DMD and low MBL are opposite requirements. The trade-off between DMD and MBL on the optimization of Δn_{co} is analyzed in Section 4.3.3.

4.3.2 Optimization Function and Algorithms

In this section, the optimization function used to search for the optimum parameters of each profile is presented, as well as the optimization algorithms for each profile. The optimization parameters of each profile can be gathered in a parameter vector (pv): $pv = [\alpha, \Delta n_{co}, \Delta n_{tr}, w_2, w_3]$ for the GCCT profile and $pv = [w_{st}, \delta n_1, \ldots, \delta n_{N_{st}}]$ for the MSI profile.

Optimization Function

The optimization function takes into account two figures: one related to DMD and another related to MBL. The DMD related figure is the maximum DMD among the guided modes and over the defined wavelength range ($maxDMD$), given by:

$$\mathrm{max}DMD\,(pv) = \max_{\lambda}\left(\max_{\mu\nu}\left|DMD^{\mathrm{LP}_{\mu\nu}}\,(\lambda, pv)\right|\right) \tag{4.10}$$

The MBL related figure is the curvature radius (R_c) for 100 turns and $MBL = 0.1\,\mathrm{dB}$ at 1625 nm. For a given xM, the R_c of each mode is calculated and the highest value is considered. Considering the ITU-T recommendation in [27], R_c must be lower than or equal to 30 mm. The optimization function (OF) is given by

$$OF\,(pv) = \mathrm{max}DMD\,(pv)\cdot\left\{1+\epsilon\cdot\left[\beta\cdot\frac{(R_c-30)}{30}\right]\right\} \tag{4.11}$$

$$\beta = \begin{cases} 0, \text{ for } R_c \leqslant 30 \\ 1, \text{ for } R_c > 30 \end{cases}$$

with R_c in millimeter units

where the ϵ factor can be 0 or 1 in order to consider or ignore the $R_c \leq 30\,\mathrm{mm}$ requirement. The $\beta(R_c - 30)/30$ factor in (4.11) introduces a penalizing factor for solutions with $R_c > 30$ mm, since β is equal to 0 for $R_c \leq 30\,\mathrm{mm}$ and equal to 1 for $R_c > 30\,\mathrm{mm}$. Note that, for each different pv tested, if the number of modes is not the desired, the OF value is set to infinity. The optimization function (4.11) is subject to different sets of constraints depending on the profile being optimized. For the GCCT profile, OF is subject to the following constraints

$$\left(\Delta n_{co}{}^{-} = 1\cdot 10^{-3}\right) \leq \Delta n_{co} \leq \left(\Delta n_{co}{}^{+} = 5\cdot 10^{-3}\right) \tag{4.12}$$

$$\left(\alpha^{-} = 1.5\right) \leq \alpha \leq \left(\alpha^{+} = 2.5\right) \tag{4.13}$$

$$\left(\Delta n_{tr}{}^{-} = -5\cdot 10^{-3}\right) \leq \Delta n_{tr} \leq \left(\Delta n_{tr}{}^{+} = 0\right) \tag{4.14}$$

$$\left(w_3{}^{-} = 0\right) \leq w_3 \leq \left(w_3{}^{+} = w_1\right) \tag{4.15}$$

$$\left(w_3{}^{-} = 0\right) \leq w_3 \leq \left(w_3{}^{+} = w_1\right) \tag{4.16}$$

$$\left(\lambda^{-} = 1530\,\mathrm{nm}\right) \leq \lambda \leq \left(\lambda^{+} = 1565\,\mathrm{nm}\right) \tag{4.17}$$

Δn_{co}^{-} in (4.12) takes into account the difficulties of manufacturing Δn_{co} lower than

$1 \cdot 10^{-3}$ [31] whereas Δn_{co}^{+} is used as upper bound of Δn_{co} taking into account that $maxDMD$ increases with Δn_{co}. (4.13)-(4.16) were defined in section 4.2.1. (4.17) bounds λ to the C-band. In the MSI profile case, OF is subject to the following constrains:

$$\left(\Delta {n_i}^{-} = -5 \cdot 10^{-3}\right) \leq \Delta n_i \leq \left(\Delta {n_i}^{+} = 5 \cdot 10^{-3}\right) \tag{4.18}$$

$$N_{st} = \left\{ \begin{array}{cccc} 16 & 32 & 64 \end{array} \right\} \tag{4.19}$$

$$\left(w_{st}^{-} = 0.5^{-}\mathrm{m}\right) \leq w_{st} \leq \left(w_{st}^{+} = 5^{-}\mathrm{m}\right) \tag{4.20}$$

(4.18) constrains the Δn_i of each step between $-5 \cdot 10^{-3}$ and $5 \cdot 10^{-3}$, taking into account the same reasoning used to set the constraints for Δn_{co} and Δn_{tr}. (4.19) constrains N_{st} to powers of 2 between 16 and 64, since a lower number of steps would not have sufficient flexibility to reduce $maxDMD$ and R_c at the same time, and a higher N_{st} would be too complex to manufacture. (4.20) constrains w_{st} between 0.5 µm and 5 µm, such that the total length of the profile ($w_{st} \cdot N_{st}$) takes values similar to the total length considered for the GCCT profile ($w_1 + w_2 + w_3$). Moreover, λ is bounded to the C-band.

GCCT Optimization Algorithm

The optimization algorithm for the GCCT profile is designed to take advantage of the $maxDMD$ function properties. In the order to present the $maxDMD$ properties, a 2M-FMF with $\Delta n_{co} = 1 \cdot 10^{-3}$, $w_2 = 3\,\mu\mathrm{m}$ and $w_3 = 3\,\mu\mathrm{m}$ is considered. Fig. 4.7(a) presents the contour map of $maxDMD$ as a function of $(\alpha, \Delta n_{tr})$. Fig. 4.7(a) shows that $maxDMD$ is a convex function of $(\alpha, \Delta n_{tr})$, such that $\min\limits_{\alpha}(maxDMD)$ as a function of Δn_{tr} or $\min\limits_{\Delta n_{tr}}(maxDMD)$ as a function of α are convex functions. Fig. 4.7(b) shows $\min\limits_{\alpha}(maxDMD)$ as a function of Δn_{tr}. Therefore, the search for the pair $(\alpha, \Delta n_{tr})$ that minimizes $maxDMD$ for a given $(\Delta n_{co}, w_2, w_3)$ point can be done one dimension at a time using for instance a golden section search (GSS) [32]. The GSS over α and the GSS over Δn_{tr} are arranged as

$$\begin{aligned} &maxDMD^{min}\left(\Delta n_{co}, w_2, w_3\right) = \min_{\alpha, \Delta n_{tr}}\left(maxDMD\left(pv\right)\right) = \\ &\mathrm{GSS}\left(\Delta n_{tr}^{-}, \Delta n_{tr}^{+}, \mathrm{GSS}\left(\alpha^{-}, \alpha^{+}, maxDMD\left(pv\right)\right)\right). \end{aligned} \tag{4.21}$$

The first and second GSS function parameters are the lower and the upper bound,

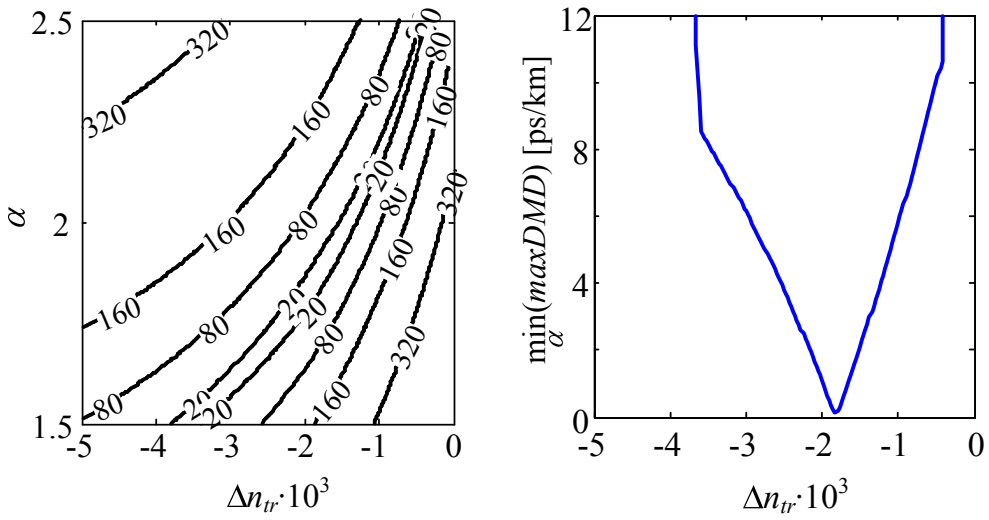

(a) (b)

Figure 4.7: (a) Contour map of $maxDMD$ [ps/km] as a function α and Δn_{tr}. (b) $\min_{\alpha}(maxDMD)$ as a function of Δn_{tr}.

respectively, of the independent variable of the function under optimization. Further results have shown that considering different numbers of modes and $(\Delta n_{co}, w_2, w_3)$ values within the domains defined in (4.12)-(4.17), the $maxDMD$ function properties presented are still valid. Finally, in order to find the full optimum pv set, an exhaustive search (ES) is performed over $maxDMD^{min}(\Delta n_{co}, w_2, w_3)$. The GSS optimizes α and Δn_{co} with a termination tolerance on $maxDMD$ of 0.001 ps/km. The ES optimizes the Δn_{co}, w_2 and w_3 with tolerances of $5 \cdot 10^{-4}$, 0.25 µm and 0.5 µm, respectively. Further reducing these tolerances by a factor of 2 changed $maxDMD$ negligibly.

MSI Optimization Algorithm

The optimization algorithm used for the MSI profile is a genetic algorithm (GA), due to the high number of optimization parameters. The individual genes are: [w_{st}, Δn_1, ..., $\Delta n_{N_{st}}$], and the individual fitness is given by the inverse of OF in (4.11) considering $\epsilon = 1$.

The initial population is randomly generated within the predefined Δn_i and w_{st} constraints given by (4.18) and (4.20), respectively. The Δn_i genes are generated using an uniform distribution and the w_{st} gene is generated using a Gaussian distribution with mean equal to $(w_1 + w_2 + w_3)/N_{st}$, considering the optimum GCCT parameters obtained with $\Delta n_{co} = 0.001$, and standard deviation equal to $(w_{st}^{+} - w_{st}^{-})/6$. The

size of the initial population is 2000. After the first generation the population size is reduced to 200. The following generations are created using crossover, mutation and selection operators.

The crossover operator randomly selects the j^{th} gene in the solution structure and, given two parents $X = [w_{st}^X, \Delta n_1^X, \ldots, \Delta n_{N_{st}}^X]$ and $Y = [w_{st}^Y, \Delta n_1^Y, \ldots, \Delta n_{N_{st}}^Y]$, the generated offspring are constructed as: $U = [w_{st}^X, \Delta n_1^X \ldots, \Delta n_{j-1}^X, \Delta n_j^Y, \ldots, \Delta n_{N_{st}}^Y]$ and $W = [w_{st}^Y, \Delta n_1^Y ..., \Delta n_{j-1}^Y, \Delta n_j^X, \ldots, \Delta n_{N_{st}}^X]$. The selection of the individuals for the crossover operation is executed using a roulette wheel selection scheme. In this scheme, the probability of an individual being selected is proportional to its fitness. The size of the offspring generated is 200.

The mutation operation is executed adding to the l^{th} gene (randomly selected) a Gaussian random variable with zero mean and standard deviation σ_l. The standard deviation σ_l is weighed by the domain of the l^{th} gene, in order to compensate for the different orders of magnitude between w_{st} and Δn_i. σ_l is given by: $(w_{st}^+ - w_{st}^-)/6$ for $l = 1$ and $(\Delta n_i^+ - \Delta n_i^-)/6$ for $l > 1$. In each generation, the mutation operation is applied to the offspring with a probability of 50 %. Additionally, 20 new individuals are added to the offspring selecting the 20 best parents (parents with higher fitness) and applying the mutation operator (the original parents are kept in the population). In the process of selection of the next generation, 10 % of the best individuals (individuals with higher fitness) are always chosen, and the remaining population is selected using the roulette wheel selection scheme already used in the crossover operation.

4.3.3 Optimization Results

GCCT profile

In this sub-section the optimum results for the GCCT profile are presented. Fig. 4.8(a) and 4.8(b) show $maxDMD$ and R_c optimum values, respectively, as a function of Δn_{co}, obtained using OF with $\epsilon = 0$ and $\epsilon = 1$. Fig. 4.8(a) shows that $maxDMD$ decreases with decreasing Δn_{co} for all numbers of modes, in line with the explanation provided in section 4.3.1, independently of ϵ. Fig. 4.8(b) shows that R_c increases when Δn_{co} decreases for $\epsilon = 0$, such that for $\Delta n_{co} < 5 \cdot 10^{-3}$ the R_c requirement is not satisfied for all the numbers of modes considered. On the other hand, considering $\epsilon = 1$, Fig. 4.8(b) shows that the R_c requirement is satisfied for all Δn_{co} values and numbers of modes considered, $1 \cdot 10^{-3} \leq \Delta n_{co} \leq 5 \cdot 10^{-3}$. Comparing the results shown in Fig. 4.8(a) obtained using $\epsilon = 0$ and $\epsilon = 1$, it can be concluded that the R_c

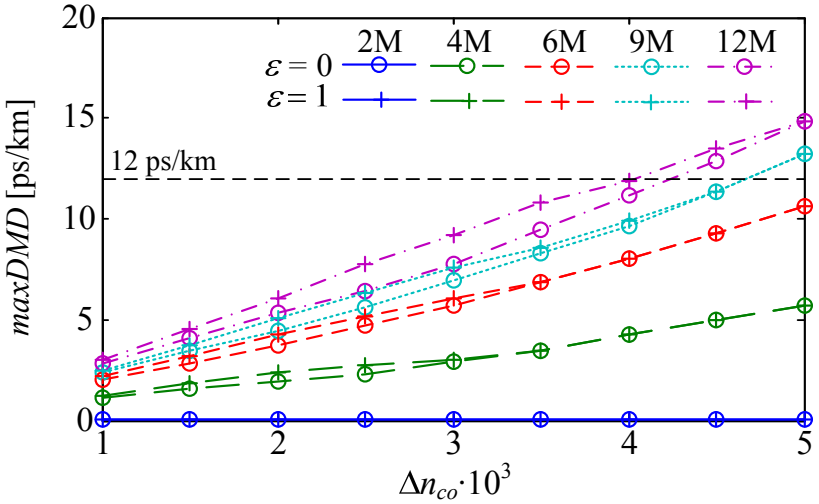

(a)

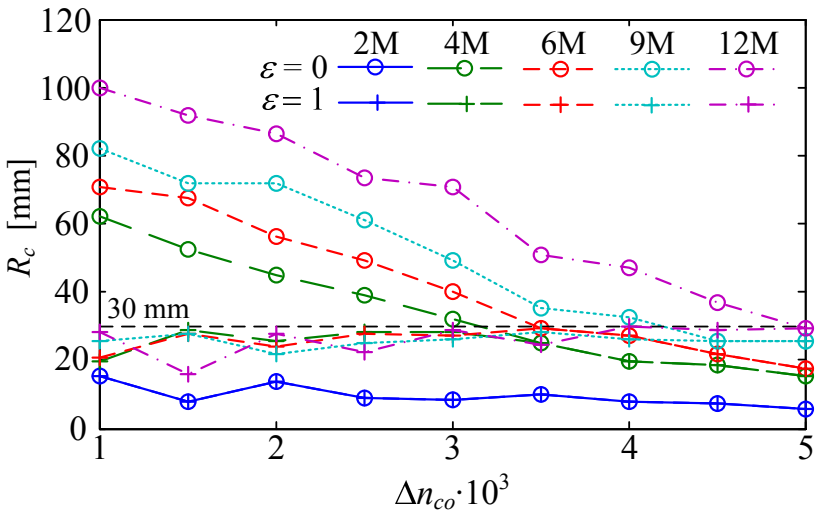

(b)

Figure 4.8: (a) $maxDMD$ [ps/km] optimum values as a function of Δn_{co} for different numbers of modes. (b) R_c [mm] as a function of Δn_{co} for different numbers of modes.

requirement can be satisfied from 2M to 12M with small $maxDMD$ degradation (lower than 0.5 ps/km for $\Delta n_{co} = 1 \cdot 10^{-3}$). Therefore, Fig. 4.8 shows that the $maxDMD$ and R_c requirements are satisfied simultaneously for $1 \cdot 10^{-3} \leq \Delta n_{co} \leq 4 \cdot 10^{-3}$ from 2M to 12M. Moreover, it can be concluded that $maxDMD$ cannot be reduced to negligible levels ($maxDMD < 0.1$ ps/km) for more than 2M. This limitation is explained noting that the field confinement effect of the trench affects each higher-order mode (LP_{02}, LP_{21}, LP_{12}, LP_{31}, ...) with different strength, since all have a considerable power concentration near the core boundary but different distributions (appendix B). Therefore, each mode has a different optimum trench dimensioning and

it is not possible to reduce the DMD of all modes to negligible values at the same time over the C-band. Moreover, increasing the number of modes, the $(\alpha, \Delta n_{tr}, w_2, w_3)$ domain satisfying $maxDMD \leq 12\,\text{ps/km}$ decreases for a given Δn_{co}.

The optimum parameters for $\Delta n_{co} = 1 \cdot 10^{-3}$ and $\epsilon = 1$ are shown in Table 4.3, as well as the respective $maxDMD$, Rc, chromatic dispersion (D) at 1550 nm (for the mode with highest D, max(D), and for the mode with lowest D, min(D)), chromatic dispersion slope (S) at 1550 nm (for the mode with highest S, max(S), and for the mode with lowest S, min(S)) and nonlinear coefficient (γ) for LP_{01} (the mode with the highest γ). Comparing with typical SSMF values, the D values are only slightly higher than $\sim$17 ps/(nm·km), whereas the S values are lower than $\sim$80 fs/(nm^2·km). The γ value is significantly lower than the SSMF typical value of 1.3 W^{-1}/km, as expected due to the higher core radius. In the appendix C, Table C.1 provides for all modes the values of the: $DMD_{\text{LP}_{\mu\nu}}$ for the worst wavelength of the C-band, D at 1550 nm, effective area (A^{eff}) at 1550 nm, and R_c.

As a main conclusion, the results presented in this section allow stating that optimizing Δn_{co} allowed to fulfill the requirement of $maxDMD \leq 12\,\text{ps/km}$ and $R_c \leq 30\,\text{mm}$, which was not achieved in appendix B.

Table 4.3: Optimized fiber parameters and characteristics for the optimum GCCT profile with $\Delta n_{co} = 1 \cdot 10^{-3}$ and $\epsilon = 1$.

	Number of modes				
	2	4	6	9	12
α	2.15544	1.96677	1.97257	1.97291	1.97228
$\Delta n_{tr} \cdot 10^3$	-3.1221	-2.9888	-3.403	-3.237	-3.3598
w_1 [µm]	19.2056	27.302	33.8922	41.9886	48.7671
w_2 [µm]	6	4.5	5.5	6	6.5
w_3 [µm]	2.5	1.5	1.5	1.5	1.5
$maxDMD$ [ps/km]	0.004	1.347	2.252	2.487	2.997
R_c [mm]	15.1	19.9	20.8	25.6	28.0
min(D); max(D)[1]	22.4;22.5	22.4;22.5	22.4;22.5	22.4;22.5	22.3;22.6
min(S); max(S)[2]	65.5;65.6	63.0;65.7	61.9;65.8	61.3;65.8	57.3;65.9
γ - LP_{01} [W^{-1}/km]	0.222	0.161	0.130	0.105	0.09

Units: [1][ps/(nm·km)], [2][fs/(nm^2·km)].

MSI Profile

In this sub-section, the optimum results for the MSI profile obtained using the algorithm described in section 4.3.2 are presented. The MSI profile is optimized for: 4M, 6M, 9M and 12M (2M is skipped since negligible $maxDMD$ levels were obtained with the GCCT profile), considering $N_{st} = \{16,\ 32,\ 64\}$.

Table 4.4 presents the $maxDMD$ and R_c of the optimum MSI profiles at the end of 400 generations, for 160 different initial populations. The results show that 64 steps are required to obtain a $maxDMD$ value lower than the $maxDMD$ of the optimum GCCT profile with $\Delta n_{co} = 1 \cdot 10^{-3}$, for 9M and 12M. Moreover, the $maxDMD$ of the best individual decreases with N_{st}, for a given xM, due to the increase of the profile flexibility with N_{st}. For $N_{st} = 64$, the $maxDMD$ reduction comparatively to the GCCT results ranges from 19 % to 31 %. Regarding the R_c values, the best individual meets the $R_c \leq 30$ mm constraint, for all the cases considered. Note that the individual fitness is given by the inverse of OF in (4.11) considering $\epsilon = 1$. In the appendix C, Table C.1 provides, for all modes, the values of: $DMD^{\mathrm{LP}_{\mu\nu}}$ for the worst wavelength of the C-band, D at 1550 nm, effective area (A^{eff}) at 1550 nm, and R_c.

Table 4.4: Characteristics for the optimum MSI profiles.

N_{st}		Number of modes			
		4	6	9	12
16	$maxDMD$ [ps/km]	1.21	3.1	3.51	5.26
	$maxDMD$ red. [%][1]	10.7	-36.8	-41.1	-75.6
	R_c [mm]	23.9	19.4	24.2	25
32	$maxDMD$ [ps/km]	1.06	2.2	2.76	3.58
	$maxDMD$ red. [%][1]	21.3	3.1	-10.7	-19.5
	R_c [mm]	21.5	19.6	28.9	24.8
64	$maxDMD$ [ps/km]	0.93	1.75	1.95	2.43
	$maxDMD$ red. [%][1]	31.3	22.9	21.8	19.1
	R_c [mm]	21.5	19.5	26.6	26.3

[1] $maxDMD$ red. [%] - is the relative difference between the $maxDMD$ of the MSI profile and the $maxDMD$ of the GCCT optimum profile with $\Delta n_{co} = 1 \cdot 10^{-3}$, for the same number of modes.

Fig. 4.9 shows the superposition of the optimum MSI profile with $N_{st} = 64$ and the optimum GCCT profile with $\Delta n_{co} = 1 \cdot 10^{-3}$, for 4M, 6M, 9M and 12M. Analyzing Fig. 4.9 it can be concluded that the optimum MSI profiles are similar to the optimum GCCT profile for $\Delta n_{co} = 1 \cdot 10^{-3}$. The similarity between profiles holds for smaller N_{st}.

In conclusion, the results presented in Table 4.4 show that the MSI profiles present lower $maxDMD$ than the minimum achieved with a GCCT profile for all xM considered with $N_{st} = 64$. However, such $maxDMD$ reduction is obtained at the expense of a more complex profile. In order to choose between these two types of profile, the tolerance to the manufacturing margins will be analyzed in section 4.3.4.

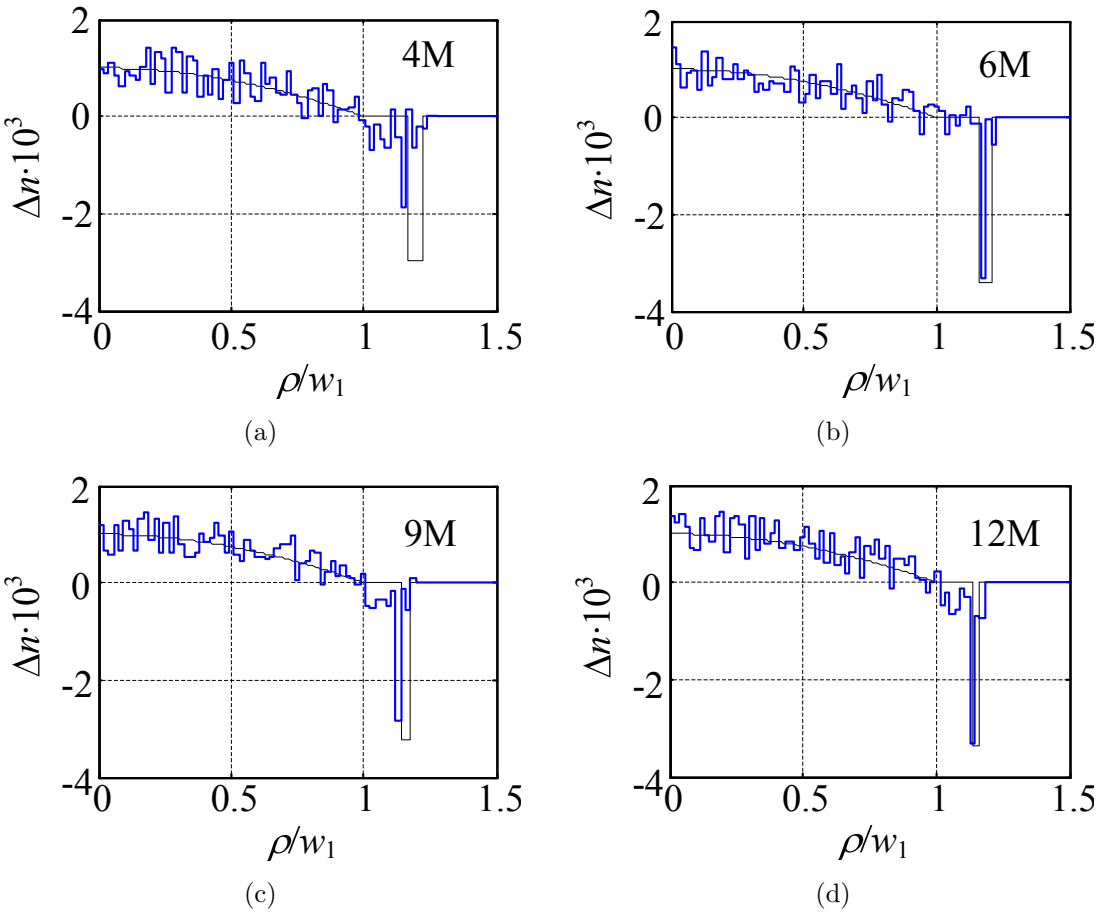

Figure 4.9: Optimum MSI profile with 64 steps and optimum GCCT profile considering $\Delta n_{co} = 1 \cdot 10^{-3}$ as a function of ρ/w_1, for: (a) 4M, (b) 6M, (c) 9M and (d) 12M.

4.3.4 Manufacturing Margins

The optimized parameters in section 4.3.3 were obtained ignoring the finite precision margins of the manufacturing control processes. These margins lead to deviation of the manufactured fiber parameters from the optimum values, causing DMD deviations. Along this section, the tolerance of the optimum profiles to parameters deviations is measured as the maximum tolerable deviation (MTD), positive or negative, such that $maxDMD$ and R_c remains lower than 12 ps/km and 30 mm, respectively. The tolerance of each parameter is calculated considering the remaining parameters fixed at their optimum values, except for the layers widths. All layers that compose the optimum profiles (GCCT or MSI) are simultaneously and proportionally changed.

In order to assess the probability of having a manufactured FMF satisfying the $maxDMD$ and R_c requirements, the MTD values have to be compared to the statistics of parameters deviations on conventional MMFs. According to [33], parameters deviations are well described by normal distributions with a given standard deviation (σ). Therefore, for a specific parameter, when the MTD value is close to σ, 2σ or 3σ the manufacturing success probability is approximately 68 %, 95 % or 99.7 %, respectively.

In this section, the σ values of the parameters are defined considering as reference the standard requirements and profile distortions reported for MMFs of category OM3. Note that the OM1 and OM2 categories are not considered because the profile distortions reported for these categories would lead to a very low probability of success in the design of FMFs [34]. The σ of Δn ($\sigma_{\Delta n}$) is $5 \cdot 10^{-5}$, according to [31], applicable to Δn_{co}, Δn_{tr} and Δn_i parameters. The σ of the layers widths (σ_w) is 2 % of the respective mean layer width (w_1, w_2, w_3, or w_{st}), taking into account that [31] states that the σ of the core radius of a conventional MMF (25 µm) is 0.5 µm. The σ of α (σ_α) is 0.003, taking into account the tolerance specified in [24].

GCCT Profile

In this sub-section the MTD of the GCCT profile parameters are presented, considering the optimum parameters values obtained in section 4.3.3 with $\epsilon = 1$.

Fig. 4.10(a), 4.10(b), 4.10(c) and 4.10(d) show the MTD of α, Δn_{co}, Δn_{tr}, and (w_1, w_2, w_3), respectively. It has been verified that the MTD is always limited by the $maxDMD$ requirement. In most cases, two trends can be identified in Fig. 4.10, namely: the increase of the MTD with the decrease of Δn_{co} and the decrease of

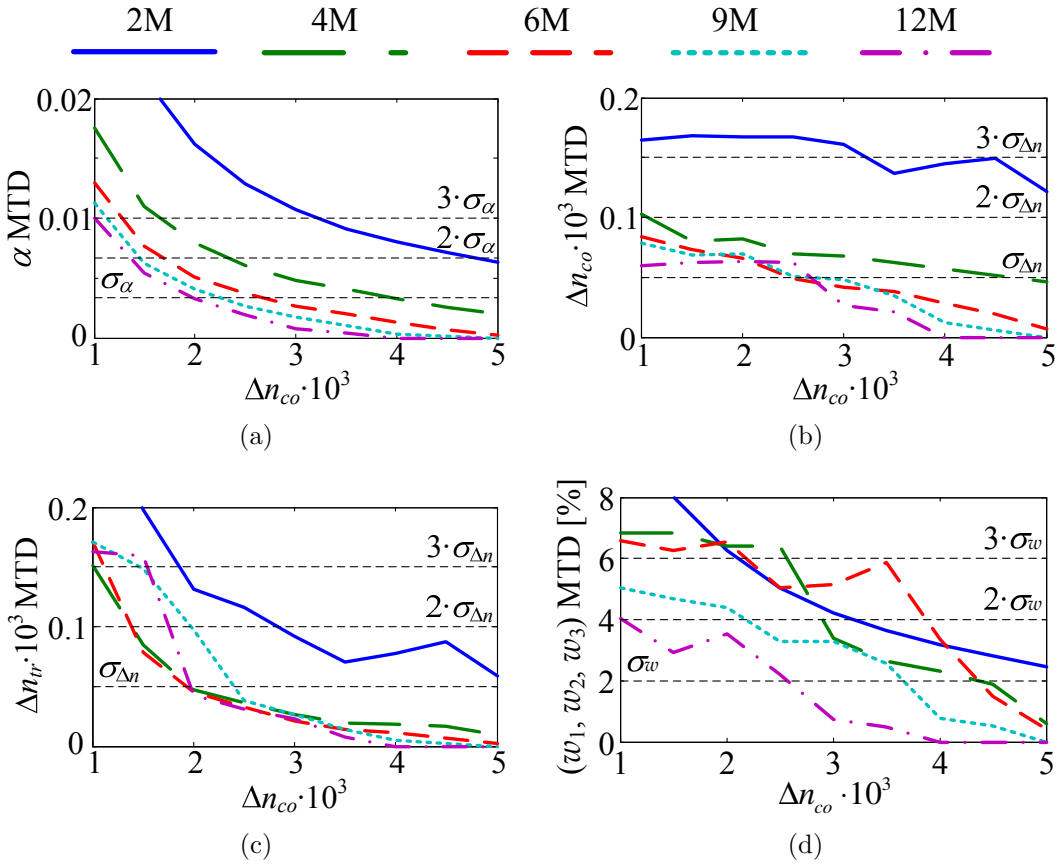

Figure 4.10: GCCT profile parameters MTD: (a) α, (b) Δn_{co}, (c) Δn_{tr} and (d) (w_1, w_2, w_3).

MTD with xM increase. Exceptions to these trends are a consequence of considering an optimization algorithm targeting the absolute minimum $maxDMD$, since further results have shown that non-optimum parameters can lead to a higher MTD. The MTD decrease with xM increase can be understood noting two different facts: in the absence of any deviation of the parameters, the absolute minimum $maxDMD$ increases with xM for a given Δn_{co}, getting closer to 12 ps/km; it has been verified that $maxDMD$ changes more abruptly around the optimum parameters with the increase of xM. Such facts are responsible for the (α, Δn_{tr}, w_2, w_3) domain reduction satisfying $maxDMD \leq 12$ ps/km with xM, as identified in section 4.3.3.

The MTD results in Fig. 4.10 allow estimating the probability of having a manufactured FMF with a $maxDMD \leq 12$ ps/km and $R_c \leq 30$ mm for a given xM. For 2M, that probability is higher than 95 % for $\Delta n_{co} < 3 \cdot 10^{-3}$. Note that the success probability for $\Delta n_{co} = 4.5 \cdot 10^{-3}$ is closer to 68 %, limited by (w_1, w_2, w_3) MTD and Δn_{tr} MTD (as in section 4.2.2). In the case of 4M to 12M, the manufacturing probability goes from 95 % to 68 %, respectively, for $\Delta n_{co} = 1 \cdot 10^{-3}$, set by Δn_{co} MTD.

MSI Profile

In this sub-section, the MTD of the MSI profile parameters Δn_i and w_{st} are presented, considering the optimum parameters values obtained in section 4.3.3. The Δn_i MTD of each step is calculated independently, but only the lowest Δn_i MTD is presented. Moreover, the Δn_i MTD for $N_{st} = 32$ and 64 is calculated considering pairs and quads of adjacent steps, since the w_{st} for $N_{st} = 16$ is used a reference. Fig. 4.11(a) and Fig. 4.11(b) show the Δn_i MTD and w_{st} MTD, respectively, as functions of xM, considering $N_{st} = \{16,\ 32,\ 64\}$. As in the MTD analysis for the GCCT profile, it has been verified that the MTD is always limited by the $maxDMD$ requirement.

Fig. 4.11(a) shows that Δn_i MTD is 5 times lower than $\sigma_{\Delta n}$, with reduced dependency on N_{st} and on xM. Fig. 4.11(b) shows that the w_{st} MTD is higher than σ_w for all N_{st} values, from 4M to 12M. These results, allow concluding that the probability of having a FMF with $maxDMD \leq 12\,\text{ps/km}$ and $R_c \leq 30\,\text{mm}$ is approximately 16 %, set by the Δn_i MTD.

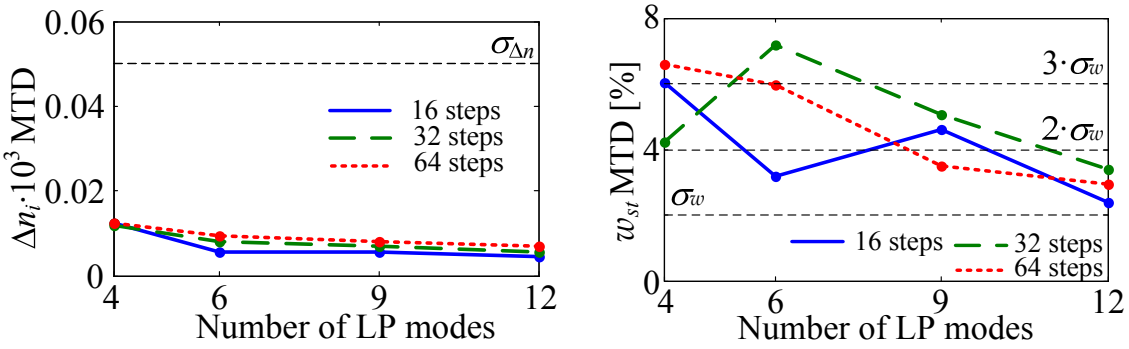

Figure 4.11: MSI profile parameters MTD: (a)Δn_i and (b) w_{st}.

4.4 Conclusions

Along this chapter, the design of FMFs with a DMD lower than 12 ps/km over the C-band was presented. The chapter is divided in two sections: section 4.2 focused on the design of 2M-FMFs suitable for the conceptual demonstration of the first MDM-FMF systems, and section 4.3 focused on the design of FMFs with up to 12M assessing the scalability potential of MDM-FMF systems.

In section 4.2, a GCCT-FMF was optimized through simulation in order to obtain

an arbitrary DMD flattened over the C-band. It has been shown that such design allows obtaining a MDD lower than 0.01 ps/km when α, Δn_{tr}, w_2, w_3 are optimized. Furthermore, it has been concluded that the optimum dimensions of the trench is almost independent of the targeted DMD. A simple design rule for a quasi-optimum α has been derived guaranteeing a MDD over the C band lower than 1.8 ps/km, for a DMD target between -200 ps/km and 200 ps/km. However, the existing fabrication control process does not have enough precision to guarantee that every pre-form produces a FMF with a DMD lower than the 12 ps/km requirement.

In section 4.3, the design of FMFs with low DMD over the C-band was investigated considering two different profiles: a GCCT profile and a MSI profile. The profiles parameters were optimized obtaining the lowest $maxDMD$ achievable for 2M to 12M, with $R_c \leq 30$ mm. The optimization results have shown that the MSI profiles present lower $maxDMD$ than the minimum achieved with a GCCT profile. Additionally, it has been concluded that $maxDMD$ and R_c scale with xM. For 12M, it was obtained a $maxDMD$ lower than 3 ps/km using a GCCT profile and lower than 2.5 ps/km using a MSI profile. Δn_{co} was shown to be the most preponderant parameter of the GCCT profile, allowing reducing $maxDMD$ at the expense of increasing R_c. Regarding the optimum MSI profiles, it was shown that 64 steps are required to achieve a $maxDMD$ improvement considering 12M. Furthermore, the impact of the fabrication margins on the optimum $maxDMD$ was analyzed and used to derive the probability of having a manufactured FMF with $maxDMD$ lower than 12 ps/km and R_c lower than 30 mm. For the GCCT profile, it was shown that the probability increases with decreasing Δn_{co} whereas the probability for the MSI profile has reduced dependency on N_{st} independently of xM. In the case of 12M, the probability was estimated to be approximately 68 % considering a GCCT profile and 16 % considering a MSI profile with 64 steps. In conclusion, the GCCT is the preferred profile with current fabrication margins.

References

[1] R. Essiambre and R. Tkach, "Capacity Trends and Limits of Optical Communication Networks," *Proceedings of the IEEE*, vol. 100, no. 5, pp. 1035–1055, May 2012.

[2] A. Ellis and D. Cotter, "Approaching the Non-Linear Shannon Limit," *IEEE/OSA Journal of Lightwave Technology*, vol. 28, no. 4, pp. 423–433, February 2010.

[3] R. Essiambre and A. Mecozzi, "Capacity limits in single-mode fiber and scaling for spatial multiplexing," in *Proc. Optical Fiber Communication Conference and Exposition*, March 2012, p. OW3D.1.

[4] P. Winzer, "Energy-Efficient Optical Transport Capacity Scaling Through Spatial Multiplexing," *IEEE Photonics Technology Letters*, vol. 23, no. 13, pp. 851–853, July 2011.

[5] B. Inan, B. Spinnler, F. Ferreira, A. Lobato, S. Adhikari, V. Sleiffer, D. van den Borne, N. Hanik, and S. Jansen, "Equalizer complexity of mode division multiplexed coherent receivers," in *Proc. Optical Fiber Communication Conference and Exposition*, March 2012, p. OW3D.4.

[6] A. Ellis and N. Doran, "Are few-mode fibres a practical solution to the capacity crunch?" in *Proc. International Conference on Transparent Optical Networks*, June 2013, pp. 1–4.

[7] R. Ryf, N. Fontaine, and R. Essiambre, "Spot-Based Mode Couplers for Mode-Multiplexed Transmission in Few-Mode Fiber," *IEEE Photonics Technology Letters*, vol. 24, no. 21, pp. 1973–1976, November 2012.

[8] K. Sato, R. Maruyama, N. Kuwaki, S. Matsuo, and M. Ohashi, "Optimized graded index two-mode optical fiber with low DMD, large Aeff and low bending loss," *Optics Express*, vol. 21, no. 14, pp. 1489–1492, July 2013.

[9] L. Grüner-Nielsen, Y. Sun, J. W. Nicholson, D. Jakobsen, K. Jespersen, R. Lingle, and B. Palsdottir, "Few Mode Transmission Fiber With Low DGD, Low Mode Coupling, and Low Loss," *IEEE/OSA Journal of Lightwave Technology*, vol. 30, no. 23, pp. 3693–3698, December 2012.

[10] N. Riesen and J. Love, "Dispersion equalisation in few-mode fibres," *Optical and Quantum Electronics*, vol. 42, no. 9-10, pp. 577–585, June 2011.

[11] E. Ip, M. Li, K. Bennett, Y. Huang, A. Tanaka, A. Korolev, K. Koreshkov, W. Wood, E. Mateo, J. Hu, and Y. Yano, "146×6×19-Gbaud wavelength- and mode-division multiplexed transmission over 10×50-km spans of few-mode fiber with a gain-equalized few-mode EDFA," in *Proc. Optical Fiber Communication Conference and Exposition*, March 2013, pp. 1–3.

[12] M. Li, B. Hoover, S. Li, S. Bickham, S. Ten, E. Ip, Y. Huang, E. Mateo, Y. Shao, and T. Wang, "Low delay and large effective area few-mode fibers for mode-division multiplexing," in *Proc. OptoElectronics and Communications Conference*, 2012, pp. 495–496.

[13] R. Maruyama, N. Kuwaki, S. Matsuo, K. Sato, and M. Ohashi, "DMD Free Transmission Line Composed of TMFs with Large Effective Area for MIMO Processing," in *Proc. European Conference and Exhibition on Optical Communication*, September 2012, p. Tu.1.F.2.

[14] R. Ryf, N. Fontaine, M. Mestre, S. Randel, X. Palou, C. Bolle, A. Gnauck, S. Chandrasekhar, X. Liu, and B. Guan, "12×12 MIMO Transmission over 130-km Few-Mode Fiber," in *Proc. Frontiers in Optics*, October 2012, p. FW6C.4.

[15] T. Mori, T. Sakamoto, M. Wada, T. Yamamoto, and F. Yamamoto, "Low DMD Four LP Mode Transmission Fiber for Wide-band WDM-MIMO System," in *Proc. Optical Fiber Communication Conference and Exposition*, March 2013, p. OTh3K.1.

[16] T. Sakamoto, T. Mori, T. Yamamoto, and S. Tomita, "Differential Mode Delay Managed Transmission Line for Wide-band WDM-MIMO System," in *Proc. Optical Fiber Communication Conference and Exposition*, March 2012, p. OM2D.1.

[17] R. Ryf, S. Randel, N. Fontaine, M. Montoliu, E. Burrows, S. Chandrasekhar, A. Gnauck, C. Xie, R. Essiambre, P. Winzer, R. Delbue, P. Pupalaikis, A. Sureka, Y. Sun, L. Grüner-Nielsen, R. Jensen, and R. Lingle, "32-bit/s/Hz Spectral Efficiency WDM Transmission over 177-km Few-Mode Fiber," in *Proc. Optical Fiber Communication Conference and Exposition*, March 2013, p. PDP5A.1.

[18] F. Ferreira, D. Fonseca, and H. Silva, "Design of Few-Mode Fibers with Arbitrary and Flattened Differential Mode Delay," *IEEE Photonics Technology Letters*, vol. 25, no. 5, pp. 438–441, March 2013.

[19] ——, "On the dependence of differential mode delay in few-mode fibers on the number of modes," in *Proc. International Conference on Transparent Optical Networks*, June 2013, p. Tu.C2.3.

[20] ——, "Design of Few-Mode Fibers with M-modes and Low Differential Mode Delay," *IEEE/OSA Journal of Lightwave Technology*, vol. 32, no. 3, pp. 353–360, February 2014.

[21] J. Dil and H. Blok, "Propagation of electromagnetic surface waves in a radially inhomogeneous optical waveguide," *IET Optoelectronics*, vol. 5, no. 5, pp. 415–428, September 1973.

[22] W. Hermann and D. Wiechert, "Refractive index of doped and undoped PCVD bulk silica," *Materials Research Bulletin*, vol. 24, no. 9, pp. 1083–1097, September 1989.

[23] K. Mukasa, K. Imamura, and R. Sugizaki, "Optimizing 2 mode fibers with Aeff of 170 μm^2 for LP01 mode and studying a possibility of realizing endlessly 2 mode operation using holey fibers," in *Proc. Optical Fiber Communication Conference and Exposition*, March 2012, p. JW2A.16.

[24] P. Matthijsse, D. Molin, F. Gooijer, and G. Kuyt, "On the Design of Wide Bandwidth Window Multimode Fibers," in *Proc. International Workshop Computing Semantics*, 2005, pp. 332–337.

[25] B. Ainslie and C. Day, "A review of single-mode fibers with modified dispersion characteristics," *IEEE/OSA Journal of Lightwave Technology*, vol. 4, no. 8, pp. 967–979, August 1986.

[26] J. Sakai and T. Kimura, "Bending loss of propagation modes in arbitrary-index profile optical fibers." *Applied Optics*, vol. 17, no. 10, pp. 1499–506, May 1978.

[27] "Characteristics of a single mode optical fibre cable," Recommendation ITU-T G.652B, Tech. Rep., October 2010.

[28] A. Yablon, "Multi-Wavelength Optical Fiber Refractive Index Profiling by Spatially Resolved Fourier Transform Spectroscopy," *IEEE/OSA Journal of Lightwave Technology*, vol. 28, no. 4, pp. 360–364, February 2010.

[29] C. Yeh and G. Lindgren, "Computing the propagation characteristics of radially stratified fibers: an efficient method," *Applied Optics*, vol. 16, no. 2, pp. 483–493, February 1977.

[30] M. Bigot-Astruc, D. Boivin, and P. Sillard, "Design and fabrication of weakly-coupled few-modes fibers," in *Proc. IEEE Photonics Society Summer Topical Meeting Series*, July 2012, pp. 189–190.

[31] A. Bourdine, "Design of Refractive Index Profile for Multimode Optical Fibers with Low Differential Mode Delay," *Journal of Optoelectronics Engineering*, vol. 1, no. 1, pp. 5–13, March 2013.

[32] W. Press, S. Teukolsky, W. Vetterling, and B. Flannery, *Numerical recipes: The art of scientific computing*, 3rd ed. Cambridge University Press, 2007.

[33] P. Krawarik and L. Watkins, "Fiber geometry specifications and its relation to measured fiber statistics," *Applied Optics*, vol. 17, no. 24, pp. 3984–3989, December 1978.

[34] A. Bourdine, D. Praporshchikov, and K. Yablochkin, "Investigation of defects of refractive index profile of silica graded-index multimode fibers," in *Proc. of the SPIE*, vol. 7992, no. 799206, April 2010, pp. 1–6.

Chapter 5

Linear Transmission Impairments in FMFs

5.1 Introduction

The guidance of multiple modes in FMFs introduce linear impairments absent in SMFs: DMD and linear modal XT. The combined effect of DMD and linear XT spread the CIR over time, increasing the required equalization complexity compared to SMFs [1]. Recently, the minimization of the CIR spread along FMFs has been investigated considering random unitary XT matrices distributed along the FMFs [2, 3]. However, given that current experimental FMFs present weak distributed XT (dXT) (-30 dB/km to -40 dB/km in Table 2.2), the XT accumulated along transmission can be increased using discrete XT, introduced at specific points. In [4] it has been shown that ideal discrete mode permutation, without MDL, within the transmission line may effectively increase the maximum distance reach by a factor of 5. However, such conclusion was based on the statistics of MIMO outage capacity, ignoring DMD and available OSNR.

Another main limitation of MDM-FMF systems reducing their maximum distance reach is the MDL/MDG introduced by MMAs. Recent studies show efforts on reducing the MMAs MDG by tuning the modal pump power and the dopant distribution as explained in section 2.3.2. Even so, current designs of MMAs present significant MDG. Thereby, the development of methods to reduce the impact of MMAs MDG in system performance are desirable.

In this chapter, a practical method to implement discrete mode permutation based on displaced core fiber splices along the transmission fiber is proposed and

validated in section 5.2. As such splices introduce MDL, the transmission distance improvement is evaluated considering ultra-long-haul transmission simulations along ILD-FMFs and DC-FMFs, supporting 2M modes (LP_{01}, LP_{11a} and LP_{11b}). Additionally, in section 5.3 two alternative methods to reduce the penalty due to MMAs MDG, thereby extending the distance reach, using strong coupling modes and ML detection are presented. Conclusions are drawn in section 5.4.

The work presented along this chapter is based on the work reported in [5–7].

5.2 Reach Improvement using Fiber Splices

In the following, the different sources of linear XT and MDL considered in this section and respective models are presented. Additionally, a description of the simulation setup and a conceptual discussion about the principle behind the use of fiber splices for reach improvement are provided. Finally, the simulation results are presented, considering different numbers of splices per span with different levels of linear XT.

5.2.1 Concept Discussion and Simulation Setup

Linear XT and MDL

There are several sources of linear XT and MDL when considering transmission along FMFs: waveguide imperfections distributed along the fiber, fiber bends and fiber splices. The XT introduced by the waveguide imperfections and the fiber bends can be described as distributed XT (dXT) along the FMF, and the splice XT (sXT) can be considered as discrete XT introduced at a specific point of the link. Along this section, linear XT (sXT or accumulated dXT) is calculated as:

$$XT = \frac{P_{\mathrm{LP}_{11a}} + P_{\mathrm{LP}_{11b}}}{P_{\mathrm{LP}_{01}}} \tag{5.1}$$

where $P_{\mathrm{LP}_{11a}}$, $P_{\mathrm{LP}_{11b}}$ and $P_{\mathrm{LP}_{01}}$ are the powers of modes LP_{11a}, LP_{11b} and LP_{01}, respectively, after the fiber segment (or splice) under test, when only the LP_{01} was launched. The dXT is modeled using the work presented in section 3.2.1, where the fiber is divided into multiple sections each with a random displacement of the core axis position. Considering a fiber step of 200 m, the maximum radial displacement ($\rho_{d,max}$), have been tuned in order to match the experimental measurements presented

in [1], where the accumulated dXT at the end of 33 km was -18 dB. Additionally, MDL arising from the waveguide imperfections and bends is neglected according to the experimental measurements presented in [1, 8].

Regarding splices, the displacement of the fiber core breaks the orthogonality between the field spatial distributions of the modes, introducing sXT and MDL. Along this section, the transfer matrix of the splices has been computed through an overlap integral of the field distribution over the fiber cross section, except when it is said explicitly that the MDL is neglected. For those cases, the transfer matrix is calculated using the CMT presented in section 3.2.1 considering only the guided-modes. The splice loss (α_S) and the MDL are computed as described in [9]. Fig. 5.1 shows the sXT, α_S and MDL as functions of the radial displacement (ρ_d). Note that the difference between the sXT given by the overlap integral and by the CMT can be considered negligible. The refractive index profile considered to obtain the results in Fig. 5.1 (and along this section) is composed by a graded core and a cladding trench, since this profile proved to be capable of guaranteeing arbitrary DMD as shown in chapter 4. The results in Fig. 5.1 are for the case $DMD = 0$ ps/km. The variation of the sXT, MDL and α_S dependencies on displacement among the FMFs considered in this section are negligible.

In practical cases, the target sXT for each splice can be set during splicing. This can be achieved using state of the art fusion splicer machines, capable of introducing a fixed loss with a 0.01 dB step (for SMFs) through an intentional core axial offset, using a 0.01 µm stepper motor (less than 0.1 % of displacement in Fig. 5.1). Assuming such accuracy, variation of sXT in steps of 0.5 dB above -25 dB is expected.

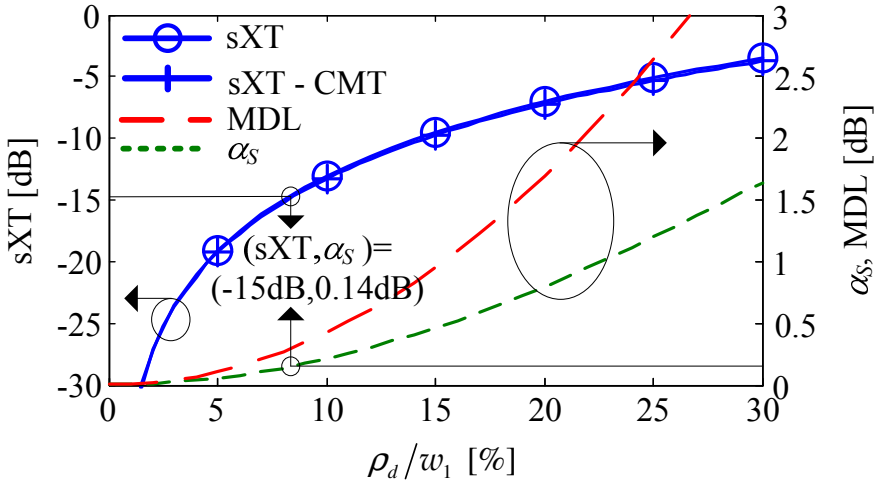

Figure 5.1: sXT, α_S, and MDL as a function of the core displacement.

Simulation Setup

The simulation setup described in section 3.4 is used in this section with particular characteristics specified in the following. Since the transmission simulations consider 2M-FMFs, the data-aided 6×6 MIMO DSP equalizer described in section 3.4 is used. In this case, TS with 4096 samples are considered allowing equalizing a maximum CIR length of approximately 15 ns. The channel estimation is based on the MMSE criterion.

The MMUXs/MDMUXs considered are based on spot couplers (described in section 2.3.1) modeled by an insertion loss of 5.2 dB, independently of the mode considered [10]. The MMA used is composed by three SM-EDFAs arranged between a MMUX and a MDMUX, as presented in section 2.3.2. The SM-EDFAs gains are set to guarantee that the launch power per mode at the output of the MMA is 5 dBm. Note that this amplifier structure allows the correction of the power imbalance due to MDL. The SM-EDFAs have a 5 dB noise figure.

The fiber span has a total length (L) of 80 km composed by m segments of equal length (L_s), each span with $2m-1$ splices. Two different configurations are considered to achieve low DMD transmission: ILD-FMFs shown in Fig. 5.2(a), and DC-FMFs shown in Fig. 5.2(b). An ILD-FMF segment is composed by two pieces of FMF of equal length and DMD equal to $lDMD$. A DC-FMF segment is composed by one positive DMD FMF with DMD equal to $pDMD$ and length L_p as well as by one negative DMD FMF with DMD equal to $nDMD$ and length L_n. The average DMD ($aDMD$) for the last segment type is:

$$aDMD = \frac{pDMD \cdot L_p + nDMD \cdot L_n}{L_s}. \tag{5.2}$$

The simulation considered $pDMD$ equal to 200 ps/km, $nDMD$ equal to -200 ps/km, $lDMD$ and $aDMD$ ranging from 0 to 9 ps/km (according to the experimental measurements presented in [8], [11]). The range for $lDMD$ and $aDMD$ takes into account practical cases of WDM signals where the DMD slope is non-negligible. The $aDMD$ was set changing L_p/L_n. The $lDMD$, $pDMD$ and $nDMD$ values of the respective FMFs were set through the optimization of the refractive index profile, as presented in section 4.2. The refractive index profile was optimized for an effective area of the LP_{01} mode of $\sim$200 μm^2, in order to guarantee that linear transmission along the FMF can be assumed with 5 dBm of launch power per mode [12]. Regarding the fiber loss, the value considered was 0.19 dB/km, independently of the mode considered, as

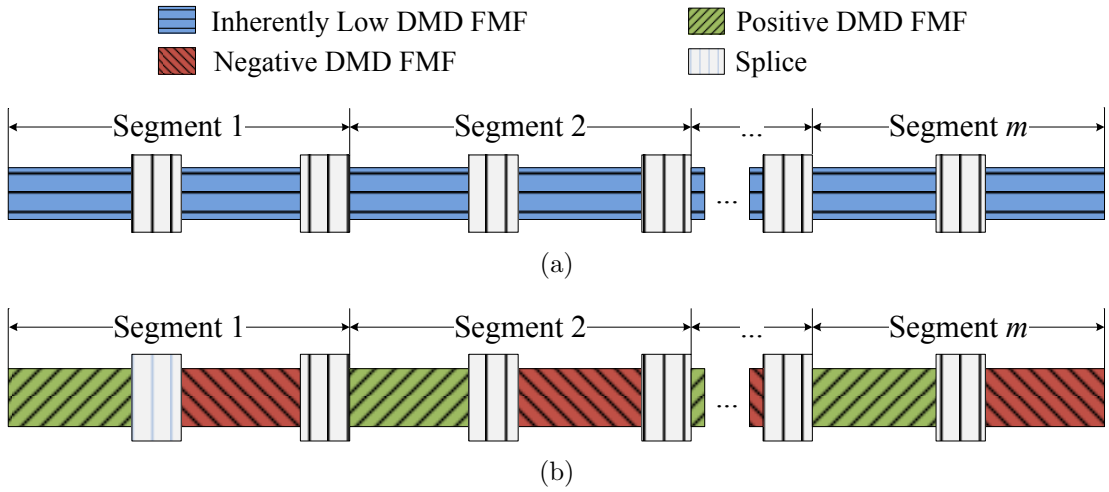

Figure 5.2: Span configuration: (a) ILD-FMF link and (b) DC-FMF link.

experimentally verified in [1, 8]. The polarization mode dispersion, dispersion and dispersion slope values are $1\,\mathrm{ps}/\sqrt{\mathrm{km}}$, $22\,\mathrm{ps/km/nm}$ and $0.06\,\mathrm{ps}/(\mathrm{nm}^2{\cdot}\mathrm{km})$, respectively, independently of the LP mode.

The figures of merit used to measure the performance of the transmission over a single wavelength of the C-band were: the ROSNR for $BER = 10^{-2}$ on the worst mode, and the available OSNR on the worst mode (determined by the launch power, the fiber losses, the MMUX/MDMUX losses, the splice MDL and the SM-EDFAs noise figure).

Conceptual Discussion

In the following the principle behind the use of fiber splices for reach improvement is explained, by analyzing the CIR time spread due to the combined effect of DMD and XT. The CIR provides a qualitative evaluation of the required equalizer complexity, particularly the time length of the CIR (CIR length), as the number of taps required to compensate correctly the transmission effects scales with the CIR length. The CIR is calculated using a MMSE estimator, obtaining the 36 impulse responses of the 6×6 MIMO channel. Afterwards, the CIR length is computed as the time interval containing 95 % of the power of the sum of the 36 impulse responses (less than 100 % in order to exclude the CIR points with very low amplitude, and thus negligible impact in the equalization) In order to evaluate the dependence of the CIR length on the transmission distance, Fig. 5.3(a) presents the CIR length for the span configuration in Fig. 5.2(a), with: $lDMD = 9\,\mathrm{ps/km}$, $m = 4$ and different levels of sXT introduced

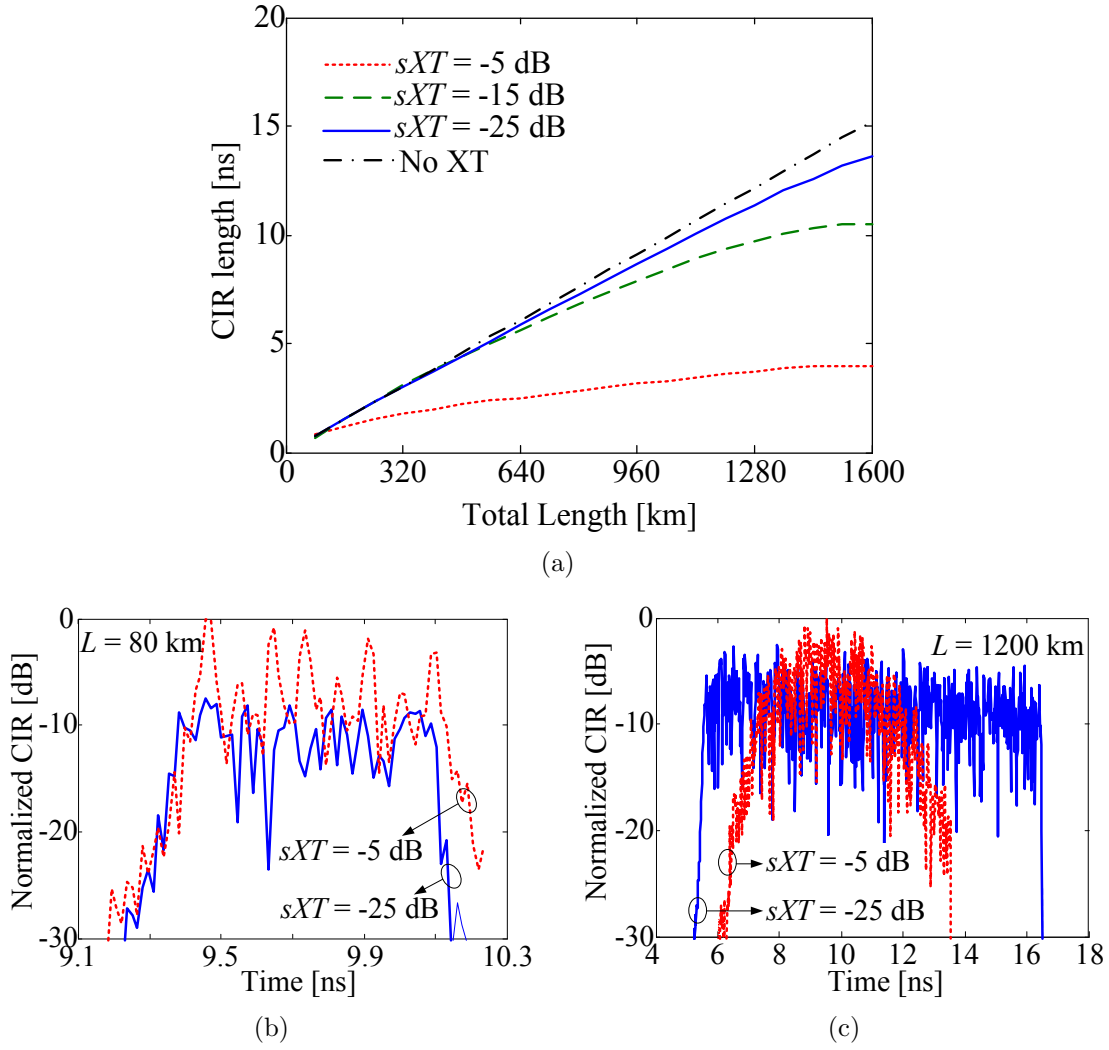

Figure 5.3: (a) CIR length as a function of fiber length, for $m = 4$ without splice MDL. Normalized CIR for $L = 80\,\text{km}$ (b) and $1200\,\text{km}$ (c).

by each splice, neglecting MDL. The purpose of neglecting the MDL at this point is to separate the two degrading effects discussed along this section: the MDL and the residual crosstalk due to a limited TS length. Fig. 5.3(a) shows that the CIR length scales almost linearly with transmission distance for $sXT = -25\,\text{dB}$ (consistent with the weak dXT), as can be concluded by comparing with the dashed line representing the CIR length in the absence of any form of XT. Increasing sXT, Fig. 5.3(a) shows that a higher transmission distance can be reached for the same CIR length, and thus for the same equalization complexity. To better understand this behavior, Fig. 5.3(b) and Fig. 5.3(c) shows the CIR for 80 km and 1200 km, respectively. For 80 km, the CIR length is almost the same for $sXT = -25\,\text{dB}$ and $-5\,\text{dB}$. However, for 1200 km, the CIR is clearly compressed for $sXT = -5\,\text{dB}$ compared to the case of $sXT = -25\,\text{dB}$.

This is explained by the extensive exchange of power between the different modes in the splices, which introduces an averaging effect of the group velocities of the respective modes, thereby reducing the increase rate of the CIR length. Note that, this method is applicable independently of the number of modes.

The analysis up to now considered the introduction of sXT by splices in the absence of MDL. However, for significant MDL levels the fiber transfer function is no longer unitary, degrading the DSP equalizer performance [6]. Since sXT, σ_S and MDL increase simultaneously with ρ_d, see Fig. 5.1, there is an optimal sXT value (m dependent) for which the penalty due MDL equals the gain due to sXT. This is analyzed in section 5.2.2 for MDM systems with 3 modes. For more than 3 modes, the optimum sXT and m are expected to vary due to the MDL impact.

5.2.2 Simulation Results

Inherently Low DMD FMF

In order to understand the impact of the proposed method on the distance reach of the span configuration presented in Fig. 5.2(a), the ROSNR and available OSNR are analyzed first. Fig. 5.4 shows the OSNR results for $lDMD = 9\,\text{ps/km}$ and different m values: (a) $m = 2$ and (b) $m = 8$. In Fig. 5.4(a) and Fig. 5.4(b) it can be seen that, by increasing sXT, higher distances can be reached for the same ROSNR due to a reduction of the CIR spread, except for $m = 8$ and $sXT = -10\,\text{dB}$. In the latter case, the performance degradation is justified by the increase of MDL, since this is the only source of penalty increasing from $m = 2$ to $m = 8$ and no penalty is visible for $m = 2$ and $sXT = -10\,\text{dB}$. Additionally it can be seen that, by increasing m and/or sXT, the available OSNR decreases, which is due to the increase of the α_S and MDL per splice and/or number of splices per span. The distance reach is calculated from Fig. 5.4, taking into account the intersection of the ROSNR curves with the available OSNR curves or with the OSNR limit (defined as a the maximum ROSNR penalty of 3 dB for back-to-back). The definition of an ROSNR penalty limit aims the exclusion of signals which are too degraded.

Fig. 5.5 shows the distance reach as a function of (sXT, α_S) given by Fig. 5.1, for different $lDMD$ values and different m values. All curves in Fig. 5.5 can be decomposed in three different regions. In the first region (low sXT values with negligible α_S values), the distance reach does not vary with m or sXT, which means that the splices do not have impact on the performance, for the evaluated cases. The

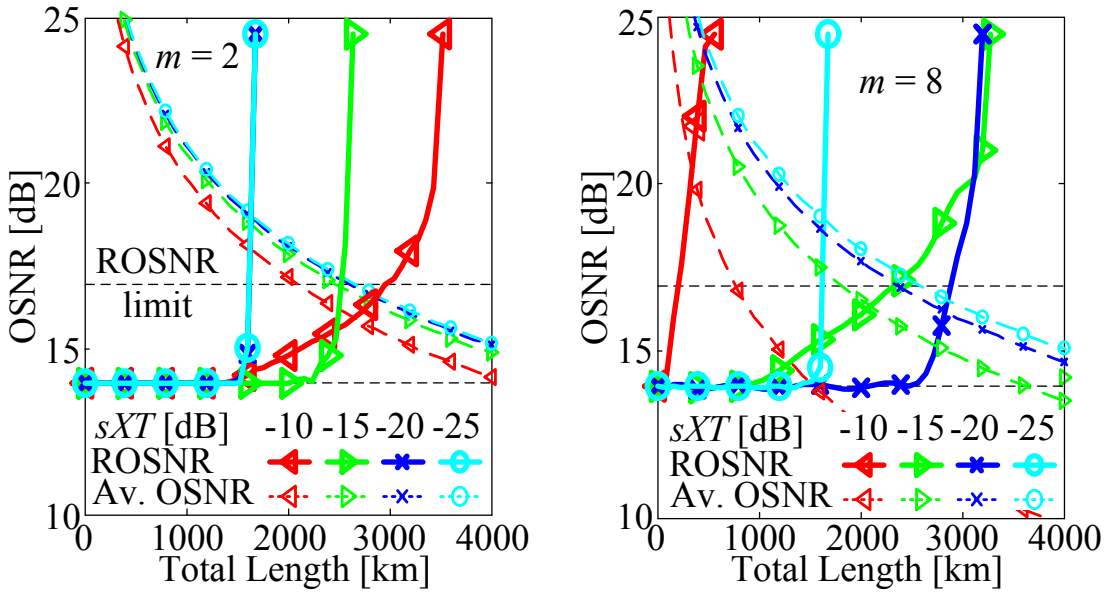

(a) (b)

Figure 5.4: ROSNR and available OSNR for the ILD-FMF link as a function of total length.

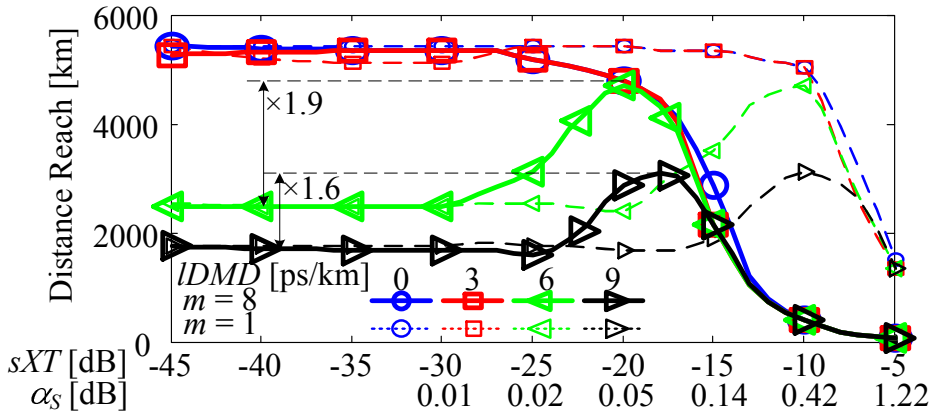

Figure 5.5: Distance reach for the ILD-FMF link as a function of (sXT, α_S).

distance reach is determined by the available OSNR (∼13.95 dB at ∼5500 km) for $lDMD \leq 3$ ps/km, and by the maximum CIR length (15 ns) for $lDMD > 3$ ps/km. For $lDMD > 3$ ps/km, the distance reach is given by 15 ns/$lDMD$ (meaning that the impact of dXT and sXT is negligible). In the second region (moderate sXT values with low α_S values), distance reach increases due to the sXT averaging effect (see section 5.2.1). For $lDMD > 3$ ps/km there is an increase by a factor from 1.6 to 1.9. However, for $lDMD \leq 3$ ps/km there is no distance reach increase since the performance is determined by the available OSNR (there would be an increase if the span

losses were reduced). Note that the sXT value corresponding to the maximum distance reach decreases with increasing m, since for a higher number of splices less sXT per splice is needed for the same CIR length reduction. In the third region (high sXT values with high α_S values), $sXT > -15\,\text{dB}$ in the $m = 8$ case and $sXT > -5\,\text{dB}$ in the $m = 1$ case, the distance reach decreases due to the high α_S and MDL values (see section 5.2.1) for any $lDMD$ value.

In practice, some fluctuation of the sXT obtained through splicing is expectable. Further results have shown that, when considering sXT following a Gaussian distribution with a standard deviation of 0.5 dB (see section 5.2.1), the distance gain remained nearly the same as for the same average (optimum) sXT.

DMD compensated FMF

In this sub-section the performance of the span configuration shown in Fig. 5.2(b) is analyzed. Fig. 5.6 shows the distance reach as a function of (sXT, α_S) given by Fig. 5.1, for different $aDMD$ and m values, calculated considering a methodology similar to the one used in section 5.2.2. The distance reach results in Fig. 5.6 for $m = 8$ are similar to the results in Fig. 5.5 for $m = 8$, with the same limiting effects. The distance reach increase factors for $m = 8$, are 1.9 for $aDMD = 6\,\text{ps/km}$ and 1.6 for $aDMD = 9\,\text{ps/km}$. However, for $m = 1$, increasing sXT only leads to an increased CIR length and consequent shorter distance reach, independently of the $aDMD$ value. The difference of performance between $m = 1$ and $m = 8$ is present even for negligible sXT (particularly for $aDMD = 3\,\text{ps/km}$). This is explained due to the presence of dXT [8] and consequent exchange of a fraction of power between the modes for which there is an excess accumulation of DMD in each segment (in comparison to $N \cdot L \cdot aDMD$, when absence of XT is considered). For the fraction of power exchange around the middle of the segment, the accumulated DMD in one segment can reach $\pm[|pDMD| \cdot L_p + |nDMD| \cdot L_n]$. For $m = 1$, accumulated DMD can reach 16 ns in one segment, a value above the maximum CIR length. On the other hand, for $m = 8$, the maximum accumulated DMD can reach only 2 ns in one segment. Therefore, for the DC-FMF case, m should be high, even for perfect splices. Finally, it can be concluded that reducing the maximum accumulated DMD over one segment to a low fraction (around 13 %) of the compensation time interval provided by the TS, the impact of $aDMD$ can be reduced by increasing the sXT as in the ILD-FMF case. Note that, concerning the eventual sXT fluctuations in practice, the comments for Fig. 5.5 apply also for Fig. 5.6.

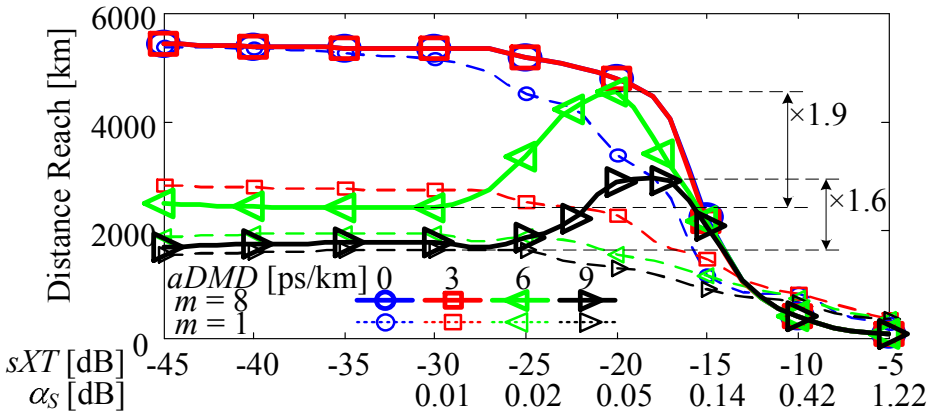

Figure 5.6: Distance reach for the DC-FMF link as a function of (sXT, α_S).

5.3 Alternative Reach Improvement Methods

In this section two alternative methods to extend the maximum reach of MDM-FMF systems using strong coupling modes (high dXT) and maximum-likelihood detection are presented. However, instead of reducing the CIR response spread, these methods aim to reduce the impairments due to MMAs MDG. All the results in this section have been obtained in collaboration with Ph.D. student Adriana Lobato (responsible for the development and implementation of the receiver), details can be find in [6, 7].

5.3.1 High Distributed Linear XT

The introduction of intentional perturbations during the FMF drawing is being considered to enhance dXT [13], analogous to the spinning used to reduce PMD in SMFs. In this sub-section, the impact of high dXT on the penalty due to MDG from MMAs is studied. The simulation setup in section 5.2 is used again, considering the 2M-ILD-FMF optimized in section 4.2 for $DMD = 9\,\text{ps/km}$. To generate low and high dXT, the maximum allowed core displacement used is 0.6 % and 4.7 % of the core radius, respectively. The average accumulated linear XT at the end of 80 km are $-20.6\,\text{dB}$ and $-1.25\,\text{dB}$, for low and high dXT, respectively. The introduction of MDG is simulated considering a MMA composed by three SM-EDFAs arranged as in Fig. 2.11 with a gain offset (G_{offset}) between the LP_{01} and the LP_{11} (LP_{11a} and LP_{11b} have the same gain). To evaluate the impact of MDG different values of G_{offset} were considered.

Fig. 5.7 shows the ROSNR penalty with respect to the back-to-back configuration with a BER of 10^{-3} as a function of the distance for low and high dXT, considering

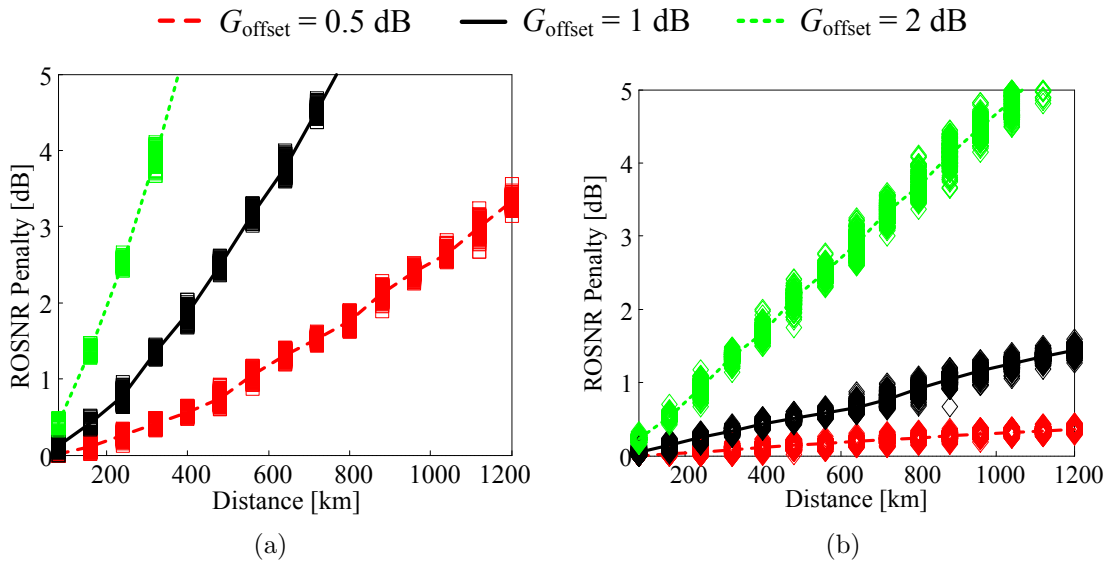

Figure 5.7: ROSNR penalty for different G_{offset} with: (a) low and (b) high dXT as a function of the transmission distance.

different G_{offset} magnitudes (0.5 dB, 1 dB, and 2 dB per span). The ROSNR penalty results have been averaged over the three spatial modes. Furthermore, since the channel transfer function is a random variable due to the random core displacement, the results of 200 channel realizations are represented with each one of the markers in the figure. The dashed and the solid lines show the average over these 200 channel realizations. As Fig. 5.7 shows, the ROSNR penalty increases with both distance and G_{offset}. In addition, it can be observed that for low dXT the ROSNR penalty is higher than in the high dXT case. Allowing an ROSNR penalty of 1 dB, high dXT provide 120 km and 580 km more reach in comparison to low dXT for a G_{offset} of 1 dB and 2 dB, respectively. For a G_{offset} of 0.5 dB, no ROSNR penalties are observable at 1 dB until 1200 km. In the high dXT regime the power exchange averages the loss per mode, which reduces the overall impact of MDG on the system performance. Thanks to high dXT and the rapidly power interchange among the modes, the loss/gain per mode averages over all modes, leading to a higher MDG/MDL tolerance compared to low dXT propagation.

5.3.2 Maximum-Likelihood Detection

In this sub-section, ML detection is used to reduce the MDG penalty in a 3×158 Gb/s PDM-QPSK orthogonal frequency division multiplexing (OFDM) MDM-FMF system. From a total of 4096 OFDM subcarriers, 81.2 % of the subcarriers are dedicated to

the actual payload and the remaining 18.8 % are used for zero-padding. An overhead of 24 % for forward error correction and Ethernet, 10 % for TS and 16.1 % for cyclic prefix (CP) was added, which results in a total gross bit rate of 475 Gbit/s. The simulation setup in section 5.3.1 is used again with exception for the modulation format and detection scheme. In the following, ML detection is compared to ZF and MMSE equalization in terms of performance for both low and high dXT.

Fig. 5.8 shows the performance of the ML detector, ZF and MMSE equalizers in terms of ROSNR penalty as a function of the distance for both low and high dXT, considering different G_{offset} magnitudes (0.5 dB, 1 dB, and 2 dB per span). The

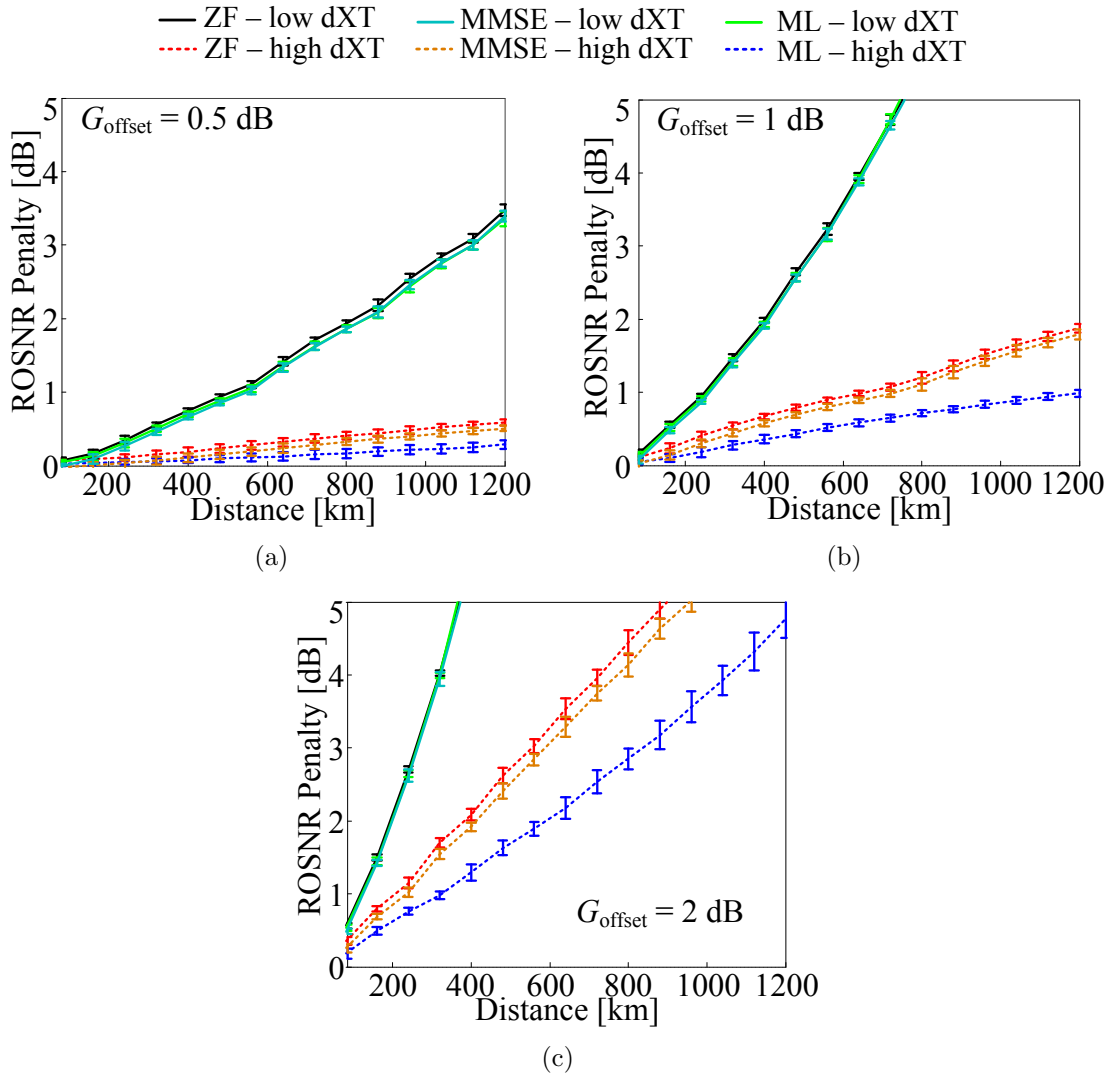

(a) (b) (c)

Figure 5.8: Average and +/ standard deviation (vertical lines) of the ROSNR penalty at a BER of 10^{-3}, ML detection, ZF, and MMSE equalization, low and high dXT and G_{offset} of (a) 0.5 dB, (b) 1 dB, and (c) 2 dB per span.

ROSNR penalty is measured with respect to the back-to-back configuration for a BER of 10^{-3}. As the channel transfer function is a random variable, 200 channels realizations were simulated. The vertical lines in Fig. 5.8 correspond to two times the standard deviation of the ROSNR penalty. As shown in section 5.3.1, Fig. 5.8 confirms that high dXT increases the MDG tolerance. In Fig. 5.8, it can also be observed that for low dXT there is almost no difference between ZF, MMSE equalization and ML detection. Fig. 5.8 also shows that MMSE outperforms the ZF equalization with a small difference of 11 % (1 dB per span of G_{offset}) and 12 % (2 dB per span of G_{offset}), comparing the average reach at 1 dB of ROSNR penalty. In contrast, for all values of G_{offset} and high dXT, the MDL penalty is significantly reduced by ML detection. At 1 dB of ROSNR penalty, the ML detector improves the maximum feasible transmission distance by 84 % (1 dB per span of G_{offset}) and 60 % (2 dB per span of G_{offset}). For a G_{offset} of 0.5 dB per span and high dXT, the ROSNR penalty does not reach 1 dB penalty until 1200 km for all studied receiver schemes.

5.4 Conclusions

Along this chapter, three methods to extend the reach of MDM-FMF systems were shown. The first based on displaced core fiber splices aimed to reduce the CIR spread and the remaining two aimed to reduce the penalty due to MDG from MMAs.

In section 5.2, it was proposed and proved that the introduction of fiber splices allows the improvement of the distance reach of MDM transmission systems. The concept was applied to ultra-long-haul transmission over ILD-FMFs and DC-FMFs. The optimum number of segments/splices per span and respective XT values were determined taking into account the consequent MDL. The results show that the distance reach can be increased by a factor from 1.6 to 1.9 for the considered transmission systems. Additionally the results show that, for the case of DC-FMFs, the distance reach can be improved just by increasing the number of segments per span, even for negligible splices XT.

In section 5.3, ML detection, ZF and MMSE equalization were compared in the presence of MDG for low and high dXT. It was shown that high dXT increases the MDG tolerance for any of the equalization and detection schemes considered. Furthermore, it was shown that ML detection significantly outperforms the ZF and MMSE equalizers in the case of high dXT. In contrast, for low dXT, all DSP schemes showed similar performance.

References

[1] R. Ryf, R. Essiambre, J. Hoyningen-Huene, and P. Winzer, "Analysis of mode-dependent gain in Raman amplified few-mode fiber," in *Proc. Optical Fiber Communication Conference and Exposition*, March 2012, p. OW1D.2.

[2] K. Ho and J. Kahn, "Statistics of Group Delays in Multimode Fiber With Strong Mode Coupling," *IEEE/OSA Journal of Lightwave Technology*, vol. 29, no. 21, pp. 3119–3128, November 2011.

[3] S. Arik, D. Askarov, and J. Kahn, "Effect of Mode Coupling on Signal Processing Complexity in Mode-Division Multiplexing," *IEEE/OSA Journal of Lightwave Technology*, vol. 31, no. 3, pp. 423–431, February 2013.

[4] S. Warm and K. Petermann, "Splice loss requirements in multi-mode fiber mode-division-multiplex transmission links." *Optics Express*, vol. 21, no. 1, pp. 519–532, January 2013.

[5] F. Ferreira, D. Fonseca, A. Lobato, B. Inan, and H. Silva, "Reach Improvement of Mode Division Multiplexed Systems Using Fiber Splices," *IEEE Photonics Technology Letters*, vol. 25, no. 12, pp. 1091–1094, June 2013.

[6] A. Lobato, F. Ferreira, M. Kuschnerov, D. van den Borne, S. Jansen, A. Napoli, B. Spinnler, and B. Lankl, "Impact of mode coupling on the mode-dependent loss tolerance in few-mode fiber transmission," *Optics Express*, vol. 20, no. 28, pp. 29 776–29 783, December 2012.

[7] A. Lobato, F. Ferreira, B. Inan, S. Adhikari, M. Kuschnerov, A. Napoli, B. Spinnler, and B. Lankl, "Maximum-Likelihood Detection in Few-Mode Fiber Transmission With Mode-Dependent Loss," *IEEE Photonics Technology Letters*, vol. 25, no. 12, pp. 1095–1098, June 2013.

[8] L. Grüner-Nielsen, Y. Sun, J. Nicholson, D. Jakobsen, R. Lingle, and B. Palsdottir, "Few mode transmission fiber with low DGD, low mode coupling and low loss," in *Proc. Optical Fiber Communication Conference and Exposition*, March 2012, pp. 1–3.

[9] P. Winzer and G. Foschini, "MIMO capacities and outage probabilities in spatially multiplexed optical transport systems." *Optics Express*, vol. 19, no. 17, pp. 16 680–16 696, August 2011.

[10] R. Ryf, M. Mestre, A. Gnauck, S. Randel, C. Schmidt, R. Essiambre, P. Winzer, R. Delbue, P. Pupalaikis, and A. Sureka, "Low-loss mode coupler for mode-multiplexed transmission in few-mode fiber," in *Proc. Optical Fiber Communication Conference and Exposition*, March 2012, p. PDP5B.5.

[11] M. Li, B. Hoover, S. Li, S. Bickham, S. Ten, E. Ip, Y. Huang, E. Mateo, Y. Shao, and T. Wang, "Low delay and large effective area few-mode fibers for mode-division multiplexing," in *Proc. OptoElectronics and Communications Conference*, 2012, pp. 495–496.

[12] F. Ferreira, S. Jansen, P. Monteiro, and H. Silva, "Nonlinear Semi-Analytical Model for Simulation of Few-Mode Fiber Transmission," *IEEE Photonics Technology Letters*, vol. 24, no. 4, pp. 240–242, February 2012.

[13] L. Palmieri and A. Galtarossa, "A preliminary analysis of spin in few-mode optical fibers," in *Proc. European Conference and Exhibition on Optical Communication*, September 2013, p. P.1.3.

Chapter 6

Nonlinear Transmission Impairments in FMFs

6.1 Introduction

MDM over FMFs has been proposed as a next-generation solution to overcome the impeding installed capacity exhaustion of current SMFs [1]. An N-fold capacity increase is obtained using a FMF with N independent modes. However, the guidance of multiple modes introduces impairments absent in SMFs, namely: DMD [2–6], linear modal XT [7–9] and IM-NL effects [10–15]. The IM-NL effects are IM-XPM and IM-FWM.

Several experimental and theoretical FMFs guiding 3 LP modes with DMD values suitable for long-haul transmission have been presented in recent years [2–6]. In [6], it has been shown how to design FMFs with up to 12 non-degenerate LP modes suitable for long-haul applications, by optimizing the refractive index profile composed by a graded core and a cladding trench. The interplay between DMD and linear XT (distributed or discrete) has also been investigated, showing that high XT levels can reduce the spread of the channel impulse response [7–9]. In [5], a practical technique for the introduction of discrete linear XT using displaced core fiber splices has been presented. For the case of NL effects, recent experimental investigations regarding propagation along FMFs have shown that IM-NLs are non-negligible, namely IM-XPM [10] and IM-FWM [11]. In [10], IM-XPM has been observed through a pump-probe scheme with a pump intensity modulated at 10 Gb/s using a GI-FMF and it was verified that the IM-XPM magnitude is comparable to intra-modal XPM. In [11], non-degenerate IM-FWM has been experimentally observed, demonstrating

that IM-FWM can be fully matched over very large frequency separations with large chromatic dispersion in each mode. Several theoretical investigations of NL transmission in FMFs have also been presented [12–15]. In [14], a generalization of Manakov equations for FMFs was presented. However, in order to correctly model the IM-NL process between degenerate modes, linear XT must be considered, as concluded in [14]. More importantly, an analytical framework allowing to find IM-XPM and IM-FWM independent penalties is required to study their effect in MDM-FMF systems carrying WDM signals. In this chapter, a set of MM-MW-CNLSE with $2 \times M \times (N+1)$ equations (2 orthogonal polarizations per mode, M modes and $N+1$ WDM channels per mode) is derived taking into consideration the existence of XT between modes. Such set of MM-MW-CNLSE allows designing MDM-WDM-FMF systems to minimize the degradation due to IM-XPM and IM-FWM.

The chapter is organized as follows. In Section 6.2, a set of MM-MW-CNLSE for MDM-WDM-FMF systems including linear XT is derived, extending the work that has been presented in [15]. In the MM-MW-CNLSE derivation, the NL processes among the WDM channels have been separated, namely: SPM, XPM, FWM, IM-XPM, and IM-FWM. Note that SPM, XPM, and FWM refer to the intra-modal NL effects present in conventional SMF systems. In Section 6.3, the MM-MW-CNLSE are validated using experimental results reported in [10] and [11] for a GI-FMF. Section 6.4 presents the assessment of the degradation for MDM-WDM-FMF transmission due to IM-XPM and IM-FWM. The main conclusions are gathered in Section 6.5.

The work presented along this chapter is based on the work reported in [16].

6.2 MM-MW-CNLSE Derivation

In order to find the nonlinear terms responsible for IM-NL among channels of a given set, the total electric field has to be written as a sum over u distinct modes, v distinct frequencies and i orthogonal polarizations, with $u = \{1, \ldots, M\}$, $v = \{-N/2, \ldots, N/2\}$ (with N even), and $i = \{1, 2\}$ ($i = 1$ refers to x-polarization and $i = 2$ refers to y-polarization). Each mode is considered to guide the same $N + 1$ wavelengths with N even, without lack of generality. The total electric field vector in the frequency domain is given by:

$$\begin{aligned}\widetilde{\mathbf{E}}(\mathbf{r},\omega) &= \frac{1}{2}\widetilde{E}_x(\mathbf{r},\omega)\,\widehat{x} + \frac{1}{2}\widetilde{E}_y(\mathbf{r},\omega)\,\widehat{y} + c.c. \\ &= \sum_{uvi}\left[\frac{1}{2}\frac{F_u(x,y)}{\sqrt{N_u}}\widetilde{A}_{uvi}(z,\omega-\omega_v)\exp\left(-\mathrm{j}\beta_{0,uvi}z\right)\widehat{i} + c.c.\right]\end{aligned} \tag{6.1}$$

where $\mathbf{r}$ is the position vector in Cartesian coordinates (x, y, z), ω is the optical angular frequency, $\widehat{i}$ is the unit linear polarization vector, j is the imaginary unit, $\sum_{uvi} = \sum_{u=1}^{M}\sum_{v=-N/2}^{N/2}\sum_{i=1}^{2}$, $\widetilde{A}_{uvi}(z,\omega-\omega_v)$ is the Fourier transform of the slowly varying wave envelope $A_{uvi}(z,t)$ ($\tilde{A}_{uvi}(z,\omega) = \int_{-\infty}^{+\infty} A_{uvi}(z,t)\exp(-\mathrm{j}\omega t)dt$, where t is the time variable), $F_u(x,y)$ is the transversal field distribution of u, $N_u = \iint_{-\infty}^{+\infty}|F_u(x,y)|^2 dxdy$ such that $|A_{uvi}(z,t)|^2$ is the instantaneous optical power, $\beta_{0,uvi}$ is the value of the frequency dependent propagation constant $\beta_{ui}(\omega)$ at ω_v, and c.c. stands for complex conjugate. Note that in (6.1), $F_u(x,y)$ is assumed to vary negligibly with polarization and ω within the C-band as well as with small waveguide imperfections and the nonlinear induced polarization [17]. $F_u(x,y)$ and $\beta_{ui}(\omega)$ are solutions of the eigenvalue equation [17]:

$$\nabla^2 F_u(x,y) + \left[\omega^2\mu_0\varepsilon_p(x,y) - \beta_{ui}^2(\omega)\right]F_u(x,y) = 0 \tag{6.2}$$

where μ_0 is the permeability of free space and $\varepsilon_p(x,y)$ is the transverse permittivity of the optical fiber. $\beta_{ui}(\omega)$ can be expanded in a Taylor series around ω_v as:

$$\beta_{ui}(\omega) = \beta_{0,uvi} + \beta_{1,uvi}\Delta\omega + \frac{\beta_{2,uvi}}{2}(\Delta\omega)^2 + \frac{\beta_{3,uvi}}{6}(\Delta\omega)^3 + \ldots \tag{6.3}$$

where $\Delta\omega = \omega - \omega_v$ and $\beta_{m,uvi} = \partial_\omega^m \beta_{ui}|_{\omega=\omega_v}$ ($m = 1, 2, \ldots$). The Taylor series in (6.3) is usually truncated, retaining the terms up to third order. $\beta_{1,uvi}$ is the inverse of the

group velocity (group delay per unit length) of ui at ω_v. Thus, the DMD between the $u_1 i_1$ and ui at ω_v is defined as:

$$DMD_{u_1 v i_1, uvi} = \beta_{1,u_1 v i_1} - \beta_{1,uvi} \tag{6.4}$$

$\beta_{2,uvi}$ can be written as a function of the chromatic dispersion (D) of ui at ω_v (D_{uvi}), as:

$$\beta_{2,uvi} = -\frac{\lambda_v^2}{2\pi c_0} D_{uvi} \tag{6.5}$$

where $\lambda_v = 2\pi c_0/\omega_v$ and c_0 is the light velocity in free space. $\beta_{3,uvi}$ can be written as a function of D_{uvi} and of the chromatic dispersion slope (S) of ui at ω_v (S_{uvi}), as:

$$\beta_{3,uvi} = \left(\frac{\lambda_v}{2\pi c_0}\right)^2 \left(\lambda_v^2 S_{uvi} + 2\lambda_v D_{uvi}\right) \tag{6.6}$$

The propagation of the total electric field in a FMF is governed by the wave equation [17]:

$$\nabla^2 \widetilde{\mathbf{E}}(\mathbf{r},\omega) = -\omega^2 \mu_0 \varepsilon_p(x,y)\, \widetilde{\mathbf{E}}(\mathbf{r},\omega) - \omega^2 \mu_0 \widetilde{\mathbf{P}}_{NL}(\mathbf{r},\omega) \tag{6.7}$$

where $\widetilde{\mathbf{P}}_{NL}(\mathbf{r},\omega)$ is the Fourier transform of the nonlinear polarization due to the third-order nonlinear silica susceptibility $\mathbf{P}_{NL}(\mathbf{r},t)$. In order to include in (6.7) the linear XT due to small waveguide imperfections along the fiber, $\varepsilon_p(x,y)$ is replaced by $\varepsilon(x,y) = \varepsilon_p(x,y) + \Delta\varepsilon(x,y)$, where $\Delta\varepsilon(x,y)$ varies randomly in each fiber section [9, 18]. In a birefringent fiber, the orthogonal polarization components of $\mathbf{P}_{NL}(\mathbf{r},t)$, $P_{NL_x}(\mathbf{r},t)$ and $P_{NL_y}(\mathbf{r},t)$, can be written as functions of $\mathbf{E}(\mathbf{r},t)$ orthogonal polarization components, $E_x(\mathbf{r},t)$ and $E_y(\mathbf{r},t)$. Omitting the dependence on $(\mathbf{r},t)$, P_{NL_x} and P_{NL_y} are written as [17]:

$$P_{NL_i} = \frac{3}{4}\varepsilon_0 \chi^{(3)}_{xxxx} \left[\left(|E_i|^2 + \frac{2}{3}|E_j|^2\right) E_i + \frac{1}{3}\left(E_i^* E_j\right) E_j\right] \tag{6.8}$$

where $(i,j) = (x,y)$ or $(i,j) = (y,x)$, ε_0 is the permittivity of free space and $\chi^{(3)}_{xxxx}$ is the third-order silica susceptibility [17].

The wave equation (6.7) can be solved replacing (6.1)-(6.3) and applying the inverse Fourier transform. Considering the slowly varying envelope approximation (in

space and time) [17], and omitting the dependence of A_{uvi} on (z,t), F_u on (x,y) and $\Delta\varepsilon$ on (x,y), the CNLSE is given by:

$$\begin{aligned}
&\sum_{uv}\left[\left(\partial_z+\mathfrak{D}\right)A_{uvi}\right]\frac{\beta_{uvi}F_u}{\sqrt{N_u}}\exp\left[\mathrm{j}\left(\omega_v t-\beta_{0,uvi}z\right)\right]= \\
&-\mathrm{j}\frac{3}{8}\varepsilon_0\mu_0\chi^{(3)}_{xxxx}\cdot\sum_{u_1v_1i_1}\sum_{u_2v_2i_2}\sum_{u_3v_3i_3}\left[\begin{array}{l}\xi_{i_1i_2i_3i}(\omega_{v_1}+\omega_{v_2}-\omega_{v_3})^2\cdot \\ \dfrac{F_{u_1}F_{u_2}F^*_{u_3}}{\sqrt{N_{u_1}N_{u_2}N_{u_3}}}A_{u_1v_1i_1}A_{u_2v_2i_2}A^*_{u_3v_3i_3}\cdot \\ \exp\left[\begin{array}{l}\mathrm{j}\left(\omega_{v_1}+\omega_{v_2}-\omega_{v_3}\right)t- \\ \mathrm{j}\left(\beta_{0,u_1v_1i_1}+\beta_{0,u_2v_2i_2}-\beta_{0,u_3v_3i_3}\right)z\end{array}\right]\end{array}\right] \\
&-\mathrm{j}\frac{1}{2}\mu_0\Delta\varepsilon\sum_{u_1v_1i_1}\omega^2_{v_1}A_{u_1v_1i_1}\frac{F_{u_1}}{\sqrt{N_{u_1}}}\exp\left[\mathrm{j}\left(\omega_{v_1}t-\beta_{0,u_1v_1i_1}z\right)\right]
\end{aligned} \tag{6.9}$$

with:

$$\mathfrak{D}=\beta_{1,uvi}\partial_t-\mathrm{j}\frac{\beta_{2,uvi}}{2}\partial_t^2-\frac{\beta_{3,uvi}}{6}\partial_t^3 \tag{6.10}$$

$$\xi_{i_1i_2i_3i}=\delta_{i_1i}\delta_{i_2i}\delta_{i_3i}+\frac{2}{3}\delta_{i_1i}\delta_{i_2j}\delta_{i_3j}+\frac{1}{3}\delta_{i_1j}\delta_{i_2j}\delta_{i_3i} \tag{6.11}$$

where * stands for complex conjugate, and $\xi_{i_1i_2i_3i}$ groups the independent polarization combinations using the Kronecker delta function defined such that $\delta_{i_1i}=1$ when $i_1=i$ and zero otherwise. The operator $\mathfrak{D}$ on the LHS of (6.9) is responsible by chromatic dispersion and DMD. The first term on the RHS of (6.9) is responsible by all the NL effects taking place between the $2\times M\times(N+1)$ waves. The second term on RHS of (6.9) is responsible by the linear XT. From (6.9), a set of CNLSE per mode can be derived, multiplying both sides by F^*_u and integrating over the x-y transverse plane. Afterwards, a set of CNLSE per wavelength and per mode can be obtained by selecting the terms oscillating at each specific frequency ω_v. In order to select the terms oscillating at ω_v in the first term on RHS of (6.9), the following frequency condition must be fulfilled:

$$\omega_{v_1}+\omega_{v_2}-\omega_{v_3}-\omega_v=0 \tag{6.12}$$

The MM-MW-CNLSE obtained is:

$$\begin{aligned}\partial_z A_{uvi} + \mathfrak{D} A_{uvi} + \frac{\alpha_{uvi}}{2} A_{uvi} = \\ - \mathrm{j} \sum_{u_1 v_1 i_1} \sum_{u_2 v_2 i_2} \sum_{u_3 v_3 i_3} \left[\begin{matrix} \xi_{i_1 i_2 i_3 i} \gamma_{u_1 u_2 u_3 u} A_{u_1 v_1 i_1} A_{u_2 v_2 i_2} A^*_{u_3 v_3 i_3} \cdot \\ \exp\left(-\mathrm{j} \Delta\beta_{uv_1 i_1, uv_2 i_2, uv_3 i_3, uvi} z\right) \end{matrix} \right] \\ - \mathrm{j} \sum_{u_1 i_1} C_{uvi, u_1 v i_1} A_{u_1 v i_1} \exp\left[\mathrm{j}\left(\beta_{0,uvi} - \beta_{0,u_1 v i_1}\right) z\right]\end{aligned} \tag{6.13}$$

with:

$$\Delta\beta_{u_1 v_1 i_1, u_2 v_2 i_2, u_3 v_3 i_3, uvi} = \beta_{0,u_1 v_1 i_1} + \beta_{0,u_2 v_2 i_2} - \beta_{0,u_3 v_3 i_3} - \beta_{0,uvi} \tag{6.14}$$

$$\gamma_{u_1 u_2 u_3 u} = \frac{n_2 \omega_v}{c_0 A^{eff}_{u_1 u_2 u_3 u}} \tag{6.15}$$

$$A^{eff}_{u_1 u_2 u_3 u} = \frac{\sqrt{N_{u_1} N_{u_2} N_{u_3} N_u}}{\iint F_{u_1} F_{u_2} F^*_{u_3} F^*_u dxdy} \tag{6.16}$$

$$n_2 \approx \frac{3}{8} \frac{\sqrt{\varepsilon_0 \mu_0}\, \chi^{(3)}_{xxxx}}{\beta_{0,uvi}} \omega_{uvi} \tag{6.17}$$

$$C_{uvi, u_1 v i_1} = \frac{\omega_v^2 \mu_0}{2\beta_{0,uvi}} \iint \Delta\varepsilon\,(x,y)\, \frac{F^*_u \cdot F_{u_1}}{\sqrt{N_u N_{u_1}}} dxdy \tag{6.18}$$

where α_{uvi} is the attenuation of uvi included in a perturbation manner [17], (6.14) is the phase mismatch between waves $u_1 v_1 i_1$, $u_2 v_2 i_2$, $u_3 v_3 i_3$ and uvi, (6.15) is the nonlinear coefficient between modes u_1,u_2,u_3 and u, (6.16) is the IM effective area (A^{eff}) of mode combination (u_1, u_2, u_3, u), (6.17) is the Kerr coefficient, approximately equal to $2.6 \cdot 10^{-20}\,\mathrm{m}^2/\mathrm{W}$ [17], and (6.18) is the linear XT coupling coefficient between mode u and mode u_1. The MM-MW-CNLSE in (6.13) can be simplified considering $A^{eff}_{u_1 u_2 u_3 u}$ properties. $A^{eff}_{u_1 u_2 u_3 u}$ is non-zero only when one or two distinct modes are involved, given the modes orthogonality. In case only one mode u is involved ($u_1 = u_2 = u_3 = u$) the NL effects present are: SPM, XPM and FWM (as in case of transmission over SMF). In case two distinct modes a and b are involved, the NL effects present are IM-XPM and IM-FWM, and the possible mode matching conditions for IM-NL terms falling in $u = a$ are:

$$u_1 = a, u_2 = b, u_3 = b, u = a \tag{6.19}$$

$$u_1 = b, u_2 = a, u_3 = b, u = a \tag{6.20}$$

$$u_1 = b, u_2 = b, u_3 = a, u = a \tag{6.21}$$

Mode matching conditions (6.19) and (6.20) may generate IM-XPM in case $bv_2 i_2 =$

bv_3i_3 and $bv_1i_1 = bv_3i_3$, respectively. Mode matching condition (6.21) may only generate IM-FWM since $bv_2i_2 \neq av_3i_3$ and $bv_1i_1 \neq av_3i_3$, with $b \neq a$. In [11], it has been experimentally demonstrated that mode matching conditions (6.19) and (6.20) can lead to an efficient IM-FWM process even for high DMD values ($\sim 100\,\mathrm{ps/km}$). Furthermore, for the mode matching condition (6.21), no IM-FWM process has been experimentally observed (above the noise floor) since the phase matching depends on effective index difference between modes b and a, and is therefore sensitive to fluctuations of the effective indexes with distance [11]. Therefore, the nonlinear terms satisfying mode matching condition (6.21) are excluded from (6.13).

Considering the above mentioned $A^{eff}_{u_1u_2u_3u}$ properties, the MM-MW-CNLSE are given by:

$$\begin{aligned}&\partial_z A_{uvi} + \mathfrak{D} A_{uvi} + \frac{\alpha_{uvi}}{2} A_{uvi} = \\ &-\mathrm{j}\left(C_{SPM} + C_{XPM} + C_{FWM} + C_{IM-XPM} + C_{IM-FWM}\right) \\ &-\mathrm{j}\sum_{u_1 i_1} C_{uvi,u_1vi_1} A_{u_1vi_1} \exp\left[\mathrm{j}\left(\beta_{0,uvi} - \beta_{0,u_1vi_1}\right) z\right]\end{aligned} \tag{6.22}$$

with:

$$C_{SPM} = \gamma_{uuuu} |A_{uvi}|^2 A_{uvi} \tag{6.23}$$

$$C_{XPM} = 2\sum_{v_1 \neq v} \gamma_{uuuu} |A_{uv_1i}|^2 A_{uvi} + \frac{2}{3}\sum_{v_1} \gamma_{uuuu} |A_{uv_1j}|^2 A_{uvi} \tag{6.24}$$

$$C_{FWM} = \sum_{v_1 i_1} \sum_{v_2 i_2} \sum_{v_3 i_3 \neq v_1 i_1 \wedge v_2 i_2} \begin{bmatrix} \xi_{i_1 i_2 i_3 i} \gamma_{uuuu} A_{uv_1 i_1} A_{uv_2 i_2} A^*_{uv_3 i_3} \cdot \\ \exp\left(-\mathrm{j}\Delta\beta_{uv_1 i_1, uv_2 i_2, uv_3 i_3, uvi} z\right) \end{bmatrix} \tag{6.25}$$

$$C_{IM-XPM} = 2\sum_{u_1 \neq u} \sum_{v_1} \gamma_{uu_1u_1u} \left(|A_{u_1v_1i}|^2 + \frac{1}{3}|A_{u_1v_1j}|^2 \right) A_{uvi} \tag{6.26}$$

$$C_{IM-FWM} = \sum_{u_1 \neq u} \sum_{v_1 i_1} \sum_{v_2 i_2} \sum_{v_3 i_3 \neq v_2 i_2} \begin{bmatrix} \psi_{i_1 i_2 i_3 i} \gamma_{uu_1u_1u} A_{uv_1 i_1} A_{u_1 v_2 i_2} A^*_{u_1 v_3 i_3} \cdot \\ \exp\left(-\mathrm{j}\Delta\beta_{uv_1 i_1, u_1 v_2 i_2, u_1 v_3 i_3, uvi} z\right) \end{bmatrix} \tag{6.27}$$

$$\psi_{i_1 i_2 i_3 i} = 2\delta_{i_1 i}\delta_{i_2 i}\delta_{i_3 i} + \frac{2}{3}\delta_{i_1 i}\delta_{i_2 j}\delta_{i_3 j} + \frac{2}{3}\delta_{i_1 j}\delta_{i_2 i}\delta_{i_3 j} + \frac{2}{3}\delta_{i_1 j}\delta_{i_2 j}\delta_{i_3 i} \tag{6.28}$$

In the first term on the RHS of (6.22) the nonlinear contributions due to SPM (C_{SPM}) (6.23), XPM (C_{XPM}) (6.24), FWM (C_{FWM}) (6.25), IM-XPM (C_{IM-XPM}) (6.26) and IM-FWM (C_{IM-FWM}) (6.27) are identified. As $A_{u_1v_1i_1}A_{u_2v_2i_2}A^*_{u_3v_3i_3} = A_{u_2v_2i_2}A_{u_1v_1i_1}A^*_{u_3v_3i_3}$ and $\Delta\beta_{u_1v_1i_1,u_2v_2i_2,u_3v_3i_3,uvi} = \Delta\beta_{u_2v_2i_2,u_1v_1i_1,u_3v_3i_3,uvi}$ in (6.13), (6.27) and (6.28) have been written in such a way that only mode combinations (u, u_1, u_1, u) appear. As a consequence, along this chapter only mode combinations (u, u_1, u_1, u)

are discussed, without lack of generality.

In order to solve (6.22), the split-step Fourier method (SSFM) is modified for multimode propagation including linear XT, as in [15]. The linear XT is modeled by random displacements of the core axis position following an uniform distribution, considering a constant displacement along each fiber section [15]. In this way, the XT accumulated along a certain fiber length L is set by the maximum radial displacement and the section length L_s. The XT from mode u to mode u_1 is defined by [9]:

$$XT_{u_1,u} = \frac{P_{u_1}}{P_u} \tag{6.29}$$

where P_u and P_{u_1} are, respectively, the power of mode u (in both polarizations) and mode u_1 (in both polarizations), after a fiber length L, when only mode u was launched. Later in this chapter, the nonlinear degradation in MDM-WDM-FMF systems is assessed considering the Q-factor [17] of the center WDM channel of a given mode. An intensity modulated (IM) direct detection (DD) WDM system is assumed. Therefore, in the following simplified theoretical expressions for the Q-factor are derived extending the work developed for SMFs [19–21]. Such expressions are derived from (6.22) considering each term in C_{XPM}, C_{IM-XPM}, C_{FWM} and C_{IM-FWM} separately as well as no linear XT, only one polarization (thus, the polarization index is dropped), a fiber length L and $\alpha_{uv} = \alpha$ for any uv.

6.2.1 XPM and IM-XPM Analytical Solution

The XPM and IM-XPM terms can be solved considering the pump-probe method used for SMFs, as in [20, 21]. The Q-factor of a probe channel in $(u, v = 0)$ is calculated considering a pump in (u_1, v_1), $Q_{u_1u}^{xXPM}$ ($xXPM$ = XPM for $u_1 = u$ and $xXPM$ = IM-XPM for $u_1 \neq u$). $Q_{u_1u}^{xXPM}$ is obtained using the Gaussian approximation presented in [20], assuming an ideal detector, an ideal pre-amplifier with gain equal to $\exp(\alpha L)$, neglecting logic 0 mean and variance, and no source of noise. $Q_{u_1u}^{xXPM}$ is given by:

$$Q_{u_1u}^{xXPM} = 2P_{pump} \Big/ \sqrt{\left(\sigma_{u_1u}^{xXPM}\right)^2} \tag{6.30}$$

with:

$$\left(\sigma_{u_1u}^{xXPM}\right)^2 = \begin{cases} \sum\limits_{v_1\neq 0}\int\limits_{-\infty}^{+\infty} \left|H_{u_1v_1,u0}^{xXPM}(\omega)\right|^2 PSD_{pump}(\omega)d\omega, & u_1 = u \\ \sum\limits_{v_1}\int\limits_{-\infty}^{+\infty} \left|H_{u_1v_1,u0}^{xXPM}(\omega)\right|^2 PSD_{pump}(\omega)d\omega, & u_1 \neq u \end{cases} \tag{6.31}$$

$$H_{u_1v_1,u0}^{xXPM}(\omega) = \frac{4\gamma_{uu_1u_1u}P_{probe}}{p^2+q^2}\cdot\left[p\sin(qL) - q\cos(qL) + q\exp(-\alpha L)\right] \tag{6.32}$$

$$p = \alpha + \mathrm{j}\omega d_{u_1v_1,u0}$$

$$q = \pi c\cdot D_{u0}\cdot\omega^2/\omega_0^2$$

$$d_{u_1v_1,u0} = \beta_{1,u_1v_1} - \beta_{1,u0}$$

where P_{pump} and P_{probe} are the average input power of the pump and of the probe, respectively. $H_{u_1v_1,u0}^{xXPM}(\omega)$ is the transfer function of the equivalent linear model of the $xXPM$ induced intensity modulation associated with the (u_1v_1) pump channel. $d_{u_1v_1,u0}$ is the walkoff parameter. $PSD_{pump}(\omega)$ is the power spectral density of an IM signal with a bit-rate up to 10 Gb/s [20] and a given pulse shape. Note that, for $u_1 \neq u$, the case $v_1 = 0$ is included in (6.31) because v_1 and $v = 0$ are in different modes they cannot refer to the same channel even for $v_1 = 0$.

6.2.2 FWM and IM-FWM Analytical Solution

The FWM and IM-FWM terms can be solved considering three continuous waves (CWs) interacting, as considered in [19] for SMFs. The Q-factor of a channel in $(u, v = 0)$ is calculated considering three CW signals in (uv_1, u_1v_2, u_1v_3), $Q_{u_1u}^{xFWM}$ ($xFWM$ = FWM for $u_1 = u$ and $xFWM$ = IM-FWM for $u_1 \neq u$). $Q_{u_1u}^{xFWM}$ is obtained using the Gaussian approximation presented in [19], assuming an ideal detector, an ideal pre-amplifier with gain equal to $\exp(\alpha L)$, neglecting logic 0 mean and variance, and no source of noise. $Q_{u_1u}^{xFWM}$ is given by:

$$Q_{u_1u}^{xFWM} = P_{u0}\Big/\sqrt{\left(\sigma_{u_1u}^{xFWM}\right)^2} \tag{6.33}$$

with:

$$\left(\sigma_{u_1u}^{xFWM}\right)^2 = \begin{cases} \sum\limits_{\substack{v_1v_2v_3 \\ v_3 \neq v_1 \wedge v_2}} 2P_{u0} \cdot P_{uv_1,uv_2,uv_3,u0}^{xFWM} \cdot CP_{uv_1,uv_2,uv_3,u0}, & u_1 = u \\ \sum\limits_{\substack{v_1v_2v_3 \\ v_3 \neq v_2}} 2P_{u0} \cdot P_{uv_1,u_1v_2,u_1v_3,u0}^{xFWM} \cdot CP_{uv_1,u_1v_2,u_1v_3,u0}, & u_1 \neq u \end{cases} \tag{6.34}$$

$$P_{uv_1,u_1v_2,u_1v_3,u0}^{xFWM} = \eta\gamma_{uu_1u_1u}^2 P_{uv_1}P_{u_1v_2}P_{u_1v_3} \cdot \left| \frac{1-\exp\left[-\left(\alpha + \mathrm{j}\Delta\beta_{uv_1,u_1v_2,u_1v_3,u0}\right)L\right]}{\alpha + \mathrm{j}\Delta\beta_{uv_1,u_1v_2,u_1v_3,u0}} \right|^2 \tag{6.35}$$

$$\eta = \begin{cases} 4, u_1 = u \wedge v_1 \neq v_2 \\ 1, u_1 = u \wedge v_1 = v_2 \\ 4, u_1 \neq u \wedge v_2 \neq v_3 \end{cases}$$

$$CP_{uv_1,u_1v_2,u_1v_3,u0} = \begin{cases} 1/8, u_1 = u \wedge v_1 \neq v_2 \neq v_3 \neq 0 \\ 1/4, u_1 = u \wedge v_1 \neq v_2 \neq v_3 \wedge v_3 = 0 \\ 1/4, u_1 = u \wedge v_1 = v_2 \wedge v_1 \neq v_3 \\ 1/8, u_1 \neq u \wedge v_2 \neq v_3 \end{cases} \tag{6.36}$$

where P_{u0} is the peak power of the IM signal in the central channel of u, P_{uv_1}, P_{uv_2}, and P_{uv_3} are the powers of CWs in (uv_1, u_1v_2, u_1v_3), $P_{uv_1,u_1v_2,u_1v_3,u0}^{xFWM}$ is the power of the $xFWM$ product generated at the center channel of mode u $(u, v = 0)$, and $CP_{uv_1,u_1v_2,u_1v_3,u0}$ is the probability of having a non-zero $A_{uv_1i_1}A_{u_1v_2i_2}A_{u_1v_3i_3}^*$ product in (6.25) and (6.27). In case $u_1 \neq u$, the summation conditions in (6.27) impose that the four channels $(uv_1, u_1v_2, u_1v_3, uv)$ are always independent, since v_1 and v belong to mode u, v_2 and v_3 belong to a different mode u_1, and (6.27) imposes $v_2 \neq v_3$. Thereby, assuming channels with equal probability of logic 1 and 0, $CP_{uv_1,u_1v_2,u_1v_3,u0}$, for $u_1 \neq u$ is 1/8 or 0. $CP_{uv_1,uv_2,uv_3,u0}$ is equal to the FWM case in SMFs [17].

6.3 MM-MW-CNLSE Validation

In this section, the MM-MW-CNLSE (6.22) is validated against experimental results for IM-XPM and IM-FWM presented in [10] and [11], respectively. The FMF considered is modeled according to the characteristics described in [10] (the same fiber was used in [11]). The FMF characteristics are considered to be independent of the polarization as in [10], thus in the following the polarization index is omitted. At $\lambda_0 = 1545\,\mathrm{nm}$ the FMF guides two non-degenerate LP modes $u =$

LP_{01} and $u_1 = \mathrm{LP}_{11}$, where u_1 is composed by two degenerate modes $u_2 = \mathrm{LP}_{11\mathrm{a}}$ and $u_3 = \mathrm{LP}_{11\mathrm{b}}$. $DMD_{u_10,u0}$ is 309 ps/km (considering $\beta_{u_10} = (\beta_{u_30} + \beta_{u_20})/2$), $DMD_{u_30,u_20} = 0$ ps/km, $L = 4.7$ km and $XT_{u_1,u} = -20$ dB. The value is set tuning the maximum core displacement for $L = 4.7$ km and $L_s = 50$ m. Moreover, for the tuned parameters, the XT_{u_3,u_2} obtained is approximately 0 dB (averaging over 20 simulations with $XT_{u_1,u} = -20$ dB). Table 6.1 presents the remaining FMF characteristics: D, S, and A^{eff}. Since $DMD_{u_10,u0}$ and DMD_{u_30,u_20} have been measured in the presence of non-negligible $XT_{u_1,u}$ [10], its actual value may be higher. Thus, in the following, $DMD_{u_10,u0}$ is varied around 309 ps/km and DMD_{u_30,u_20} is varied around 0 ps/km.

Table 6.1: Characteristics of the GI-FMF [10] and [11] at $\lambda_0 = 1545$ nm.

	$a = \mathrm{LP}_{11\mathrm{a}}$	$a = \mathrm{LP}_{11\mathrm{b}}$	$a = \mathrm{LP}_{01}$
D_{a0} [ps/(nm·km)]	19.8	19.8	18.7
S_{a0} [fs/(nm^2·km)]	92.1	92.1	78.9

A^{eff}_{abba}[μm^2]	$a = \mathrm{LP}_{11\mathrm{a}}$	$a = \mathrm{LP}_{11\mathrm{b}}$	$a = \mathrm{LP}_{01}$
$b = \mathrm{LP}_{11\mathrm{a}}$	79.8	239.4	120.1
$b = \mathrm{LP}_{11\mathrm{a}}$	239.4	79.8	120.1
$b = \mathrm{LP}_{01}$	120.1	120.1	59.6

6.3.1 IM-XPM

In [10], a pump-probe method was used to measure the relative strength of the IM-XPM process, considering a pump modulated at 10 Gb/s by an IM signal. The signal powers at the fiber input were: $P_{pump} = 17$ dBm and $P_{probe} = 2.6$ dBm. The pump was launched in the u_1 mode while the probe was launched in the u mode. The probe was located at 1561.245 nm and the pump was swept over the C-band. The relative spectral broadening factor (SBF) of the probe as a function of the probe-pump wavelength separation was measured. In the following, the IM signal is generated considering deBruijn sequences with 2^9 bits and a raised cosine pulse shape with roll-off set to 0.5.

In this chapter, (6.22) is numerically solved considering the same conditions as in [10] and the SBF is measured according to the definition in [10]. The root mean squared error (RMSE) between the experimental and simulation spectral broadening factor is calculated ($SBF\text{-}RMSE$). Fig. 6.1 shows the contour map of $SBF\text{-}RMSE$ as a function of $DMD_{u_10,u0}$ and DMD_{u_30,u_20}. The results in Fig. 6.1 have been obtained averaging over 20 simulations with different random core displacements presenting $XT_{u_1,u} = -20\,\text{dB}$. In Fig. 6.1, it can be seen that the lowest $SBF\text{-}RMSE$ is obtained for $DMD_{u_10,u0} = 311\,\text{ps/km}$ and $DMD_{u_30,u_20} = 0\,\text{ps/km}$. Note that the optimum $DMD_{u_10,u0}$ value is higher than the 309 ps/km reported in [10], agreeing with the explanation presented above. Furthermore, a close match between the experimental and simulation SBF can be seen in Fig. 6.1 inset for the optimum DMD values.

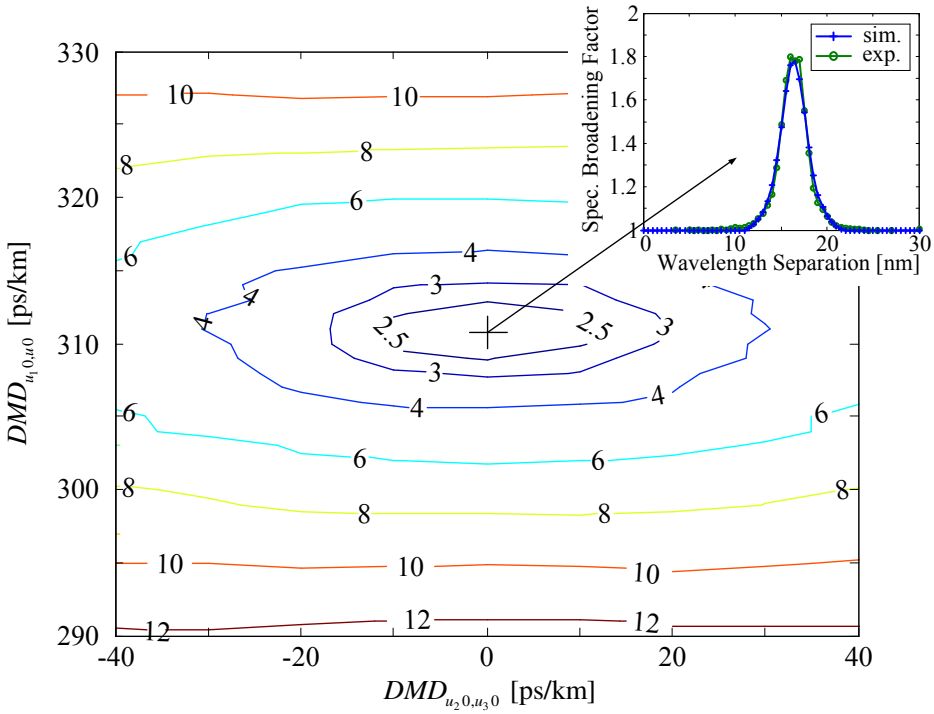

Figure 6.1: Contour map of $SBF\text{-}RMSE$ [$\cdot 10^{-2}$] as a function of $DMD_{u_10,u0}$ and DMD_{u_30,u_20}. Inset: Overlap of the experimental and simulation SB for the optimum DMD values.

6.3.2 IM-FWM

In [11], the relative strength of the IM-FWM process was measured launching three CWs with different wavelengths. Two CWs were launched in u, referenced as u_{pump} and u_{probe}, and one CW was launched in u_1, referenced as $u_{1,pump}$. Given this configuration, the idlers appear in u_1 (this is, u_2 and u_3) according to the mode matching condition (6.19). The signals powers at the fiber input were: $P_{u_{1,pump}} = 16\,\text{dBm}$, $P_{u_{pump}} = 18\,\text{dBm}$, and $P_{u_{probe}} = 6\,\text{dBm}$. Note that the $u_{1,pump}$ power is considered to be halved between u_2 and u_3. Three different sets of pump and probe wavelengths were considered, as summarized in Table 6.2. In each of the three sets, $\lambda_{u_{1,pump}}$ and $\lambda_{u_{pump}}$ are held fixed and $\lambda_{u_{probe}}$ takes three different values.

Table 6.2: Sets of wavelengths considered in [11].

	Set A	Set B	Set C
$\lambda_{u_{1,pump}}$ [nm]	1530	1530	1530
$\lambda_{u_{pump}}$ [nm]	1554	1546	1546
$\lambda_{u_{probe}}$ [nm]	1546	1552	1547
	1547	1553	1548
	1548	1554	1549

In this section, the power of each idler is calculated numerically by solving (6.22), and analytically by using (6.35). In order to compare the simulation and experimental results, for each combination of the wavelength sets in Table 6.2, the power ratio (PR) between the idler power measured experimentally and the idler power calculated (analytically and numerically) is calculated, when idler experimental power is above the noise floor in [11]. Only the highest PR value is presented, PR_{max}. In this way, for a given wavelength set, the PR for any of the idlers generated is equal to or lower than PR_{max}.

Fig. 6.2 shows PR_{max}, which has been calculated analytically using (6.35), as a function of $DMD_{u_10,u0}$ (gray continuous lines) for: (a) wavelength set A, (b) wavelength set B, and (c) wavelength set C. The analytical results in Fig. 6.2 show that the IM-FWM efficiency varies abruptly with small changes of the $DMD_{u_10,u0}$ value

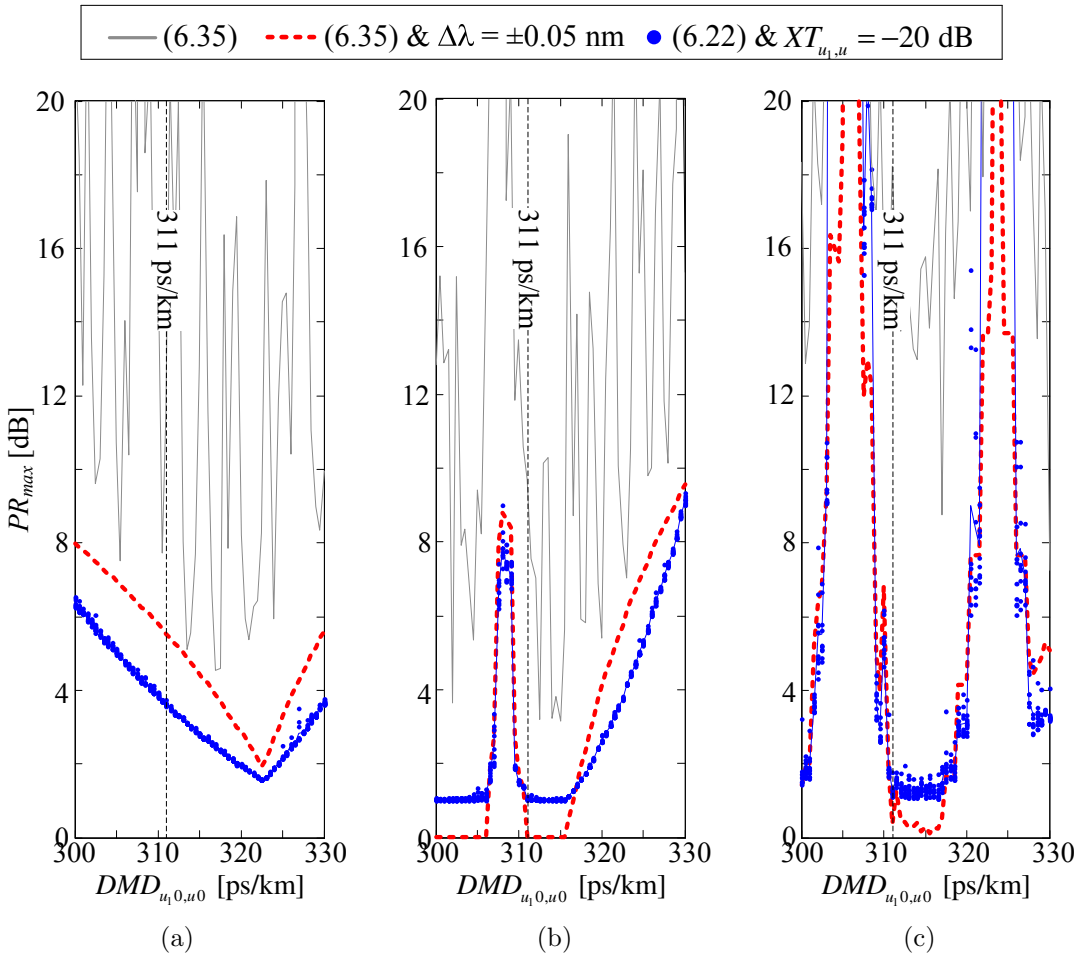

Figure 6.2: PR_{max} as a function of $DMD_{u10,u0}$ for wavelength set: (a) A, (b) B, (c) C.

(~ 1 ps/km). The PR_{max} variation with $DMD_{u10,u0}$ can be smoothed assuming a precision error on the CWs wavelengths (always present in practice). Thus, PR_{max} has been recalculated choosing the wavelength drift leading to the minimum error. Fig. 6.2 shows PR_{max} recalculated analytically assuming a maximum ± 0.05 nm wavelength precision ($\Delta\lambda$) (red dashed lines). In this case, the PR_{max} variation with $DMD_{u10,u0}$ is lower and, for $DMD_{u10,u0} = 311$ ps/km (the optimum value found in Section 6.3.1), PR_{max} is approximately 5.5 dB for set A and smaller than 0.5 dB for sets B and C. Furthermore, using (6.22), PR_{max} was calculated for 20 different random core displacements with $XT_{u_1,u} = -20$ dB. In this case, PR_{max} for $DMD_{u10,u0} = 311$ ps/km is approximately 3.5 dB for set A and 1 dB for sets B and C. In conclusion, the results obtained through a full numerical simulation considering linear XT using (6.22) show a good agreement with the experimental results.

6.4 MDM-WDM-FMF Transmission

In this section, a MDM-WDM-FMF system is studied. The system performance is evaluated through the transmission of a WDM signal with $N+1$ channels in each FMF mode. The figure of merit measured is the maximum input power (MP) such that the central channel of a given mode has a Q-factor of 7 (bit error ratio of 10^{-12}), assuming equal power on all channels. A 10 Gb/s IM-DD WDM system is assumed as in section 6.3.1. MP is calculated numerically solving (6.22), and using (6.30) and (6.33). A WDM fixed grid centered at ω_0 and with an angular frequency separation of $\Delta\omega_g$ is considered. Thereby, the optical angular frequency of a given carrier v can be written as $\omega_0 + v \cdot \Delta\omega_g$, with v between $-N/2$ and $N/2$. The simulation setup considers $L = 80$ km, $L_s = 50$ m, $N = 80$ and 50 GHz frequency separation between adjacent channels. The FMF presented in Section 6.3 is used considering the same characteristics with the following exceptions. Considering the maximum core displacement used in Section 6.3, $XT_{u_1,u} = -8$ dB (and $XT_{u_3,u_2} \approx 0$ dB in average) with $L = 80$ km. Moreover, two different scenarios concerning the $DMD_{u_10,u0}$ frequency slope are studied. The $DMD_{u_10,u0}$ frequency slope is given by:

$$\partial_{\omega_v} DMD_{u_1 v,uv}|_{\omega_v=\omega_0} = \beta_{2,u_10} - \beta_{2,u0} = -\frac{\lambda_0^2}{2\pi c_0}\left(D_{u_10} - D_{u0}\right) \tag{6.37}$$

One scenario considers D_{u0} and D_{u_10} taken from Table 6.1, and thus $DMD_{u_10,u0}$ has a nonzero frequency slope, scenario referred as non-flat DMD. The second scenario considers $D_{u0} = D_{u_10}$ (with D_{u_10} from Table 6.1), thereby $DMD_{u_10,u0}$ has zero frequency slope (as shown in [5]), scenario referred as flat DMD. Moreover, for all scenarios considered below, the impact of the chromatic dispersion slope values in Table 6.1 has been found to be negligible. In the following, the penalties induced by $xXPM$ and $xFWM$ are compared in order to find the dominant effect. The MP values limited by Q_{ba}^{xXPM} and Q_{ba}^{xFWM} are presented as: MP_{ba}^{xXPM} and MP_{ba}^{xFWM}, respectively. MP_{ba}^{xXPM} and MP_{ba}^{xFWM} are calculated taking into account all $xXPM$ and $xFWM$ terms involving modes a and b falling into $(a, v = 0)$. Since the penalty induced on the central channels of modes u_2 and u_3 are in average approximately equal, only the penalty for u_2 is shown.

6.4.1 XPM/IM-XPM

According to (6.32), the $xXPM$-induced penalty in the center channel of mode a considering a pump in (b, v) is highly dependent on the walkoff between the channels ($d_{bv,a0}$): the lower is the walkoff magnitude, the higher is the induced penalty. Therefore, $d_{bv,a0}$ is analyzed before the presentation of the results. $d_{bv,a0}$ can be re-written using the Taylor series expansion in (6.3) around $v = 0$ (truncated to second order) as:

$$d_{bv,a0} = -vD_{b0}\Delta\omega_g\left(\lambda_0^2/2\pi c_0\right) + DMD_{b0,a0} \tag{6.38}$$

In the XPM case ($b = a$), only the first RHS term of (6.38) is nonzero, and the smallest walkoff magnitude is $D_{b0}\Delta\omega_g(\lambda_0^2/2\pi c_0)$, since v cannot be zero. The IM-XPM case ($b \neq a$) can be divided in two sub-cases: pairs of degenerate modes with $DMD_{b0,a0} \approx 0\,\text{ps/km}$ and $D_{b0} \approx D_{a0}$ (as found for $b = u_3$ and $a = u_2$ in Section 6.3), and pairs of non-degenerate modes. For a pair of degenerate modes (b, a) with $DMD_{b0,a0} \approx 0\,\text{ps/km}$ and $D_{b0} \approx D_{a0}$, $d_{bv,a0}$ is approximately equal to $d_{av,a0}$, and the main difference is that v can be zero. Therefore, the signal degradation for a pair of degenerate modes is mainly due to IM-XPM since, for XPM, the walkoff is always nonzero. Regarding pairs of non-degenerate modes, the IM-XPM induced penalty is highest and lowest for $DMD_{b0,a0}$ multiple of $\pm D_{b0}\Delta\omega_g(\lambda_0^2/2\pi c_0)$ and $\pm D_{b0}\Delta\omega_g(\lambda_0^2/2\pi c_0)/2$, respectively. In other words, the penalty for a given pair of channels, is highest for the $DMD_{b0,a0}$ value symmetrically equal to the walkoff induced by chromatic dispersion $vD_{b0}\Delta\omega_g(\lambda_0^2/2\pi c_0)$. Additionally, for a given $DMD_{b0,a0}$ value, the IM-XPM induced penalty in the center channel of mode a is mainly due to the channel of mode b with the lowest walkoff, given by the frequency index v that minimizes $|DMD_{b0,a0} - vD_{b0}\Delta\omega_g(\lambda_0^2/2\pi c_0)|$. Therefore, in order to minimize the IM-XPM induced penalty over the entire WDM grid, FMFs with $|DMD_{b0,a0}|$ higher than $N \cdot D_{b0}\Delta\omega_g(\lambda_0^2/2\pi c_0)$ over the transmission wavelength range considered are required ($\sim 630\,\text{ps/km}$ for $D_{b0} = 19.8\,\text{ps/(km·nm)}$ and $N = 80$), set by the frequency separation between the extreme WDM channels ($v = -N/2$ and $v = N/2$). However, the use of FMFs with such high DMD values in long-haul applications might be impractical even for DMD compensated links, as shorter compensation step and/or higher equalization complexity would be required [22].

Fig. 6.3 shows MP_{ba}^{xXPM} as a function of $DMD_{u_1 0,u0}$ for each pair of modes (b, a): (a) $a = u_2$ and (b) $a = u$. These results were obtained numerically solving (6.22) for $XT_{u_1,u} = -8\,\text{dB}$ and using (6.30) for $XT_{u_1,u} = XT_{u_3,u_2} = -\infty\,\text{dB}$, considering flat

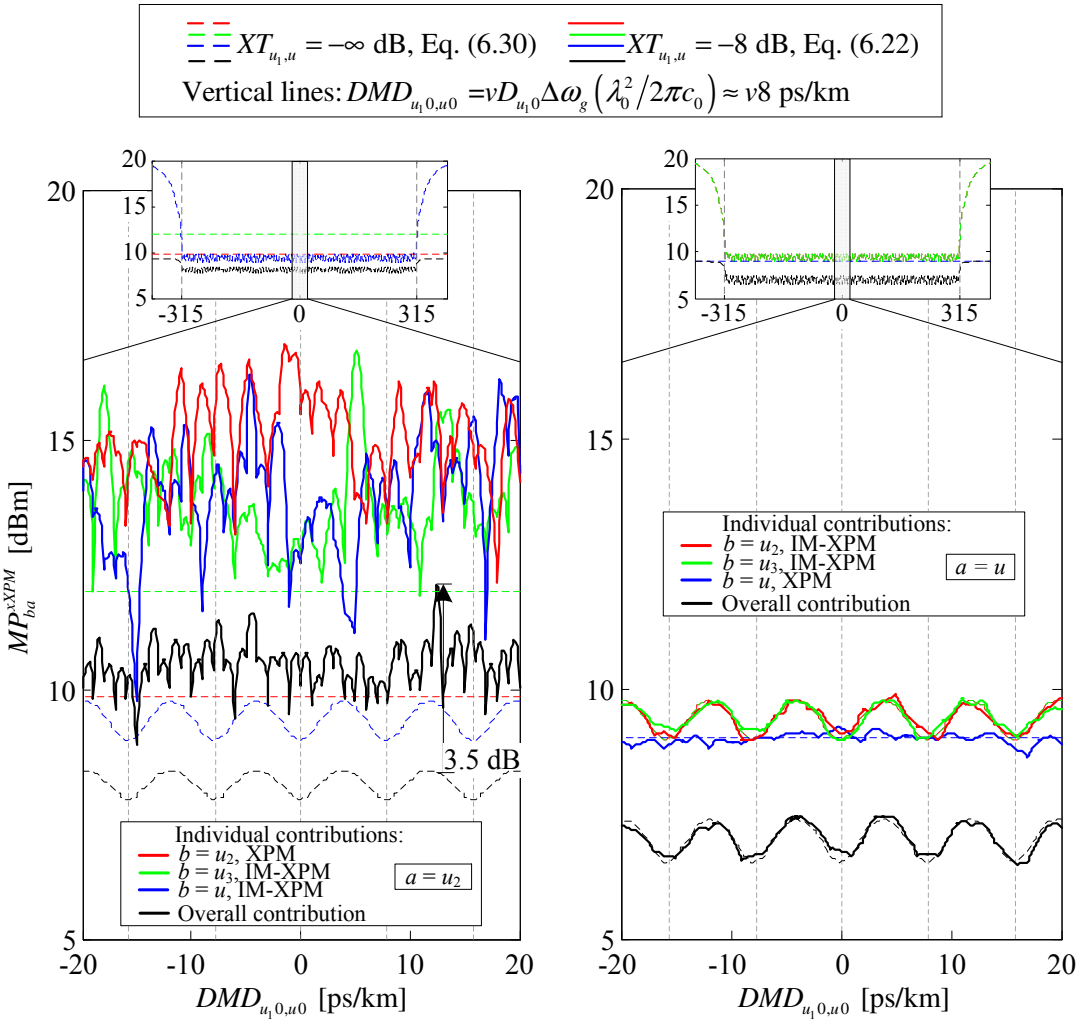

Figure 6.3: MP_{ba}^{xXPM} as a function of $DMD_{u10,u0}$, for each pair of modes (b, a): (a) $a = u_2$ and (b) $a = u$.

$DMD_{u_10,u0}$. The results for $XT_{u_1,u} = -\infty$ dB are analyzed first. Fig. 6.3(a) shows that XPM and IM-XPM induced penalties have similar magnitude as MP_{ba}^{xXPM} has similar values for $b = u_2$ and $b = u$ (the maximum difference is 1 dB for $DMD_{u_10,u0}$ multiple of $\pm D_{u_10}\Delta\omega_g(\lambda_0^2/2\pi c_0)$. The same comment applies to Fig. 6.3(b), as MP_{ba}^{xXPM} has similar values for $b = u$ and $b \neq u$ (the maximum difference is 1 dB for $DMD_{u_10,u0}$ multiple of $\pm D_{u_10}\Delta\omega_g(\lambda_0^2/2\pi c_0)/2$. In [10], it has also been experimentally verified that the IM-XPM magnitude is comparable to XPM. In the presence of $XT_{u_1,u} = -8$ dB, Fig. 6.3(a) shows a significant reduction of XPM and IM-XPM induced penalties, since the overall MP_{ba}^{xXPM} increase can be as high as 3.5 dB. However, Fig. 6.3(b) shows that XPM and IM-XPM induced penalties are not affected significantly. The different impact of XT on u and (u_2, u_3) is explained noting that the XT between u_2 and u_3 is much stronger than between u_1 and u, at the end of only 4.7 km $XT_{u3,u2}$ is already approximately 0 dB in average (see Section 6.3). Regarding the DMD frequency slope, additional results have shown that its impact on the XPM/IM-XPM induced penalty in the center channel of a given mode is negligible, as (6.38) shows. Additionally, the insets in Fig. 6.3 show that to reduce the IM-XPM induced penalty to negligibly levels, $|DMD_{u_10,u0}|$ has to be increased over $|N/2 \cdot D_{u_10}\Delta\omega_g(\lambda_0^2/2\pi c_0)|$ (~ 315 ps/km for $D_{u0} = 19.8$ ps/(km·nm)), set by the frequency separation between the central channels and one of the extreme WDM channels ($v = 0$ and $v = \pm N/2$). Note that the IM-XPM induced penalty for the pair (u_3,u_2) is independent of $DMD_{u_10,u0}$.

Finally, comparing the overall MP_{ba}^{xXPM} in Fig. 6.3(a) and in Fig. 6.3(b), for $XT_{u1,u} = -8$ dB, it can be concluded that the system performance is determined by the XPM and IM-XPM induced penalties in u (with approximately equal magnitude), in the absence of FWM/IM-FWM.

6.4.2 FWM/IM-FWM

According to (6.35), the $xFWM$-induced penalty is highly dependent on the phase mismatch $\Delta\beta_{av_1,bv_2,bv_3,a0}$. The smaller is the phase mismatch the larger is the induced penalty. Therefore, the phase mismatch is analyzed before presenting the results. The phase mismatch (6.14) can be re-written using the Taylor series expansion in (6.3) around $v = 0$ (truncated to second order) and the frequency condition for an idler in the central frequency, given by $v_3 = v_1 + v_2$. $\Delta\beta_{av_1,bv_2,bv_3,a0}$ is written as:

$$\frac{\Delta\beta_{av_1,bv_2,bv_3,av}}{v_1\Delta\omega_g} = v_2\frac{\lambda_0^2}{2\pi c_0}D_{b0}\Delta\omega_g - DMD_{b0,a0} - v_1\Delta\omega_g\frac{1}{2}\left(\partial_{\omega_v}DMD_{u_1v,uv}|_{\omega_v=\omega_0}\right) \tag{6.39}$$

Note that $v_1 \neq 0$ in any case, since $v_1 = v_3 - v_2$ and $v_3 \neq v_2$ (v_3 and v_2 belong to mode b). In the FWM case ($b = a$), only the first RHS term of (6.39) is nonzero, and its minimum magnitude is $D_{b0}\Delta\omega_g(\lambda_0^2/2\pi c_0)$ because v_2 cannot be zero ($v_2 = v_3 - v_1$ and $v_3 \neq v_1$ since both belong to mode a). The IM-FWM case can be divided into three sub-cases: pairs of degenerate modes with $DMD_{b0,a0} \approx 0\,\text{ps/km}$ and $D_{b0} \approx D_{a0}$ (as found for $b = u_3$ and $a = u_2$ in Section 6.3), pairs of non-degenerate modes with flat DMD, and pairs of non-degenerate modes with non-flat DMD. For pairs of degenerate modes with $DMD_{b0,a0} \approx 0\,\text{ps/km}$ and $D_{b0} \approx D_{a0}$, the RHS of (6.39) is approximately $v_2D_{b0}\Delta\omega_g(\lambda_0^2/2\pi c_0)$, similarly to FWM, and the main difference is that v_2 can be zero (v_3 and v_1 belong to different modes). Therefore, the RHS of (6.39) is approximately zero for $v_2 = 0$ and any v_1 value between $-N/2$ and $N/2$ (except $v_1 = 0$). In such conditions, N IM-FWM terms with negligible phase mismatch fall into the center channel of a, inducing a high penalty in comparison to the other cases (independently of the DMD between the remaining modes that might be guided simultaneously). In the case of non-degenerate modes with flat DMD, the RHS of (6.39) is equal to $-DMD_{b0,a0} - v_2D_{b0}\Delta\omega_g(\lambda_0^2/2\pi c_0)$. Therefore, the $DMD_{b0,a0}$ values leading to maximum and minimum IM-FWM induced penalty are multiples of $\pm D_{b0}\Delta\omega_g(\lambda_0^2/2\pi c_0)$ and $\pm D_{b0}\Delta\omega_g(\lambda_0^2/2\pi c_0)/2$, respectively, as for IM-XPM (thus, the $|DMD_{b0,a0}|$ value required for a reduced IM-FWM penalty over the entire WDM grid is the same). In the last case, non-degenerate modes with non-flat DMD, the third term in the RHS of (6.39) cannot be neglected, therefore the $DMD_{b0,a0}$ values leading to maximum and minimum IM FWM induced penalty identified for the flat DMD case are shifted.

Fig. 6.4 shows MP_{ba}^{xFWM} as a function of $DMD_{u_10,u0}$ for each mode combination. These results were obtained numerically solving (6.22) for $XT_{u_1,u} = -8\,\text{dB}$ and using (6.33) for $XT_{u_1,u} = XT_{u_3,u_2} = -\infty\,\text{dB}$, considering flat $DMD_{u_10,u0}$. The results for $XT_{u_1,u} = -\infty\,\text{dB}$ are analyzed first. Fig. 6.4(a) shows that IM FWM with $b = u_3$ (this is, IM-FWM between $\text{LP}_{11\text{a}}$ and $\text{LP}_{11\text{b}}$) is the dominant penalty (lower MP_{ba}^{xFWM} value), and that FWM ($b = u_2$) is the effect leading to lower penalty. The severe

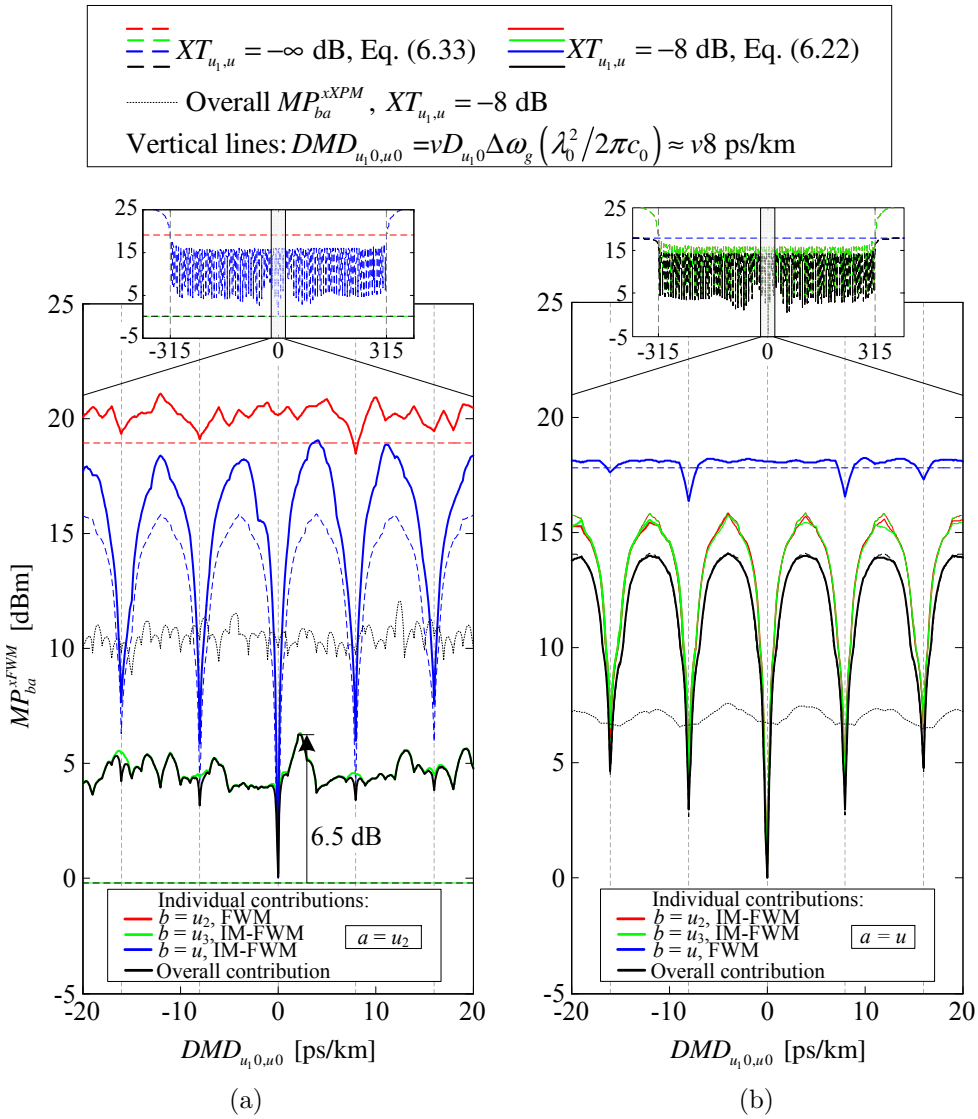

(a) (b)

Figure 6.4: MP_{ba}^{xFWM} as a function of $DMD_{u10,u0}$, for each pair of modes (b, a): (a) $a = u_2$ and (b) $a = u$.

degradation due to IM-FWM is related with the high number of frequency combinations verifying the phase matching condition between degenerate modes, as explained above. Moreover, in Fig. 6.4(a), it can be seen that the IM-FWM induced penalty with $b = u$ (this is, IM-FWM between the pair of non-degenerate modes) is characterized by periodical notches at multiple of $\pm D_{u0}\Delta\omega_g(\lambda_0^2/2\pi c_0)$, as explained above. In practical cases, due to the variation of $DMD_{u_10,u0}$ along the fiber length [23], the maximum induced penalty may be reduced to the MP_{ba}^{xFWM} values for $DMD_{u_10,u0}$ multiple of $\pm D_{u0}\Delta\omega_g(\lambda_0^2/2\pi c_0)/2$, as shown in Fig. 6.4(a). Fig. 6.4(b) shows that IM-FWM is the dominant source of penalty characterized by periodical notches at multiples of $\pm D_{u0}\Delta\omega_g(\lambda_0^2/2\pi c_0)$ (in practical cases these notches may be reduced as previously explained). In the presence of $XT_{u_1,u} = -8\,\text{dB}$, Fig. 6.4(b) shows that FWM and IM-FWM induced penalties in u, involving only pairs of non-degenerate modes, are not affected significantly. On the other hand, for pairs degenerate modes, Fig. 6.4(a) shows that $XT_{u_1,u}$ has a significant impact on the penalty induced by FWM and IM-FWM, such that the increase of MP_{ba}^{xFWM} can reach 6.5 dB. The explanation for the different impact of XT in u and (u_2, u_3) is the same presented for IM-XPM. Additionally, the insets in Fig. 6.4 show that to reduce the IM-FWM induced penalty to negligibly levels, $|DMD_{u_10,u0}|$ has to be increased over $|N/2 \cdot D_{u0}\Delta\omega_g(\lambda_0^2/2\pi c_0)|$ (315 ps/km for $D_{u0} = 19.8\,\text{ps/(km·nm)}$), as in section 6.4.1. Note that the IM-FWM induced penalty for the pair (u_3, u_2) is independent of $DMD_{u_10,u0}$.

Fig. 6.5 shows MP_{ba}^{xFWM} considering all IM-FWM terms ($b = u_2$ and u_3) falling into $a = u$ as a function of $DMD_{u_10,u0}$, for flat DMD and non-flat DMD. From Fig. 6.5, it can be seen that having non-flat DMD decreases the maximum degradation possible (at multiples of $\pm D_{u0}\Delta\omega_g(\lambda_0^2/2\pi c_0)$) but increases the minimum degradation possible (at multiples of $\pm D_{u0}\Delta\omega_g(\lambda_0^2/2\pi c_0)/2$). This agrees with the theoretical explanation provided above about the phase mismatch for pairs of non-degenerate modes with non-flat DMD. In conclusion, the IM-FWM induces higher signal degradation than FWM in any of the FMF modes. The IM-FWM between degenerate modes determines the system performance in the absence of XPM/IM-XPM.

Finally, comparing overall MP_{ba}^{xXPM} and MP_{ba}^{xFWM} in Fig. 6.4, it can be concluded that the degradation for the pair of degenerate modes (LP_{11a}, LP_{11b}), due to IM-FWM, limits the overall MDM-WDM-FMF system performance. Moreover, the performance of LP_{01} is limited by IM-XPM with a magnitude similar to XPM, as shown in Fig. 6.3(b). In this comparison, the IM-FWM periodical notches shown in Fig. 6.4 were excluded, since in practical cases $DMD_{u_10,u0}$ varies along the fiber length [23]. Moreover, in this section, it has been concluded that the degradation

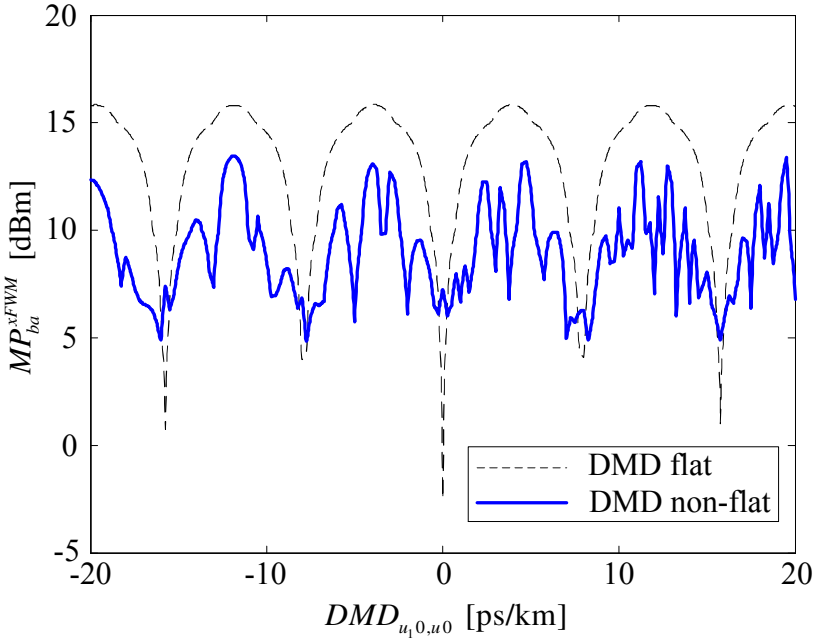

Figure 6.5: MP_{ba}^{xFWM} considering all IM-FWM terms falling into u as a function of $DMD_{u_10,u0}$, for flat DMD and non-flat DMD.

for the pair of degenerate modes and for the pairs of non-degenerate modes can be reduced designing FMFs with enhanced linear XT (using a fiber spinning process [24], for example) and $DMD_{u_10,u0}$ higher than $N \cdot D_{u0}\Delta\omega_g(\lambda_0^2/2\pi c_0)$, respectively.

6.4.3 MM-MW-CNLSE Validation for MDM-WDM Signals

In order to assess the validity of MM-MW-CNLSE (6.22) for a WDM scenario, the results obtained with (6.22) and using the MM-CNLSE with one envelope per mode presented in section 3.2.2 [15], are compared. The simulations consider: $N = 4$, equal power on all carriers, $XT_{u_1,u} = -\infty$ dB and $DMD_{u_10,u0} = D_{u0}\Delta\omega_g(\lambda_0^2/2\pi c_0)$. In such conditions, the dominant source of penalty in $\mathrm{LP_{11a}}$/$\mathrm{LP_{11b}}$ is $xFWM$ and in $\mathrm{LP_{01}}$ is $xXPM$, as shown in Fig. 6.3 and Fig. 6.4. The Q-factor of the center channel of each mode is measured after transmission and ideal filtering. Four sets of results are presented: (6.22) only with $xXPM$ terms, (6.22) only with $xFWM$ terms, (6.22) with $xXPM$ and $xFWM$ terms, and MM-MW-CNLSE in [15]. Fig. 6.6 shows Q^2 of the center channel as a function of the power per carrier, for each mode: $\mathrm{LP_{11a}}$, $\mathrm{LP_{11b}}$, and $\mathrm{LP_{01}}$. In Fig. 6.6, a good agreement can be seen between (6.22) (considering $xXPM$ and $xFWM$ terms) and MM-MW-CNLSE [15] for the three

modes. Moreover, the dominant source of penalty in $\mathrm{LP}_{11a}/\mathrm{LP}_{11b}$ is $xFWM$ and in LP_{01} is $xXPM$, as expected. Further results have also shown good agreement for other values of $DMD_{u_10,u0}$ and DMD_{u_30,u_20}.

In conclusion, the degradation of the center channel of a given mode can be obtained calculating independently the degradation coming from $xXPM$ and from $xFWM$. Moreover, further results have shown a perfect match between the analytical solutions (6.30) and (6.33), and the numerical solutions of (6.22). Such analytical solutions can be used to avoid the numerical simulation of $xXPM$ and $xFWM$ terms leading to negligible inaccuracy.

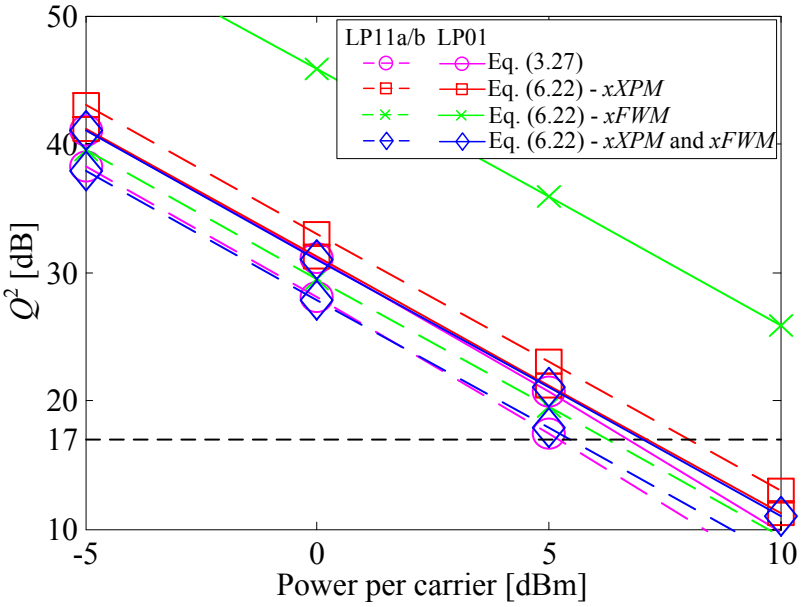

Figure 6.6: Q^2 as a function of the power per carrier.

6.5 Conclusions

In this chapter, the impact of IM-NLs on MDM-WDM-FMF systems has been investigated. For such purpose, a set of MM-MW-CNLSE including linear XT was derived. The MM-MW-CNLSE allowed studying IM-XPM and IM-FWM separately from each other and from FWM and XPM. The MM-MW-CNLSE has shown a good match to experimental results provided in the literature for IM-XPM and IM-FWM. Afterwards, the impact of XPM/IM-XPM and FWM/IM-FWM on MDM-WDM-FMF systems was assessed. The impact of linear XT on the IM-NL efficiencies has shown to be significant only for the IM-NL between pairs of degenerate modes. The domi-

nant NL effect limiting the MDM-WDM-FMF system performance was found to be IM-FWM between the degenerate modes (LP_{11a} and LP_{11b}). The performance of the non-degenerate mode (LP_{01}) was found to be limited by IM-XPM with a magnitude similar to XPM. The DMD frequency slope has shown to increase significantly the IM-FWM degradation between pairs of non-degenerate modes and to have negligible impact on the IM-XPM penalty. Moreover, it has been verified that the degradation of the center channel of a given mode in a MDM-WDM-FMF system can be obtained calculating independently the degradation coming from XPM/IM-XPM and from FWM/IM-FWM. Finally, it has been concluded that, in order to have reduced IM-NL efficiency between non-degenerate modes over the entire WDM grid, a DMD higher than 630 ps/km is required for 81 channels separated by 50 GHz, considering a chromatic dispersion of 20 ps/(km·nm), thereby imposing difficulties for long-haul applications. The IM-NL efficiency between degenerate modes can be reduced by designing FMFs with enhanced linear XT (using a fiber spinning process, for example).

References

[1] R. Essiambre and R. Tkach, "Capacity Trends and Limits of Optical Communication Networks," *Proceedings of the IEEE*, vol. 100, no. 5, pp. 1035–1055, May 2012.

[2] L. Grüner-Nielsen, Y. Sun, J. W. Nicholson, D. Jakobsen, K. Jespersen, R. Lingle, and B. Palsdottir, "Few Mode Transmission Fiber With Low DGD, Low Mode Coupling, and Low Loss," *IEEE/OSA Journal of Lightwave Technology*, vol. 30, no. 23, pp. 3693–3698, December 2012.

[3] R. Ryf, S. Randel, A. Gnauck, C. Bolle, A. Sierra, S. Mumtaz, M. Esmaeelpour, E. Burrows, R. Essiambre, P. Winzer, D. Peckham, A. McCurdy, and R. Lingle, "Mode-Division Multiplexing Over 96 km of Few-Mode Fiber Using Coherent 6×6 MIMO Processing," *IEEE/OSA Journal of Lightwave Technology*, vol. 30, no. 4, pp. 521–531, February 2012.

[4] K. Sato, R. Maruyama, N. Kuwaki, S. Matsuo, and M. Ohashi, "Optimized graded index two-mode optical fiber with low DMD, large Aeff and low bending loss," *Optics Express*, vol. 21, no. 14, pp. 1489–1492, July 2013.

[5] F. Ferreira, D. Fonseca, and H. Silva, "Design of Few-Mode Fibers with Arbitrary and Flattened Differential Mode Delay," *IEEE Photonics Technology Letters*, vol. 25, no. 5, pp. 438–441, March 2013.

[6] ——, "Design of Few-Mode Fibers with M-modes and Low Differential Mode Delay," *IEEE/OSA Journal of Lightwave Technology*, vol. 32, no. 3, pp. 353–360, February 2014.

[7] K. Ho and J. Kahn, "Statistics of Group Delays in Multimode Fiber With Strong Mode Coupling," *IEEE/OSA Journal of Lightwave Technology*, vol. 29, no. 21, pp. 3119–3128, November 2011.

[8] S. Arik, D. Askarov, and J. Kahn, "Effect of Mode Coupling on Signal Processing Complexity in Mode-Division Multiplexing," *IEEE/OSA Journal of Lightwave Technology*, vol. 31, no. 3, pp. 423–431, February 2013.

[9] F. Ferreira, D. Fonseca, A. Lobato, B. Inan, and H. Silva, "Reach Improvement of Mode Division Multiplexed Systems Using Fiber Splices," *IEEE Photonics Technology Letters*, vol. 25, no. 12, pp. 1091–1094, June 2013.

[10] R. Essiambre, M. Mestre, R. Ryf, A. Gnauck, R. Tkach, A. Chraplyvy, Y. Sun, X. Jiang, and R. Lingle, "Experimental Observation of Inter-Modal Cross-Phase Modulation in Few-Mode Fibers," *IEEE Photonics Technology Letters*, vol. 25, no. 6, pp. 535–538, March 2013.

[11] ——, "Experimental Investigation of Inter-Modal Four-Wave Mixing in Few-Mode Fibers," *IEEE Photonics Technology Letters*, vol. 25, no. 6, pp. 539–542, March 2013.

[12] C. Koebele, M. Salsi, G. Charlet, and S. Bigo, "Nonlinear Effects in Mode-Division-Multiplexed Transmission Over Few-Mode Optical Fiber," *IEEE Photonics Technology Letters*, vol. 23, no. 18, pp. 1316–1318, September 2011.

[13] G. Rademacher, S. Warm, and K. Petermann, "Analytical description of cross-modal nonlinear interaction in mode multiplexed multimode fibers," *IEEE Photonics Technology Letters*, vol. 24, no. 21, pp. 1929–1932, November 2012.

[14] S. Mumtaz, R. Essiambre, and G. Agrawal, "Nonlinear Propagation in Multimode and Multicore Fibers: Generalization of the Manakov Equations," *IEEE/OSA Journal of Lightwave Technology*, vol. 31, no. 3, pp. 398–406, February 2013.

[15] F. Ferreira, S. Jansen, P. Monteiro, and H. Silva, "Nonlinear Semi-Analytical Model for Simulation of Few-Mode Fiber Transmission," *IEEE Photonics Technology Letters*, vol. 24, no. 4, pp. 240–242, February 2012.

[16] F. Ferreira, D. Fonseca, and H. Silva, "Impact of Inter-Modal Nonlinearities on Mode- and Wavelength-Division-Multiplexing Systems," *submitted to IEEE/OSA Journal of Lightwave Technology*, 2014.

[17] G. Agrawal, *Nonlinear Fiber Optics*, 3rd ed. Academic Press, 2001.

[18] D. Marcuse, *Theory of Dielectric Optical Waveguides*. Academic Press, Inc., 1974, chapters 3 and 5.

[19] K. Inoue, K. Nakanishi, K. Oda, and H. Toba, "Crosstalk and power penalty due to fiber four-wave mixing in multichannel transmissions," *IEEE/OSA Journal of Lightwave Technology*, vol. 12, no. 8, pp. 1423–1439, August 1994.

[20] R. Luis and A. Cartaxo, "Analytical characterization of SPM impact on XPM-induced degradation in dispersion-compensated WDM systems," *IEEE/OSA Journal of Lightwave Technology*, vol. 23, no. 3, pp. 1503–1513, March 2005.

[21] A. Cartaxo, "Impact of modulation frequency on cross-phase modulation effect in intensity modulation-direct detection wdm systems," *IEEE Photonics Technology Letters*, vol. 10, no. 9, pp. 1268–1270, September 1998.

[22] N. Bai and G. Li, "Equalizer tap length requirement for mode group delay-compensated fiber link with weakly random mode coupling," *Optics Express*, vol. 22, no. 4, pp. 4247–4255, February 2014.

[23] A. Bourdine, D. Praporshchikov, and K. Yablochkin, "Investigation of defects of refractive index profile of silica graded-index multimode fibers," in *Proc. of the SPIE*, vol. 7992, no. 799206, April 2010, pp. 1–6.

[24] L. Palmieri and A. Galtarossa, "A preliminary analysis of spin in few-mode optical fibers," in *Proc. European Conference and Exhibition on Optical Communication*, September 2013, p. P.1.3.

Chapter 7

Conclusion and Future Work

7.1 Conclusions

The main objectives of the present thesis have been the investigation and design of MDM-FMF systems. The major impairments introduced by FMFs, MMUXs/ MDMUXs and MMAs have been modeled, allowing to develop several techniques to reduce their impact. In the following, the main conclusions of each chapter are gathered.

In chapter 2, a review of MDM-FMF systems implementations reported in the literature has been presented, as well as for the main components, namely: FMFs, MMUXs/MDMUXs, MMAs, and MIMO-DSP. An extensive review of FMFs presented in the literature allowed to identify the main refractive index profiles presenting lower DMD: GCCT and MSI. Moreover, the two schemes considered in the literature to obtain low DMD fiber spans were presented: ILD-FMFs and DC-FMFs. According to the literature, the MMAs can be divided in three groups: MM-EDFAs, MM-RFAs, and M parallel SM-EDFAs. From these three groups, the last one has been chosen for MDM-FMF systems simulation along this thesis since it has been used to establish the present experimental transmission distance record in laboratory. Although this MMA is impractical for long-haul transmission in a real network, it represents the best performance scenario for the other MMAs presented. In the development of MDM-FMF systems the MMUXs based on PMs proved to be crucial due to their higher MER. Still, the MMUXs based on photonic lanterns are likely to be the choice for future MDM-FMF systems due to their lower IL and easier scalability on the number of modes. Finally, the different MIMO-DSP domain implementations, TDE or FDE, were presented as well as the different fiber matrix estimation techniques, blind or

TS based. It has been concluded that a FDE-MIMO TS based equalizer presents the lowest complexity for long-haul MDM-FMF systems.

In chapter 3, the general models used to study and design long-haul MDM-FMF systems along this thesis have been derived taking into account the main impairments present in FMFs, MMUXs/MDMUXs and MMAs. A NSAM for propagation over FMFs has been developed, it is composed by a SA solution method for the coupled linear differential equations describing the linear XT and by a set of MM-CNLSE. The MM-CNLSE derived considers the main sources of signal degradation present in FMFs: chromatic dispersion, DMD, linear XT, and nonlinear effects. Considering the linear XT acting independently of the other effects, the SSFM method can be modified for multimode propagation and the linear XT is introduced using the SA solutions derived. Furthermore, the optimization design of MMUXs/MDMUXs based on PMs for 112 Gb/s coherently detected PDM-QPSK signals has been presented, assessing the mask resolution, phase noise and alignment requirements. A mask resolution of 256×256 is required for selective launching/detecting $\mathrm{LP}_{11\mathrm{a/b}}$ considering a mask alignment tolerance below 0.8 pixel. Moreover, it has been shown that the linear XT introduced by a MMUX/MDMUX based on PMs is approximately equal or lower than the dXT accumulated over a fiber length of 80 km. Finally, the general simulation setup for long-haul MDM-WDM-FMF systems used along this thesis has been presented, integrating the simulation models developed along the chapter. A set of SMT and MDM transmission simulations over a SI-TMF has been presented, providing a qualitative validation of the weak coupling strength and of the low nonlinear effects in SI-FMFs. Moreover, the MDM simulations shown that for long-haul transmission higher-order MIMO processing is required to recover the transmitted signals.

In chapter 4, the design of FMFs with a DMD lower than 12 ps/km over the C-band suitable for long-haul transmission has been presented, focusing on the design of 2M-FMFs suitable for the conceptual demonstration of the first MDM-FMF systems and on the design of FMFs with up to 12M assessing the scalability potential of MDM-FMF systems. The design of 2M-FMFs has considered a GCCT refractive index profile. By optimizing the core grading exponent and the dimensioning of the trench, a deviation lower than 0.01 ps/km from a target DMD has been observed over the C-band. Additionally, it has been found that the dimensioning of the trench is almost independent of the target DMD, thereby enabling the use of a simple design rule which guarantees a maximum DMD deviation of 1.8 ps/km for a DMD target between -200 ps/km to 200 ps/km. However, the existing fabrication control process does not have enough precision to guarantee that every pre-form produces a FMF

with a DMD lower than the 12 ps/km requirement. The design of FMFs with up to 12M has considered a GCCT profile and a MSI profile. The profiles parameters were optimized in order to achieve: the lowest possible DMD and MBL lower than the ITU-T standard recommendation. The optimization results have shown that the MSI profiles present lower DMD than the minimum achievable with a GCCT profile. Moreover, it has been shown that the optimum DMD and the MBL scale with the number of modes for both profiles. The optimum DMD obtained for 12M is lower than 3 ps/km using a GCCT profile and lower than 2.5 ps/km using a MSI profile. The optimization results revealed that the most preponderant parameter of the GCCT profile is the refractive index relative difference at the core axis, Δn_{co}. Reducing Δn_{co}, the DMD is reduced at the expense of increasing the MBL. Regarding the MSI profiles, it has been shown that 64 steps are required to obtain a DMD improvement considering 12M. Finally, the impact of the fabrication margins on the optimum DMD was analyzed. The probability of having a manufactured FMF with 12M modes and DMD lower than 12 ps/km is approximately 68 % using a GCCT profile and 16 % using a MSI profile. In conclusion, the GCCT is the preferred profile with current fabrication margins.

In chapter 5, three methods to extend the reach of MDM-FMF systems have been proposed. The first method reduces the CIR spread and the remaining two methods reduce the penalty due to MDG from MMAs. The first method proposes the introduction of discrete mode permutation using displaced core fiber splices along the transmission fiber. The concept has been applied to ultra-long-haul transmission over ILD-FMFs and DC-FMFs. The results have shown that the distance reach can be increased by a factor from 1.6 to 1.9 for the considered transmission systems. Additionally the results have shown that, for the case of DC-FMFs, the distance reach can be improved just by increasing the number of DC-FMF segments composing a single fiber span, even for negligible splices XT. The second and third method propose the use of FMFs with high distributed linear XT and ML detection, respectively. ML detection, ZF and MMSE equalization have been compared in the presence of MDG for low and high dXT. It has been shown that high dXT increases the MDG tolerance for any of the equalization and detection schemes considered. Furthermore, it has been shown that ML detection significantly outperforms the ZF and MMSE equalizers in the case of high dXT. In contrast, for low dXT all DSP schemes showed similar performance.

In chapter 6, the impact of IM-NLs on MDM-WDM-FMF systems has been investigated. For such purpose, a set of MM-MW-CNLSE including linear XT was

derived. The MM-MW-CNLSE allowed studying IM-XPM and IM-FWM separately from each other and from FWM and XPM. The MM-MW-CNLSE has shown a good match to experimental results provided in the literature for IM-XPM and IM-FWM. Afterwards, the impact of XPM/IM-XPM and FWM/IM-FWM in MDM-WDM-FMF systems was assessed. The impact of linear XT on the IM-NL efficiencies has shown to be significant only for the IM-NL between pairs of degenerate modes. The dominant NL effect limiting the MDM-WDM-FMF system performance was found to be IM-FWM between the degenerate modes (LP_{11a} and LP_{11b}). The performance of the non-degenerate mode (LP_{01}) was found to be limited by IM-XPM with a magnitude similar to XPM. The DMD frequency slope has shown to increase significantly the IM-FWM degradation between pairs of non-degenerate modes and to have negligible impact in the IM-XPM penalty. Moreover, it has been verified that the degradation of the center channel of a given mode in a MDM-WDM-FMF system can be obtained calculating independently the degradation coming from XPM/IM-XPM and from FWM/IM-FWM. Finally, it has been concluded that, in order to have reduced IM-NL efficiency between non-degenerate modes over the entire WDM grid, a DMD higher than 630 ps/km is required, considering 81 channels separated by 50 GHz and a chromatic dispersion of 20 ps/(km·nm), thereby imposing difficulties for long-haul applications. The IM-NL efficiency between degenerate modes can be reduced by designing FMFs with enhanced linear XT (using a fiber spinning process, for example).

7.2 Future Work

As a final note, some of the topics that were not pursued in this thesis, due to time limitations, are enumerated:

1. Design of LPFG with low loss and high mode extinction ratio, suitable for MMUXs/MDMUXs and for the introduction of discrete linear XT along the fiber length.

2. Design of FMFs aiming simultaneously low DMD and high resilience to fabrication margins.

3. Design of FMFs with high linear XT in order to reduce IM-NLs between degenerate modes.

4. Investigation of the nonlinear tolerance in MDM-WDM-FMF systems considering different modulation formats with high constellation orders.

Appendix A

Semi-Analytical Solutions for Three Modes

Following the derivation described in section 3.2.1, the analytical equations for $a_{u,i}$ and $(d_z^i A_u)_{z=0}$ as a function of $\Delta\beta_{u,u_1}$ and C_{u,u_1} for $M = 3$ are presented below.

$$\begin{bmatrix} a_{1,0} \\ a_{1,1} \\ a_{1,2} \\ a_{1,3} \\ a_{1,4} \end{bmatrix} = \begin{bmatrix} 1 \\ \\ \mathrm{j} \cdot (-2 \cdot \Delta\beta_{12} - \Delta\beta_{13}) \\ \\ -\Delta\beta_{12}^2 - 2 \cdot \Delta\beta_{13} \cdot \Delta\beta_{12} + C_{12}^2 + C_{13}^2 \\ \\ \mathrm{j} \cdot (C_{23}^2 \Delta\beta_{13} \cdot \Delta\beta_{12}^2 - \Delta\beta_{12} \cdot \ C_{12}^2 - 2 \cdot \Delta\beta_{12} \cdot \ C_{13}^2 \\ -\Delta\beta_{12} \cdot \ C_{23}^2 - \Delta\beta_{13} \cdot \ C_{12}^2 - 2 \cdot \ C_{12} \cdot \ C_{13} \cdot \ C_{23}) \\ \\ -\Delta\beta_{12} \cdot (\Delta\beta_{13} \cdot \ {C_{12}}^2 + 2 \cdot \ C_{23} \cdot \ C_{12} \cdot \ C_{13} + \Delta\beta_{12} \cdot \ {C_{13}}^2) \end{bmatrix}$$

$$\begin{bmatrix} a_{2,0} \\ a_{2,1} \\ a_{2,2} \\ a_{2,3} \\ a_{2,4} \end{bmatrix} = \begin{bmatrix} \text{-1} \\ -3 \cdot \Delta\beta_{12} \cdot \text{j} + \Delta\beta_{13} \cdot \text{j} \\ 3 \cdot \Delta\beta_{12}^2 - 2 \cdot \Delta\beta_{13} \cdot \Delta\beta_{12} - C_{12}^2 - C_{13}^2 - C_{23}^2 \\ \text{j} \cdot (\Delta\beta_{12}^3 - \Delta\beta_{13} \cdot \Delta\beta_{12}^2 - 2 \cdot \Delta\beta_{12} \cdot\ C_{12}^2 - \Delta\beta_{12} \cdot\ C_{13}^2 \\ -2 \cdot \Delta\beta_{12} \cdot\ C_{23}^2 + \Delta\beta_{13} \cdot\ C_{12}^2 + 2 \cdot\ C_{12} \cdot\ C_{13} \cdot\ C_{23}) \\ \Delta\beta_{12} \cdot (\Delta\beta_{12} \cdot\ C_{12}^2 - \Delta\beta_{13} \cdot\ C_{12}^2 + \Delta\beta_{12} \cdot\ C_{23}^2 - 2 \cdot\ C_{12} \cdot\ C_{13} \cdot\ C_{23})) \end{bmatrix}$$

$$\begin{bmatrix} a_{3,0} \\ a_{3,1} \\ a_{3,2} \\ a_{3,3} \\ a_{3,4} \end{bmatrix} = \begin{bmatrix} \text{-1} \\ \text{j} \cdot (\Delta\beta_{12} - 3 \cdot \Delta\beta_{13}) \\ 3 \cdot \Delta\beta_{13}^2 - 2 \cdot \Delta\beta_{12} \cdot \Delta\beta_{13} - C_{12}^2 - C_{13}^2 - C_{23}^2 \\ \text{j} \cdot (\Delta\beta_{13}^3 - \Delta\beta_{12} \cdot \Delta\beta_{13}^2 - \Delta\beta_{13} \cdot\ C_{12}^2 - 2 \cdot \Delta\beta_{13} \cdot\ C_{13}^2 \\ -2 \cdot \Delta\beta_{13} \cdot\ C_{23}^2 + 2 \cdot\ C_{12} \cdot\ C_{13} \cdot\ C_{23} + \Delta\beta_{12} \cdot\ C_{13}^2) \\ -\Delta\beta_{13} \cdot (\Delta\beta_{12} \cdot\ C_{13}^2 - \Delta\beta_{13} \cdot\ C_{13}^2 - \Delta\beta_{13} \cdot\ C_{23}^2 + 2 \cdot\ C_{12} \cdot\ C_{13} \cdot\ C_{23}) \end{bmatrix}$$

$$
\begin{bmatrix} d_z^0 A_1 \\ d_z^1 A_1 \\ d_z^2 A_1 \\ d_z^3 A_1 \end{bmatrix}_{z=0} =
\begin{bmatrix}
A_1 \\
\\
-\mathrm{j} \cdot (C_{12} \cdot \ A_2 + C_{13} \cdot \ A_3) \\
\\
-C_{12} \cdot (C_{12} \cdot \ A_1 + C_{23} \cdot \ A_3) + \Delta\beta_{12} \cdot \ C_{12} \cdot \ A_2 \\
+\Delta\beta_{13} \cdot \ C_{13} \cdot \ A_3 - C_{13} \cdot (C_{13} \cdot \ A_1 + C_{23} \cdot \ A_2) \\
\\
-\mathrm{j} \cdot \ C_{12} \cdot (-C_{23} \cdot (C_{13} \cdot \ A_1 + C_{23} \cdot \ A_2) - \Delta\beta_{12} \cdot \ C_{12} \cdot \ A_1 \\
+\Delta\beta_{23} \cdot \ C_{23} \cdot \ A_3 - C_{12} \cdot (C_{12} \cdot \ A_2 + C_{13} \cdot \ A_3)) \\
-\mathrm{j} \cdot \ C_{13} \cdot (-C_{23} \cdot (C_{12} \cdot \ A_1 + C_{23} \cdot \ A_3) - \Delta\beta_{13} \cdot \ C_{13} \cdot \ A_1 \\
-\Delta\beta_{23} \cdot \ C_{23} \cdot \ A_2 - C_{13} \cdot (C_{12} \cdot \ A_2 + C_{13} \cdot \ A_3)) \\
-\mathrm{j} \cdot 2 \cdot \Delta\beta_{13} \cdot \ C_{13} \cdot (C_{13} \cdot \ A_1 + C_{23} \cdot \ A_2) \\
-\mathrm{j} \cdot 2 \cdot \Delta\beta_{12} \cdot \ C_{12} \cdot (C_{12} \cdot \ A_1 + C_{23} \cdot \ A_3) \\
+\mathrm{j} \cdot \Delta\beta_{12}^2 \cdot \ C_{12} \cdot \ A_2 + \mathrm{j} \cdot \Delta\beta_{13}^2 \cdot \ C_{13} \cdot \ A_3
\end{bmatrix}
$$

$$
\begin{bmatrix} d_z^0 A_2 \\ d_z^1 A_2 \\ d_z^2 A_2 \\ d_z^3 A_2 \end{bmatrix}_{z=0} =
\begin{bmatrix}
A_2 \\
\\
-\mathrm{j} \cdot (C_{12} \cdot\ A_1 + C_{23} \cdot\ A_3) \\
\\
-C_{23} \cdot (C_{13} \cdot\ A_1 + C_{23} \cdot\ A_2) - \Delta\beta_{12} \cdot\ C_{12} \cdot\ A_1 \\
+\Delta\beta_{23} \cdot\ C_{23} \cdot\ A_3 - C_{12} \cdot (C_{12} \cdot\ A_2 + C_{13} \cdot\ A_3) \\
\\
-C_{12} \cdot (-C_{12} \cdot (C_{12} \cdot\ A_1 + C_{23} \cdot\ A_3) + \Delta\beta_{12} \cdot\ C_{12} \cdot\ A_2 \\
+\Delta\beta_{13} \cdot\ C_{13} \cdot\ A_3 + C_{13} \cdot (C_{13} \cdot\ A_1 \cdot \mathrm{j} + C_{23} \cdot\ A_2 \cdot \mathrm{j}) \cdot \mathrm{j}) \cdot \mathrm{j} \\
-\mathrm{j} \cdot\ C_{23} \cdot (-C_{23} \cdot (C_{12} \cdot\ A_1 + C_{23} \cdot\ A_3) - \Delta\beta_{13} \cdot\ C_{13} \cdot\ A_1 \\
-\Delta\beta_{23} \cdot\ C_{23} \cdot\ A_2 - C_{13} \cdot (C_{12} \cdot\ A_2 + C_{13} \cdot\ A_3)) \\
+\mathrm{j} \cdot\ 2 \cdot \Delta\beta_{12} \cdot\ C_{12} \cdot (C_{12} \cdot\ A_2 + C_{13} \cdot\ A_3) \\
-\mathrm{j} \cdot\ 2 \cdot \Delta\beta_{23} \cdot\ C_{23} \cdot (C_{13} \cdot\ A_1 + C_{23} \cdot\ A_2) \\
+\mathrm{j} \cdot \Delta\beta_{12}^2 \cdot\ C_{12} \cdot\ A_1 + \mathrm{j} \cdot \Delta\beta_{23}^2 \cdot\ C_{23} \cdot\ A_3
\end{bmatrix}
$$

$$
\begin{bmatrix} d_z^0 A_3 \\ d_z^1 A_3 \\ d_z^2 A_3 \\ d_z^3 A_3 \end{bmatrix}_{z=0} =
\begin{bmatrix}
A_3 \\
\\
-\mathrm{j} \cdot (C_{13} \cdot \ A_1 + C_{23} \cdot \ A_2) \\
\\
-C_{23} \cdot (C_{12} \cdot \ A_1 + C_{23} \cdot \ A_3) - \Delta\beta_{13} \cdot \ C_{13} \cdot \ A_1 \\
-\Delta\beta_{23} \cdot \ C_{23} \cdot \ A_2 - C_{13} \cdot (C_{12} \cdot \ A_2 + C_{13} \cdot \ A_3) \\
\\
-\mathrm{j} \cdot \ C_{13} \cdot (C_{12} \cdot (-C_{12} \cdot \ A_1 + C_{23} \cdot \ A_3) + \Delta\beta_{12} \cdot \ C_{12} \cdot \ A_2 \\
+\Delta\beta_{13} \cdot \ C_{13} \cdot \ A_3 - C_{13} \cdot (C_{13} \cdot \ A_1 + C_{23} \cdot \ A_2)) \\
-\mathrm{j} \cdot \ C_{23} \cdot (-C_{23} \cdot (C_{13} \cdot \ A_1 + C_{23} \cdot \ A_2) - \Delta\beta_{12} \cdot \ C_{12} \cdot \ A_1 \\
+\Delta\beta_{23} \cdot \ C_{23} \cdot \ A_3 - C_{12} \cdot (C_{12} \cdot \ A_2 + C_{13} \cdot \ A_3)) \\
+\mathrm{j} \cdot \ 2 \cdot \Delta\beta_{13} \cdot \ C_{13} \cdot (C_{12} \cdot \ A_2 + C_{13} \cdot \ A_3) \\
+\mathrm{j} \cdot \ 2 \cdot \Delta\beta_{23} \cdot \ C_{23} \cdot (C_{12} \cdot \ A_1 + C_{23} \cdot \ A_3) \\
+\mathrm{j} \cdot \Delta\beta_{13}^2 \cdot \ C_{13} \cdot \ A_1 + \mathrm{j} \cdot \Delta\beta_{23}^2 \cdot \ C_{23} \cdot \ A_2
\end{bmatrix}
$$

Appendix B

Optimization of ILD-FMFs and DC-FMFs

This appendix presents the design of FMFs with low DMD over the C-band, considering a refractive index profile with a graded core and a cladding trench. By optimizing the core grading exponent and the dimensioning of the trench, the lowest DMD achievable is obtained for different numbers of LP modes. Additionally, considering the concatenation of two FMFs with profiles of the same type but with different parameters values, both profiles are optimized in order to minimize the residual DMD. For both cases, the accumulated DMD increase rate with the number of LP modes is presented, as well as the maximum distance reach for MDM transmission.

B.1 Introduction

The ever growing demand for higher data rate is rapidly exhausting the capacity available for SMFs, determined by the nonlinear Shannon limit. In order to overcome the upcoming capacity crunch, the space dimension of optical fibers is emerging as an attractive solution. In order to exploit the space dimension, the use of FMFs and MDM has been recently proposed [1]. Using MDM, a gain of N-fold can be theoretically achieved for a FMF with N independent guided modes [2]. However, the multitude of guided modes introduces DMD and linear modal XT, which originates a CIR spread over a time interval [3]. In order to mitigate such effect, the complexity

of the equalizer for MDM systems is significantly higher than that for SMFs.

The DMD is one of the main parameters that determine the reach of a MDM system. Two different approaches have been proposed to limit the accumulation of DMD: the use of FMFs with ILD-FMFs and the use of DC-FMFs (see chapter 4). The experimental reports about these approaches considered mostly FMFs with 2 LP modes (2M) [1, 4–6]. However, in order to further increase capacity, the use of fibers with higher order modes is necessary [7].

In this appendix, it is presented the design of ILD-FMFs and DC-FMFs supporting 4 and 6 non-degenerate LP modes, with the lowest possible DMD over the C-band, considering the GCCT profile used in section 4.2. In section B.2, the refractive index profile under consideration is described, as well as the optimization functions (OFs). Section B.3 presents the optimization results, showing that it is possible to reduce the DMD of the worst mode to $\sim$5 ps/km for 4M-FMFs and to $\sim$10 ps/km for 6M-FMFs. The main conclusions are presented in section B.4.

B.2 Fiber Profile Description and Optimization

The refractive index profile under consideration is composed by a graded core and a cladding trench, as already used in section 4.2. In this appendix, the mathematical description of the profile presented in section 4.2 is followed. The core is characterized by the relative refractive index difference at the core axis Δn_{co}, by the power-law exponent α and by the core radius w_1. The trench dimensioning is characterized by the radial distance to the end of the core w_2, by the trench width w_3, and by the relative refractive index difference at the trench Δn_{tr}. During the optimization, the guided modes supported by the fiber and their characteristics, as well as the effective group index of each mode $\mathrm{LP}_{\mu\nu}$, $\overline{n}_g^{\mathrm{LP}_{\mu\nu}}$, were calculated using the method described in [8].

There are two parameters that can be defined without optimization: w_1 and Δn_{co}. w_1 should be as large as possible in order to reduce the nonlinear coefficients for all

modes. Therefore, the highest normalized frequency V (calculated as in section 4.2) that guarantees a certain number of LP modes is used, considering $\Delta n_{co} = 4.5 \times 10^{-3}$, $\alpha = 2$, $\Delta n_{tr} = 0$ and the lowest wavelength (λ) of the C-band 1530 nm. For 4M and 6M, V is 7.25 and 9, and the corresponding w_1 is 12.83 and 15.92 µm, respectively.

In order to search for the optimum α and dimensioning of the trench (Δn_{tr}, w_2, w_3), OFs are introduced. The DMD of each mode ($\mathrm{LP}_{\mu\nu}$) is measured relatively to the LP_{01} mode and is given by:

$$DMD_{\mathrm{LP}_{\mu\nu}}(\lambda) = \frac{1}{c}[\overline{n}_g^{\mathrm{LP}_{\mu\nu}}(\lambda) - \overline{n}_g^{\mathrm{LP}_{01}}(\lambda)] \tag{B.1}$$

where c is the light velocity in vacuum. As a consequence, for a single FMF there are as many DMD values as LP modes minus one.

The optimum search process requires two different OFs: one for the ILD-FMFs and one for the DC-FMFs. The OF for the ILD-FMFs, OF_{ILD} is given by:

$$\begin{aligned} OF_{ILD}(\beta) &= (1-\beta)\cdot DM + \beta \cdot DV \\ DM &= \max_{\lambda}\left(\max_{\mu\nu}\left|DMD_{\mathrm{LP}_{\mu\nu}}(\lambda)\right|\right) \\ DV &= \max_{\mu\nu}\left(\max_{\lambda}\left(DMD_{\mathrm{LP}_{\mu\nu}}\right) - \min_{\lambda}\left(DMD_{\mathrm{LP}_{\mu\nu}}\right)\right) \end{aligned} \tag{B.2}$$

The objective of (B.2) is the simultaneous minimization of the DMD maximum magnitude (DM) and of the DMD maximum variation over the C-band (DV) weighted by the β parameter, for the worst mode of a single FMF. By using different terms for DM and DV it is possible to analyze them independently and determine if they can be simultaneously minimized (or only separately). Figure B.1 provides an example for the calculation of the OF_{ILD} terms for a 2M-FMF. The OF for the DC-FMFs, OF_{DC} is given by:

$$OF_{DC}(\phi) = \max_{\lambda}\left(\max_{\mu\nu}\left|(1-\phi)\cdot pDMD_{\mathrm{LP}_{\mu\nu}}(\lambda) - \phi \cdot nDMD_{\mathrm{LP}_{\mu\nu}}(\lambda)\right|\right) \tag{B.3}$$

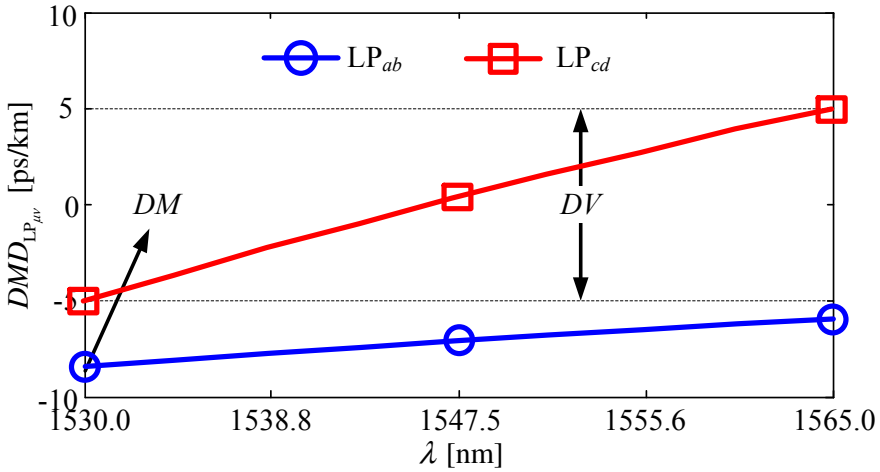

Figure B.1: OF_{ILD} calculation example.

The objective of (B.3) is the minimization of the residual DMD ($rDMD$) for the combination of a pFMF (with $DMD_{\mathrm{LP}_{\mu\nu}} = pDMD_{\mathrm{LP}_{\mu\nu}}$ and length $(1-\phi)$) and a nFMF (with $DMD_{\mathrm{LP}_{\mu\nu}} = nDMD_{\mathrm{LP}_{\mu\nu}}$ and length ϕ). The $rDMD$ of each mode ($\mathrm{LP}_{\mu\nu}$) is calculated as: $rDMD_{\mathrm{LP}_{\mu\nu}} = pDMD_{\mathrm{LP}_{\mu\nu}} \times (1-\phi) + nDMD_{\mathrm{LP}_{\mu\nu}} \times \phi$. Note that $rDMD$ maximum magnitude can be low for a pFMF or nFMF (or both) with high DMD maximum magnitude. Finally, the OFs presented are subject to constraints similar to those used in section 4.2.

B.3 Optimization Results

B.3.1 ILD-FMFs

In this sub-section the optimum DMD results obtained for ILD-FMFs are presented. The DM and DV are shown in Fig. B.2(a) and (b) as functions of λ for 4M and 6M, respectively. Fig. B.2(c) and (d) show the $DMD_{\mathrm{LP}_{\mu\nu}}$ as a function of λ for the optimum parameters $(\alpha, \Delta n_{tr}, w_2, w_3)$ obtained for 4M and 6M, respectively, with $\beta = 0$. These results show that for β below 0.9, the DM and DV of the optimum DMD obtained are non-negligible. In order to obtain a significant DV reduction, β has to be increased above 0.9. However, for such range of β, the DM reaches values not tolerable for long haul transmission [7]. This means that a ILD-FMF cannot have

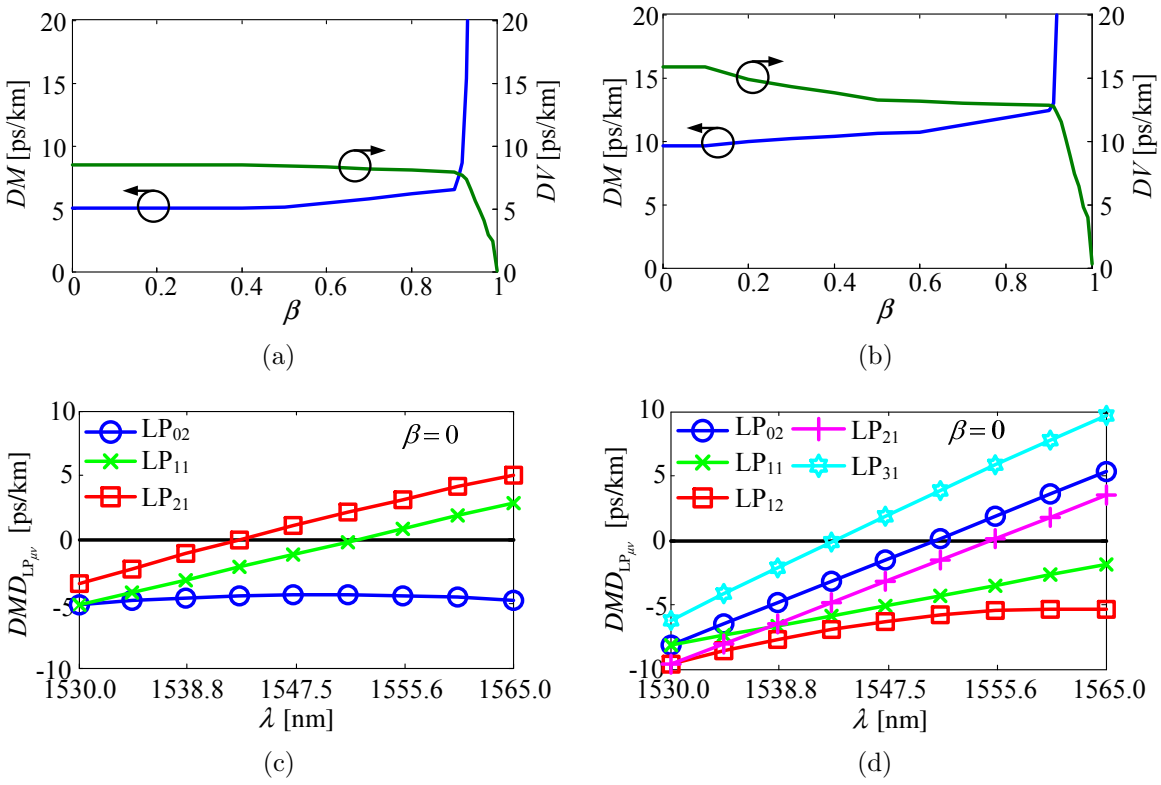

Figure B.2: DM and DV as a function of β, for: (a) 4M and (b) 6M. $DMD_{LP_{\mu\nu}}$ as a function of λ for the optimum parameters with $\beta = 0$, for: (c) 4M and (d) 6M.

simultaneously a low DM and a low DV, and that a low DV implies a high DM, for more than 2M [7]. These limitations are explained noting that the field confinement effect of the trench affects not only the LP_{11} mode (the first higher-order mode) but also the other higher-order modes (LP_{02}, LP_{21}, LP_{12}, LP_{31}), since all of them have a considerable power concentration near the core boundary. Therefore, it is not possible to reduce the DMD of all modes at the same time over the C-band (further results have shown that not even for a single λ value). Finally, it can be concluded that the DMD for FMFs with more than 2M cannot be reduced to negligible values for the refractive index profile considered, as shown in section 4.2 for 2M. Even so, the DMD values presented in Fig. B.2(c) and (d) are compatible with long haul transmission [7]. The remaining properties of the optimized FMFs have been computed for $\lambda = 1550\,\text{nm}$ according to the method described in [8]: the curvature radius (R_c) for a macrobending loss (MBL) of 0.5 dB, the chromatic dispersion (D), the chromatic dispersion slope (S) and the nonlinear coefficient (γ). The R_c value determined is below 7.5 mm.

The D value is around 21 ps/(nm·km), only slightly higher than the dispersion of ∼17 ps/(nm·km) characteristic of SSMF. The S value is around 0.068 ps/(nm^2·km), lower than the value of ∼0.08 ps/(nm^2·km) typical of SSMF. The γ value for the LP_{01} mode (the most restrictive) is around 0.74 for 4M and 0.6 for 6M, significantly lower than the SSMF typical value of 1.3. The decrease of the γ value with the number of modes was expectable due to the increase of the core radius.

B.3.2 DC-FMFs

In this sub-section, two different optimization processes for the design of DC-FMFs are implemented using (B.3). The first process (P1) optimizes the nFMF parameters considering a pFMF with fixed parameters $(\alpha, \Delta n_{tr}, w_2, w_3)$, for 4M and 6M. The 4M-pFMF considered (obtained using the results presented in section B.3.1) has $DM \approx 100$ ps/km and $DV \approx 3$ ps/km (corresponding to $\beta = 0.98$). The 6M-pFMF considered has $DM \approx 140$ ps/km and $DV \approx 5$ ps/km (corresponding to $\beta = 0.98$). These DM values are similar to those used in [5]. The second process (P2) searches for the optimum parameters $(\alpha, \Delta n_{tr}, w_2, w_3)$ for the pFMF and for the nFMF simultaneously, considering that they have the same w_2 and w_3. The OF_{DC} results obtained using P1 and P2 are presented in Fig. B.3(a). Fig. B.3(a) shows that both methods give similar results for $\phi < 0.5$, similar to the DM results obtained in Section B.3.1 for $\beta = 0$. The increase of OF_{DC} obtained using P1 for $\phi > 0.5$ in Fig.B.3(a), can be justified by the limitation on the nDMD values/shape imposed by the fixed pDMD and ϕ (pFMF is getting longer than the nFMF with ϕ and thus the nFMF DM has to increase with ϕ). For P2, since none of the FMFs are fixed, the OF_{DC} converges to solutions with low $rDMD$ for every ϕ. Note that the $rDMD$ maximum magnitude obtained using P1 is slightly lower than the one obtained using P2 and than the DM values obtained in section B.3.1. The optimum $rDMD$ results with $\phi = 0.5$, using P1 and P2, for 4M and 6M, are shown in Fig. B.3(b), (c), (d) and (e). These results show that for DC-FMFs it is not possible to reduce neither the $rDMD$ maximum magnitude, neither the $rDMD$ maximum variation over the C-band to negligible lev-

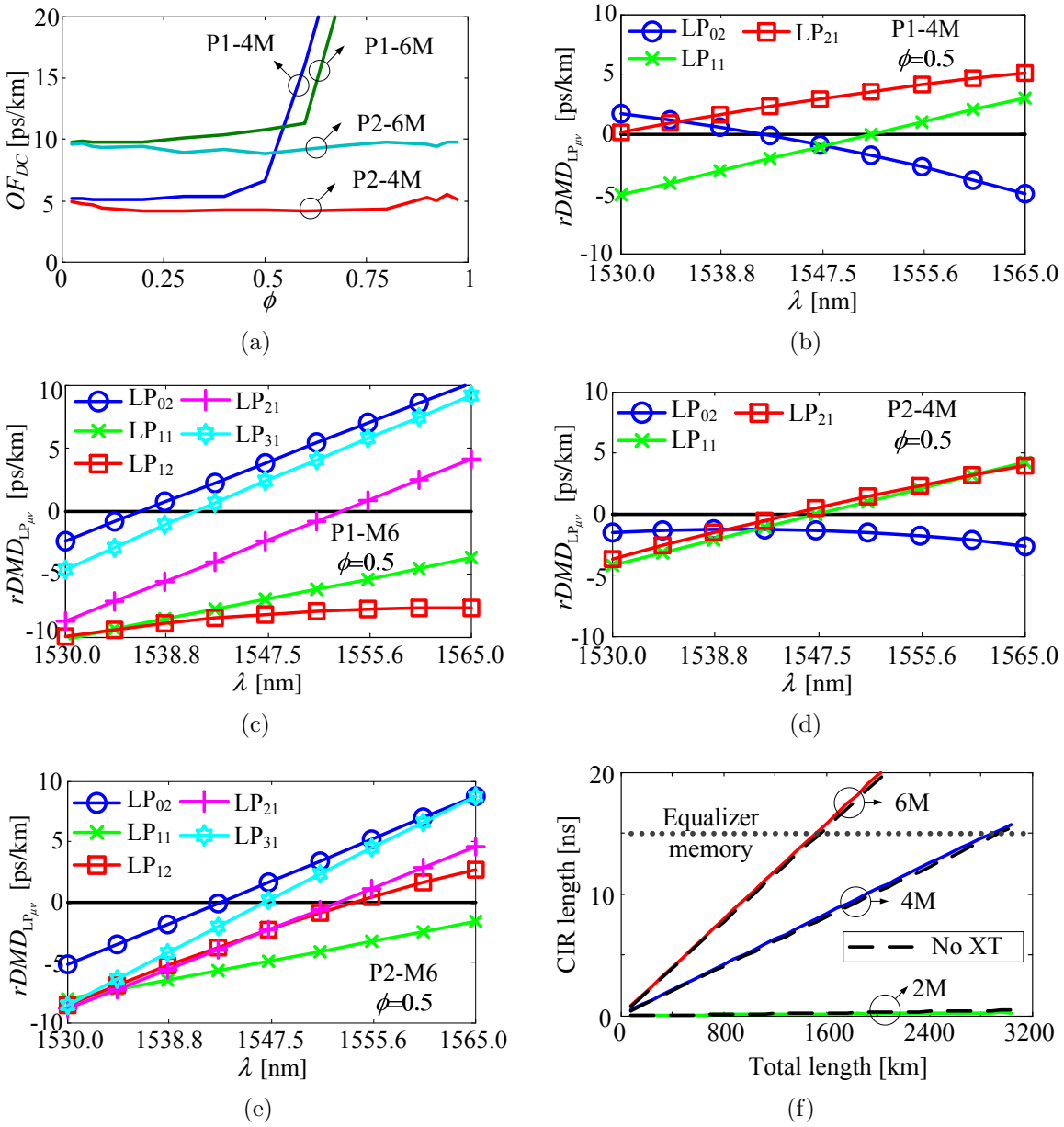

Figure B.3: (a) OF_{DC} as a function of ϕ obtained using P1 and P2, for 4M and 6M. $rDMD$ as a function of λ obtained using: (b) P1 for 4M, (c) P1 for 6M, (d) P2 for 4M and (e) P2 for 6M. (f) CIR length as a function of the total length for the optimum ILD-FMFs in section B.3.1.

els, as found in section B.3.1 for ILD-FMFs. Regarding the characteristic parameters R_c, D, S and γ of the fibers designed following the given OF_{DC}, their values are very similar to the values obtained in Section B.3.1 and therefore, similar comments are applicable.

The results presented above allow concluding that a refractive index profile with graded core and a cladding trench is suitable for the design of ILD-FMFs and DC-FMFs with 4M and 6M, though it is not possible to reduce the DMD and $rDMD$ to negligible levels over the whole C-band. In order to evaluate the increase rate of the CIR length with the number of LP modes and with the total length, transmission simulations over the optimum ILD-FMFs obtained in section B.3.1 have been performed. The transmission simulations considered the distributed XT (dXT) introduced by waveguide imperfections and fiber bends, as considered and modeled in [9]. Fig. B.3(f) shows the CIR length (calculated as in section 4.2) as a function of the total length. The results show that the CIR length scales almost linearly with total length due to the weak dXT, independently of the number of LP modes, as can be concluded by comparing with the dashed line representing the CIR length in the absence of any form of XT. Considering an equalizer capable of compensating the transmission effects contained within a time interval of 15 ns [9], the maximum transmission distance for the 4M-ILD-FMF is 2880 km and for the 6M-ILD-FMF is 1520 km. Further results have shown that for the optimized DC-FMFs similar maximum transmission distances can be obtained considering segments of ∼5 km (see section 5.2).

B.4 Conclusions

In this appendix, a graded-index FMF with a cladding trench is optimized through simulation in order to obtain a low DMD over the C-band for 4M and 6M. It has been shown that such design allows obtaining ILD-FMFs with DMD of approximately 5 and 10 ps/km for 4M and 6M, respectively. Similar $rDMD$ values have been obtained for DC-FMFs. Therefore, for FMFs with more than 2M and for the profile considered it is not possible to reduce the DMD to negligible levels. Even so, the optimized FMFs are suitable for long-haul transmission over the C-band. The maximum distance reach for the optimum 4M-FMFs is 2880 km and for the optimum 6M-FMFs is 1520 km, considering a equalizer with a 15 ns memory.

References

[1] R. Ryf, R. Essiambre, J. Hoyningen-Huene, and P. Winzer, "Analysis of mode-dependent gain in Raman amplified few-mode fiber," in *Proc. Optical Fiber Communication Conference and Exposition*, March 2012, p. OW1D.2.

[2] R. Essiambre and A. Mecozzi, "Capacity limits in single-mode fiber and scaling for spatial multiplexing," in *Proc. Optical Fiber Communication Conference and Exposition*, March 2012, p. OW3D.1.

[3] A. Lobato, F. Ferreira, B. Inan, M. Kuschnerov, D. van den Borne, S. Jansen, B. Spinnler, and B. Lankl, "The Impact of Differential Mode Delay on Mode-Division Multiplexed Coherent Optical OFDM Transmission," in *Proc. Optical Fiber Communication Conference and Exposition*, March 2012, p. OTu2C.2.

[4] L. Grüner-Nielsen, Y. Sun, J. Nicholson, D. Jakobsen, R. Lingle, and B. Palsdottir, "Few mode transmission fiber with low DGD, low mode coupling and low loss," in *Proc. Optical Fiber Communication Conference and Exposition*, March 2012, pp. 1–3.

[5] P. Matthijsse, D. Molin, F. Gooijer, and G. Kuyt, "On the Design of Wide Bandwidth Window Multimode Fibers," in *Proc. International Workshop Computing Semantics*, 2005, pp. 332–337.

[6] S. Randel, R. Ryf, A. Gnauck, M. Mestre, C. Schmidt, R. Essiambre, P. Winzer, R. Delbue, P. Pupalaikis, and A. Sureka, "Mode-multiplexed 6×20-GBd QPSK transmission over 1200-km DGD-compensated few-mode fiber," in *Proc. Optical Fiber Communication Conference and Exposition*, March 2012, p. PDP5C.5.

[7] B. Inan, B. Spinnler, F. Ferreira, D. van den Borne, A. Lobato, S. Adhikari, V. Sleiffer, M. Kuschnerov, N. Hanik, and S. Jansen, "DSP complexity of mode-division multiplexed receivers," *Optics Express*, vol. 20, no. 10, pp. 10 859–10 869, April 2012.

[8] F. Ferreira, D. Fonseca, and H. Silva, "Design of Few-Mode Fibers with Arbitrary and Flattened Differential Mode Delay," *IEEE Photonics Technology Letters*, vol. 25, no. 5, pp. 438–441, March 2013.

[9] F. Ferreira, D. Fonseca, A. Lobato, B. Inan, and H. Silva, "Reach Improvement of Mode Division Multiplexed Systems Using Fiber Splices," *IEEE Photonics Technology Letters*, vol. 25, no. 12, pp. 1091–1094, June 2013.

Appendix C

Optimum xM-FMFs Characteristics

The mode characteristics of the optimum profiles found in section 4.3 with $\Delta n_{co} = 1{\cdot}10^{-3}$ and $\epsilon = 1$ are shown in Table C.1, namely: $DMD_{\mathrm{LP}_{\mu\nu}}$ for the worst wavelength of the C-band, D at 1550 nm, effective area (A^{eff}) at 1550 nm, and R_c.

Table C.1: Characteristics for the Optimum GCCT Profile and Optimum MSI profile.

	Number of modes								
	2	4	4	6	6	9	9	12	12
	GCCT	GCCT	MSI	GCCT	MSI	GCCT	MSI	GCCT	MSI
	$DMD_{\mathrm{LP}_{\mu\nu}}$ [ps/km]								
LP_{11}	0	-1.35	0.91	-1.58	1.04	-1.14	-1.63	-1.21	1.06
LP_{02}		-1.35	0.92	1.98	-1.7	-1.58	1.95	-1.27	1.18
LP_{21}		-1.35	-0.93	-2.25	-1.74	-2.49	-1.72	-2.49	1.44
LP_{12}				-1.58	0.77	-1.14	-1.88	-1.21	2.28
LP_{31}				-2.25	1.75	-1.85	-1.93	-2.77	1.86
LP_{03}						-2.4	1.65	2.81	2.43
LP_{22}						-2.49	-0.98	-2.77	2.29
LP_{41}						-1.85	1.86	-1.79	2.21
LP_{13}								-2.49	-2.27
LP_{32}								-1.79	-1.87
LP_{51}								-3	-2.33
	R_c [mm]								
LP_{01}	12.4	14.8	16.1	14.8	13.9	17.5	18.1	18.7	17.5
LP_{11}	15.1	17.5	19.1	16.9	15.8	19.6	20.5	20.7	19.4
LP_{02}		19.8	21.5	18.7	17.5	21.4	22.3	22.3	20.7
LP_{21}		19.9	21.5	18.7	17.5	21.4	22.5	22.3	20.8
LP_{12}				20.8	19.5	23.8	24.9	24.4	22.8
LP_{31}				20.3	19	23.3	24.3	23.9	22.3
LP_{03}						25.4	26.5	26.1	24.2
LP_{22}						25.6	26.6	26.2	24.3
LP_{41}						24.9	26	25.6	23.7
LP_{13}								28	26.3
LP_{32}								27.7	25.9
LP_{51}								27	25

Continued on next page

Continued from previous page

	Number of modes								
	2	4	4	6	6	9	9	12	12
	GCCT	GCCT	MSI	GCCT	MSI	GCCT	MSI	GCCT	MSI
	D [ps/(nm·km)]								
LP_{01}	22.5	22.5	22.5	22.5	22.5	22.5	22.5	22.5	22.5
LP_{11}	22.4	22.5	22.5	22.5	22.5	22.5	22.5	22.5	22.5
LP_{02}		22.4	22.3	22.5	22.5	22.5	22.5	22.5	22.5
LP_{21}		22.5	22.4	22.5	22.5	22.5	22.5	22.5	22.5
LP_{12}				22.4	22.3	22.5	22.5	22.5	22.5
LP_{31}				22.5	22.5	22.5	22.5	22.5	22.5
LP_{03}						22.4	21.9	22.6	22.5
LP_{22}						22.5	22.2	22.5	22.5
LP_{41}						22.5	22.4	22.5	22.5
LP_{13}								22.3	22.2
LP_{32}								22.5	22.4
LP_{51}								22.5	22.5
	A_{eff} [µm^2]								
LP_{01}	476	645	653	813	727	1007	926	1167	1078
LP_{11}	627	959	869	1096	1014	1355	1135	1571	1497
LP_{02}		1390	1095	1680	1553	2077	1745	2393	2143
LP_{21}		1250	1179	1462	1410	1805	1712	2094	1908
LP_{12}				1724	1585	2213	2112	2561	2415
LP_{31}				1731	1689	2166	2057	2508	2397
LP_{03}						2928	2849	3593	3311
LP_{22}						2667	2472	3202	2863
LP_{41}						2454	2288	2870	2596
LP_{13}								3307	3400
LP_{32}								3616	3677
LP_{51}								3145	3059

Index